



Institute of Physical Chemistry  
Polish Academy of Sciences  
Kasprzaka 44/52  
01-224 Warsaw, Poland

# **Nanoengineering of Thin Layers Of Semiconductor Photocatalysts In A Microreactor Environment For Lignin- Based Model Compounds Valorization**

A thesis submitted in conformity with the requirements for the degree of

Doctor of Philosophy

in the field of

Chemical Sciences

prepared within the International Doctoral Studies in Chemistry of the Institute of Physical  
Chemistry (IPC), Polish Academy of Sciences (PAS),  
Warsaw, Poland

by

**Swaraj Rashmi Pradhan**

Supervised by

dr hab. inż. Juan Carlos Colmenares (Assoc. Prof. IPC, PAS)

Warsaw, December 2022

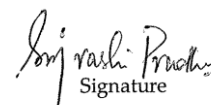
## Declaration of originality

I, Swaraj rashmi Pradhan, declare that the research included within the present thesis was conducted by myself or in collaboration with and supported by others, as described in the acknowledgments section.

I attest that I have exercised reasonable care to ensure that the work is original, and does not, to the best of my knowledge, violate any Polish or International law, infringe any third party's copyright or other Intellectual Property Right, or contains any confidential material.

I accept that the Polish Academy of Sciences has the right to use plagiarism detection software to check the electronic version of the thesis. I confirm that no part of my thesis has been or will be submitted for obtaining a degree or diploma by the Institute of Physical Chemistry, Polish Academy of Science, or any other educational institution.

The copyright of this thesis rests with the author, and no quotation from it or information derived from it may be published without the author's prior written consent.



Signature

Warsaw, 29 December 2022

Signature

# Acknowledgments

This Ph.D. would not have been possible without the support of my supervisor, Prof. Dr. Juan Carlos Colmenares. I thank him for extending his unconditional support, encouragement, freedom, and guidance during my Ph.D. study. I have learned a lot from his feedback and very forward-looking suggestions. I am thankful for all our fruitful discussions and his valuable comments on my manuscript, which kept me motivated to explore many aspects of photocatalysis and microflow chemistry.

I would like to thank:

Dr. Dariusz Łomot for supporting and transferring his exceptional technical expertise in the specialized laboratory instruments and for helping me with experimental setups.

Dr. Dmytro Lisovytskiy for XRD and XRF measurements, Dr. Wojciech Lisowski for XPS measurement, Prof. Rafał Szmigielski and Dr. Klara Nestorowicz for the analysis and interpretation of GC-MS data, and Dr. K. Sobczak (CNBCh University of Warsaw) for HR-TEM measurements.

The administrative staff of the Institute of Physical Chemistry, especially Ms. Edyta Słojewska, Dr. Agnieszka Pietrzyk-Le, Ms. Joanna Wiszniowska, and Ms. Simona Popławska, for their help and cooperation.

Prof. Dr. Fernando Colmenares from the Faculty of Engineering, Universidad Cooperativa de Colombia, Medellín, Colombia, for supporting my research as an external advisor.

I would like to extend my gratitude to all my teachers who helped me face the challenges and reach this step in life.

I have been lucky to be surrounded by great colleagues who supported me whenever I sought help for work and my personal life. I would like to thank Hermes Llain Jimenez, Dr. Vaishakh Nair, Abdul Qayyum, Laura Wrońska, Karolina Kawka, Agnieszka Dżugan, Dr. Rafael de Lima Oliveira, Behdokht Hashemi Hosseini, and Dr. Marta Paszkiewicz-Gawron. Special thanks to Dr.

Ayesha Khan, Dr. Jovana Prekodravac, and Dr. Dimitrios Giannakoudakis for letting me be crazy in the lab.

I would like to thank Alcina, Jyoti, Neha, Rashmi, Tanvi, and Viki for being my home away from home. You have made this journey much more enjoyable. Thanks for being the family I can count on anytime I need. Life would not have been the same without you all!

I would also like to thank Abhishek, Anupama, Ankita, Devika, Debjita, Karthik, Karthika, Ganesh, Luca, Mattia, Mounika, Niriqsha, Praveen, Princy, Ranju, Sangami, Sakthi, Sarath, Sahir, Shakeel for providing the much-needed distraction from my Ph.D.

I always cherish the support and warm friendship from Amisha, Amit, Nishith, Dev bhai, and Maru di for standing with me virtually from different corners of the world. Time zone never stopped you from being in touch, kept me smiling, and helped me in every possible way.

A heartfelt thanks to Hari, Nelam, Vineeta di, and Arvind bhaiya for coming into my life during the end days of this journey and standing beside me for every tear and laugh. Thanks for listening to all my problems and just fading them away through your positivity. Your love is my biggest strength, and I am so thankful for being a part of your lives.

My sincere gratitude to my strength and solace, my parents, who were always there for me. I know how much they want me to stay near them, and I thank them for still supporting my every decision and being proud of me. Special thanks to Sibbu, Didi, Jiju, Tia, Tej, and Suchi for being my constant source of motivation.

Special thanks to Dr. Nikhil (my partner in crime) for his unconditional love, continuous support, patience, and understanding. Thank you for supporting me during difficult times and encouraging me to keep working towards my goal.

Lastly, I'd like to thank my inner self for enthusing me to achieve what I have always wanted.

Unfortunately, I cannot mention everyone here, but I extend my gratitude to every single person who supported me, from the beginning of this journey until this very moment in life.



I would like to acknowledge and thank the support from National Science Centre in Poland for providing the framework and financial support for my Ph.D. within the SonataBis 5 Project No. 2015/18/E/ST5/00306.

## List of Publications

1. **Pradhan, S. R.**; Colmenares-Quintero, R. F.; Quintero, J. C. C. Designing Microflowreactors for Photocatalysis Using Sonochemistry: A Systematic Review Article. *Molecules* 2019, 24 (18). <https://doi.org/10.3390/molecules24183315>.
2. **Pradhan, S. R.**; Nair, V.; Giannakoudakis, D. A.; Lisovytskiy, D.; Colmenares, J. C. Design and Development of TiO<sub>2</sub> Coated Microflow Reactor for Photocatalytic Partial Oxidation of Benzyl Alcohol. *Mol. Catal.* 2020, 486 (February), 110884. <https://doi.org/10.1016/j.mcat.2020.110884>.
3. Giannakoudakis, D. A.; Qayyum, A.; Nair, V.; Khan, A.; **Pradhan, S. R.**; Prekodravac, J.; Rekos, K.; LaGrow, A. P.; Bondarchuk, O.; Łomot, D.; et al. Ultrasound-Assisted Decoration of CuO<sub>x</sub> Nanoclusters on TiO<sub>2</sub> Nanoparticles for Additives Free Photocatalytic Hydrogen Production and Biomass Valorization by Selective Oxidation. *Mol. Catal.* 2021, 514. <https://doi.org/10.1016/j.mcat.2021.111664>.
4. **Pradhan, S. R.**; Lisovytskiy, D.; Colmenares, J. C. Flow Photomicroreactor Coated with Monometal Containing TiO<sub>2</sub> Using Sonication: A Versatile Tool for Visible Light Oxidation. *Catal. Commun.* 2022, 162, 106375. <https://doi.org/10.1016/j.catcom.2021.106375>.
5. **Pradhan, S. R.**; Paszkiewicz-Gawron, M.; Łomot, D.; Lisovytskiy, D.; Colmenares, J. C. Bimetallic TiO<sub>2</sub> Nanoparticles for Lignin-Based Model Compounds Valorization by Integrating Optocatalytic Flow-Microreactor . *Molecules* 2022, 27(24), 8731. <https://doi.org/10.3390/molecules27248731>.

## Patent application

1. Dariusz Łomot, **Swaraj Rashmi Pradhan**, Juan Carlos Colmenares Quintero. Patent application P.430411 (30.06.2019): "A flow microreactor system and the way of conducting photocatalytic processes using it".

# Active participation at scientific conferences

## Oral presentations:

1. **Swaraj Rashmi Pradhan**, Karolina Kawkab, Juan Carlos Colmenares, 5th International Conference on FOSSIL & RENEWABLE ENERGY, March 01-03, 2021, Houston, TX, USA.
2. **Swaraj Rashmi Pradhan**, Juan Carlos Colmenares, 5th International Conference on New Photocatalytic Materials for Environment, Energy and Sustainability (NPM -5) and The 6th International Conference on Photocatalytic and Advanced Oxidation Technologies for the Treatment of Water, Air, Soil and Surfaces (PAOT-6), January 28, 2022, Virtual.
3. **Swaraj Rashmi Pradhan**, Dmytro Lisovytskiy, Juan Carlos Colmenares, The 54th National Catalytic Colloquium, June, 2022, Krakow, Poland.

## Poster presentations:

1. **Swaraj Rashmi Pradhan**, Vaishakh Nair, Juan Carlos Colmenares, 17th International Conference on Chemistry and the Environment (ICCE 2019), Thessaloniki, Greece.
2. **Swaraj Rashmi Pradhan**, Dimitrios A. Giannakoudakis, Agnieszka Dżugan, Juan Carlos Colmenares, 5th EUGSC, Sept 2021, Virtual.
3. **Swaraj Rashmi Pradhan**, Dmytro Lisovytskiy, Juan Carlos Colmenares, The 11th European Conference on Solar Chemistry and Photocatalysis: Environmental Applications (SPEA11), June 2022, Turin, Italy.
4. **Swaraj Rashmi Pradhan**, Dmytro Lisovytskiy, Juan Carlos Colmenares, The 9th IUPAC International Conference on Green Chemistry (9th ICGC), September 2022, Athens, Greece.

## Abstract

This thesis aims to synthesize novel thin layers of materials assisted by ultrasound techniques with photocatalytic properties on the internal wall of fluoropolymer microtube reactor for selective oxidation of lignin-based model compounds. The materials were further modified with metals like Fe, Cu, and Co for advance studies. It was expected that such materials will exhibit high surface areas and interesting properties. The critical step was to deposit sol-gel synthesized semiconductor metal oxides ( $\text{TiO}_2$ ,  $\text{ZnO}$ ) layer on the internal wall of polymeric (copolymers of tetrafluoroethylene and perfluoroethers - perfluoroalkoxy alkane) PFA microtube by a method assisted by ultrasounds. Oxidation reactions conducted in micro spaces can allow precise control of parameters like reaction time, temperature, mixing, reproducibility and safety. Continuous flow reactions may also prevent or reduce side reactions and decomposition caused by over irradiation. Irradiation can be easily controlled by controlling of the flow rate of the pumping system. These above kind of controls are expected to increase selectivity, conversion, and yield.

The research plan includes the synthesis of nanoparticles modified with metals via the sol-gel method. Various characterization like  $\text{N}_2$  physisorption, X-ray diffraction analysis, UV-Vis diffuse reflectance spectroscopy, etc., is part of the initial step. Doping of titania with metals for the application in heterogeneous photocatalysis improve the visible light response of the  $\text{TiO}_2$ . The synthesized catalysts were deposited onto the wall of microreactor and the characterization of microtubes was done through scanning electron microscope, optical microscope, to visualize immobilized catalyst layer. Microflow photocatalytic oxidation tests proved that the Fe- $\text{TiO}_2$  material has the highest photocatalytic conversion (28 %) of benzyl alcohol compared with the other  $\text{TiO}_2$  samples under visible light irradiation. The next goal was to investigate the photocatalytic performance of all the synthesized nanoparticles for the selective oxidation of different lignin-based model compounds such as benzyl alcohol, coniferyl alcohol, cinnamyl alcohol, and vanillyl alcohol in liquid phase under different light sources (UV and Visible). The alcohols containing hydroxy and methoxy groups (coniferyl and vanillin alcohol) showed high conversion (93 % and 52 %, respectively) with 8 % and 17 % selectivity towards their respective aldehydes, with the formation of other side products. The findings offer an insight into the ligand-

to-metal charge transfer (LMCT) complex formation, which was identified to be the main reason for the activity of synthesized catalysts under visible light.

## Abstrakt

Celem pracy jest synteza, wspomagana technikami ultradźwiękowymi, nowych cienkich warstw o właściwościach optokatalitycznych na wewnętrznej ścianie reaktora mikrorurowego z fluoropolimeru w celu selektywnego utleniania związków modelowych na bazie ligniny. Materiały te były następnie modyfikowane metalami takimi jak Fe, Cu i Co w celu przeprowadzenia zaawansowanych badań. Spodziewano się, że będą cechować się dużą powierzchnią właściwą i reaktywnością. Krytycznym etapem było osadzenie zsyntezowanych metodą zol-żel półprzewodnikowych tlenków metali ( $\text{TiO}_2$ ,  $\text{ZnO}$ ) na wewnętrznej ścianie polimerowej (kopolimery tetrafluoroetyleny i perfluoroeterów - perfluoroalkoxy alkane) mikrorurki PFA metodą wspomaganą ultradźwiękami. Reakcje utleniania prowadzone w mikroprzestrzeniach mogą ułatwić precyzyjną kontrolę parametrów takich jak czas reakcji, temperatura, mieszanie, powtarzalność i bezpieczeństwo. Reakcje w ciągłym przepływie mogą również zapobiegać lub ograniczać reakcje uboczne i rozkład spowodowany nadmiernym napromieniowaniem świetlnym, które może być łatwo kontrolowane w systemie pompowym. Oczekuje się, że powyższe poczynania zwiększą selektywność, konwersję i wydajność.

Plan badań obejmuje syntezę nanocząstek modyfikowanych metalami metodą zol-żel. Różne metody charakteryzacji, takie jak fizysorpcja  $\text{N}_2$ , analiza dyfrakcji rentgenowskiej, spektroskopia rozproszonego odbicia UV-Vis, itp. są częścią wstępnego etapu. Domieszkowanie tytanu metalami w heterogenicznej fotokatalizie poprawia czułość  $\text{TiO}_2$  na światło widzialne. Zsyntetyzowane katalizatory osadzono na ścianie mikroreaktora, a charakterystykę mikrorurek przeprowadzono za pomocą skaningowego mikroskopu elektronowego oraz mikroskopu optycznego, w celu uwidocznienia unieruchomionej warstwy katalizatora. Badania fotokatalitycznego utleniania w mikroreaktorze dowiodły, że materiał Fe- $\text{TiO}_2$  wykazuje najwyższą konwersję fotokatalityczną (28 %) alkoholu benzylowego w porównaniu z innymi próbkami  $\text{TiO}_2$  pod wpływem promieniowania światła widzialnego. Kolejnym celem było zbadanie wydajności fotokatalitycznej wszystkich zsyntetyzowanych nanocząstek dla selektywnego utleniania różnych związków modelowych opartych na ligninie, takich jak alkohol benzylowy, alkohol koniferylowy, alkohol cynamylowy i alkohol wanilinowy w fazie ciekłej pod różnymi źródłami światła (UV i widzialne). Alkohole zawierające grupy hydroksylowe i

metoksyłowe (alkohol koniferylowy i wanilinowy) wykazywały wysoką konwersję (odpowiednio 93 % i 52 %) z 8 % i 17 % selektywnością w kierunku odpowiednich aldehydów, z tworzeniem innych produktów ubocznych. Wyniki dają wgląd w tworzenie kompleksu z przeniesieniem ładunku z ligandu na metal (LMCT), który okazał się być główną przyczyną aktywności zsyntetyzowanych katalizatorów w świetle widzialnym.

# Table of Contents

Declaration of originality .....	ii
Acknowledgments .....	iii
List of Publications.....	vi
Active participation at scientific conferences.....	vii
Abstract.....	viii
Abstrakt .....	x
Acronyms and Abbreviations .....	xvi
Chapter 1 .....	19
1. Introduction .....	19
1.1 Valorization of lignin.....	19
1.1.1 Need for a paradigm shift from existing methods .....	19
1.1.2 Role of sonication in surface modification .....	21
1.1.3 Semiconductor to achieve targeted goal .....	22
1.2 Research hypothesis and objectives.....	23
1.3 Organization of thesis .....	25
Chapter 2 .....	27
2. Designing Microflow reactors for Photocatalysis Using Sonochemistry: A Systematic Review Article .....	28
2.1 Introduction.....	28
2.2 Theoretical Background.....	30
2.3 Side by side comparative evaluation of flow system to batch .....	32
2.4 Ultrasound: A useful tool for chemists .....	34
2.4.1 Synthesis of Materials.....	35
2.4.2 For immobilization of catalyst inside the microtube .....	36



2.4.3 For photocatalytic experiments.....	36
2.5 Early Works on Microreactors.....	37
2.6 Immobilization of nanoparticles inside the microtube.....	43
2.7 Photocatalytic experiment.....	47
2.8 Microreactor with ultrasound for photocatalysis: A new way forward .....	48
2.9 Future Challenges and Conclusions.....	51
Chapter 3 .....	53
3. Design and Development of TiO <sub>2</sub> coated microflow reactor for photocatalytic partial oxidation of benzyl alcohol.....	54
3.1 Introduction.....	54
3.2 Experimental Section.....	56
3.2.1 Materials .....	56
3.2.2 Synthesis and Characterization of catalysts .....	56
3.2.3 Ultrasound-assisted deposition of catalyst inside the microtube .....	57
3.2.4 Photocatalytic selective partial oxidation of benzyl alcohol.....	57
3.3 Results and Discussion .....	59
3.3.1 Deposition of catalyst inside PFA microtube .....	59
3.3.2 Effect of pre-treatment before deposition of catalyst .....	59
3.3.3 Effect of ultrasound during deposition of catalyst.....	61
3.3.4 Photocatalytic studies.....	61
3.3.5 Characterization and photocatalytic reaction in S-PFA microtube.....	65
3.4 Conclusions.....	68
Chapter 4.....	69
4. Flow photomicroreactor coated with monometal containing TiO <sub>2</sub> using sonication: a versatile tool for visible light oxidation .....	70
4.1 Introduction.....	70
4.2 Experimental Section .....	71

4.2.1	Materials .....	71
4.2.2	Synthesis and deposition of catalysts.....	71
4.2.3	Characterization of catalysts and samples .....	71
4.3	Results and Discussion .....	72
4.3.1	Optimization of metal loading in TiO <sub>2</sub> -based composite .....	72
4.3.2	Characterizations of the synthesized catalysts .....	74
4.4	Conclusions.....	80
Chapter 5	.....	81
5.	Bimetallic TiO <sub>2</sub> Nanoparticles for Lignin-Based Model Compounds Valorization by Integrating Optocatalytic Flow-Microreactor .....	82
5.1	Introduction.....	82
5.2	Experimental .....	84
5.2.1	Materials .....	84
5.2.2	Catalyst synthesis.....	84
5.2.3	Microreactor preparation .....	84
5.2.4	Catalytic performance test .....	85
5.3	Characterization .....	86
5.4	Results and Discussion .....	87
5.5	Conclusions.....	102
Chapter 6	.....	104
6.	Research summary .....	104
6.1	Contributions and impacts .....	104
6.2	Challenges and future perspectives.....	107
Chapter 7	.....	109
APPENDIX I	.....	109
APPENDIX II	.....	128

APPENDIX III.....	141
Supporting information .....	141

# Acronyms and Abbreviations

## A

AcN	Acetonitrile
AQY	Apparent quantum yield

## B

BET	Brunauer-Emmet-Teller
BJH	Barrett, Joyner, Halenda
BnAld	Benzaldehyde
BnOH	Benzyl alcohol

## C

CinOH	Cinnamyl alcohol
CinAld	Cinnamyl aldehyde
ConOH	Coniferyl alcohol
ConAld	Coniferyl aldehyde
CoT	0.25% of Co-TiO <sub>2</sub>
CuT	0.5% Cu-TiO <sub>2</sub>

## D

DMSO	Dimethylsulfoxide
------	-------------------

## E

EDXRF	Energy dispersive X-ray Fluorescence
EtOH	Ethanol

## F

FeT	0.5 at% of Fe-TiO <sub>2</sub>
FTIR	Fourier-Transform Infrared Spectroscopy

## **G**

GC-MS                      Gas Chromatography-Mass Spectrometry

## **H**

HAADF                     High Angle Annual Dark Field

HPLC                      High-Performance Liquid Chromatography

HR-SEM                    High Resolution Scanning Electron Microscopy

## **L**

LED                        Light-Emitting Diode

LMCT                     Ligand-to-Metal Charge Transfer

LSPR                      Localized Surface Plasmon Resonance

## **P**

PDMS                     Polydimethylsiloxane

PFA                        Perfluoroalkoxy Alkane

P-PFA                     Pretreated PFA

PT-PFA                    Pre-treated and deposited with P25 (commercially available TiO<sub>2</sub>) microreactor

## **S**

S-PFA                     Sol-gel synthesized TiO<sub>2</sub> deposited microtube

## **T**

TEM                        Transmission Electron Microscopy

TiO<sub>2</sub>-SG                    Sol-gel synthesized TiO<sub>2</sub>

T-PFA                     P25 coated tubes

TTIP                        Titanium (IV) Isopropoxide

## **U**

US                         Ultrasound

UV	Ultraviolet
UV-vis DRS	UV-visible Diffuse Reflectance Spectra
<b>V</b>	
VanOH	Vanillyl alcohol
VanAld	Vanillyl aldehyde
<b>X</b>	
XPS	X-ray photoelectron spectroscopy
XRD	X-ray diffraction
<b>Z</b>	
ZnO-SG	Sol-gel synthesized ZnO

# Chapter 1

## 1. Introduction

### 1.1 Valorization of lignin

The rise in consumption and production (manufacturing) to support the rapidly growing global population has adversely impacted the environment.<sup>1</sup> The sustainable disposal or reuse of industrial by-products is an active area of research in green chemistry. Lignin is a waste generated by paper and pulp mills that have been linked to severe aquatic and environmental problems. These industries produce tons of extracted lignin per year as a byproduct.<sup>2</sup> These have been classified as toxic substances, and in recent years, a promising treatment based on the total oxidation of hazardous organic compounds has been reported.<sup>3,4</sup>

Recently, researchers widely studied UV active heterogeneous photocatalysis because of their environmental friendly characteristics to photosensitize the complete mineralization of a wide range of organic substrates like phenols and pesticides, without the production of any harmful by-products.<sup>3</sup> These systems have limitations such as photo corrosion of catalyst, and it requires unique experimental setup. This thesis will delve into these processes in greater detail in the following chapters.

#### 1.1.1 Need for a paradigm shift from existing methods

The concurrence of chemical engineering and organic chemistry gave rise to “Flow Chemistry”—the term used by the scientific community to describe the chemistry occurring during a continuous flow process in contrast to conventional batch chemistry.<sup>5,6</sup> The conventional batch suspension-based system gives rise to a large gradient in temperature, reaction time, and concentration over spatial position because of vigorous stirring.<sup>7</sup> Moreover, the nanoparticles should be filtered after the photocatalytic reaction, which requires time and energy. On the other hand, we can overcome these problems by shifting to photocatalytic materials immobilized on the internal wall of the microreactor, as the solution is subject to flow inside the microreactor.

In a typical microfluidic-based photocatalyst system, a solution stream containing the target organic compounds flows through the microchannel, with the catalyst immobilized on the inner wall of the reactor. Photocatalysts react to decompose the organic pollutants, and a strong oxidant (such as a hydroxyl radical) is generated when was illuminated by UV light.<sup>8</sup>

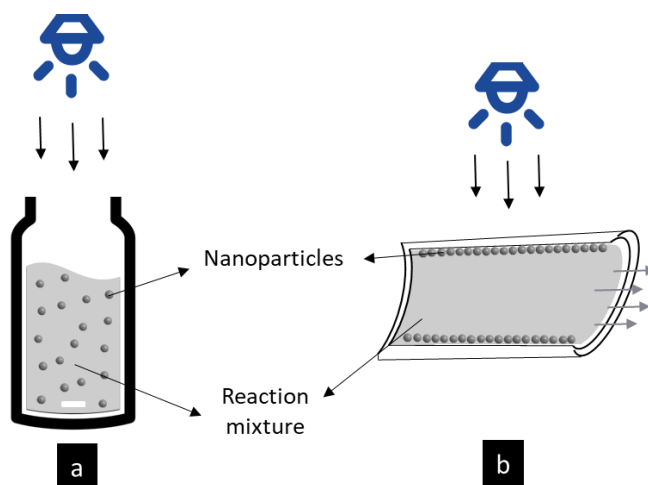


**Figure 1.** Conventional batch suspension-based system (a) and wall-coated microflow system (b).

Compared to the batch system, the microflow system has several advantages, such as (1) The short diffusion distance can help to increase the contact of photocatalytic materials with the compounds more efficiently. (2) By altering the microreactor geometry, the surface area of the photocatalytic materials can be increased. (3) The reuse of photocatalytic materials in a microfluidic-based system (Figure 1) is possible without any additional recovery process.<sup>9</sup> (4) Scaling up is reliable in a microflow system. (5) Selectivity and reproducibility can be improved for a reaction (6) The fast mixing and heat exchange can be achieved in the flow system.<sup>10</sup>

A microflow reactor can provide a small diffusion length and uniform light irradiation, thus enabling highly efficient photocatalysis and green chemistry processing.<sup>11</sup> In this work, we focus on a commercially available fluoropolymer-based microtube (PFA - perfluoroalkoxy alkane, a type of polymeric fluorocarbons) that demonstrates up to 96% for visible light and up to 91% for UV light transparency as well as admirable chemical stability.<sup>12</sup> Also, to maximize the photon utilization, a PFA tubing can be easily bent into different shapes (highly flexible). Though the uses of these tubing have been demonstrated for continuous-flow homogeneously catalyzed photochemical reactions<sup>13</sup>, they have



been rarely employed with heterogeneous catalysts. The reason behind this is the solid suspension may cause a clogging problem that requires laborious separation. These problems can be minimized by immobilizing the photocatalysts onto the walls of the microreactor. However, the chemical inertness of fluoropolymer makes immobilization challenging. Researchers have made effort by using methods like thermal processing (near a melting point of PFA of 285 °C)<sup>14</sup> and wet chemical processing<sup>15</sup> to facilitate the adhesion of photocatalysts to the fluoropolymer. However, because of the hydrophobic and chemically inert nature, the agent for a fluoropolymer is quite limited.<sup>16</sup>

The successful use of catalyst-coated microreactor for various use would largely depend on incorporation of catalyst on the wall of microreactor. In order to obtain the wall-coated micro reactor with a high number of exposed active sites, the control over stability and size of preferred metal phase of photocatalysts are crucial. With this, the accessibility towards reacting molecules increases leading to better performances from both the reactor system and chemistry point of view. Recently, ultrasonic and microfluidics are introduced to revisit existing knowledge toolboxes to produce a technology-push hoping to commercialize modern inventions.

### 1.1.2 Role of sonication in surface modification

Sonochemistry (acoustic cavitation) begins the growth and collapse of micrometer-sized bubbles in a liquid. When a bubble collapses in the presence of a significantly larger surface, it undergoes a noticeably uneven collapse, which gives rise to the crash of a high-speed jet of liquid into the surface. This can cause ultrasonic cleaning, localized erosion, and enhancement of surface chemistry. Integrating ultrasound with microflow reactors has proven to be one of the promising methods to address above discussed clogging and mixing issues that exist in conventional batch reactors (Figure 1).<sup>17,18</sup>

These small-scale microreactors offer a solution to non-uniformly generated acoustic field issues since the size range of ultrasonic effects is within the size range of that of the channels.<sup>19</sup> The work on the functionalization of microreactors is sparse in literature. One of the main aim of this work is to provide a sonication-based method to modify the surface of PFA polymer tube using relatively mild reagents in a micro-space aqueous-based system. Recently, Sadowski et al.,<sup>20</sup> a group from Jagiellonian University, Krakow, has demonstrated that after surface modification of a polymer, increasing the number of available OH, it is possible to functionalize it with TiO<sub>2</sub>.

### 1.1.3 Semiconductor to achieve targeted goal

The low-cost, highly efficient photocatalysis process provides an alternative solution to remove the contaminants from the wastewater by producing less byproduct. In some typical photocatalytic wastewater treatments, the organic dyes are eliminated by employing semiconductor materials ( $\text{TiO}_2$  and  $\text{ZnO}$ ) under UV irradiation.<sup>21</sup> The semiconductor thin layer attained by conventional sol-gel processing is typically amorphous and exhibit higher specific surface area. Conversion from the amorphous to the crystalline phase generally needs an annealing step (temperatures higher than 300 °C), which in most cases lead to a collapse of the pore system, and an increase of the particle size of the metal supported on semiconductor with reduced specific surface area. Additionally, the use of microtubes in this work (made of perfluoroalkoxyalkane PFA, melting point 315 °C, max. operating temperature approx. 260 °C) restricts operations to lower temperatures. In recent years, low-temperature synthetic protocols towards nanoscale, crystalline, porous, and high surface area semiconductors have been developed in which the research on semiconductor-based thin layers preparation is still a point of contention.<sup>22</sup> Taking into account the case of  $\text{TiO}_2$ , the crystallinity is often poor from the synthesis process, and it is challenging to control the formation of the polymorphs. Regardless of all the research efforts, many of the synthesis procedures are still very difficult to predict the final properties of the product based on the present knowledge.

In the last decade, the advancement of metallic catalysts has been one of the most dynamic research topics in nanoscience.<sup>23</sup> Because of the synergetic effect between two metals, the properties of bimetallic catalysts significantly differ from their monometallic analogs. As far as photocatalysis is concerned, the addition of second metal improved the physicochemical and photocatalytic properties of the materials.

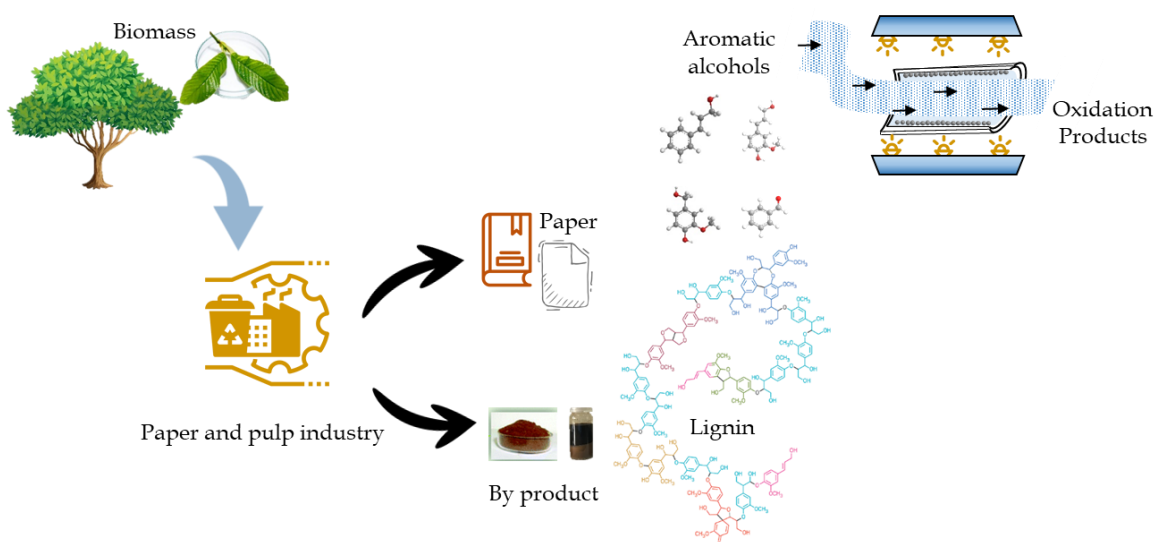


**Figure 2.** Lignin-based model compound valorization in wall-coated microreactor system.

## 1.2 Research hypothesis and objectives

This work proposes a novel methodology for the preparation of thin-layer nano-catalysts, which has strong potential to reduce Europe's reliance on imported rare earth/precious (toxic) metals by reducing their use (even replacing them) with those abundant transition metals (e.g., Fe, Cu, Co). We explored the use of noble metals (such as Au) as effective co-catalysts for the above metals by reducing the over potential for surface photochemical reactions. The intensity of light upon the catalyst varies on the location of the batch reactor whereas in microflow system the intensity on the whole system is homogenous.

In this doctoral research, I aim to valorize lignin-based model compounds by exploiting catalyst coated microflow system. In the scope of this work, it is believed that ultrasound will help in deposition of catalyst inside PFA tube without the use of any binder. I further explored the effectiveness of the microflow system in achieving the necessary environment for our targeted application (compared to the conventional batch system).

The research hypothesis formulated for this Ph.D. thesis are outlined as follows:

*Hypothesis 1:* Activity of catalyst can be improved for lignin-based model compounds (benzyl alcohol, BnOH) oxidation in microflow over batch system with better yield of product.

Objective:

1. Evaluate the photocatalytic activity of in batch as well as in microflow system, with an aim to study the partial oxidation of benzyl alcohol.
2. Investigate the difference of structure of catalyst before and after deposition onto the wall of microreactor by X-ray diffraction (XRD), N<sub>2</sub> physisorption, scanning electron microscopy (SEM), optical microscope and UV-vis diffuse reflectance spectroscopy (DRS).

*Hypothesis 2:* Use of ultrasound for surface modification can further help in better deposition of catalyst onto the wall of PFA tube.

Objective:

1. Understand the effect of ultrasound on PFA tube surface by analyzing it by SEM and optical microscope.
2. Correlate the photocatalytic activity of the wall coated microtube prepared with and without the presence of ultrasound under UV light.

*Hypothesis 3:* Introduction of transition metal (metal-containing; e.g., Cu, Fe, Co) and co-catalytic amount of noble metal (bimetal containing; e.g., Cu, Fe with Au) can improve the photocatalytic activity of the synthesized catalysts.

Objective:

1. Develop a low temperature (80 °C) sol-gel synthesis method for the synthesis of TiO<sub>2</sub> and metal doped TiO<sub>2</sub>.
2. Understand the effect of metal doped TiO<sub>2</sub> by characterizing them through wide range of techniques, e.g. XRD, N<sub>2</sub> physisorption, SEM and UV-vis DRS.

*Hypothesis 4:* Alcohol can be chemisorbed over TiO<sub>2</sub> and form a visible light-active ligand-to-metal charge transfer (LMCT)-complex involving the methoxy (OCH<sub>3</sub>) and hydroxy (OH) group of alcohols with TiO<sub>2</sub>.

Objective:

1. Understand the LMCT-complex formation between the OH, OCH<sub>3</sub> group of alcohol and TiO<sub>2</sub>, through various characterization techniques (FT-IR spectroscopy, UV-Visible DRS spectroscopy).
2. Evaluate the role of surface hydroxy (OH) groups of TiO<sub>2</sub> in LMCT-mediated visible light activation of TiO<sub>2</sub> through heat treatment (to remove the surface OH groups).

### 1.3 Organization of thesis

This Ph.D. was done as a part of the SonataBis CATSEE project. The thesis is written as cumulative doctoral thesis, where the core chapters are presented in the form of publications that are published in international scientific peer-reviewed journals.

Chapter 1 introduces the background to this research topic, with specific focus on the research objectives and hypothesis that will be addressed during this doctoral work. Chapter 2 builds a comprehensive literature review of microflow reactors and ultrasound approaches. The current state of art methods adopted for TiO<sub>2</sub> immobilization onto the surface of the microreactor are discussed elaborately.

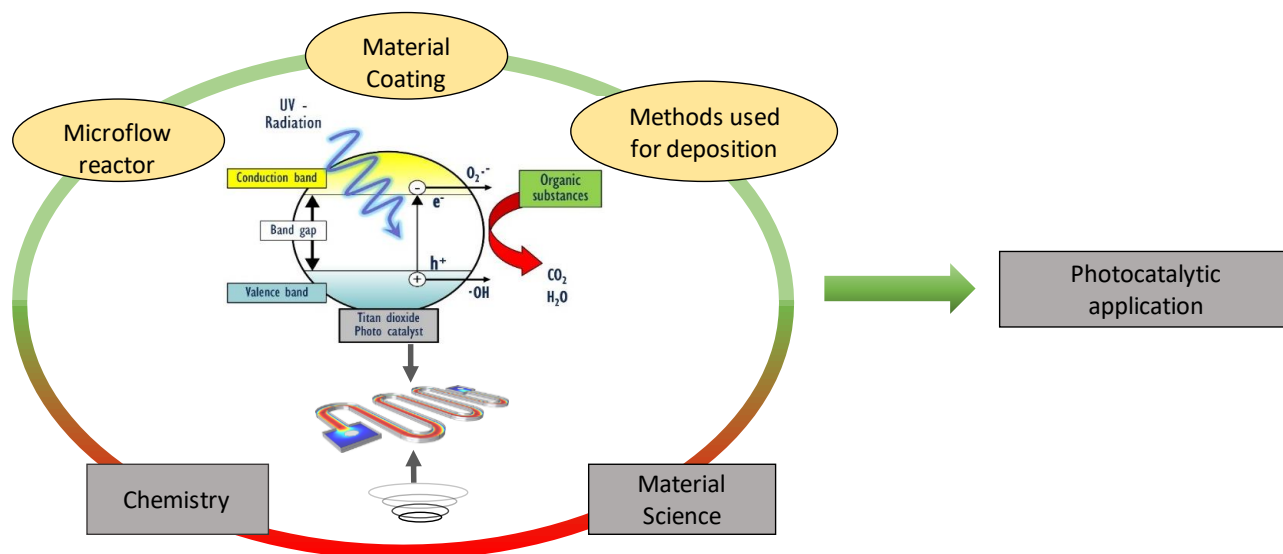
Chapter 3 proposes a new “green chemistry” oriented approach to prepare a thin layer microreactor system towards additive-free selective photocatalytic partial oxidation of a lignin-based model compound, benzyl alcohol. The results show that microreactor system displays better photo-reactivity with regards to both benzyl alcohol conversion and benzyl aldehyde selectivity. The utilization of ultrasonication (US) during the coating process leads to an enhanced mass deposition, and as a result, better photoreactivity compared to deposition without US.

Chapter 4 used pre-developed sol-gel method to synthesize monometallic TiO<sub>2</sub>. I optimized the atomic percentage of metal on TiO<sub>2</sub> and characterized it to explain the photocatalytic activity. Chapter 5 develops a bimetallic TiO<sub>2</sub> catalyst adopted for the improvement of photocatalytic activity. Our studies reveal that the LMCT complex formation of TiO<sub>2</sub> with the methoxy and hydroxy groups (directly connected with the aromatic ring) exists in the structure of coniferyl alcohol (ConOH) and vanillyl alcohol (VanOH), which was crucial to activate the TiO<sub>2</sub> catalyst under visible light.

I provided the optimizations, characterizations of the instruments I used during my study, and some pre-experimental data in Appendix I. In Appendix II, I showcased the synthesis of ZnO following the similar sol-gel method as  $\text{TiO}_2$  and studied the photocatalytic activity for BnOH oxidation. As ZnO has similar properties like  $\text{TiO}_2$ , I carried out experiments with ZnO by considering the optimized parameters from experiments with  $\text{TiO}_2$ .

In Appendix 3, I presented the supplementary information for the core chapters of this thesis.

## Chapter 2



*The present chapter discusses the research work described in a published manuscript, authored by Swaraj rashmi Pradhan, Ramón Fernando Colmenares-Quintero and Juan Carlos Colmenares. (Molecules 24 (2019) 3315; doi:10.3390/molecules24183315)*

**Abstract:** Use of sonication for designing reactors, especially deposition of catalyst inside a microreactor is a very new approach. There are many reports which prove that microreactor is a better setup compared to batch reactors for carrying out catalytic reactions. The microreactors have better energy efficiency, reaction speed, safety, a much finer degree of process control, better molecular diffusion and heat-transfer properties compared to conventional batch reactor. The use of microreactor for photocatalytic reactions is also being considered to be the appropriate reactor configuration due to its improved irradiation profile, higher spatial illumination homogeneity and better light penetration through the entire reactor depth. Ultrasounds are the acoustic cavitation generated by interaction of the sound waves with the reacting compounds resulting in intense mixing. Moreover, this mixing results in enhanced mass transfer among the reacting species leading to higher process efficiency. Furthermore, it has been used for synthesis of materials, degradation of organic compounds, fuel production etc. efficiently. The recent increase in energy demands as well as the stringent environmental stress due to pollution has resulted in the need to develop green chemistry based processes to generate and remove contaminants in a more environmental-friendly and cost-effective manner. Using this method in microfluidic system it is possible to carry out synthesis and deposition of catalysts inside the reactor. In addition, the synergetic effect generated by photocatalysis and sonochemistry in a microreactor can be used for production of different chemicals which have high value in pharmaceuticals and chemical industries. The current review highlights the use of both photocatalysis and sonochemistry for developing microreactors and its applications.

## 2. Designing Microflow reactors for Photocatalysis Using Sonochemistry: A Systematic Review Article

### 2.1 Introduction

With the continuous and prosperous development of modern civilizations, environmental contamination has spread far and wide. Faced with this issue, humankind reached a consensus on the need for environmental treatment and remediation. Green chemistry is the implementation of twelve principles<sup>24</sup> (Figure 3) that lowers the use or generation of hazardous substances in the design, manufacture, and application of chemical products.<sup>25</sup> The innovation of newer approaches is increasingly demanding our society to be sustainable and also for preserving the environment. It is crucial for those approaches to be less dependent on sources, which are self-depleting or effuse greenhouse gas in use.

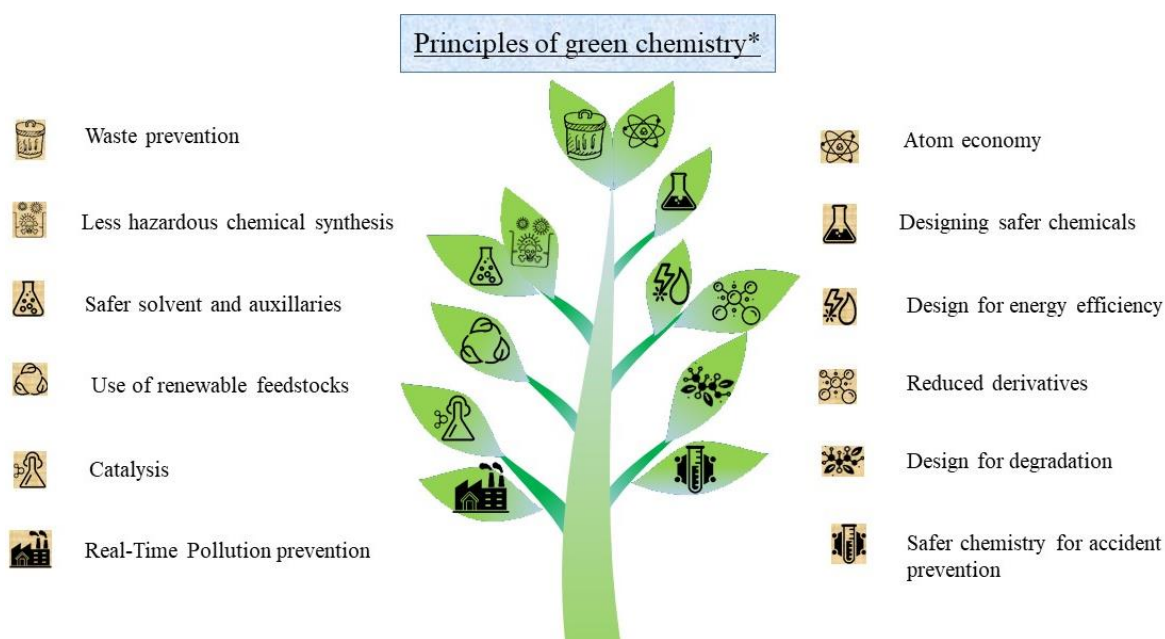


**Figure 3.** *The Twelve Principles of Green Chemistry.*

Photocatalysis occupies an essential place in the ecological equilibrium as a good example of Green Chemistry.<sup>26</sup> Photocatalysis activates reactions depending on light as an energy source, which is ultimately clean and superabundantly available from the sun. Therefore, research on solar energy utilization has continued to be an important topic.<sup>25,27</sup> Photocatalysis in microreactor is attracting many



researchers because of its greener aspect. Microreactor is regarded as a green synthetic approach due to reduced reagent requirements, minimized energy consumption, lessening of by-products, and shorter reaction time.<sup>28</sup> Nowadays, many groups are working on synthesizing catalysts inside a microreactor. Among the catalysts, titania-based catalysts are well-known photocatalyst under UV light and have been identified as a technology playing an important role in solving many of the problems in water purification.<sup>29</sup>

In this review article, after a brief introduction, theoretical backgrounds of the flow microreactor, ultrasound, and their combined studies have been discussed. Ultrasound irradiation is recognized as a viable, environmentally benign technique to conduct chemical reactions.<sup>30</sup> The application of ultrasound waves has been considered as an agreeable technique in chemistry. Early works on catalyst synthesis in a microreactor using ultrasound and their comparison with conventional batch experiments and future challenges have been reviewed here.

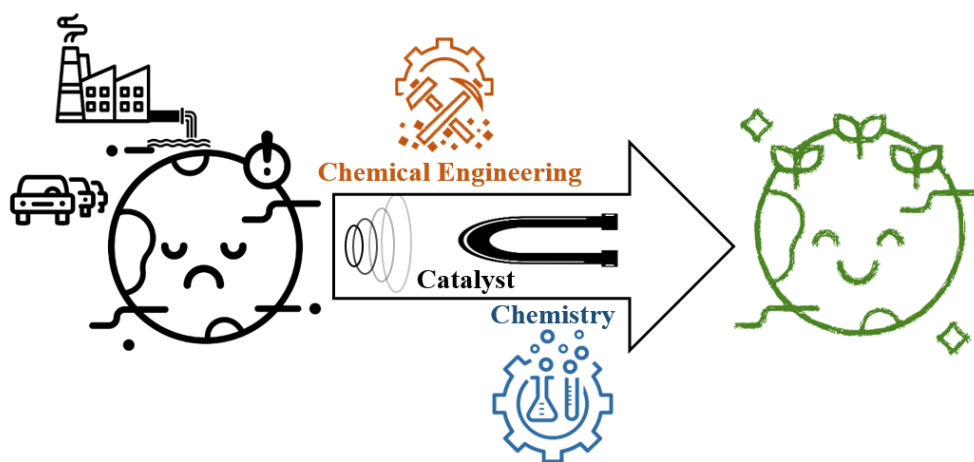


**Figure 4.** Two branches trying to produce greener chemistry.

As illustrated in Figure 4, the scientific community is trying to make our planet green by combining chemical engineering (e.g., manufacturing microchannel by ultrasound) with material chemistry (e.g., photocatalyst). The major purpose of this review article is to highlight the challenges ahead of the design and development of (photo)catalytic microfluidic reactors using ultrasound. To the best of our knowledge, this is the first technical review in the field of microflow reactor for photocatalysis using sonochemistry, which can be promising for the upcoming studies in this branch of science.

## 2.2 Theoretical Background

There are broadly speaking two types of flow-reactor system that have been used for synthetic photochemistry i.e.; micro and macroflow.<sup>31</sup> Micro-synthesis technique in both interdisciplinary engineering and sciences connects physics, chemistry, biology, and engineering arts for various applications. A microfluid segment in microreactor has been defined as a minimum unit having properties that can be used to improve various operations and reactions in microspace.<sup>28</sup> Microreactors offer new possibilities of reactions. Microreactors have proved to be highly effective for catalytic reactions due to its indispensable advantages like large surface to volume ratio ( $> 10,000 \text{ m}^2/\text{m}^3$ ) and consequently, attain high heat and mass transfer rate, uniform illumination without light attenuation, and resultant satisfactory catalytic effect.<sup>32,33</sup> Also, the contact time, shape and size of the interface between fluids can be easily and precisely controlled.<sup>34,35</sup> These attributes make microreactors ideal for fast reactions, highly exothermic reactions, and even explosive reactions.

Recently, much attention has been paid to the development of microreactor technology for various applications, such as synthesis of chemical compounds, environmental protection, biomedical and pharmaceutical studies, healthcare, among others.<sup>32,36</sup> In a review article, Moraveji et al. discussed on two disadvantages of flow reactor, which are, pressure drop and type of photocatalytic microreactor to be considered.<sup>37</sup> Yue et al. tried to overcome these issues by incorporation of a photocatalyst thin layer.<sup>33</sup> The small volume capacity of microreactors has allowed the efficient development of more sophisticated continuous flow reactions on increasingly complex molecular targets since they greatly reduce the quantities of materials needed to optimize reaction conditions minimizing footprint and waste.<sup>38</sup>

In the past decade, continuous flow microreactors have received considerable attention for performing organic transformations in safer and efficient ways. Even if microfluidic systems have a wide range of users in several fields, their commercialization is still limited.<sup>36</sup> It is now possible to reach the maximum selectivity of exothermic or endothermic, complex, extremely fast, and multiphase chemical reactions using a photocatalytic microreactor.<sup>39</sup> Very efficient degradation and different organic molecule synthesis, along with selective cleavage of peptides and proteins, have been done using micro-photoreactors immobilized with  $\text{TiO}_2$  catalyst, which can be very favorable for the synthesis of

chemicals, pharmaceuticals, and proteomics.<sup>40</sup> Figure 5 shows a typical example of a photocatalytic microreactor used for wastewater treatment.

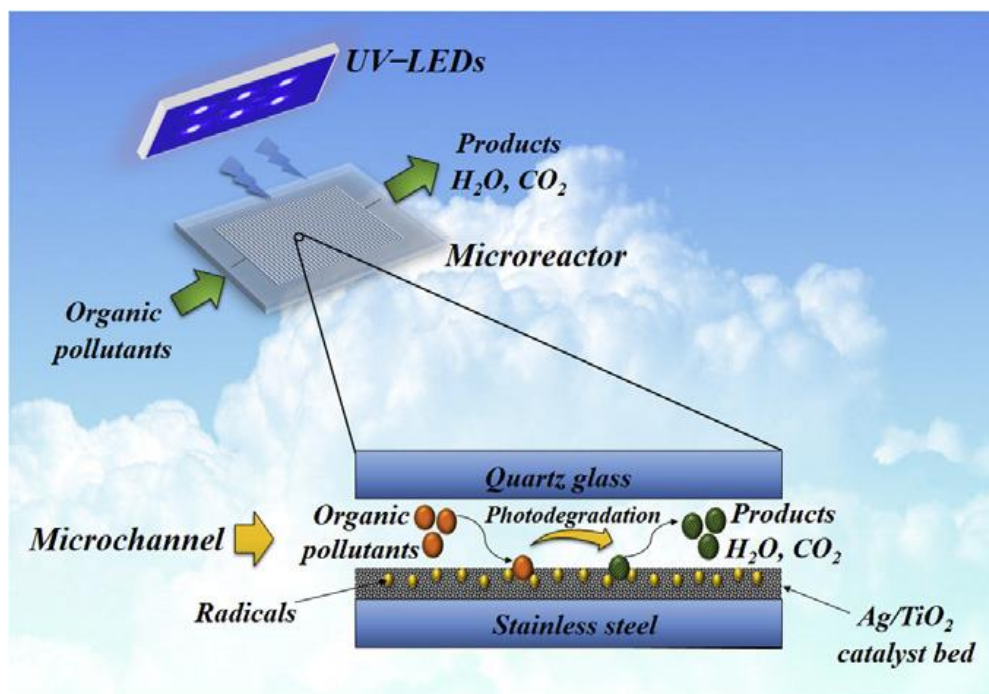


**Figure 5.** UV-LEDs assisted preparation of silver deposited TiO<sub>2</sub> catalyst bed inside microchannels as a high-efficiency micro-photoreactor for cleaning polluted water. Reprinted from<sup>41</sup> with permission of Elsevier.

Ultrasound has been applied in several research fields. These include, but are not limited to, structural modification of materials, and their transmissions, imaging, medical treatment, materials processing, acoustic microscopy, and more recently, wireless communications.<sup>17</sup> Use of ultrasound in a liquid facilitates the breaking of chemical bonds through sonolysis process, resulting in the formation of free radicals. Acoustic cavitation, bubble formation in a liquid exposed to pressure fields, causes several chemical and physical effects.<sup>42</sup> These processes are useful for the synthesis of nanomaterials, incrementation of catalytic chemical reactions, destruction of pharmaceutical waste, wastewater treatment, degradation of organic pollutants, and are representative of a method of production of fuels.<sup>43</sup> In conventional systems, ultrasound is also used to intensify liquid-liquid processes because of its efficient agitation effects and non-invasive nature.<sup>17,44</sup> It accelerates chemical reactions by intensifying mass transfer.

Currently, ultrasonics and microfluidics are introduced to revisit existing knowledge toolboxes to produce a technology-push hoping to commercialize modern inventions. Upon irradiation of an ultrasound wave, acoustic cavitation forms, such as cavitation microstreaming, shock wave, and jetting.<sup>45</sup> In this year (2019) until the time of submission, only five articles had been indexed by Scopus, which are retrievable by the combined keywords “microreactor” and “ultrasound.” The number of research articles published in the last decade is represented in Figure 6.

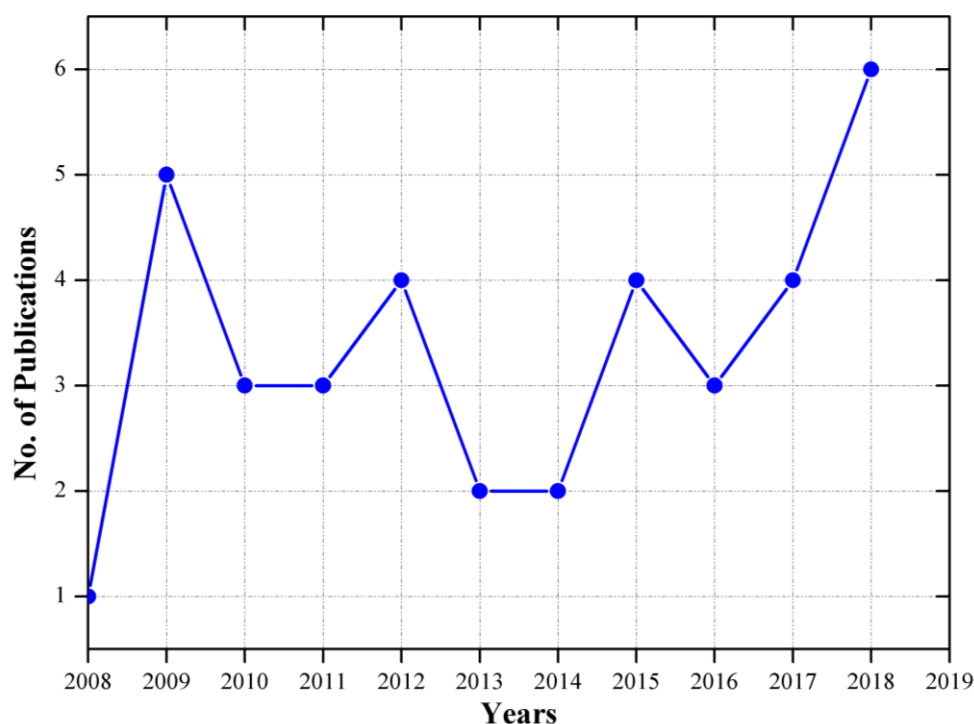


**Figure 6.** Work done with microreactor together with ultrasound in respective years (source: Scopus, July-2019).

### 2.3 Side by side comparative evaluation of flow system to batch

Microfluidics has many advantages compared with bulk chemistry, the first being slow diffusion. Therefore, to make the reaction faster, the distance required for interaction has to be smaller. The smaller channel dimensions also help to minimize the amount of sample required for analysis with reducing the by-products.<sup>36</sup> Recent advancement in this field has signified that miniaturization of reactors can be profitable in terms of kinetics, safety, and cost.<sup>46</sup> Because of its advantages, the synthesis of nanoparticles in microfluidics has become prominent in the past years.<sup>28</sup> The use of continuous microreactor led to the improvement of irradiation over the reaction mixture and offers a considerably reduced reaction time

and better yields of products compared to batch reactors.<sup>47</sup> Batch reactors have a major disadvantage in the linear decrease in the intensity of the electromagnetic radiation with the square of the distance of the light source used.<sup>48,49</sup> The photocatalytic microreactors avoid this disadvantage by having a homogeneous illumination over the whole surface of the microchannel exposed to the light source.<sup>50</sup> Otherwise, the molecules undergoing photodegradation, under the control of the injection flow, constantly leave the reaction environment, avoiding the presence of by-products in the reaction mixture. The application of these devices to synthetic photochemistry started to spread from the 21st century.<sup>31</sup>

There are several techniques for the prototyping of microfluidic systems,<sup>51</sup> and different methods for the preparation of TiO<sub>2</sub> films in photocatalytic microreactors.<sup>52</sup> These techniques should be fast and cost-effective from the design stage to the final system test. To fulfill the requirements, the production must be based on a simple technique and utilize low-cost instrumental resources.<sup>50</sup> Nanoparticle synthesis using continuous flow methods can produce a narrow size distribution of nanoparticles, which cannot be possible in a batch reactor. It has been proven that total reaction rate and photocatalyst mass transfer can be tuned with specific control, especially on size and shape, but also control over porosity, crystallinity, and thickness.<sup>37</sup>

Noël et al. stated two important reasons for photochemistry achieving a remarkable increase in attention from researchers in academia and industry. The first reason is the exposure of visible light photo redox catalysis for organic synthetic chemistry. The second is the use of continuous-flow reactors.<sup>53</sup> In one of their publications, they compared their results in flow to those obtained in batch experiments.<sup>54</sup> They reported a negligible loss in activity when the reaction was performed in flow. In fact, in the flow reaction, they observed higher activity at very short residence times. This result concluded with the major advantages of flow chemistry. It stated that increased mass- and heat-transfer allows the flow reactor to have very fast and efficient heating. These properties make it ideal for fast reactions.

The same authors have also suggested a list of nine good reasons to utilize photo flow.<sup>53</sup> The reasons are as follows:

1. Improved irradiation of the reaction mixture;
2. Reliable scale-up;

3. Improved reaction selectivity and increased reproducibility;
4. Fast mixing;
5. Fast heat exchange;
6. Multiphase chemistry;
7. Multistep reaction sequences;
8. Immobilized catalysts;
9. Increased safety of operation.

Noël et al. developed a completely automated microfluidic system that can handle solids efficiently at high concentrations through acoustic irradiation.<sup>54</sup> They experimented with the amination reaction of aryl triflates, aryl bromides, and aryl chlorides. Working with the flow system assisted in carrying out the reactions at a very short time and in figuring out the conversions and yields accurately. They concluded that their system is ideal for multistep syntheses, which requires a heterogeneous reaction. Furthermore, microflow photocatalytic reactors have shown to be a competent setup compared to batch,<sup>55</sup> as can be seen in the selective organic synthesis in heterogeneous photocatalysis in a microflow, which is still in an underdeveloped stage as compared to traditional batch systems.

## 2.4 Ultrasound: A useful tool for chemists

Ultrasonic irradiation increases turbulence in the liquid phase, decreasing mass transfer limitations, and increasing the catalytically active surface area via the de-agglomeration and fragmentation of the particles.<sup>56</sup> Different effects of ultrasonic waves have shown in Figure 7. Nucleation, cavitation, bubble dynamics/ interactions, thermodynamics, and chemical processes are the mechanisms of sonolysis.

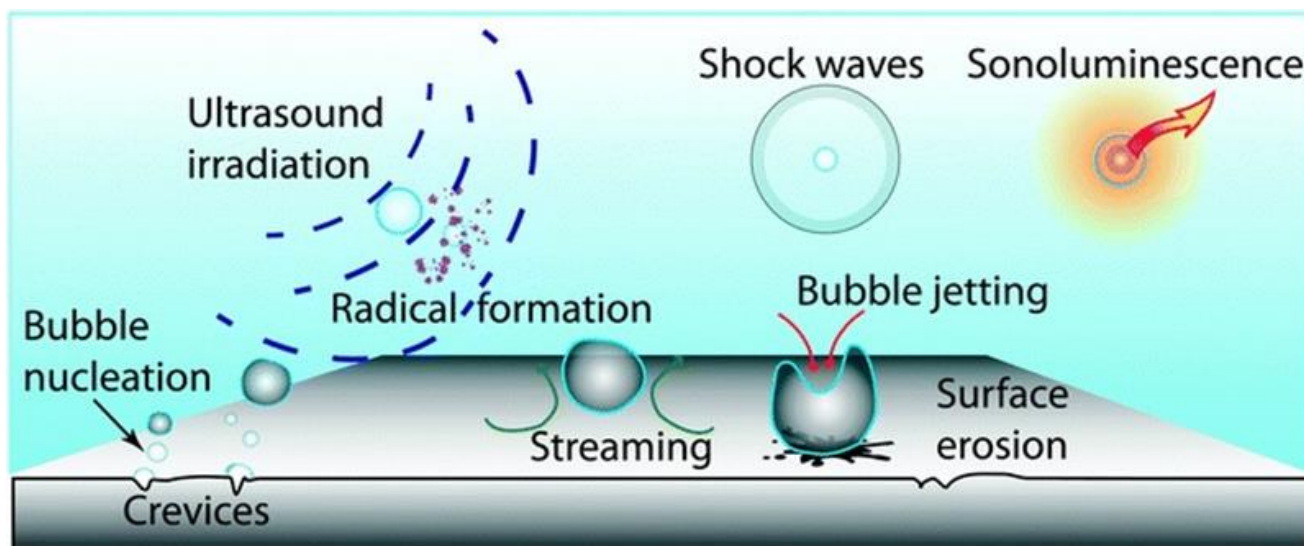


*Figure 7. Effect of sonication. Reprinted from <sup>17</sup> with permission of Royal Society of Chemistry.*

Bridging and constriction are important mechanisms that lead to clogging in microfluidic devices, which can be eliminated via acoustic irradiation and fluid velocity, respectively<sup>57</sup>. Rivas et al., in their article, discussed the ultrasound approaches to control the particle formation inside the microchannel.<sup>55</sup>

### 2.4.1 Synthesis of Materials

There has been a large amount of research in synthetic fields under ultrasonic environments, such as the synthesis of nano inorganic materials. There are comparatively fewer studies on the effect of solids on sonochemical activity.<sup>42</sup> Countless articles exist up until today on the use of ultrasound for material synthesis. This process deals with the formation, gradual growth, and bursting bubbles (Figure 7). Application of ultrasound to the solution, for nanomaterial synthesis, produces shock waves, leading to an increase in temperature and pressure necessary for chemical reactions<sup>36</sup> (a diagram has been given to demonstrate the synthesis of nanoparticles using microtube and ultrasonic bath, Figure 8). A simple, ultrasound-assisted wet impregnation method was applied to synthesize materials by Colmenares et al.<sup>58</sup>

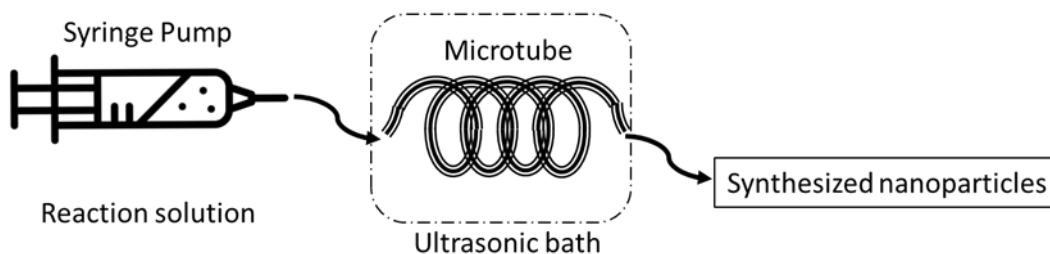


**Figure 8.** Diagram of use of ultrasound in a flow reactor for synthesis of nanoparticles.

## 2.4.2 For immobilization of catalyst inside the microtube

Deposition of metal particles on a substrate by ultrasound is a process in which both the reduction of the oxidized metal precursor and the deposition of the resulting metallic particles are driven by ultrasonic irradiation. This technique has been employed to coat metallic particles on various substrates. Earlier investigations indicated that the technique could yield well-dispersed metal nanoparticles tightly adhered to the surface of a substrate.<sup>59,60</sup> It can be stated that ultrasound plays a vital role in developing thin-film of well-dispersed nanoparticles. Many researchers have taken advantage of ultrasound to immobilize nanoparticles. Recently, Liu et al. worked on the deposition of metallic platinum nanoparticles on CdS for photocatalytic hydrogen evolution using ultrasound.<sup>61</sup> However, the development of a more adaptable system that is more synthetically feasible is needed.<sup>54</sup>

## 2.4.3 For photocatalytic experiments

In a review article, Qui et al. discussed heterogeneous sonocatalysts for treatment of organic pollutants in aqueous phase.<sup>62</sup> They discussed briefly the development of sonocatalysts from the past to the present in accordance with the different types of catalytic mechanisms. Teh et al., in another review article, discussed the development and modification of titania-based photocatalysts for pollutant-degradation using ultrasound technology.<sup>63</sup> They also stated the key operating parameters of ultrasound, followed by its application in the synthesis of the photocatalyst. Colmenares et al. synthesized magnetically separable materials by following the improved wet impregnation method assisted by ultrasonic irradiation. They developed a simple method for the preparation of magnetically separable  $\text{TiO}_2/\text{maghemite-silica}$  photo-active nanocomposites. The resulting nanomaterials were further tested for their photocatalytic activities in the liquid phase of selective oxidation of benzyl alcohol in both aqueous



and organic phase.<sup>58</sup> The unusual reaction conditions (extremely high temperatures and pressures forming quickly in liquids because of acoustic cavitation phenomena) of the ultrasonic irradiation technique were key factors in achieving homogeneously impregnated materials with nano-sized particles, and in the formation of heterojunctions. The catalysts were found to be highly photocatalytically active. Yu et al. also worked on photocatalyst synthesis.<sup>64</sup> They synthesized three-dimensional and thermally stable mesoporous TiO<sub>2</sub> with high photocatalytic activity by high-intensity ultrasound-induced agglomeration.

## 2.5 Early Works on Microreactors

Microfluidic technology can be used profitably for the synthesis of nanomaterials and their catalytic studies. Efficient heat and mass transport in the miniaturized reaction chambers of microfluidic chips impart greater control at the molecular level. The microfluidic pathway offers an edge over the normal batch processes in terms of laminar flow, short molecular diffusion distance, and effective mixing.<sup>36,37,53</sup> Previously, many groups concentrated their work on exploring microfluidic photocatalytic microreactors for environmental application. Das et al. wrote a review article focusing on the fabrication techniques and operating parameters for this type of microreactor.<sup>65</sup>

Based on the method used to incorporate catalysts on the inner wall of the microreactor, it can be divided into three classes: (i) packed-bed, (ii) monolithic, and (iii) inner wall-functionalized<sup>32</sup> (Figure 9). The packed-bed reactor can be explained as the immobilization of a catalyst on insoluble support and is haphazardly assembled in the reactor, whereas in a monolithic reactor, the catalyst is made in the shape of structured material. In an inner wall-functionalized reactor, the catalyst is covalently attached to the interior wall of the reactor. To ensure a smooth flow of reagents, minimization in the mass transfer resistance was provided. Because of the complexity of the synthesis, their application is still limited.<sup>53</sup> Tao et al. proposed a synthesis procedure based on microfluidics for the production of Ag@Cu<sub>2</sub>O core-shell nanoparticles.<sup>66</sup> Sachdev et al. presented a microfluidic method for the synthesis of hollow Au shells and Fe<sub>3</sub>O<sub>4</sub>@Au core-shell nanoparticles within an emulsion droplet<sup>67</sup> ('@' stands for core-shell by the respective authors).

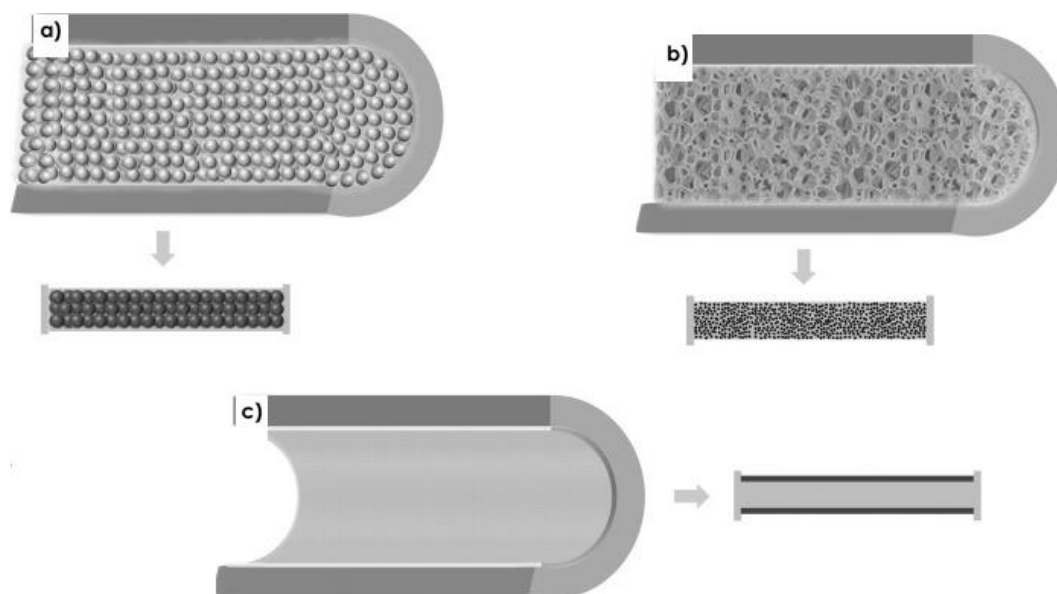


**Figure 9.** Schematic representation of the cross-section of a microchannel in packed-bed (a), monolithic (b), and wall coated (c) microreactors. Reprinted from<sup>31</sup> with permission of Wiley.

Flow chemistry has started to make an extensive impact on the way many chemists carry out synthesis over the last 15 years.<sup>31</sup> Microfluidics has significant applications in various fields.<sup>68,69</sup> In the year 2015, Yao et al. published a review article related to various applications of microreactors.<sup>28</sup> This review article was mainly based on structures and applications of microreactors in the synthesis of nanoparticles, and also on bio-substances, organics, and polymers. The whole article focused on multiphase microreactors. Knowles et al. used dual-channel microreactors for transformations, which are synthetically useful.<sup>31</sup> The same reactor was also applied for the synthesis of the antimalarial artemisinin, and the conversion of  $\alpha$ -terpinene to ascaridole successfully. An additional application of microflow photochemistry includes the synthesis of vitamin D3.<sup>30</sup>

Nanoparticle synthesis in microreactor types for on-chip photocatalyst synthesis has been reviewed, along with challenges in handling the nanoparticles in microsystems.<sup>37</sup> The most important design parameter of photocatalytic reactors is the illuminated specific surface area of the photocatalyst. Matsushita et al. have developed a photocatalytic microreactor system, which has a considerably large surface area per unit volume.<sup>49</sup> Research over the past decade focused on enabling multi-step processes by developing complex microchemical systems. The prime example of such multistep microchemical

synthesis is multi-step Heck synthesis carried out in continuous flow.<sup>17</sup> Microfluidic systems provide a platform for a broad range of syntheses. These allow automated optimization<sup>70</sup> and rapid experimentation (e.g., reaction conditions, catalysts).<sup>71</sup> Moreover, microfluidic systems allow safe synthesis and increase the feasible reaction space (performing synthesis in supercritical solvents). Additionally, the residence time of species and the reactor temperature can be precisely controlled. All these studies focused on the use of microreactors for chemical synthesis in flows.<sup>17</sup>

In a review article, the importance of continuous-flow photo-microreactors in water treatment, organic synthetic chemistry, and materials science was described.<sup>53</sup> Some recent examples pointed to complex applications, such as the synthesis of complex biologically active molecules.<sup>72</sup> Automated and self-optimizing flow processes have been developed to reduce manual labor.<sup>53</sup> In a recent article, Cambié et al. stated that a multidisciplinary approach would be the best strategy to overcome the remaining hurdles in chemistry. Intense collaborations between academia and industry are the most important part. To address the challenges of the future, industrial income has become more vital because of the drop in funding opportunities.<sup>53</sup> Considerable research in this field has been done in the last decade, and making further progress will be challenging.

In another article, Shchukin et al.<sup>73</sup> stated the advantages of microflow photocatalytic process as (i) possibility of providing definite characteristics to the microreactor by removing additional functionalities; (ii) high active area for reaction with increased yield of photoreactions; (iii) less volume (micron and submicron), allowing one to perform photochemical synthesis in the highly organized solvent; (iv) reduced concentration and heating effects on adding reagents in the reaction; (v) possibility of modelling and mimicking photo-induced processes in nature on the micron and submicron level. So far, many articles have reported on several microns and submicron-confined environments for performing photocatalytic processes. However, there are only a few examples of spatially confined individual reactors for the semiconductor-catalyzed photodegradation reactions to date.<sup>71</sup> The study of reaction kinetics and mechanisms, influence of different parameters (e.g., size of the microreactor), adsorption of the reactants and intermediates, and solvent structure in the interior, among others, on the photosynthetic technique, along with a comparison of reaction products with those obtained by catalytic photolysis in non-confined media (e.g., in the slurry of dispersed photocatalyst) is scarce in the

literature. These details can help in understanding the chemical and physicochemical processes occurring in the environment, as well as the development of spatially confined photosynthetic approaches. The results of conventional heterogeneous photocatalysis can be improved by exploiting the physical processes that occur in confined geometries with controlled diffusion of the reagents.<sup>25</sup>

Various photocatalytic reactors have been reviewed for different applications.<sup>25,74</sup> Most of them can be classified into microreactors and slurry reactors. Some can be handled with suspended photocatalysts immobilized in the latter by considering the specific surface area of the catalyst and uniform light penetration in the reactor volume by various approaches.<sup>75</sup> The slurry reactors provide several active sites per unit volume. These microreactors were often used for air treatment.<sup>76</sup> Because of the limited designs available, photocatalytic reactors are still not commonly implemented in industrial processes. In the case of a three-phase microreactor with dispersing catalyst nano-powder, the higher adsorption rate was found in wastewater treatment. It has been seen that the photocatalytic activity decreases with particle size.<sup>77</sup> The mean particle size also can be easily adjusted by the pH of the solution and choice of solvent.<sup>78</sup> The accumulated particles inside a micro path make the recycling process difficult after the photocatalytic step.<sup>65</sup>

The typical flow systems found in the catalytic layer immobilized channel are slug flow or annular flow (Figure 10), depending on the operating conditions.<sup>79</sup> The important leverage of a microreactor with the immobilized thin-film catalyst is that it does not require a discrete step to separate the photocatalyst after the reaction. The high surface area of the catalyst also helps in increment of mass transfer in bulk and inter-phase. For example, oxygen that accepts electrons and, resultantly, does not allow recombination of electron-hole pair in the photocatalysis, leads to high reaction efficiency.<sup>80</sup> The lower interfacial catalyst surface area per mass is the main disadvantage of the inner surface-immobilized photocatalytic thin film of microreactors.<sup>81</sup> The combined effects of mass transfer with photocatalytic reaction have been studied in Charles et al.'s and Corbel et al.'s works.<sup>82,83</sup>

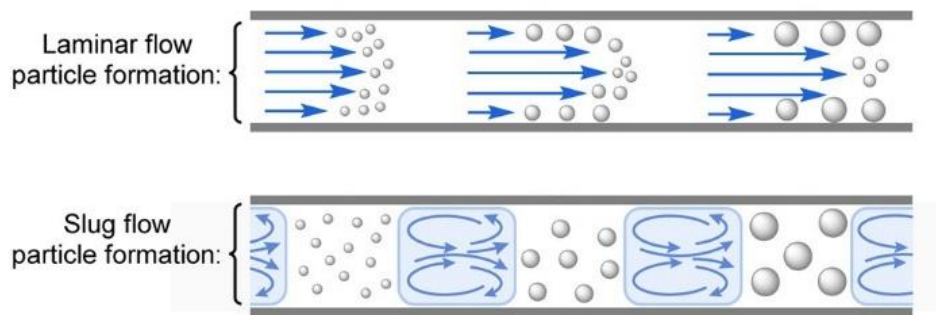


**Figure 10.** Particle formation in single-channel microreactor. Reprinted from <sup>52</sup> with permission of American Chemical Society.

Different microreactors have been developed to upsurge the reaction efficiency,<sup>84</sup> such as micro-capillary reactors,<sup>14</sup> single-microchannel reactors,<sup>41,85</sup> and planar reactors, although it's photocatalytic, as well as energy efficiency, still needs to be improved.<sup>86</sup> In a review article, Heggo et al. discussed the work of different researchers to attain high throughput. Some researchers tried to achieve this by increasing the length or number of microchannels, whereas others tried to enlarge the dimension by keeping one dimension in the microscale.

In a review article, Woolley et al. discussed the materials (silicon, glass, and ceramics) and polymers (elastomers, thermoplastics, and paper) that scientists are using in microreactors for different purposes (microreactor's fabrication). Hybrid devices have shown promising ability to gain the benefits of each material's strengths.<sup>36</sup> Professor George Whitesides used polydimethylsiloxane (PDMS) to create inexpensive microfluidic devices, and Yoshida's microreactor initiatives in Japan built up considerable interest in the microreactor area.<sup>28</sup> Das and Srivastava inspected various techniques to construct microstructures, such as mechanical micro-cutting, lithography, and etching technology. On the basis of the material of the devices, they divided the micro-photoreactors into four groups: ceramic microreactors, polymeric microreactors, metallic microreactors, and glass microreactors.<sup>65</sup>

Signs of progress done in the modification and design of the structure of microreactors over the last ten year has been reported, and it has also introduced the improvement in organic reactions and synthesis of inorganic materials. Exemplary reviews have been published on the reaction process, the impact on

downstream processing, and the product properties.<sup>87,88</sup> Multiphase microfluidic devices have also been discussed to synthesize inorganic and metal nanoparticles.<sup>28</sup>

Some polymers, on the other hand, are presented as a good alternative for use in photochemistry and have been applied for the intensification of photochemical processes.<sup>89</sup> This paper focused on multichannel microreactors, which can be used for a wide range of liquid-phase organic synthesis reactions. The reactor system showed better potential because of the presence of several microchannels and the simplicity of parallelly arranging a number of these devices.<sup>89</sup> In a study, Ramos et al. investigated the possibility of employing UV-transparent polymer microtubes as supports for TiO<sub>2</sub> (titanium dioxide) photocatalysts, and their applicability in the oxidation of organic pollutants.<sup>14</sup>

Because of the advancement in syntheses such as increased mass and heat transfer, operational safety, the potential for purifying continuously, control over residence time, and scalability by parallel operation of several devices, the usage of microfluidic devices has attracted consideration from the pharmaceutical industry.<sup>90</sup> Despite these advantages, one of the biggest hurdles in the development of flow chemistry methods is the handling of solids, such as precipitates during the reaction, leading to clogging of the microchannels. Among all the approaches, the use of ultrasound is an effective way to avoid clogging. In order to prevent the particles from interacting with the reactor walls, segmented liquid-liquid flow can be used.<sup>91</sup> Though this is an efficient way to handle solids, the efficiency of the reaction can be reduced by using an additional solvent. Recently, Buchwald et al. presented a biphasic system of an organic solvent and water, which could solubilize both the organic and inorganic components of a reaction.<sup>92,93</sup>

Microfluidic reactors have been developed to implement miniaturized laboratories for (i) synthesis of organic and inorganic compounds, and (ii) analytical tests and biomedical applications.<sup>50</sup> In these situations, the process parameters (P, T, V, and concentration) must be highly controlled in well-defined time units, in order to reduce raw material costs, analysis time, and risks in reagent handling, or potentially dangerous flammable, explosive, corrosive, and carcinogenic products, and bacteriological agents. From the advantages of the method, it can be stated that high temperature and long-time are not required. It is noteworthy that the diameter of the core-shell can be controlled by the concentration of the inner particle in the organic phase, and the diameter of hollow shells can be adjusted by varying the

flow rate.<sup>37</sup> Y. Matsushita et al. examined the feasibility of the micro-reaction system on organic photoreactions, finding that the photocatalysis of  $\text{TiO}_2$  can be categorized into two types: homogeneous photocatalytic reaction and heterogeneous photocatalytic reaction systems. Among the different types of catalyst-based photochemical reactions, homogeneous-based photocatalysis has been broadly studied in microfluidic-based flow systems for selective organic synthesis.<sup>55</sup>

## 2.6 Immobilization of nanoparticles inside the microtube

Most research on photocatalytic reactions has been carried out using dispersed powders in conventional batch reactors. However, systems with the immobilized catalyst can avoid the separation of dispersed powders (preventing light penetration) after the reaction, as they have low interfacial surface areas. Thus, Matsushita et al. have developed photocatalytic microreactors with an immobilized  $\text{TiO}_2$  layer.<sup>94</sup> The thermal oxidation,<sup>95</sup> physical vapor deposition,<sup>96</sup> chemical vapor deposition,<sup>97,98</sup> dip-coating<sup>99</sup>, spin-coating,<sup>100</sup> electrospun,<sup>101</sup> sputtering,<sup>102</sup> sol-gel,<sup>103</sup> and electrodeposit<sup>104</sup> methods are techniques for the film formation step needed in the design of immobilized photoreactors. Figure 11 represents a sol-gel-based deposition of  $\text{TiO}_2$  inside a glass microtube.

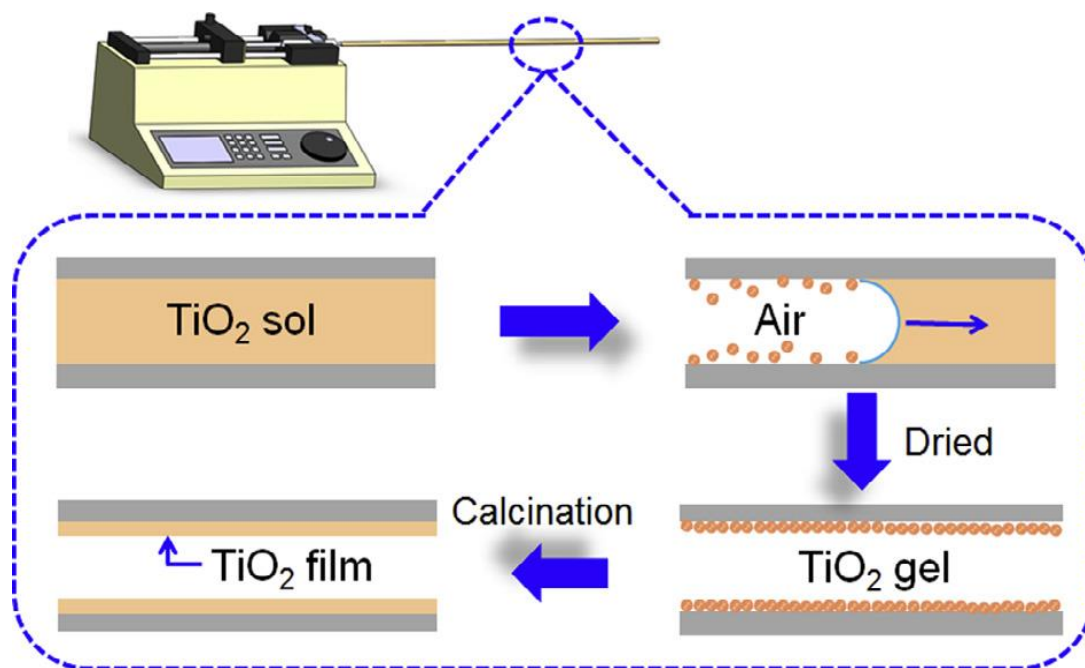


**Figure 11.**  $\text{TiO}_2$  thin film inside microtube using sol-gel method. Reprinted from <sup>78</sup> with permission of Elsevier.

Recently, Sohrabi et al.,<sup>37</sup> in their review article, discussed the challenges as well as opportunities of microfluidic reactors. They stated that the main challenges in microfluidic nanoparticle synthesis and application are the crystallization of the photocatalyst, the poly-dispersity of particles and channel clogging, and the carryover of suspended photocatalysts. It would be worthwhile to devote much effort in the wall-coated microreactor by selecting suitable surfactants and manipulating polymerization conditions.<sup>105</sup> Lopez-Orozco et al. claimed that the high surface reactivity would enable the attachment of functional groups to synthesized microreactors inside nanocomposites or the microchannel. The evolution of the research on composite-based microreactors has been quite encouraging.<sup>106</sup> In the simplest case, the intrinsic activity of the wall of the reactor is sufficient to catalyze the reaction.

In most cases, a sufficient number of active sites cannot be provided by the surface of the microreactor or improve the existing surface area—some surface modification is required. Moreover, a surface pre-treatment can help to improve the adhesion of coatings to attain maximum potential for immobilization of the catalyst. Plasma oxidative treatment, thermal or chemical oxidation, UV radiation, anodic oxidation, and chemical modification are some methods that have been used for pre-treatment.<sup>107</sup>

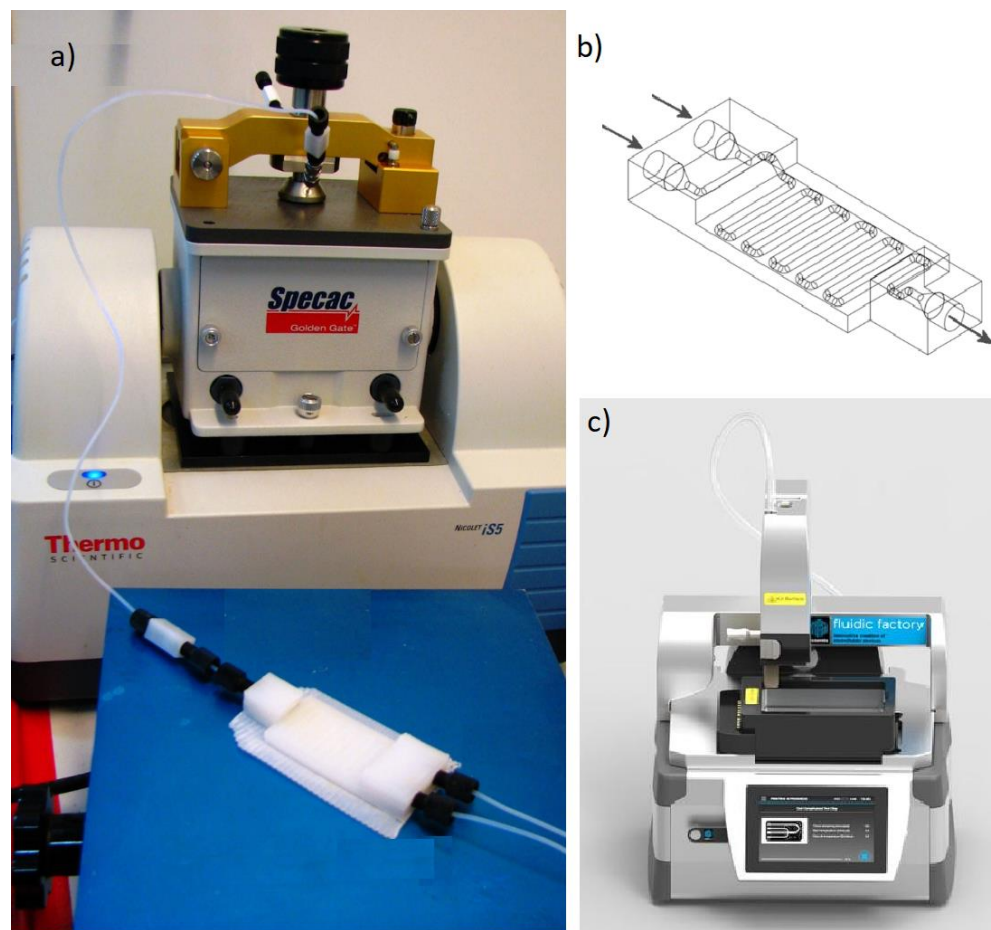
A microreactor with the photocatalytic thin film deposited on its inner spaces is a substitute for the slurry photocatalytic reactors.<sup>108</sup> H. Nakamura et al., in their article, discussed the modification of the inner wall of a microreactor and coating it for photocatalytic and enzymatic reaction studies. They used self-arrangement of colloidal particles to modify the microreactor inner wall. They observed an increase in conversion rate as well as yield.<sup>109</sup> Yue demonstrated the process of synthesis in microflow by improving heat and mass transfer rates. He explained some applications of catalytic processes in microfluidic reactors, for instance, selective hydrogenation, aerobic oxidation of alcohols, and direct hydrogen peroxide synthesis. He also discussed the multiphase flow in wall-coated microreactors and gas-liquid flow patterns in packed-bed microreactors.<sup>33</sup> The study on the amine N-alkylation processes in a microreactor with immobilized TiO<sub>2</sub> has also been discussed earlier.<sup>49</sup> More examples of immobilized titania inside various types of microreactors are presented in the following Table 2.1.



Table 2.1. Immobilization of catalyst inside different types of microreactor

Reference	Type of microreactor	Method of TiO <sub>2</sub> immobilization	Outcomes from TiO <sub>2</sub> characterization
40	metal-titanium foil	Anodization and hydrothermal treatment	Good mechanical properties of titania nanotube film, nanotubes of TiO <sub>2</sub> (TEM, SEM)
78	glass capillaries	Sol-gel	Homogenous dispersion, narrow particle size distribution (SEM, TEM)
41	stainless steel microreactor	Sol-gel	Uniform distribution of catalyst on surface, Crystalline size is 32 nm, Reflectance spectra of pure TiO <sub>2</sub> is 393 nm (HRTEM, XRD, DRS)
94	self-adhesive fluorine resin (EFEP) channel and switched between two glass plates	Sputtering	Growth of anatase peaks (XRD)
110	Silica capillary	Wash coating and calcination	the thickness of the deposited layer 88 nm (FEG-SEM)
111	Dual-film optofluidic microreactor	Hydrothermally prepared nanorod growth on fluorine-doped tin oxide (FTO) glass	2.4- $\mu$ m- thick film of TiO <sub>2</sub> nanorods inside glass tube (SEM)
112	coil-type photoelectrocatalytic microreactor	Anodization	25 nm thickness and 12 to 15 $\mu$ m length of titania nanotubes (FESEM)
113,114	FEP microtube	Ultrasound-based deposition	Structural transformation of polymer tube with ultrasound, thickness of catalyst layer was 3-6 $\mu$ m (Confocal microscopy, SEM)

On another note, many interesting novel contributions come from three-dimensional (3D) printed microchannels, which can be fabricated from plastic, metals, or glass. These types of microchannels can be made efficiently and quickly and are capable of manufacturing structures from microns to several centimeters. Different types of 3D printers are shown in the following Figure 12.



**Figure 12.** Flow system setup and ATR-IR flow cell with connections (a), Schematic representation of the three-dimensional (3D)-printed reactionware devices showing the internal channels (b) and 3D printer (c) ('a' and 'b' are reprinted from [95] with permission of American Chemical).

In a microfluidic device that was produced by rapid prototyping and was economically feasible and simple, a coating of  $\text{TiO}_2$  nanoparticles was applied, forming a photocatalytic microfluidic reactor destined to the degradation of organic dyes. It is important to point out that rapid prototyping of microfluidic devices is also relevant for the testing of small quantities of photocatalytic nanomaterials that are being developed in the research laboratories and that still lack the characterization of their

photocatalytic efficiency. This new methodology will allow us to quickly test synthesized materials in reduced quantities, in addition to generating less waste. This more sustainable approach respects green chemistry requirements.<sup>115</sup> The possibility of varying the geometry of the microreactor, creating larger contact areas and a stronger bond between the photocatalytic coating and the surfaces of the microreactor, can further improve the photo-degradation efficiency of the microfluidic device, allowing for the increase of the flow velocity and, from this, the increasing of the volume of the treated solution. Different designs of the geometry of the device, implementation of a dye solution reflux system, photocatalyst chemical functionalization, and a light-emitting diode-based UV light system are being tested to improve the performance of the photocatalytic microreactor for potential applications in selective oxidation of functional groups of organic compounds<sup>50</sup>.

Ultrasonic waves were used to break up agglomerations of particles.<sup>54,116</sup> The use of light transparent fluorinated ethylene propylene microtubes (excellent visible light transmission, UV transmission: ~80%, temperature: -270 to 205 °C) with TiO<sub>2</sub> leads to maximum usage of light for activating the photocatalyst for higher phenol degradation.<sup>113</sup> The design of a highly effective photoreactor is decisive to get the highest reaction rates with the immobilized form of a catalyst. Use of sonication for designing reactors, especially the deposition of a catalyst inside a microreactor, is a novel approach.

## 2.7 Photocatalytic experiment

The amount of light absorption of a photocatalyst at a given wavelength can be determined by the light intensity.<sup>117</sup> The photocatalyst activation step, the formation rate of electron-hole, is strongly dependent on the light intensity, and light distribution within the reactor undoubtedly determines the overall efficiency of the photocatalytic process. A light source of minimal space and lower photon cost is suitable for the microreactor system to take advantage of the miniaturized reaction vessel. Thus, Matsushita et al. employed UV-LEDs for the excitation light source of a photocatalyst.<sup>49</sup> Furthermore, it limited the depth of light penetration because of the absorption and scattering,<sup>118</sup> as expressed by the Bouguer–Lambert–Beer law.<sup>119</sup> It should be noted that safety issues should be paid attention to, even in photochemical reactors for bio-applications,<sup>120</sup> and with toxic or hazardous compounds.<sup>121</sup> Saien and Soleymani<sup>75</sup> explained the slurry photocatalytic microreactor as a favorable technique in dispersing TiO<sub>2</sub> particles. Some experiments for the degradation of phenol used a high energy 125 W UV mercury

lamp.<sup>25</sup> The manufacture of a microfluidic device with the nanostructured TiO<sub>2</sub> coating has been described as being integrated on the inner surface of the microchannels in the work of Pandoli et al. Subsequently, efficiency was evaluated for the degradation of aqueous solutions of organic dyes in continuous flow under the action of UV light.<sup>50</sup> Currently, photochemistry using microspace is a major attraction of the scientific community for green chemistry application (Figure 13).

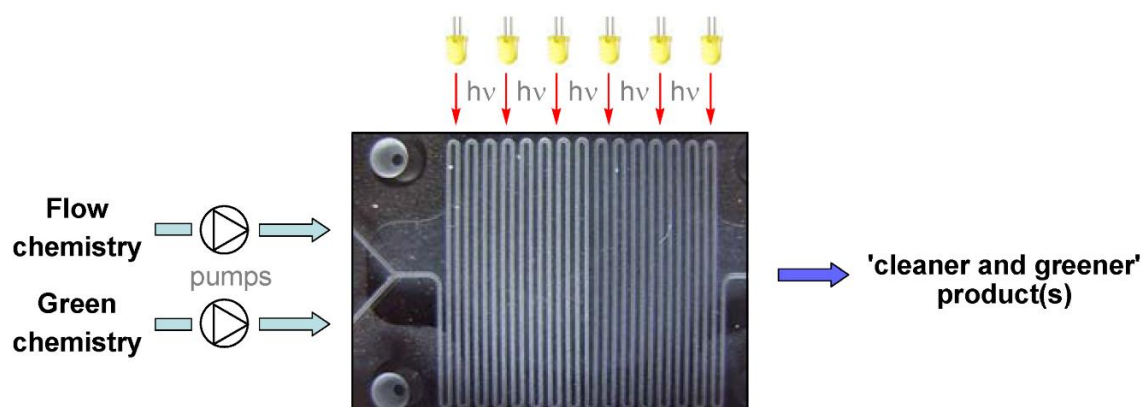


**Figure 13.** Concept of microflow photochemistry. Reprinted from <sup>84</sup> with permission of MDPI.

## 2.8 Microreactor with ultrasound for photocatalysis: A new way forward

Sonochemical processes are highly efficient in terms of selectivity, reaction time, and operational simplicity<sup>113,122–126</sup> while being used for the synthesis of various semiconductor-based nanoparticles in batch reactions. Combination of the ultrasound transducer and the microfluidic reactor<sup>126</sup> has gained the attention of many researchers. Such designed systems can then be applied to microfluidic liquid-liquid extraction,<sup>127</sup> degradation of contaminants,<sup>122,128,129</sup> and particle synthesis.<sup>130,131</sup> These types of reactors are broadly used in laboratories and industrial applications, but the analysis and comparison of results obtained with them are extremely difficult, which has limited the scaling-up of sonochemical reactors in the industry.<sup>132</sup>

Many studies have been performed, and thus it is well verified that the advantages of ultrasound technique includes short reaction times, improved conversion, enhanced yields, and mild conditions.<sup>133</sup> A capillary microreactor, together with ultrasound, was designed and presented by Aljbour et al. to carry out some chemical reactions. They investigated the hydrolysis of benzyl chloride in a two-phase

slug flow system. The increase in the rate of the hydrolysis reaction has been noticed with an increase in temperature, along with the effect of ultrasound. They noticed that the impact of ultrasound slowed down with an increase in the temperature. They also noted that the flow rate inside capillaries escalated the mass transfer between phases. The ultrasound helped in increment of the intensity of the internal circulations by splitting the large slugs into smaller sized slugs.<sup>30</sup> Sonication has been initially applied to homogeneous reactions; however, this approach has now been employed to heterogeneous reactions.<sup>134</sup> Ultrasound has some disadvantages, such as inefficient energy transfer via impedance and secondary effects such as streaming, sound field attenuation, heating, bulk mixing, emitter erosion, and sound emission. The parameters that influence sonochemical reactions and consider how they may be implemented to achieve systematic optimization has been discussed earlier.<sup>43</sup> Recently, Colmenares and co-workers were able to demonstrate for the first time an ultrasound-aided deposition of commercial  $\text{TiO}_2$  nanoparticles in an FEP-based microtube (Figure 14) using a probe-type ultrasonic system.<sup>113,114</sup> From AT-IR spectra, CH stretching peak in the modified tube, which was absent in the unmodified FEP microtube, confirmed that ultrasound brings some chemical changes in the inner walls of the FEP microtube.

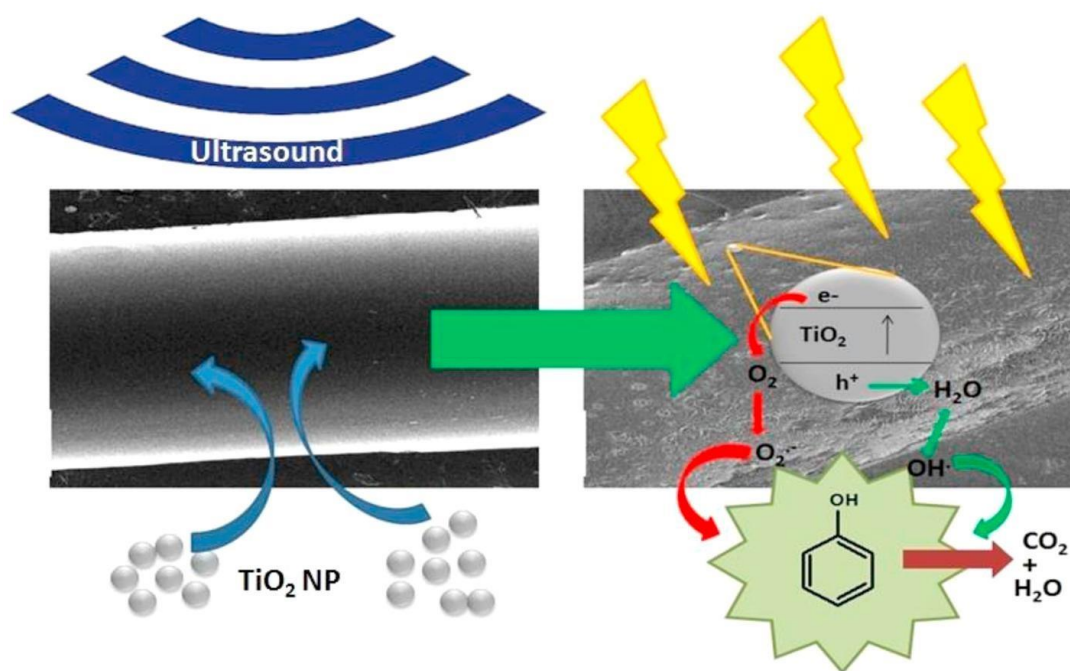


**Figure 14.** Photocatalytic phenol degradation in ultrasound ( $\text{TiO}_2$ ) deposited FEP microtube. Reprinted from <sup>114</sup> with permission of Elsevier.

Current progress in photocatalysis on microreactor systems using ultrasound has been reviewed by Matsushita et al. They stated that the relative effect of ultrasound is more pronounced at a lower temperature compared to silent conditions. According to them, the reason is that the ultrasonic waves enhanced contact between reactants by damaging the phase boundary. In the silent condition, the contact between phases showed more mass transfer limitation. Increment of the vapor pressure of the liquid medium, as a result of elevated temperature, lead to easier effective cavitation.<sup>135</sup> This trend is more detectable at higher flow rates because of the lower exposure time to the ultrasonic irradiation. Rivas et al. focused on the control of cavitation as a means to improve the energy efficiency of sonochemical reactors, as well as in the solid handling with ultrasound. They discussed some examples of microfluidic clogging prevention, numbering-up, and scaling-up strategies. In their work, they tried to reduce the clogging of the microreactor and lengthen the operational time of the reactor [19]. Ultrasound-assisted capillary microreactors have also been proposed and tested as a potential reactor for the multiphase aqueous-organic system. The effect of ultrasound irradiation under different temperatures, capillary lengths, and flow velocity was also examined.<sup>17</sup>

Sonochemistry could play a key role in overcoming limitations caused by solid formations by introducing ultrasound in conventional flow systems and microreactors.<sup>136,137</sup> Mass transfer limitation in microreactors can now be partially overcome by the help of ultrasound. The well-defined configuration of microreactors makes this easy and provides an ideal platform to investigate and control the acoustic cavitation process.<sup>137</sup> Colmenares et al. established a novel low energy (< 80 °C) ultrasound-based deposition method using a probe-type ultrasonic system for coating of commercial TiO<sub>2</sub> nanoparticles in the inner walls of FEP microtubes, knowing its importance in catalysis and photocatalysis fields.<sup>113,114</sup> The method is simple to implement and is environmentally friendly with low heat generation and has been filed for a patent.<sup>114</sup> The FEP microtube was pretreated with water using the ultrasound process, which resulted in physical changes of the inner surface of the FEP microtube, creating rough spots and an etched surface—facilitating the stable immobilization, under sonication, of TiO<sub>2</sub> nanoparticles on FEP internal walls. It has been demonstrated that the change in the surface characteristics (functionalization by pretreatment and TiO<sub>2</sub> nanoparticle deposition) of the inner walls of the fluoropolymer is due to the physical effect of ultrasound (a promising device for phenol degradation in water). Another work of Colmenares et al. reported, for the first time, the selective

oxidation of benzyl alcohol to benzaldehyde in a photocatalytic microreactor under UV-LED as the light source.<sup>55</sup> In this work, they used an ultrasonic bath (with a temperature close to ambient) for immobilization of ZnO inside a microtube.

## 2.9 Future Challenges and Conclusions

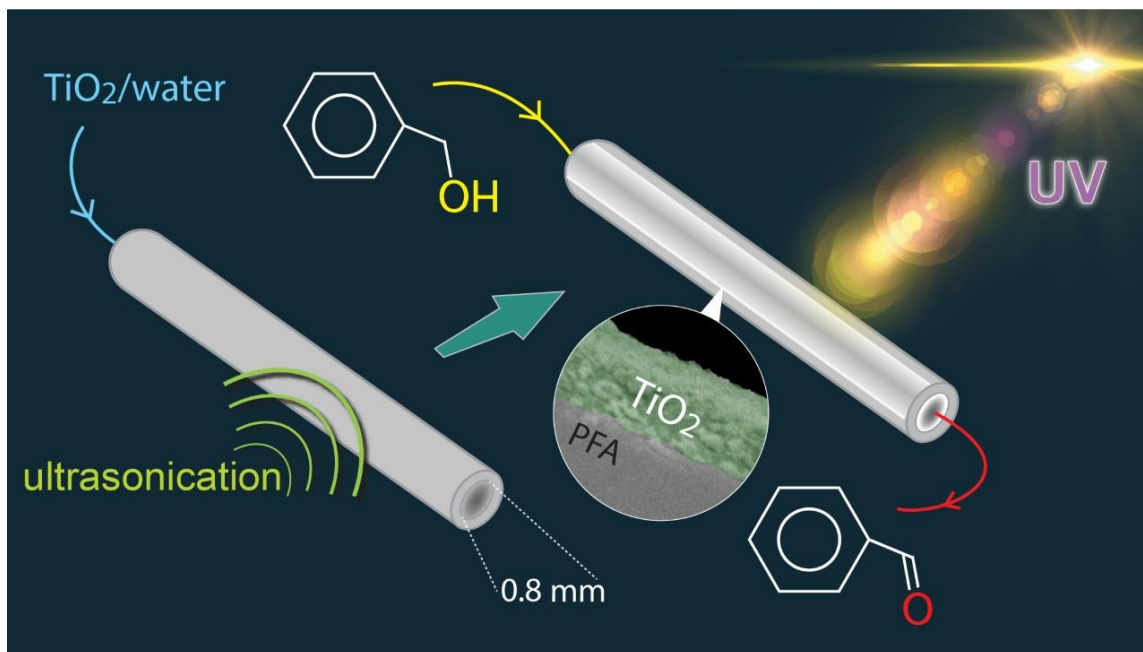
Since its introduction three decades ago, the field of microfluidics has witnessed significant growth in scientific research done across multiple disciplines, especially towards biological and medical applications. The advantages provided by the unique physical and chemical interactions of particles that take place inside the microscale channels, along with the coupling of multiple functionalities, has continued to drive the scientific advances of microfluidics. Outstanding research has been done in terms of materials and functions, their integration, and applications of microfluidics. In microfluidics, glass and silicon have been traditionally used most frequently, but recently polymeric materials have gained considerable attention, especially in the area of low-cost, and disposable devices. Still, there is a need to develop better material with improved properties, as the current generation of the material comes with its inherent advantages and disadvantages. The further improvement of the current method (e.g., different microreactor lengths, the application of different nanoparticles, physical and chemical effect optimization of ultrasound) will provide new ways, not only for environmental applications but also for new green organic synthesis protocols.<sup>113</sup> Even with this state of research, microfluidics has not been accepted outside of academia. However, acceptance of new technologies outside of academic research has always been slow, and more work should be done to promote wider and practical applicability of microfluidics. Heterogeneous photocatalysis in a microflow system for generation of value-added chemicals is a novel green chemistry approach requiring the understanding of photocatalysis, microfluidics, and reactor design. Research on the development of low energy and environmentally friendly-based photo-microreactor systems for photocatalysis is yet to be explored. In the areas of environmental and spatial analysis, effort should focus on creating robust and portable devices that can operate unattended for long periods. There are also some challenges related to 3D microreactors to be overcome, including chemical compatibility and operation at high pressures and temperatures.<sup>138</sup>

The interesting use of ultrasound irradiation in catalyst synthesis is gaining more and more value from both the fundamental and application point of view. Sonication is giving us a great opportunity as a

real green and cost-effective methodology and is foreseen to hold great potential in the near future.<sup>122</sup> Using low energy-based ultrasound for photocatalyst synthesis inside polymer-based microtubes (that does not deteriorate with age) will pave a new path towards the greener approach.



## Chapter 3



*The present chapter discusses the research work described in a published manuscript, authored by Swaraj rashmi Pradhan, Vaishakh Nair, Dimitrios A. Giannakoudakis, Dmytro Lisovytskiy and Juan Carlos Colmenares. (Molecular Catalysis 486 (2020) 110884; doi:10.1016/j.mcat.2020.110884)*

**Abstract:** The synthesis of valuable organic compounds from naturally available and renewable biomass is an open field of research towards adaptation in real-life applications. Photocatalytic valorization is assumed as a potential candidate, although the lower efficiency of the traditional batch photocatalytic reactor sets some drawbacks. Recently, photocatalytic microreactors revealed as a prosperous candidate for various photocatalytic reactions, especially for selective oxidation. This area of research is challenging due to the development of the proper photocatalytic microreactor for the targeted application. Deposition of the catalyst on the internal surface of the microreactor, the sufficient utilization of the irradiation, optimization of the reaction parameters are among the most vital parameters that should be considered upon the design. Although, to obtain the most active material and tune its crucial features to maximize its catalytic performance inside the microreactors is the uppermost important part. This work introduces ultrasound-assisted  $\text{TiO}_2$  deposition on the inner walls of a perfluoroalkoxyalkane microtube under mild conditions. The deposition experiments were carried out with commercial and sol-gel synthesized  $\text{TiO}_2$ . The materials were characterized by XRD, UV-Vis DRS, Scanning Electron Microscopy (SEM), and nitrogen sorption. The photocatalytic activities of the  $\text{TiO}_2$  nano-engineered fluoropolymer based microreactors were evaluated for the oxidation of benzyl alcohol in flow.

### 3. Design and Development of TiO<sub>2</sub> coated microflow reactor for photocatalytic partial oxidation of benzyl alcohol

#### 3.1 Introduction

Lignin is a significant organic waste coming out from paper and pulp industries. With continuous modernization, environmental contamination has spread extensively. Faced with this issue, humankind reached a consensus on the need for environmental treatment and remediation, which requires planning and implementation using the concepts of both photocatalysis and chemical engineering. Recently, more attention has been paid to the development of microreactor technology for various applications, such as synthesis of chemical compounds, environmental protection, biomedical and pharmaceutical studies, healthcare, etc.<sup>32,36</sup> Among the various photo-active candidates, titania-based materials, and especially the nano-scaled ones, are well-known and performing photocatalyst under UV light.<sup>139</sup> Due to its versatility, efficient photo activity, high stability, low cost, and safety to the environment and humans, titanium dioxide (TiO<sub>2</sub>) has been systematically used in many environmental and energy applications.<sup>140</sup>

Microreactor based catalytic approaches are regarded as green synthetic methods due to decreased requirements in reagent, minimized energy consumption, lessening of by-products, and shorter reaction time.<sup>28</sup> The photocatalytic reaction in a microreactor generally can be categorized into two types: homogeneous photocatalytic reaction and heterogeneous photocatalytic reaction systems.<sup>84</sup> There are various photocatalytic reactions have been carried out for selective oxidation of benzyl alcohol.<sup>141</sup> Among these catalyst based photochemical reactions, homogeneous photocatalysis has been extensively studied in microfluidic-based flow systems for selective organic synthesis,<sup>55</sup> but the major drawback in the homogenous catalyst system is the separation of catalyst and, in general, the purification needed in order to obtain the desired compounds. Catalyst separation difficulties can be avoided upon the twist to heterogeneous catalytic approaches, for instance by immobilization of the photocatalyst on a fixed support. Also, it is a great challenge to design and develop continuous flow microreactors capable of utilizing the power of light successfully. Generally, the microreactor performance can be enhanced by decreasing its size. This principle can also be valid for heterogeneous photocatalytic microreactors since a higher transfer rate of reactants and uniform illumination without attenuation are easily possible.

According to the method of incorporation of the catalyst, microreactors can be divided into three classes: (i) packed-bed; (ii) monolithic; and (iii) wall coated<sup>32</sup>. The packed and monolithic type of photo-microreactors have lower optical access due to complicated internal arrangement of the photocatalyst in the microreactor; more complex catalyst forms are better for potential applications such as catalyst filaments, wires, and membranes. On the other hand, wall-coated microreactors were introduced as a better approach for photocatalysis experiment as the penetration of light through the wall is simple compared to the other continuous-flow microreactors.<sup>29</sup>

It is also well verified that the advantages of ultrasound-assisted technique are the increased conversion, improved yields, short reaction times under mild conditions.<sup>133</sup> However, this approach has now been also employed for heterogeneous reactions,<sup>134</sup> or sophisticated materials synthesis.<sup>58</sup> Ultrasound is frequently used in conventional systems to intensify liquid-liquid processes due to its efficient agitation effects and non-invasive nature.<sup>17,44</sup> The ultrasonic irradiation increases turbulence in the liquid phase, decreasing mass transfer limitations, and increasing the catalytically active surface area via the de-agglomeration and fragmentation of the particles.<sup>56</sup> This technique has additionally been employed to coat metallic particles on various substrates.<sup>59,60</sup> Many researchers took advantage of ultrasound to immobilize the nanoparticles on metallic surface. To have immobilized thin film on the inner wall to avoid downstream catalyst recovery we could use microreactors.<sup>77</sup>

Previously, we proposed a novel and prosperous approach to prepare wall coated microtube.<sup>113</sup> Herein, we reported a ultrasound-based approach for photocatalysis inside a wall coated (with synthesized as well as commercial  $\text{TiO}_2$ ) fluoropolymer based micro-capillary for the oxidation of benzyl alcohol (BnOH) towards benzaldehyde (BnAld). The step-wise approach is shown in Figure 15. Also, a thorough comparison of a commercial  $\text{TiO}_2$  (P25) with a sol-gel nanostructured synthesized catalyst has been explored.

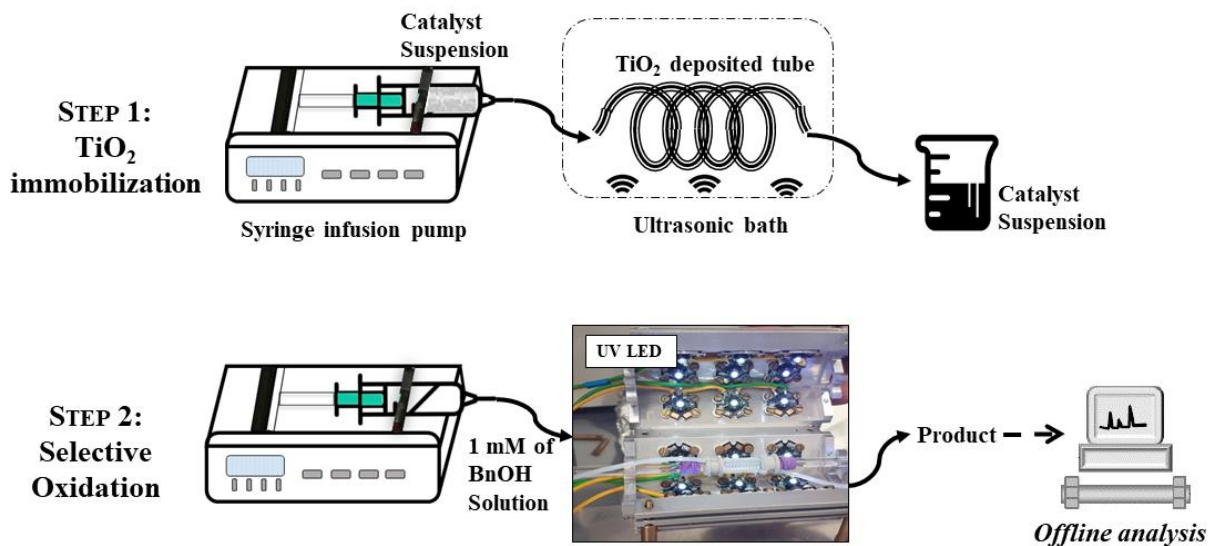


**Figure 15.** Procedure for catalyst immobilization and photocatalysis experiment inside microreactor.

## 3.2 Experimental Section

### 3.2.1 Materials

Titanium (IV) Isopropoxide (TTIP, 98%, Acros Organics), TiO<sub>2</sub> nanoparticles (P25, Evonik), Benzyl alcohol (BnOH, 99.5 %, ChemPure), ethanol (99.8 %), methanol (HPLC grade), acetonitrile (AcN, HPLC grade), 0.1 % of H<sub>3</sub>PO<sub>4</sub>, Propan-2-ol (99.7 %, POCH), a SunFire™ Chromatography column (C18 3.5μm, Waters) with 4.6 × 150 mm of bed support, and Perfluoroalkoxy alkane (PFA, 0.8mm ID) were used.

### 3.2.2 Synthesis and Characterization of catalysts

The synthesis of TiO<sub>2</sub> nanoparticles was carried out using Titanium (IV) isopropoxide (TTIP) based on the sol-gel based method. In a 25 mL vial, 4 mL of TTIP was dissolved in 15 mL of 2-propanol, followed by sonication for 60 min using an ultrasonic bath (100% power, 37 kHz on continuous sweep mode; temperature ~26 °C). Afterward, Milli-Q water (5 mL) was added to the solution at a rate of 0.167 mL min<sup>-1</sup> using a syringe infusion pump (Programmable Double Syringe Pump (WPI), NE-4000) under the influence of ultrasound at room temperature. After 60 min, the suspension was transferred to centrifugation vials, rinsing the reaction vial with 10 mL of Propan-2-ol. The solid product was separated and cleaned (with water and ethanol) during centrifugation. For the second and last cycle of centrifugation, 25 mL of Propan-2-ol and 20 mL of Milli-Q water were added to the tube. After this

separations process, the remaining clean and white product was collected and kept in an oven for drying at 80 °C for 12 hrs. The obtained white material was ground in an agate mortar and transferred to a sealed vial.

Both commercial TiO<sub>2</sub> P25 (Evonik) and synthesized catalysts (TiO<sub>2</sub>-SG) were characterized by UV-visible diffuse reflectance spectra (UV-vis DRS) and Powder X-ray diffraction (XRD). Additionally, surface morphology study was performed by high resolution scanning electron microscopy (HR-SEM), and the textural properties were determined by Nitrogen sorption. More details on characterization can be found in the supporting information.

### 3.2.3 Ultrasound-assisted deposition of catalyst inside the microtube

The optimization of catalyst deposition inside the PFA microtube was performed based on results obtained from a design experiment software (Design Expert 11),<sup>142,143</sup> considering the following parameters: length of the tube, power of ultrasound irradiation, and duration of deposition. The deposition carried out inside the ultrasonic bath (Sonorex-digital RC, 37 kHz, 120W) at room temperature. Details on deposition and optimization of position of reactor inside US bath can be found in section S 4 and A1.3.

### 3.2.4 Photocatalytic selective partial oxidation of benzyl alcohol

Photocatalysis studies in the batch system (detailed discussed in section A2.2) were carried out to optimize the key parameters like different solvents, mixing speed and loading of the catalyst. In the photocatalytic experiment, 1mM BnOH solution was prepared with BnOH by adding solvents (acetonitrile (AcN), Milli-Q water, 10:90 (v/v) AcN/water and 90/10 (v/v) AcN/water). Different catalyst loadings (0.5, 1, 2 g/ L of commercial TiO<sub>2</sub>) were prepared by mixing catalysts with 1mM of BnOH in AcN to optimize the catalyst concentration. The reaction mixture was stirred at different mixing speeds (200, 400, 600 RPM) at room temperature (Figure S1, S2, S3). Prior to light experiments under UV irradiation (375 nm, power = 2.86 W/ m<sup>2</sup>), dark adsorption studies were carried out in order to determine the adsorption/reactivity in the dark and the duration to reach adsorption equilibrium (30 min). To maintain the temperature inside the system constant (~ 25 °C), a home-made cooling system was designed and immersed inside the water bath.

After the ultrasound-assisted deposition, the P25 coated tubes (T-PFA) were kept inside an oven for drying at 80 °C for 12 hrs. The commercial catalyst was used as a benchmark and to optimize all the parameters for the photocatalytic experiments/deposition. The same procedure (after optimization) was followed for the deposition of sol-gel synthesized TiO<sub>2</sub> into the microtube, and the obtained microreactors are referred to as S-PFA. The microtubes after drying were used for the photocatalytic experiments under UV irradiation by LED (375nm, intensity = 2.86 W/ m<sup>2</sup>, by Radiometer).

*Table 3.1. Information of tubes selected for the catalyst deposition and photocatalytic studies (from design expert), and conversion and selectivity in microflow system after 30min of illumination.*

<b>T-PFA Tube No.</b>	<b>Ultrasonic Power (W)</b>	<b>Length of tube(cm)</b>	<b>Time of deposition (min)</b>	<b>Weight of catalyst deposited (mg)</b>	<b>Conversion (%)</b>	<b>Selectivity (%)</b>
A1	84	40	75	0.1	5	62
A2	48		30	0.2	6	83
A3	120		100	0.4	6	88
A4	48		120	0.2	7	54
A5	120	30	120	0.3	4	85
B1	48		75	0.2	5	84
B2	120		75	0.3	8	87
B3	84		30	0.2	9	74
B4	84	50	120	0.4	3	80
C1	48		75	0.3	6	86
C2	120		75	0.2	8	75
C3	84		30	0.2	10	63
C4	84		120	0.3	5	76

From the batch experiments, the parameters like concentration of catalyst, solvent, time of light irradiation were taken into consideration for determining the experimental parameters for the continuous flow photocatalysis tests. The tube of 30 cm length (Deposition condition: 120 W ultrasonic power, 75 min of deposition) showed better selectivity and conversion (Table 3.1).

### 3.3 Results and Discussion

#### 3.3.1 Deposition of catalyst inside PFA microtube

The first goal was to determine the optimum parameters to deposit the semiconductor catalyst phase inside the microtubes, considering two factors; the amount of the deposited catalyst and, more importantly, the best photocatalytic oxidation of benzyl alcohol (BnOH) to benzaldehyde (BnAld). At this step, we used the commercial TiO<sub>2</sub> P25 (Evonik) as catalyst and a low cost and low power (120 W (100 %) US power, 37 kHz in continuous sweep mode) ultrasonic bath.

Ultrasonic assistance was taken into consideration for having a positive effect either during the deposition of the active phase or for the pre-treatment of the inner walls of the tube before the deposition. Initially, we determined if the ultrasound irradiation (US) plays a crucial role during the deposition. Following similar process, tubes were prepared with or without US during the deposition (section A1.4, Figure A I.4). The results showed that the ultrasound-assisted deposition led to an ~50% higher mass deposition as well as to a higher conversion of benzyl alcohol compared to the deposition in the absence of US. For that reason, we adapted the ultrasound-assisted deposition approach for all the following evaluations.

#### 3.3.2 Effect of pre-treatment before deposition of catalyst

Several chemical and physical effects are resulted from ultrasound are caused due to acoustic cavitation, corrosion, high temperature, the formation and collapse of bubbles in a liquid exposed to oscillating pressure fields.<sup>42</sup> So, the next target was to verify if the pre-treatment of the PFA tubes by ultrasound irradiation (US-pre-treatment) can influence the deposition and, as a result, the photocatalytic activity of the decorated with P25 microtubes. The microtubes were firstly pre-treated with US inside the ultrasonic bath, by passing 5 mL Milli-Q water (1 mL/ min ) through a clean tube under the influence of ultrasound, with the obtained tube referred to as P-PFA.

No weight loss was observed after the US-treatment, although, as can be seen from the SEM images (Figure 16 a, b), the surface of the inner walls became smoother. Two deposited tubes were obtained by ultrasound-assisted deposition of P25 phase to the clean PFA and US pre-pretreated one, referred to as T-PFA and PT-PFA, respectively. The deposition of titania nanoparticles takes place on the modified

surface of the inner walls of the PFA microtube by physical interaction of nanoparticle suspension and the inner wall of the microtube.

The cross-section SEM images revealed that in the case of T-PFA, the thickness of the coating layer could be more pronounced, reaching up to  $7.3\ \mu\text{m}$  in height (Figure 16 c). In the case of the latter, the maximum height of the P25 deposited layer was found  $3.6\ \mu\text{m}$  (Figure 16 d). We assign the higher in deposition thickness in the case of the US-pre-treated tube to the smoother surface compared to no US-pre-treatment microtubes. We have to point out that the catalyst deposition was not perfect in homogeneity (based on SEM analysis), and we gave more research effort towards this direction.

The maximum mass of catalyst loading was found to be equal (average of  $0.01\ \text{mg}/\text{cm}$ ) in both cases, suggesting the same effect of US either during the deposition or US-pre-treatment prior the deposition.

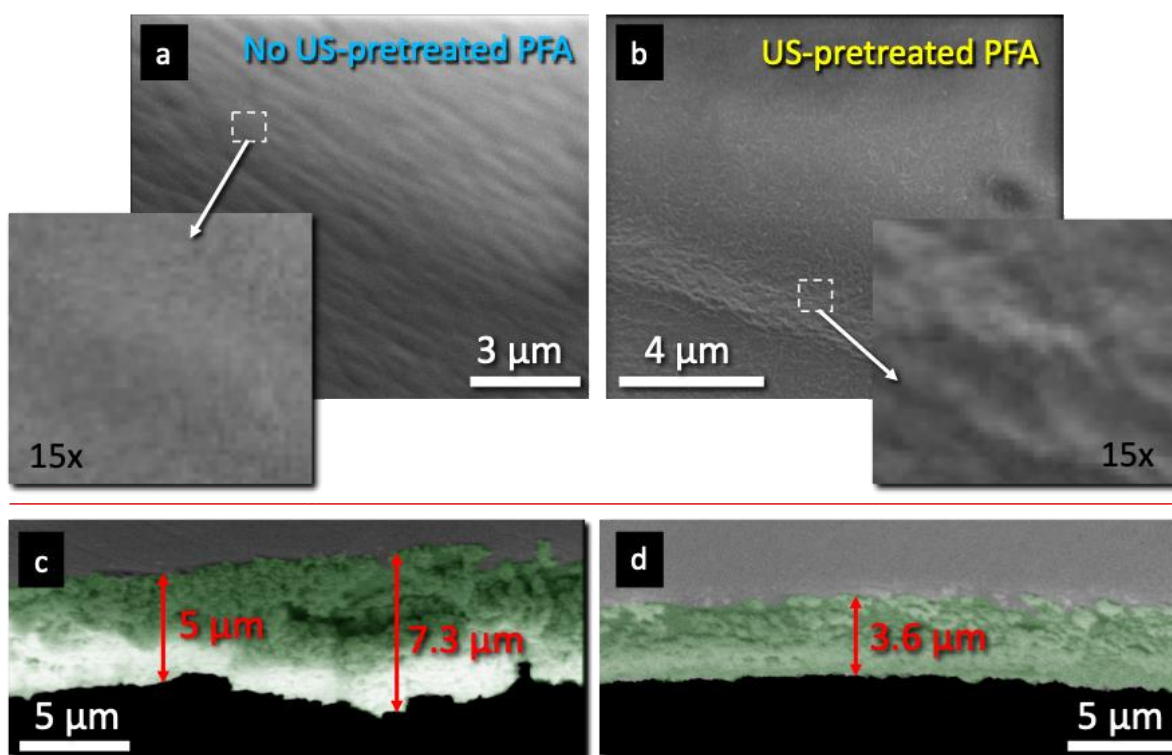


**Figure 16.** SEM images of the inner walls of unmodified PFA microtube (a), ultrasonication pretreated PFA (P-PFA) microtube (b), and cross-section images of P25-TiO<sub>2</sub> deposited microtube (T-PFA) (c), sol-gel synthesized TiO<sub>2</sub> deposited microtube (S-PFA) (d).



### 3.3.3 Effect of ultrasound during deposition of catalyst

The experiments were conducted for the optimized concentration of commercial  $\text{TiO}_2$ , i.e., 0.5 g/L. Two microreactors were prepared to test the photocatalytic oxidation of BnOH in acetonitrile. For the first microreactor, the ultrasonic bath was used during the deposition of catalyst and the other was done in the absence. The photocatalytic activity was analyzed, and the results are shown in Figure S5. There was an increment in selectivity and conversion after 10 min of irradiation time with US assisted deposition method. This increment in the activity might be because of the better immobilization or dispersion of catalysts in the presence of ultrasound.

### 3.3.4 Photocatalytic studies

The PT-PFA (pre-treated and deposited with P25) microreactor showed BnOH conversion and BnAld selectivity 6 and 65 %, respectively. In the case of T-PFA microreactor, the BnOH conversion was almost equal (5 %), although the selectivity to BnAld was 17 % higher than that of PT-PFA. This can be linked to the different deposition extent, as observed from the SEM. In both cases, no leaching of  $\text{TiO}_2$  occurred (Figure S6). Based on the above-discussed results, we discarded the option of US-pre-treatment, and we focused on the utilization of US during the nano-engineering/deposition step of the preparation of the catalyst deposited microreactors, as both processes had an almost similar effect. By this approach, we could avoid the step of ultrasound pre-treatment and use the commercial microtubes after cleaning.

The following and predominant research goal in this study was to determine if the deposition of the synthesized  $\text{TiO}_2$  phase can lead to improve the oxidative performances compared to benchmark P25. For this purpose,  $\text{TiO}_2$  nanoparticles were synthesized based on a sol-gel synthetic route ( $\text{TiO}_2$ -SG).

The optical features of the synthesized ( $\text{TiO}_2$ -SG) and commercial  $\text{TiO}_2$  (P25) in their powder form were evaluated based on the UV-vis diffuse reflectance spectra (Figure S7) and the derived Tauc plots (Figure 17 a) after applying the Kubelka-Munk function.<sup>144,145</sup> The light absorption for P25 occurred for wavelength lower than 412 nm, while for  $\text{TiO}_2$ -SG, lower than 388 nm. The extrapolation from the Tauc plots revealed that the estimated band gaps are  $\sim 3.2$  and  $\sim 3.3$  eV for P25 and  $\text{TiO}_2$ -SG, respectively, values consistent with those reported in the literature for anatase phase.<sup>146</sup>

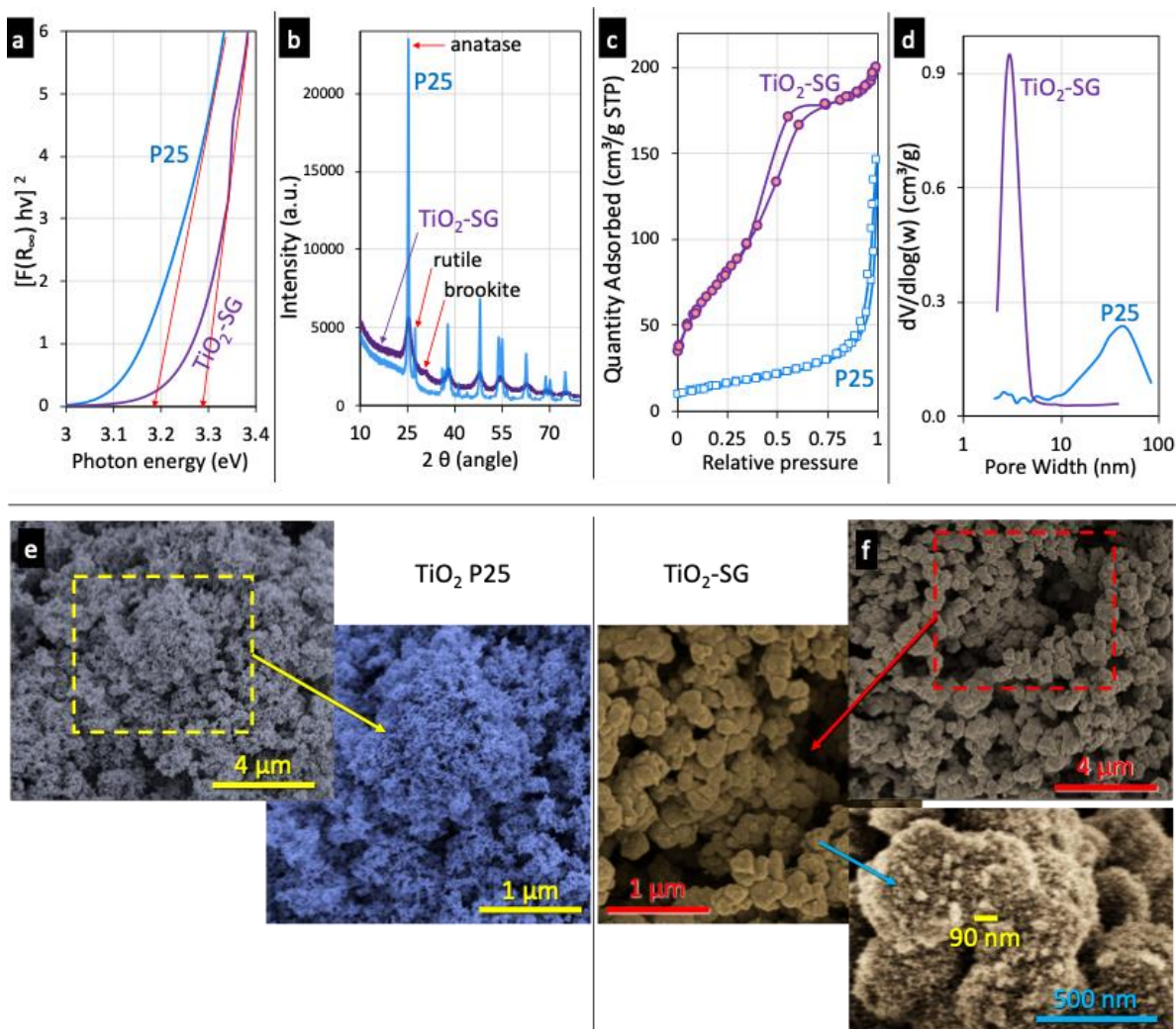


**Figure 17.** Characterization plots of P25 and TiO<sub>2</sub>-SG catalysts bandgap calculation (a), XRD patterns (b), N<sub>2</sub> adsorption/desorption isotherm(c), pore size distribution (d) and SEM images of P25 (e) and TiO<sub>2</sub>-SG (f) nanoparticles (Colored in order to have clear separation).

The XRD patterns of the powders are collected in Figure 17 b. Both samples revealed the reflections at 25.3°, 37.9°, 47.8°, 54.5°, and 62.7°, characteristic for the (101), (004), (200), (105), and (204) diffraction peaks of the anatase crystal structure (JCPDS 02- 0406)<sup>147</sup>. Although, in the case of the synthesized material, all the peaks were found broader and of lower intensity, suggesting the smaller in size crystallinity compared to P25. The dimensions of the crystal phases were estimated by the Scherrer equation (Table 3.2)<sup>148</sup>. The size of the anatase crystallinity was 3.7 nm for the synthesized material, while for the P25 was found 17.7 nm.

Although, both samples revealed to possess a dual-phase crystallinity, anatase and rutile for P25, and anatase and brookite for TiO<sub>2</sub>-SG. The latter phase can be identified from the characteristic diffraction peak (121) at 30.3° and of rutile (110) at 27.4°. <sup>147</sup>

The analysis of the phases composition by full profile analysis by using Rietveld method<sup>149</sup> showed that TiO<sub>2</sub>-SG consists of ~ 69 % anatase phase and ~ 31 % of brookite phase, while P25 ~ 87 % anatase and ~ 13 % rutile. The crystallinity of the titanium dioxide is a key feature in photochemical utilization. Palmisano et al., synthesized different phases of TiO<sub>2</sub> and did a comparative study for the photocatalytic selective oxidation with commercial P25.<sup>150</sup> They concluded that commercial TiO<sub>2</sub> is less photocatalytically active compared to synthesized. Also, Kandiel et al., in a similar type of study, showed that pure brookite phase titania nanoparticles show higher photocatalytic efficiency for the oxidation of methanol, compared to pure anatase phase nanoparticles or P25.<sup>151</sup> To have a thorough comparison, we synthesized amorphous phase TiO<sub>2</sub> by following the same procedure. As an additional step, we kept the suspension on a magnetic stirrer for 12 hrs before centrifugation. This amorphous catalyst was found to be photocatalytically inactive (Figure S8).

Table 3.2. Details of the crystallographic and textural features of the studied materials.

Sample	Anatase:Rutile:Brookite phases (%)	Anatase (nm)	Rutile (nm)	Brookite (nm)	Specific surface area (m <sup>2</sup> / g)	Pore volume (BJH) (cm <sup>3</sup> / g)	Pore size (nm)
P25	87:13:0	17.7	24.8	-	53	0.22	16.3
TiO <sub>2</sub> -SG	69:0:31	3.7	-	5.4	284	0.29	3.2

Another crucial factor for the utilization of material as a photo-catalyst is the textural features. The nitrogen adsorption/desorption isotherm of TiO<sub>2</sub>-SG (Figure 17 c) showed with a shape of Type I and Type IV combination; the former at the low range of relative pressure less than 0.1 and the latter for  $p/p^0 > 0.1$ . This is indicative of materials with a broad distribution in the size of pores from big microporous to narrow mesoporous (Figure 17 d). The hysteresis loop of H<sub>2</sub> type suggests a complex pore structure, with the pore necks to have a wide distribution in size.<sup>152</sup> The pore size distribution revealed that the main volume of the pores for TiO<sub>2</sub>-SG is in the range from 2.2 to 5 nm, while for P25 from 7.5 to 8 nm.

This synthesized catalyst revealed a significant high surface area for metal oxides  $284 \text{ m}^2/\text{g}$ , more than five times higher compared to P25. The total pore volume of  $\text{TiO}_2\text{-SG}$  was found  $0.29 \text{ cm}^3/\text{g}$ , a value around 32 % greater than the one of P25. The smaller in size pores and the higher surface area as well as total pore volume for the synthesized material can be important assets since upon the entrance of the organic compound inside the pore, can be stay more, while the higher porosity can arise an elevated availability of the catalytic sites and better light utilization.<sup>153</sup>

From the SEM analysis of the commercial P25 and synthesized  $\text{TiO}_2$  (Figure 17 e, f), it is clear that the synthesized catalyst forms agglomerates with sizes from 250 to 550 nm consisting of nanoparticles with size less than 35 nm. P25 showed a network of nanoparticles of size less than 35 nm, although no extended aggregation can be observed.

The ability of the material to absorb and scatter the incoming light irradiation also affects their photocatalytic activity, with the size of the particles to play a key role.<sup>154,155</sup> This can be further confirmed from the following photocatalytic evaluation of the materials. Prior to the photocatalysis experiments under UV irradiation, adsorption studies in the dark were carried out, and the adsorption equilibrium reached after 30 min, with no conversion. The oxidative photocatalytic activity of P25 and  $\text{TiO}_2\text{-SG}$  in their powder form was evaluated under the irradiation of UV light ( $2.86 \text{ W}/\text{m}^2$ ) in batch experiments.

After the optimization of various parameters (more details at the supplementary information), the optimal parameters were determined to be  $0.5 \text{ g}/\text{L}$  of catalyst,  $1 \text{ mM}$  of BnOH in acetonitrile, and stirring at 400 RPM at room temperature. Based on the evolutions of the BnOH conversion and selectivity to BnAld up to 60 min (Figure 18), it can be concluded that P25 outperformed the synthesized  $\text{TiO}_2$  from the conversion point of view. Regarding the selectivity, it was, reaching an almost stable value of 28% for P25, while for  $\text{TiO}_2\text{-SG}$ , the selectivity was always above 80 %. Another important outcome is that the conversion of BnOH was continuously increasing for P25, while for  $\text{TiO}_2\text{-SG}$  was stable. Taking into consideration that BnAld was not decomposed between 30 and 60 min, it can be concluded that the surface of  $\text{TiO}_2\text{-SG}$  particles or the active catalytic sites were either blocked or they do not possess the ability for further oxidation or/and decomposition of BnAld. There were no other aromatic byproduct formed (like benzoic acid) or aliphatic ones during this photocatalysis test.

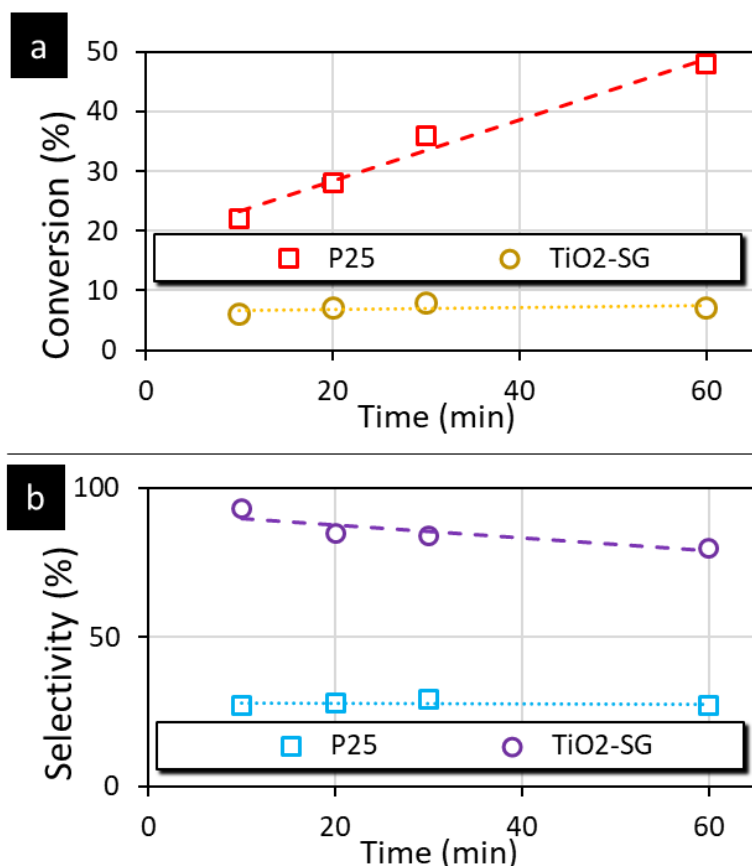


**Figure 18.** Comparison between the conversion and selectivity of commercial P25 with synthesized TiO<sub>2</sub>-SG in batch photocatalysis system (0.5 g/ L, 400 RPM, 1 mM BnOH in AcN, room temperature).

### 3.3.5 Characterization and photocatalytic reaction in S-PFA microtube

The morphology of the TiO<sub>2</sub> - SG coated PFA microtube was analyzed by SEM. From the cross-section analysis of S-PFA (Figure 19 a) can be seen that the thickness of the deposited layer of the TiO<sub>2</sub>-SG can reach up to 5  $\mu$ m, which is similar to the thickness observed in the case of P25 decoration. The HR-SEM micrographs of S-PFA, from the top, (Figure 19 b, c) demonstrate that the deposition occurred without significant alterations of the morphological features of the TiO<sub>2</sub>-SG particles. The presence of larger in size aggregates maybe can lead to a positive impact on the reactivity by disturbing the flow of the solution inside the microtube and preventing the formation of a stable layer of the solvent above /around the upper surface of the deposited phase. The heterogeneous flow can lead to increase in mixing and elevated contact time of the liquid with the catalyst particles.

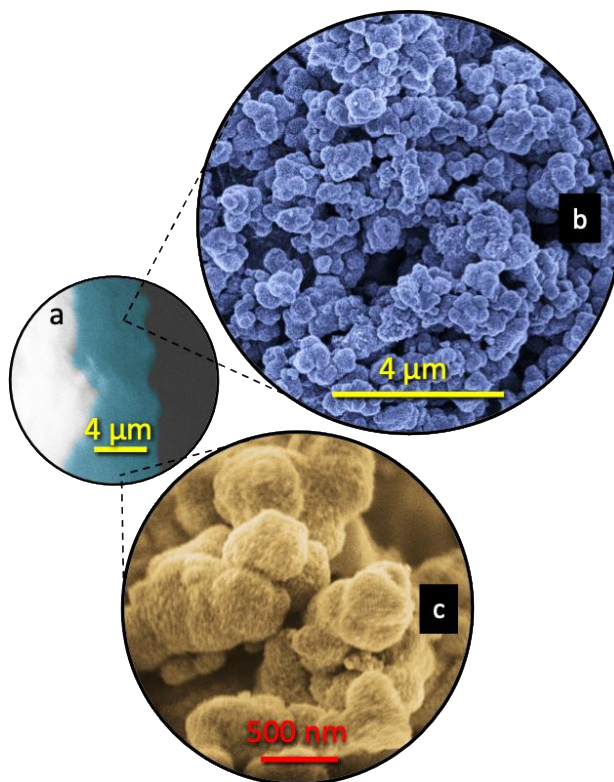


**Figure 19.** SEM and HR-SEM micrographs of the inner walls deposited with the synthesized  $\text{TiO}_2$  microreactor (S-PFA) at different magnifications.

In order to compare the results from commercial P25 with the synthesized catalyst, the same experiment was carried out, and the result is shown in Figure 20. The decrease in conversion from batch to flow system can be because of the size of the tube and the amount of catalyst inside the tube. The specific conversion rate was calculated using the given formula,

$$\text{Specific Conversion Rate} = (\mu\text{mol} / \text{m}^2 \text{ min}) = \frac{C_{\text{BnOH}_0} - C_{\text{BnOH}_t}}{A_c \times \text{time}}$$

Where  $A_c$  is the active surface area (specific surface area multiplied with the concentration of catalyst) of the catalyst taking part in the photocatalytic BnOH conversion.

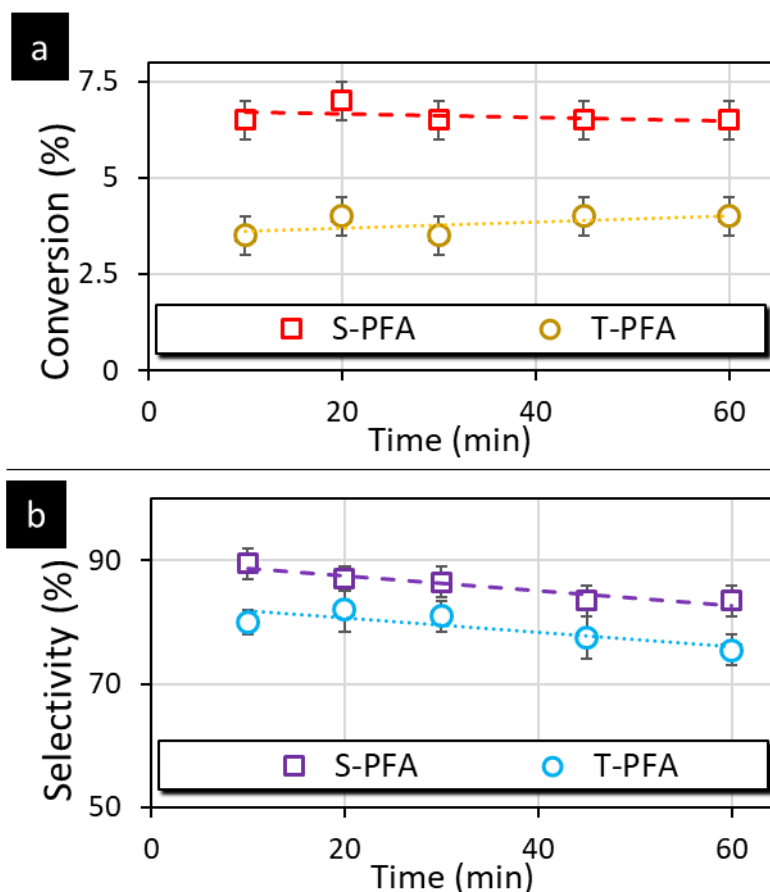


**Figure 20.** Conversion of BnOH and BnAld selectivity of commercial P25 deposited (T-PFA) and synthesized  $\text{TiO}_2$  deposited (S-PFA) microtube.

The synthesized catalyst deposited microtube shows the specific conversion rate of  $6 \mu\text{mol}/\text{m}^2 \text{ min}$  and 87 % of BnAld selectivity after 30 min of irradiation time. From the results, it is clear that the sol-gel synthesized catalyst shows comparatively better selectivity and conversion in one hour of irradiation time compared to commercial P25  $\text{TiO}_2$ .

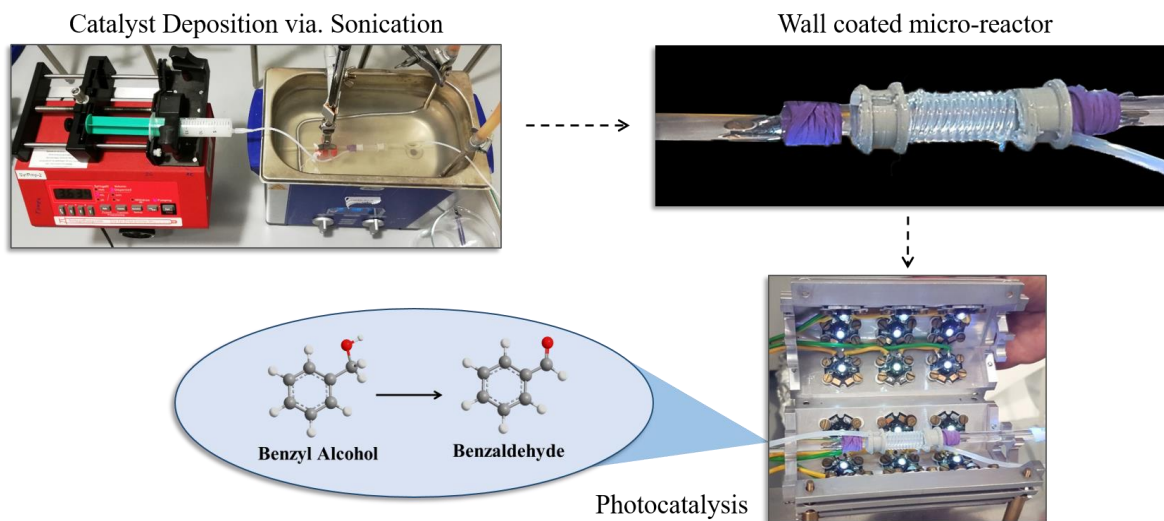
The use of continuous flow microreactors led to improve irradiation over the reaction mixture and offer considerably shorter reaction time and better yields of products compared to batch reactors.<sup>47</sup> Before photocatalytic experiments, the photolysis test in microtube was performed for the same flow rate ( $0.134 \text{ mL}/\text{min}$ ) and it showed null conversion. The commercial P25  $\text{TiO}_2$  catalyst, after 30 min of irradiation time, showed 79 % BnAld selectivity in a micro photoreactor, which was 32% in a batch reactor. This catalyst had a specific conversion rate of  $13 \mu\text{mol}/\text{m}^2 \text{ min}$  in the batch reactor whereas in the flow reactor, the specific conversion rate decreased to  $5 \mu\text{mol}/\text{m}^2 \text{ min}$ .

### 3.4 Conclusions

In summary, we presented herein a “green chemistry” oriented approach to coat the inner walls of a microtube with a thin layer of photoactive  $\text{TiO}_2$  in order to utilize the obtained microreactors towards the selective photocatalytic partial oxidation of a lignin-based model compound, benzyl alcohol, without the use of any addition reagent (like oxidant). The utilization of ultrasonication (US) during the coating process plays a vital role, leading to an enhanced mass deposition, and as a result, better photoreactivity compared to deposition without US. Going a step further, we synthesized nanostructured titanium dioxide ( $\text{TiO}_2$ -SG) nanoparticles following a sol-gel synthetic pathway and compared with the commercially available P25. The main difference between the commercial and the synthesized samples is that the latter except the anatase crystallinity also revealed brookite phase crystals, while P25 is a mixture of anatase and rutile.  $\text{TiO}_2$ -SG also showed a very high specific surface area ( $284 \text{ m}^2/\text{g}$ ) for a metal oxide-based material, almost five times higher than that of P25. After a detailed optimization of the photocatalytic parameters, it was found that in batch, the synthesized catalyst has a significantly lower oxidative conversion performance compared to P25. The most essential and exciting outcome was that upon deposition on the microreactor’s walls, the synthesized material revealed a better photoreactivity on regards to both benzyl alcohol conversion and benzyl aldehyde selectivity, a trend in absolute contrast with the batch experiments case. We link this to the higher availability of the active sites upon the deposition on the tube’s walls and the high surface area of the synthesized nanoparticles. The catalyst synthesis makes the whole approach environment-friendly as it does not include any calcination step unlike  $\text{TiO}_2$  P25. Further exploration on the utilization of nano-engineered microreactors as an additive-free eco-friendly, in terms of simplicity, safety, time, energy, material cost, and environmental impact approach for the selective upgrade of biomass-derived compounds were performed by our research group to enhance the capability of the photoreactors and to determine which factors and features of the catalyst play the most crucial role.



## Chapter 4



The present chapter discusses the research work described in a published manuscript, authored by Swaraj rashmi Pradhan, Dmytro Lisovytskiy and Juan Carlos Colmenares. (*Catalysis Communications* 162 (2022) 106375; doi: 10.1016/j.catcom.2021.106375)

**Abstract:** Ultrasonication was used for deposition of the synthesized monometallic  $\text{TiO}_2$  in the wall of a microtube. A detailed investigation of the photocatalytic activity was made by varying the atomic percentage of metals doped on  $\text{TiO}_2$ . The sol-gel synthesized materials were analyzed by X-ray diffraction (XRD), UV-Vis DRS, Scanning Electron Microscopy (SEM), and nitrogen physisorption. The photocatalytic activities of the monometallic  $\text{TiO}_2$  fluoropolymer-based microreactors were evaluated for the oxidation of benzyl alcohol in flow. Microflow photocatalytic oxidation tests proved that the Fe- $\text{TiO}_2$  material has the highest photocatalytic conversion of benzyl alcohol compared with the other titania samples under UV and visible light irradiation.

## 4. Flow photomicroreactor coated with monometal containing TiO<sub>2</sub> using sonication: a versatile tool for visible light oxidation

### 4.1 Introduction

Lignin is the major by-product of the paper and pulp industries. The complex structure of lignin is a stumbling block that prevents its conversion to a value-added product, which can be helped by the depolymerization of lignin to model lignin compounds. Since benzyl alcohol is a key structural unit of most lignin model compounds, the scientific community is focused on studying its reactivity and transformation strategies.<sup>156–159</sup> The oxidation of aromatic alcohols (benzyl alcohol) to their corresponding carbonyl compounds (especially aldehydes) is one of the important organic transformations as carbonyl compounds are widely used in food, beverages, and pharmaceutical industries and also as precursors in chemical industries.<sup>160</sup>

In recent years, the photo-assisted transformation of benzyl alcohol to benzaldehyde has attracted a great deal of attention as a potential alternative to replace the industrial synthesis route effectively. Photocatalysis is considered a sustainable, environment-friendly advanced technology because of its clean, energy-saving, and low-cost operation. Among various semiconductor photocatalysts used in the past three decades, TiO<sub>2</sub> received the most attention due to its biological and chemical inertness, cost-effectiveness, and the strong oxidizing power of the photo-generated holes.<sup>161</sup> However, one of the major problems of using pure TiO<sub>2</sub> is that only ultraviolet light (UV) photons can displace the valence band electrons of TiO<sub>2</sub> due to its high bandgap energy (3.2 eV), which utilizes only 5% of the available solar radiation. Prior studies have demonstrated that doping TiO<sub>2</sub> with transition metal ions can enhance its photocatalytic activity and have been well explored for alcohol oxidation.<sup>3,150,162–164</sup>

The use of microfluidic reactor has enabled the safe use of molecular oxygen as a green oxidant and enabled readily obtaining a range of benzaldehydes within short reaction times.<sup>165</sup> The chemistry of solid catalyst immobilization on the internal walls of microreactors used in photocatalysis is nowadays well-known.<sup>37,53</sup> Recently, Pradhan et al.<sup>166</sup> have proposed a novel ultrasound based approach for deposition, which helped in better immobilization of catalyst on the wall of the microreactor. In this

current work, we showcase the effect of metal (Fe, Cu, and Co) doped  $\text{TiO}_2$  catalyst inside a fluoropolymer-based microcapillary for the oxidation of benzyl alcohol (BnOH) under UV and visible light irradiation.

## 4.2 Experimental Section

### 4.2.1 Materials

$\text{TiO}_2$  nanoparticles (P25, Evonik) were used as received and often used as a benchmark photocatalyst. Titanium (IV) Isopropoxide (TTIP, 98 %, Acros Organics), Benzyl alcohol (BnOH, 99.5 %, ChemPure), ethanol (EtOH, 99.8 %), methanol (HPLC grade), acetonitrile (AcN, HPLC grade), 0.1 % of  $\text{H}_3\text{PO}_4$  (aq.), propan-2-ol (99.7 %, POCH) were used. Iron (III) nitrate (98 %), cobalt (II) acetate tetrahydrate (98 %), copper (II) acetate monohydrate (98%) were used as received for metal precursors. To prepare solutions, deionized water (Milli-Q) was used. A SunFire<sup>TM</sup> Chromatography column (C18 3.5  $\mu\text{m}$ , Waters) with 4.6×150mm of bed support and Perfluoroalkoxy alkane (PFA, 0.8mm ID, BOLA) were used.

### 4.2.2 Synthesis and deposition of catalysts

The photocatalysts were prepared using sol-gel synthesis method. All the chemicals were used as received without further purification. To synthesize different atomic percentages of metal-containing nanocomposites, metal precursors were dissolved in 2-propanol and followed the previously established sol-gel route.<sup>166</sup> For low-temperature synthesis, sol-gel is an ingenious approach; it is also easier to incorporate metal into  $\text{TiO}_2$ .<sup>160</sup> The metal precursors copper acetate, cobalt acetate, and iron nitrate were used to synthesize Cu- $\text{TiO}_2$ , Co- $\text{TiO}_2$ , and Fe- $\text{TiO}_2$ , respectively. After catalyst synthesis, ultrasonic-assisted depositions were performed using ultrasonic bath (Sonorex-digital RC, 37 kHz, 100% amplitude) in sweep mode. The tube was placed in the ultrasonic bath (Figure S9). The catalyst suspension was passed through a cleaned PFA microtube under the influence of ultrasound using a syringe pump for 75 minutes. For detailed information, please refer to supporting information.

### 4.2.3 Characterization of catalysts and samples

The synthesized samples were characterized using a UV/VIS/NIR spectrophotometer Jasco V-570 equipped with an integrating sphere, and the bandgap was calculated from the Tauc plot derived from

UV-vis diffuse reflectance spectra after applying the Kubelka-Munk function.<sup>144,145</sup> Powder X-ray diffraction (XRD) measurements were performed employing the Bragg-Brentano configuration. This type of arrangement was provided using PANalytical Empyrean diffraction platform, powered at 40kV  $\times$  40mA and equipped with a vertical goniometer, with theta-theta geometry using Ni filtered Cu K $\alpha$  radiation ( $\lambda = 1.5418 \text{ \AA}$ ). XRD patterns were collected from 10 ° to 80 ° with a step size of 0.008 ° and counting time up to 60 s per step. The average crystallite size ( $D$ , in nm) was determined according to the Scherrer equation:

$$D = k \lambda / \beta \cos \theta$$

where  $D$  is the average crystallite size of the catalyst (nm),  $\lambda$  is the wavelength of the Cu K $\alpha$  X-ray radiation ( $\lambda = 0.154056 \text{ nm}$ ),  $k$  is a coefficient usually taken as 0.9,  $\beta$  is the full width at half maximum intensity of the peak observed at  $2\theta$  (radian), and  $\theta$  is the diffraction angle. The elemental maps of the samples were obtained by scanning electron microscopy (SEM) by using a FEI Nova NanoSEM 450. Textural properties of TiO<sub>2</sub> were determined by N<sub>2</sub> physisorption using a micromeritics automated system (Micromeritics Instrument Corporation, Norcross, GA, USA) with the Brunauer- Emmet-Teller (BET, for surface area measurement) and the Barret-Joyner-Halenda (BJH, for porosity measurement) methods. Before adsorption measurements, samples were degassed under vacuum (0.1 Pa) for 12h at 80 C.

After photocatalytic experiments, samples were collected and examined using the energy dispersive X-ray fluorescence (EDXRF) spectrometer (Mini- Pal 4, PANalytical.Co.) with Rh tube with silicon drift detector to check the metals and titania residual. To identify and quantify alcohol, aldehyde, and acid present, the collected samples were analyzed using high-pressure liquid chromatography (HPLC, Waters) using a mobile phase containing a mixture of organic solvents and a 0.05% H<sub>3</sub>PO<sub>4</sub> (5M) aqueous solution (CH<sub>3</sub>CN: CH<sub>3</sub>OH: H<sub>2</sub>O = 20: 2.5: 77.5 v/v).

## 4.3 Results and Discussion

### 4.3.1 Optimization of metal loading in TiO<sub>2</sub>-based composite

Photocatalytic experiments in the batch reactor were carried out to optimize the atomic percentage of metal in TiO<sub>2</sub> before moving to microflow reactor system. Firstly, studies with different atomic

percentages (0.25, 0.5, 1, and 1.5) of copper in Cu-TiO<sub>2</sub> were performed. A cylindrical UV - LED system (375 nm wavelength) was used as a light source whose intensity was 16.6 W/ m<sup>2</sup> (measured by Delta OHM HD 2302.0 radiometer). Photocatalytic experiments in the batch reactor were performed with 0.5 g/ L of catalyst concentration for 60min under UV light, taken from our previous work.<sup>166</sup> Figure 21 shows the photocatalytic selective oxidation of BnOH for each atomic percentage of Cu doped TiO<sub>2</sub> catalyst and comparison with sol-gel synthesized TiO<sub>2</sub> (TiO<sub>2</sub>-SG) after one hour of irradiation time. Parallely, similar batch photocatalytic experiments were performed with Co-TiO<sub>2</sub> and Fe-TiO<sub>2</sub> as well.

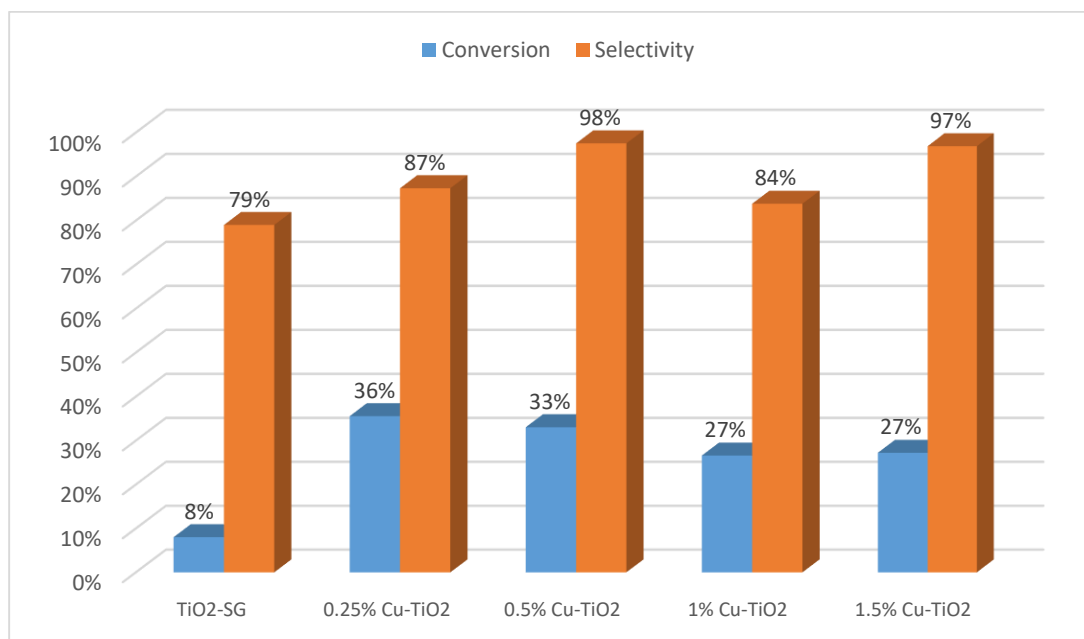


**Figure 21.** Comparison of photocatalytic activity between synthesized TiO<sub>2</sub> and different atomic percentages of Cu-TiO<sub>2</sub> (0.5g/ L) under UV light with 1mM BnOH in batch photoreactor after 60 min of irradiation.

Compared to all atomic percentages of Cu, BnAld selectivity for 0.5% Cu-TiO<sub>2</sub> (CuT) is increased compared to 1 % Cu-TiO<sub>2</sub>. Increasing the atomic percentage of Cu further, though, there is a slight increase in the selectivity, but there is a decline in BnOH conversion. Also, CuT showed better BnOH conversion (33 %) with 94 % benzaldehyde (BnAld) selectivity compared to the synthesized TiO<sub>2</sub> (TiO<sub>2</sub>-SG). On the other hand, by decreasing the atomic percentage of Co from 0.5 at % to 0.25 at % in the case of Co-TiO<sub>2</sub>, there was a considerable increment in the activity (Figure S10). After one hour of photocatalytic experiment, the lesser atomic percentage of metal showed 32% BnOH conversion with 84% towards BnAld selectivity. 0.5 at % of Fe-TiO<sub>2</sub> showed different activity compared to the other two

metal catalysts discussed above. The BnOH conversion for this catalyst was increased to 45 %, but the selectivity lowered to 34 % after one hour of irradiation time (Figure S10).

From the above batch photocatalytic selective oxidation experiments, we selected optimized atomic percentage of metals in metal TiO<sub>2</sub> (0.5 at % of Cu-TiO<sub>2</sub> (CuT), 0.5 at % of Fe-TiO<sub>2</sub> (FeT), and 0.25 % of Co-TiO<sub>2</sub> (CoT)) for microflow deposition and further experimentation.

### 4.3.2 Characterizations of the synthesized catalysts

The XRD patterns of the sol-gel synthesized catalysts were collected in Figure 22. Both TiO<sub>2</sub>-SG and FeT samples revealed the reflections at 25.3°, 37.9°, 47.8°, 54.5°, and 62.7°, characteristic for the (011), (004), (020), (015), and (024) diffraction peaks of the anatase crystal structure (similar to JCPDS 02- 0406 card). In addition to peaks from anatase, both the catalysts show the presence of peaks originating from the brookite phase, (211) at 30.3°. In the case of the FeT material, the peaks of the anatase phase were found narrow and of higher intensity, suggesting a larger crystallite size (D) than TiO<sub>2</sub>-SG (Table 4.1). Also, from the XRD patterns of all metal-containing TiO<sub>2</sub>, there are no visible peaks from metal-containing phases (or pure metal phases), but only from titanium oxides (most probably because of very low content of metals).

*Table 4.1. Textural and structural properties of synthesized catalysts*

Photocatalyst	Anatase:Rutile:Brookite phases (%)	Specific surface area (m <sup>2</sup> / g)	Pore volume (BJH) (cm <sup>3</sup> / g)	Average Pore size (nm)	Bandgap (eV)	Average crystallite size D (nm)
<b>TiO<sub>2</sub>-SG</b>	69:0:31	284	0.29	3.2	3.3	3.7
<b>CuT</b>	-	577	0.12	3.2	3.4	-
<b>FeT</b>	66:0:34	161	0.31	4.2	3.1	5.9
<b>CoT</b>	-	566	0.22	3.2	3.4	-

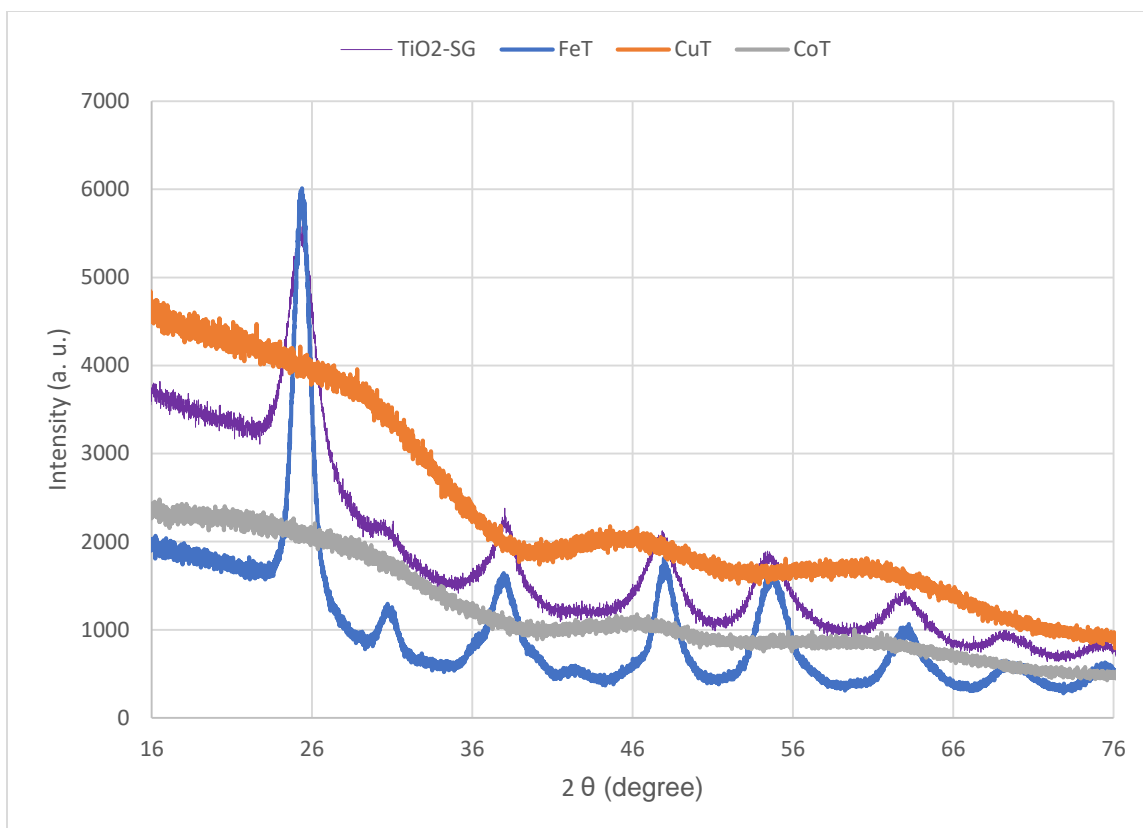


**Figure 22.** XRD patterns of different monometallic synthesized  $\text{TiO}_2$  catalysts Key: For used catalysts sol-gel synthesized  $\text{TiO}_2$  (purple), 0.5 at % Fe- $\text{TiO}_2$  (blue), 0.5 at % Cu- $\text{TiO}_2$  (orange) and 0.25 at % Co- $\text{TiO}_2$  (grey). (For interpretation of the references to color in this figure legend, the reader is referred to the web version of this article.).

The average crystallite size ( $D$ ) of the anatase was 3.7 nm for the  $\text{TiO}_2$ -SG, while for the FeT was found 5.9 nm. In contrast, CuT material had no visible peaks of nano/ polycrystalline  $\text{TiO}_2$  phases and appeared amorphous. Cu heteroatoms were thought to intrude on crystal nucleation and growth.<sup>167</sup> Also, CoT showed an amorphous structure. The synthesized catalysts were not treated at high temperatures (not calcination step) to keep our synthetic method green. Studies showed that the crystalline pure anatase phase of Co- $\text{TiO}_2$  would be visible upon treatment of sample at 450 °C, and after that the rutile phase starts to grow.<sup>168</sup> Also, another possible explanation is that doping of metal could inhibit the crystalline growth of  $\text{TiO}_2$  particles.<sup>169</sup>

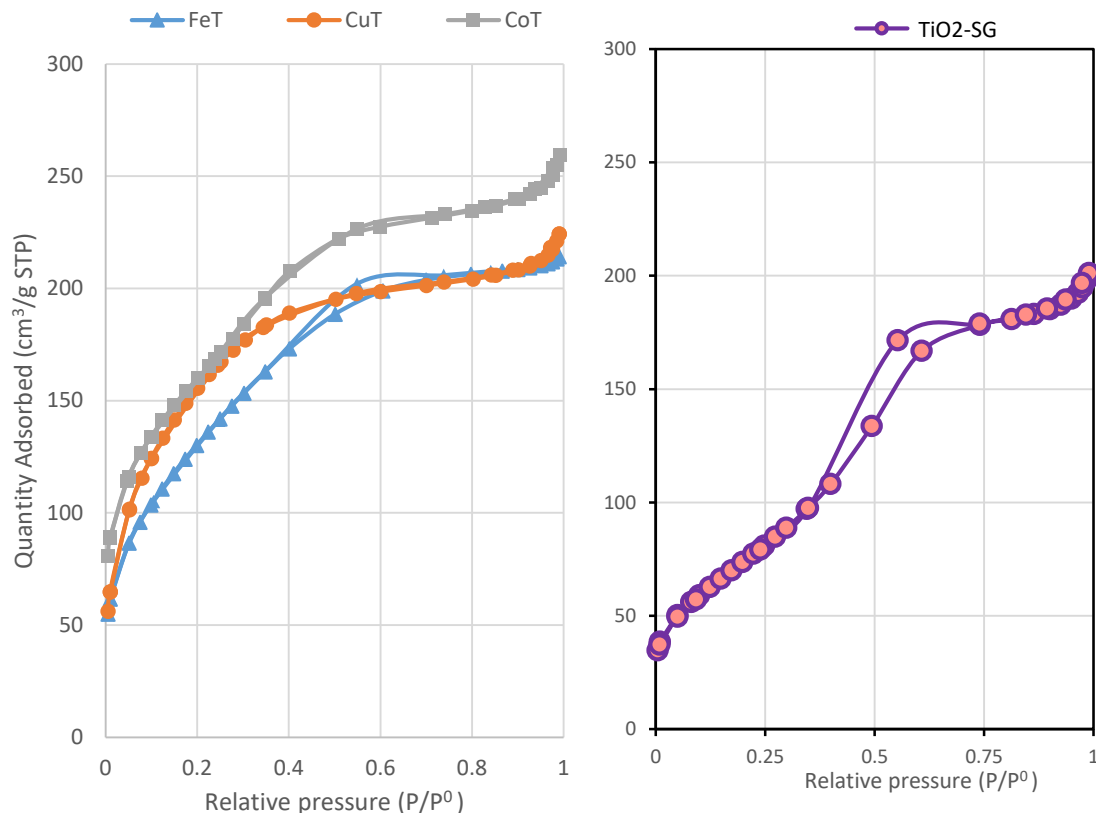


**Figure 23.** Comparison of N<sub>2</sub> sorption isotherm of monometallic TiO<sub>2</sub> (0.5 at % of Cu-TiO<sub>2</sub> (CuT), 0.5 at % of Fe-TiO<sub>2</sub> (FeT) and 0.25 at % of Co-TiO<sub>2</sub> (CoT) with sol-gel synthesized TiO<sub>2</sub> (TiO<sub>2</sub>-SG) catalyst. (For interpretation of the references to color in this figure legend, the reader is referred to the web version of this article.).

The CuT and CoT catalysts showed type II adsorption isotherm, which is for very small pores or microporous adsorbents (Figure 23). In this case, adsorption occurs by filling the micropores. The adsorbate adsorption rate depends on the available pore volume instead of the total interior surface area. A combination of type II and type IV adsorption isotherms was detected for FeT and TiO<sub>2</sub>-SG, which shows the pore size distribution from big microporous to narrow mesoporous.<sup>170</sup> H<sub>2</sub> type hysteresis loop of FeT and SolT suggests a complex pore structure made up of interconnected networks of different sizes and shapes.<sup>152</sup> The average pore size distribution was calculated using BJH (Barrett-Joyner-Halenda) method. The pore size, pore-volume, bandgap, crystallite size, and specific surface area of all synthesized materials are presented in Table 4.1. Among all the synthesized photocatalysts, FeT catalysts showed low surface area (161 m<sup>2</sup>/g) compared to others, and showed the better photocatalytic



activity in a microflow reactor. The higher porosity of FeT can increase the availability of the catalytic sites and better light utilization.<sup>153</sup>

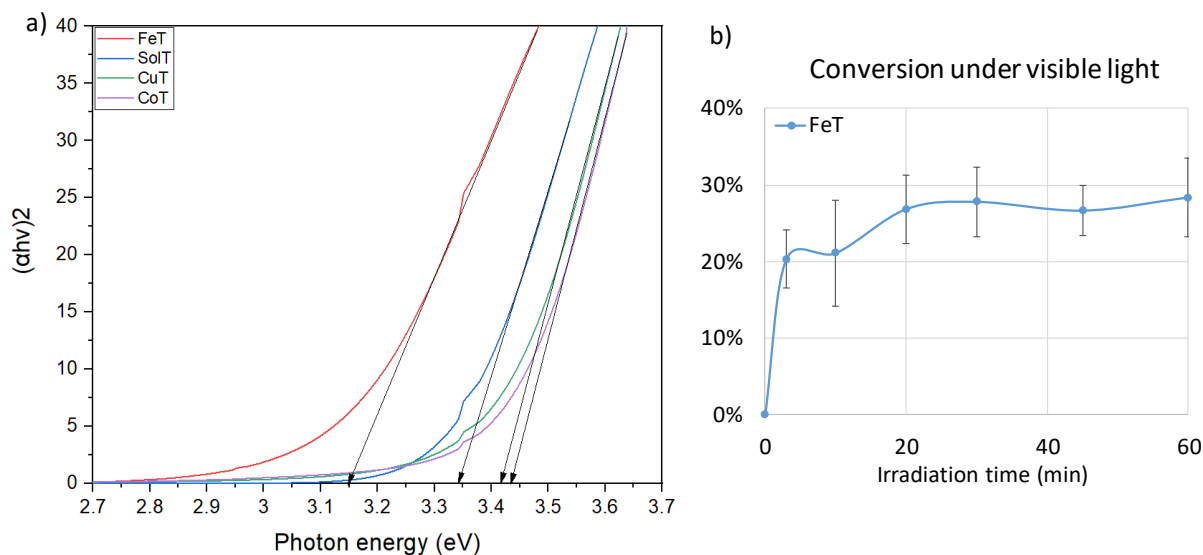


**Figure 24.** Bandgap calculation of sol-gel synthesized  $\text{TiO}_2$  ( $\text{TiO}_2\text{-SG}$ ) and monometallic  $\text{TiO}_2$  (0.5 at % of  $\text{Cu-TiO}_2$  (CuT), 0.5 at % of  $\text{Fe-TiO}_2$  (FeT) and 0.25 at % of  $\text{Co-TiO}_2$  (CoT) catalysts (a), and Photocatalytic activity of synthesized 0.5 at %  $\text{Fe-TiO}_2$  (FeT) under visible light with 1mM BnOH in microflow system (b).

For synthesized  $\text{TiO}_2$ , the bandgap was around 3.3 eV, CuT and CoT have a bandgap of 3.4 eV (Figure 24 a). The bandgap was found lowered by  $\sim 0.2$  eV for FeT catalyst. All the above catalysts ( $\text{TiO}_2\text{-SG}$ , FeT, CuT, and CoT) were immobilized inside the PFA microtube using a sonication-promoted technique described earlier in the manuscript. Optimized parameters from batch systems and design expert calculation (Design Expert 11) were considered for the microflow reactor.<sup>166</sup> The flow rate was set to reproduce enough space-time according to the reactor's dimensions. During the photolysis test for 30 min, benzyl alcohol (in flow microreactor) showed negligible conversion in the dark, hence, no reactivity was confirmed for all the catalysts.

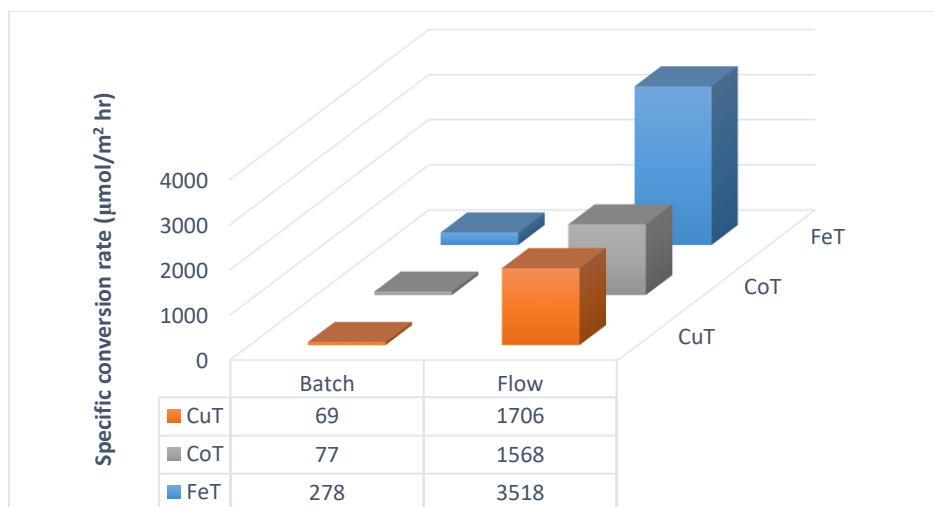


**Figure 25.** Comparison between all synthesized monometallic  $\text{TiO}_2$  photocatalytic conversion under UV light with 1mM BnOH in batch and microflow system (0.5 at % of Cu- $\text{TiO}_2$  (CuT), 0.25 at % of Co- $\text{TiO}_2$  (CoT), and 0.5 at % of Fe- $\text{TiO}_2$  (FeT)).

By moving from batch to microflow, the specific conversion rate increased for all the catalysts. This trend might be due to the higher availability of catalyst active sites upon the deposition on the microreactor walls, and taking advantage of high surface to volume ratio very characteristic when working in microspace. Continuous flow microreactors offered considerably shorter reaction time and led to improved irradiation over the reaction mixture than batch reactors. Also, ultrasonic irradiation increases turbulence in the liquid phase, improving the catalyst active surface area via the de-agglomeration and fragmentation of the nanoparticles<sup>56</sup>. The photocatalytic experiment under UV light showed that FeT has a better specific conversion rate, 3518  $\mu\text{mol}/\text{m}^2\text{ hr}$ , than other catalysts (Figure 25) which value is almost three times higher than that of  $\text{TiO}_2\text{-SG}$  (1048  $\mu\text{mol}/\text{m}^2\text{ hr}$ ). The specific conversion rate was calculated using the given formula,

$$\text{Specific Conversion Rate} = (\mu\text{mol}/\text{m}^2\text{ hr}) = \frac{C_{\text{BnOH}_0} - C_{\text{BnOH}_t}}{A_c \times \text{time}}$$

Where  $A_c$  is the active surface area of the catalyst taking part in the photocatalytic BnOH conversion. In microflow photocatalysis, though the BnOH conversion was better compared to batch, there was negligible selectivity towards benzaldehyde. This is in contrast with the observations in the batch reaction, where the BnAld selectivity was higher (35%, Figure S11). The possible reason might be that

the retention time of the sample inside the microflow reactor is not sufficient for the desorption of the oxidized product from the monometallic catalytic reactor surface. When similar experiments were carried out under visible light (515 nm) system, microtubes deposited with CuT and CoT did not show any activity. However, the FeT deposited PFA tube system showed 28 % (specific conversion rate: 9222  $\mu\text{mol} / \text{m}^2 \text{ hr}$ ) BnOH conversion under visible light (Figure 24 b). The enhanced photocatalytic activity was mainly attributed to increment in crystallite size of anatase phase, high porosity, and low surface area of the FeT catalyst.

Catalyst deposited tubes were characterized by SEM and optical microscope for surface morphology studies. From the cross-section analysis of PFA tubes (Figure 26) can be seen that the thickness of the deposited layer of the catalyst can vary between 2- 4  $\mu\text{m}$ , which is similar to the thickness observed in the case of  $\text{TiO}_2$ -SG deposition.<sup>166</sup>

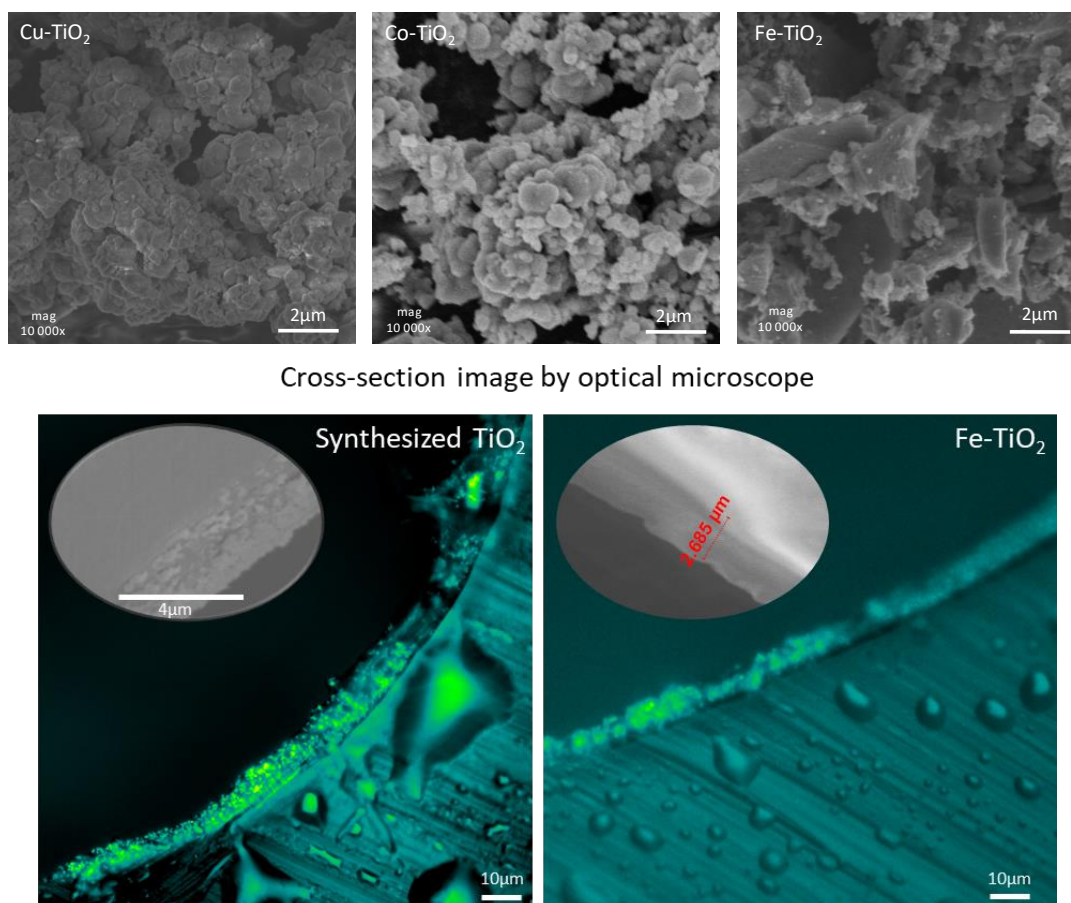


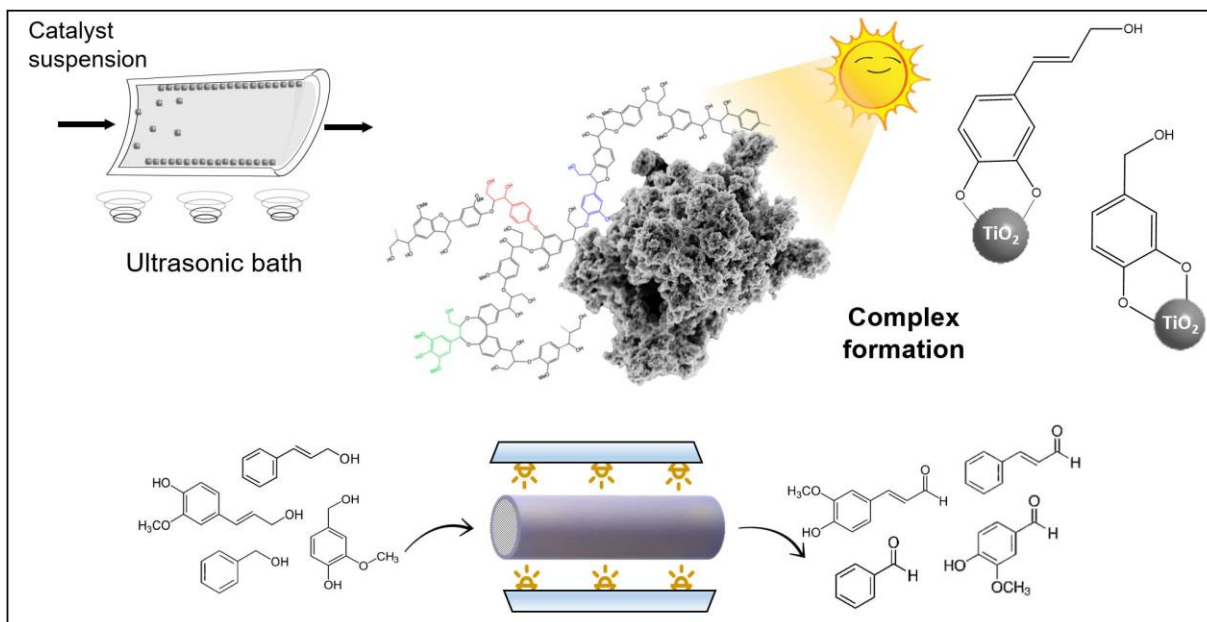
**Figure 26.** SEM micrographs image of the inner walls of microtube deposited with 0.5 at% of Cu-TiO<sub>2</sub> (CuT), 0.25% of Co-TiO<sub>2</sub> (CoT), and 0.5 at% of Fe-TiO<sub>2</sub> (FeT) catalysts.

The SEM micrographs of CuT and CoT catalyst deposited PFA tube, from the top (Figure 26) demonstrate that after the deposition, there are agglomerations of particles with the size of nearly  $1\mu\text{m}$  inside the wall. The presence of big aggregates leads to reduced activity by disturbing the flow of the solution inside the microtube. Because of the flake-like structure of FeT, the hindrance in continuous microflow is minimized compared to that of the highly agglomerated Co and Cu -  $\text{TiO}_2$ . The morphology of this FeT flake catalyst provides more surface access to BnOH for photocatalytic conversion. The small agglomerations (200 - 300nm) and well dispersion in the case of FeT (Figure 26) can lead to improved transfer of light and better interaction of reagent with the surface of the catalyst. Moreover, no leaching from the catalyst deposited microtube after an hour of the experiment was confirmed with the ED-XRF analysis (Figure S12).

#### 4.4 Conclusions

$\text{TiO}_2$  photocatalysts doped with different metals (Cu, Co, and Fe) were synthesized following the sol-gel method and characterized by different techniques successfully. The metal-containing  $\text{TiO}_2$  showed higher photocatalytic activity under UV irradiation than the synthesized  $\text{TiO}_2$  in the batch system. Compared to the batch reactor, the photocatalytic conversion of benzyl alcohol in the microflow system increased. The use of sonication during catalyst deposition in microreactor can lead to enhanced mass deposition, which helps in better conversion. Among all the metal  $\text{TiO}_2$  samples, the 0.5 at% Fe- $\text{TiO}_2$  (cheap and abundant metal) photocatalyst exhibited the highest BnOH conversion under visible light (515 nm) in microflow system. This could be explained by the higher crystallite size observed in XRD analysis. We were able to make an additive (oxidants) free visible light active system for oxidation of lignin-based model compound, benzyl alcohol.

## Chapter 5



*The present chapter discusses the research work described in a submitted for publication manuscript, authored by Swaraj rashmi Pradhan, Marta PaszkiewiczGawron, Dariusz Łomot, Dmytro Lisovyskiy and Juan Carlos Colmenares. (Molecules)*

**Abstract:** The challenge of improving the activity of  $\text{TiO}_2$  by modifying with metals, and using it for targeted applications in microreactor environments is an active area of research. Recently, microreactors have emerged as successful candidates for many photocatalytic reactions, especially for the selective oxidation process. Current work introduces ultrasound-assisted catalyst deposition on the inner walls of a perfluoro-alkoxy alkane (PFA) microtube under mild conditions. We report Cu-Au/ $\text{TiO}_2$ , and Fe-Au/ $\text{TiO}_2$  nanoparticles synthesized using the sol-gel method. The obtained photocatalysts were thoroughly characterized by UV-Vis diffuse-reflectance spectroscopy (DRS), high-resolution scanning electron microscopy (HR-SEM), high-resolution transmission electron microscopy (HR-TEM), X-ray diffraction analysis (XRD), Fourier-transform infrared spectroscopy (FTIR), X-ray photoelectron spectroscopy (XPS), and  $\text{N}_2$  physisorption. The photocatalytic activity under UV (375 nm) and visible light (515 nm) was estimated by the oxidation of lignin-based model aromatic alcohols in batch and fluoropolymer-based flow systems. The bimetallic catalyst exhibited improved photocatalytic selective oxidation. Herein, four aromatic alcohols were individually investigated and compared. In our experiments, the alcohols containing hydroxy and methoxy groups (coniferyl and vanillin alcohol) showed high conversion (93% and 52%, respectively) with 8% and 17% selectivity towards their respective aldehydes, with the formation of other side products. The results offer an insight into the ligand-to-metal charge transfer (LMCT) complex formation, which was found to be the main reason for the activity of synthesized catalysts under visible light.

## 5. Bimetallic TiO<sub>2</sub> Nanoparticles for Lignin-Based Model Compounds Valorization by Integrating Optocatalytic Flow-Microreactor

### 5.1 Introduction

TiO<sub>2</sub> is used as a photocatalyst for degradation of impurities, a component of self-cleaning coatings, cosmetics and for production of hydrogen in the water decomposition reaction.<sup>171,172</sup> Despite the numerous application possibilities, however, industrial use is very limited. TiO<sub>2</sub> due to wide band gap, it is capable of absorbing only UV radiation, which constitutes only 3 to 5% of solar radiation. The consequence of this is the fact that TiO<sub>2</sub> still does not have satisfactory photocatalytic efficiency under visible light irradiation.<sup>173,174</sup> The use of UV lamps as a radiation source, due to the high energy consumption, significantly increases the cost of the process, which is an important factor limiting the broader use of this method in removing pollutants on an industrial scale. Consequently, many studies focused on the visible response of TiO<sub>2</sub> photocatalysts by: (i) doping with metal or non-metal ions, (ii) hetero-junctions creation with other semiconductors<sup>163,175</sup>, (iii) sensitization<sup>176</sup>, (iv) formation of a surface complex with energy transfer<sup>177,178</sup> or (v) surface modification with noble metals nanoparticles.<sup>179</sup> By doping TiO<sub>2</sub> with transition-metal ions (Fe, Cu, Co, Mn, Ni) was reported to be effective for the enhancement of the photocatalytic activity by changing the banding structure of TiO<sub>2</sub> due to the interstitial doping Ti<sup>3+</sup> states as well as the formation of surface oxygen vacancies, which, together, causes the red-shift absorption edge of TiO<sub>2</sub>.<sup>162,169,180,181</sup> Among the noble metals, gold pays more attention in selective photo-oxidation reactions under visible light irradiation.<sup>182</sup> In the past few decades, the rapid expansion of gold (Au) catalysis has developed many new approaches to the aerobic oxidation of alcohols.<sup>183,184</sup> However, bimetallic catalysts have been observed to outperform their monometallic counterparts in conventional heterogeneous catalysis.<sup>23,185</sup> The noble bimetallic nanoparticles have been extensively studied for application in photocatalysis.<sup>186</sup>

Because of their high-value products for the fine chemical, agrochemical, and pharmaceutical sectors, alpha beta-unsaturated aldehydes are essential to a sustainable chemical economy.<sup>187</sup> For example, cinnamyl aldehyde (CinAld) serves as an insect repellent, and also discussing the flavor and aroma of

cinnamon, CinAld is both a food and perfume additive. These aldehydes are usually derived by selective oxidation of their corresponding alcohols.

Catalyst testing in flow microreactors has many advantages over traditional batch reactors. These are, but not limited to, the followings: (i) operating parameters such as temperature, pressure, and feed concentrations can be easily varied in flow microreactors to get an insight into the reaction mechanism and kinetics;<sup>10</sup> (ii) consumption of chemicals and waste production is significantly reduced; (iii) easy testing of catalyst stability under different reaction conditions. Liquid phase catalytic oxidation chemistry in continuous-flow microreactors has recently been summarized from technological and chemical perspectives.<sup>188</sup>

Considering the potential of metals containing TiO<sub>2</sub> catalytic materials and flow microreactors as a powerful tool for catalyst testing, studying the bimetallic catalysts in a flow microreactor for photocatalytic selective oxidation of lignin-based model compound into the value-added product is an exciting field of research. In this work, the photocatalytic activity of synthesized bimetallic TiO<sub>2</sub> nanoparticles was evaluated under UV-light and visible-light irradiations both in batch and microflow systems, using benzyl alcohol (BnOH), vanillin alcohol (VanOH), cinnamyl alcohol (CinOH), and coniferyl alcohol (ConOH) as model compounds of organic-based waste, lignin. The structural properties of the synthesized catalysts were analyzed by X-ray diffraction (XRD) and Fourier-transform infrared (FTIR) spectroscopy. The optical properties were investigated using UV-vis diffuse reflectance (DRS), surface morphology study was performed by high-resolution scanning electron microscopy (HR-SEM), high-resolution transmission electron microscopy (HR-TEM), and the textural properties were determined by nitrogen sorption. We demonstrated that the addition of second metal to metal TiO<sub>2</sub> nanoparticles increased the selective oxidation of BnOH to 100% towards benzaldehyde (BnAld). Also, the complex formation between TiO<sub>2</sub> and other aromatic alcohols (containing methoxy and hydroxy groups) activated the sol-gel synthesized catalyst under visible light. Under batch experiment condition, ConOH and VanOH showed conversion of 93 % and 52 %, respectively under visible light (515nm).

## 5.2 Experimental

### 5.2.1 Materials

Titanium (IV) tetraisopropoxide (TTIP, 98 %, ACROS ORGANICS, Geel-belgium), benzyl alcohol (BnOH, 99.5 %, CHEMPUR, Poland), coniferyl alcohol (ConOH, 98%, ABCR, Karlsruhe-Germany), cinnamyl alcohol (CinOH, 98%, ACROS ORGANICS, New Jersey-USA), vanillyl alcohol (VanOH, 98%, ABCR, Karlsruhe-Germany), ethanol (EtOH, 99.8 %, POCH, Poland), acetonitrile (ACN, HPLC grade, POCH, Poland), propan-2-ol (99.7%, CHEMPUR, Poland) were used as received. Copper (II) acetate monohydrate ( $\text{Cu}(\text{CH}_3\text{COO})_2 \cdot \text{H}_2\text{O}$ , 98%, ABCR, Karlsruhe-Germany), iron (III) nitrate nonahydrate ( $\text{Fe}(\text{NO}_3)_3 \cdot 9\text{H}_2\text{O}$ , 98%, ABCR, Karlsruhe-Germany), copper (II) nitrate trihydrate ( $\text{Cu}(\text{NO}_3)_2 \cdot 3\text{H}_2\text{O}$ , pure, CHEMPUR, Poland), and tetrachloroauric (III) acid trihydrate ( $\text{HAuCl}_4 \cdot 3\text{H}_2\text{O}$ , > 99.5%, ROTH, Karlsruhe-Germany) were used as received as metal precursors.

### 5.2.2 Catalyst synthesis

The bimetallic Cu-Au/TiO<sub>2</sub>, and Fe-Au/TiO<sub>2</sub> nanoparticles were prepared based on the previously established sol-gel method.<sup>166</sup> The required amount of metal precursors (ratio of atomic percent of Au to Cu or Fe was adjusted to 1:4) were added to 15 mL of isopropanol and stirred (magnetic stirrer) at 600 RPM. Under the rotational condition, 4 mL of TTIP was added dropwise to the mixture. Subsequently, Milli-Q water (5 mL) was added to the solution at a rate of 0.167 mL/ min using a syringe infusion pump (Programmable Double Syringe Pump (WPI), NE-4000). After 6 hrs of aging with mixing at 1000 RPM, the resulting solid samples were obtained by centrifugation, washing with deionized water and ethanol, and drying at 80 °C in oven for 24 hrs.

### 5.2.3 Microreactor preparation

A visible-light transparent perfluoroalkoxy alkane (PFA, 0.8 mm ID, BOLA: S 1811-02) tube was used as microreactors.<sup>166,189</sup> 0.5 g/ L concentration (previously optimized<sup>166</sup>) of nanoparticles was dispersed in Milli-Q water by ultrasonication for 15 minutes using an ultrasonic bath (Elma Elmasonic P, 37 kHz, 70% power). 20 mL of the homogeneous nanoparticle suspension was passed through the cleaned PFA microtube under the influence of ultrasound using a syringe pump. The spiralized fragment (Figure 27b) was the effective length subjected to the ultrasound treatment (Elma Elmasonic P, 37 kHz, 100%



power) for 75 minutes (the flow rate of the suspension was 0.26 mL/ min). The tube was placed in the oven for 24 hrs at 80 °C, and later cleaned by passing Milli-Q water and ethanol, dried with airflow, and then in the oven for 1 hr at 80 °C. After this procedure, the catalyst-coated PFA tube was used for photocatalytic experiments (Figure 27 b).

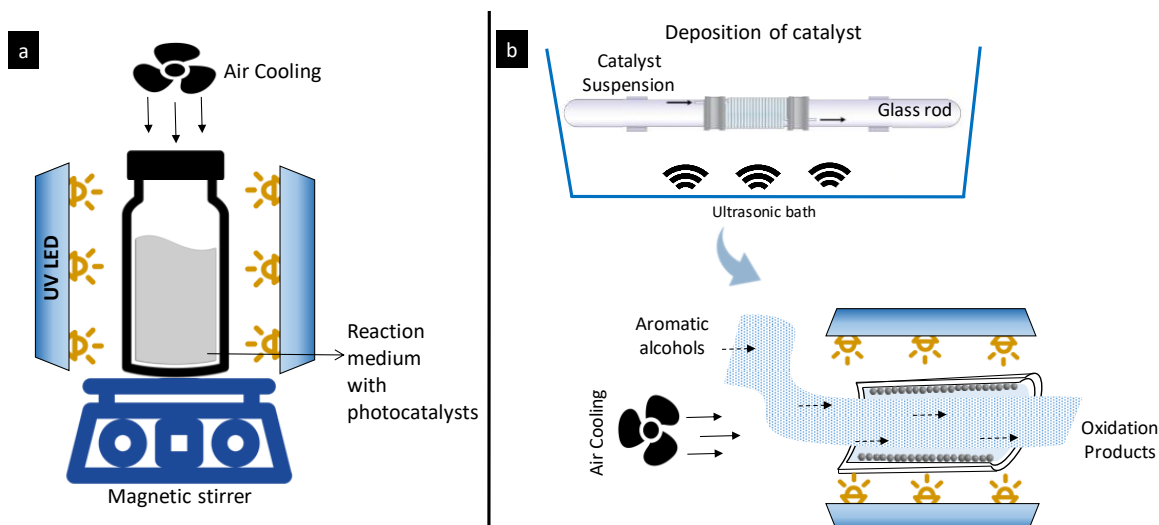


**Figure 27.** Experimental set up of batch (a) and microflow (b) photocatalytic system along with preparation of wall-coated microreactor.

## 5.2.4 Catalytic performance test

The photocatalytic oxidation of the aromatic alcohols over the synthesized catalysts was carried out in batch (Figure 27 a) and microflow reactors (Figure 27 b, Figure S13). A UV-LED and Vis - LED systems were used as light sources (375, and 515 nm wavelength, respectively). The flow rate was set at 0.167 mL/ min (after optimization) to reproduce enough space-time according to the reactor's dimensions, and the whole experiment was carried out for 60 min.<sup>166</sup> Experiments in the batch photocatalytic reactor were performed using 20 mL of the reaction solution and 0.5 g/ L of catalyst concentration for 60 min under UV light. Alcohol conversion, specific conversion rate, and selectivity to each product were calculated according to the following equations:

$$\text{Conversion (\%)} = \frac{\text{Converted moles of aromatic alcohols}}{\text{Initial moles of aromatic alcohols}} \times 100\%$$

$$\text{Selectivity (\%)} = \frac{\text{Produced moles of aromatic aldehydes}}{\text{Converted moles of aromatic alcohols}} \times 100\%$$

$$\text{Specific Conversion Rate} = (\mu\text{mol} / \text{m}^2 \cdot \text{hr}) = \frac{C_{OH_0} - C_{OH_t}}{S_c \times \text{time}}$$

Where,  $C_{OH_0}$  = Initial concentration of aromatic alcohols,  $C_{OH_t}$  = concentration of aromatic alcohols after time,  $t$ , and  $S_c$  is the specific surface area (surface area multiplied by the catalyst concentration) of the catalyst taking part in the photocatalytic conversion.

### 5.3 Characterization

The synthesized samples were characterized using diffuse reflectance spectroscopy (DRS, Shimadzu UV-2600i), and the bandgap was calculated from the Tauc plot. Powder X-ray diffraction (XRD) measurements were performed employing the Bragg-Brentano configuration. This type of arrangement was provided using PANalytical Empyrean diffraction platform, powered at 40kV  $\times$  40mA and equipped with a vertical goniometer, with theta-theta geometry using Ni filtered  $\text{CuK}\alpha$  ( $\lambda = 1.5418 \text{ \AA}$ ) radiation. The elemental maps of the samples were also obtained by FEI Nova Nanolab 200 scanning electron microscopy (SEM). Textural properties of  $\text{TiO}_2$  were determined by  $\text{N}_2$  physisorption using a micromeritics automated system (Micromeritics Instrument Corporation, Norcross, GA, USA) with the Brunauer- Emmet-Teller (BET) and the Barret-Joyner-Halenda (BJH) methods. Before adsorption, samples were degassed under vacuum (0.1 Pa) for 12 hrs at 80 °C. The presence of functional groups on the surface of the catalyst and substrate was determined using the Bruker Tensor II Fourier-transform (FT) IR spectrometer.

Samples collected from the outlet of the catalyst deposited PFA capillary were examined using the energy dispersive X-ray fluorescence (EDXRF) spectrometer (Mini- Pal 4, PANalytical Co.) with Rh tube and silicon drift detector to check the titania residual and other metals. The spectra were collected in an air atmosphere, without a filter, at a tube voltage of 30 kV. To identify and quantify alcohols, aldehydes, and acids present, the collected samples were analyzed using high-pressure liquid chromatography (HPLC, Waters) with mass spectrometry using a mobile phase containing a mixture of organic solvents and a 0.05%  $\text{H}_3\text{PO}_4$  (5M) aqueous solution ( $\text{CH}_3\text{CN}:\text{CH}_3\text{OH}:\text{H}_2\text{O} = 20:2.5:77.5 \text{ v/v}$ ).

## 5.4 Results and Discussion

Oxidation of benzyl alcohol (BnOH) was often used as a model reaction for the oxidation of aromatic alcohols. In order to verify the reactivity of the prepared Cu-Au/TiO<sub>2</sub>, and Fe-Au/TiO<sub>2</sub> catalysts in batch and the performance in the microreactor system, oxidation of BnOH was initially carried out under UV light (375 nm). From the photocatalytic experiment, it was found that modification of TiO<sub>2</sub> with bimetals increased the selective oxidation of BnOH to aldehydes under UV light. In a batch system, the synthesized Cu-Au/TiO<sub>2</sub> with copper acetate precursor (CuA-Au/TiO<sub>2</sub>) catalyst has a significantly higher conversion of BnOH (60%) compared to other bimetallic catalysts with 100% selectivity towards benzaldehyde (BnAld) (Figure 28).

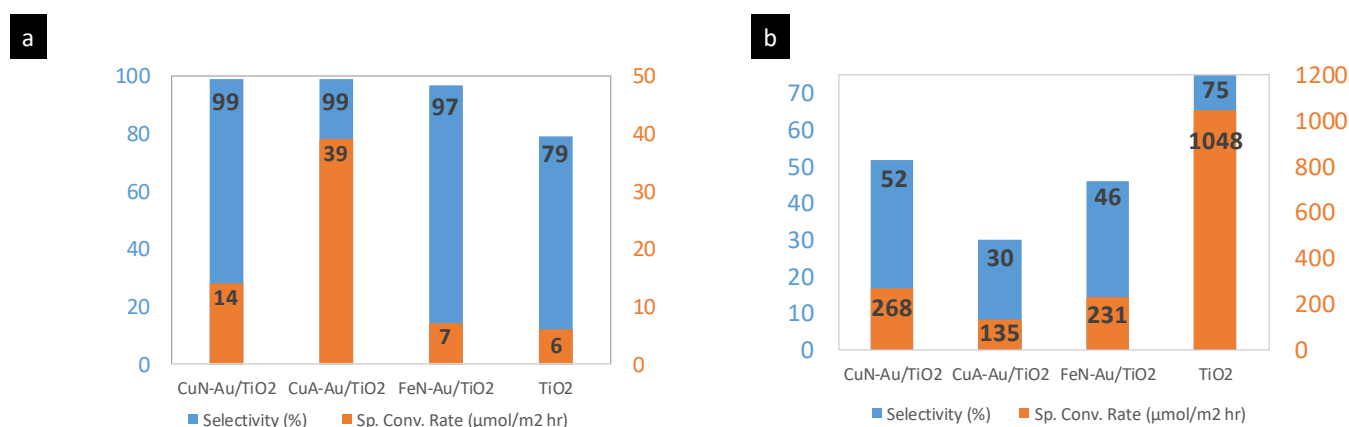


**Figure 28.** Photocatalytic activity of sol-gel synthesized bimetallic TiO<sub>2</sub> in batch (a) and microflow system after 60 min of the photocatalytic experiment (b) with 1mM BnOH under UV light.

Upon the deposition of catalysts on the walls of the microreactor, the synthesized bimetallic materials revealed better photo reactivity in regards to both BnOH specific conversion rates, an absolute contrast trend with the batch experiments (Figure 28). After 3 hrs of light experiment, the specific conversion rate of Cu-Au/TiO<sub>2</sub> prepared using copper nitrate precursor (CuN-Au/TiO<sub>2</sub>) in the batch was 14  $\mu\text{mol}/\text{m}^2\text{ hr}$ , whereas, in the microflow system, it reached 268  $\mu\text{mol}/\text{m}^2\text{ hr}$ .

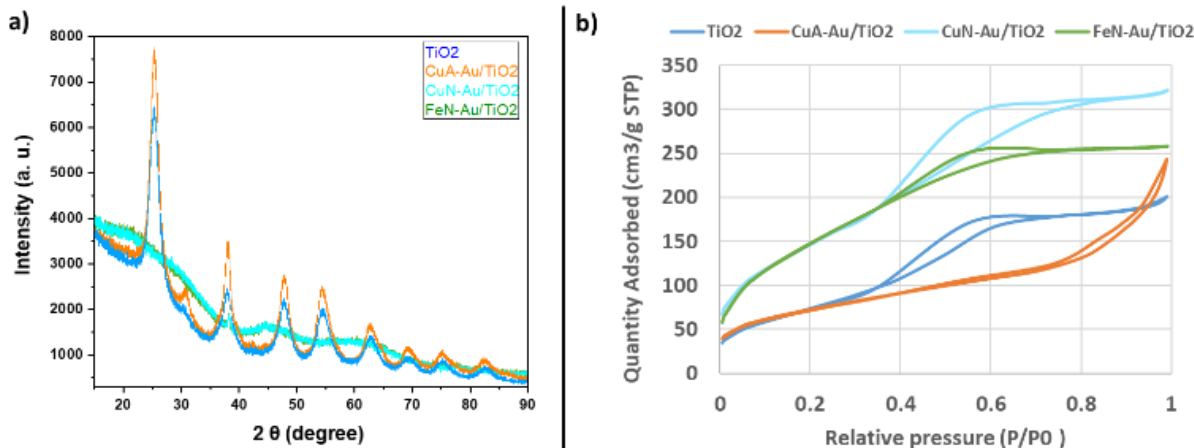


**Figure 29.** XRD patterns of different bimetallic synthesized catalysts (a),  $N_2$  sorption isotherm of bimetallic  $TiO_2$  (b) compared to sol-gel synthesized  $TiO_2$  catalyst.

The specific surface areas determined from  $N_2$  physisorption for the Cu-Au/ $TiO_2$  and Fe-Au/ $TiO_2$  varied from 251 to 547  $g/m^2$ , which was predominantly controlled by the type of precursor used for synthesis (Figure 29). The use of nitrate precursor during the synthesis procedure caused a significant increase (about two times) in the specific surface area with reduced crystallinity (Figure 29 a) compared to pure  $TiO_2$ . Au phase is not a dominant phase for these catalysts, therefore small peak of Au is observed. Amorphous phases dominate in CuN-Au/ $TiO_2$  and FeN-Au/ $TiO_2$  samples, such phases do not give peaks in the XRD pattern, and on the background of such phases even a small peak from nanocrystalline gold is easily detectable. The crystallite size of Au for each catalysts are shown in Table 5.1.

A combination of type II and IV adsorption isotherms was noticed for sol-gel synthesized  $TiO_2$  and the bimetallic catalysts with nitrate precursors (Figure 29 b).<sup>190</sup>  $H_2$  type hysteresis loop of these catalysts suggested complex pore structure.<sup>152</sup> On the other hand, the bimetallic catalyst with acetate precursor (CuA-Au/ $TiO_2$ ) showed type IV adsorption isotherm,<sup>190</sup> suggesting the presence of mesopores. The shape of the hysteresis loops was of type H3, which indicates the presence of aggregates of slit-shaped conical pores composed of primary particles, which can give rise to piled-up pores.<sup>191</sup>

Table 5.1. Crystallographic, structural, and textural features of the synthesized bimetallic catalysts.

Sample	Anatase: Brookite: Gold crystalline phases (%)	Specific surface area (m <sup>2</sup> / g)	Average pore size (nm)	Pore volume (BJH) (cm <sup>3</sup> / g)	Average crystallite size (Dcr)[nm] (Au phase)  by XRD
TiO <sub>2</sub>	69:31:0	284	3.2	0.3	n/a
CuA-Au/TiO <sub>2</sub>	68:31:0.44	251	6.8	0.3	11 (200)
CuN-Au/TiO <sub>2</sub>	-	541	3.1	0.4	18 (111)
FeN-Au/TiO <sub>2</sub>	-	547	2.8	0.2	18 (111)

The Tauc plots (Figure S14) revealed that the bandgaps for all the synthesized catalysts were ~3.4eV. Also, BJH (Barrett-Joyner-Halenda) method was used to calculate the average pore size distribution, and the values are provided in Table 5.1.

The average pore size was lower for samples synthesized using nitrate precursors than for samples that were prepared with acetate precursors. This observation can be explained by a partial modification of the TiO<sub>2</sub> surface by nitrate decomposition and evolving gaseous NO<sub>x</sub> during the synthesis procedure. Photocatalytic activity in the microflow system (Figure 28 b) of CuN-Au/TiO<sub>2</sub> and FeN-Au/TiO<sub>2</sub> accompanied by their larger specific area, which in consequence, may provide more active sites and shorten the bulk diffusion length of charge carriers, thus suppressing bulk recombination.<sup>192</sup> However, pore volume was much higher for the sample CuN-Au/TiO<sub>2</sub> (0.4 cm<sup>3</sup>/ g) than for FeN-Au/TiO<sub>2</sub> (0.2 cm<sup>3</sup>/ g), even though nitrogen salts were used in both cases during the preparation. This dependency can be caused by the steric hindrance during the growth of the TiO<sub>2</sub> crystallites via Ostwald ripening.<sup>193</sup> The molecular structure of iron (III) nitrate nonahydrate is bigger than copper (II) nitrate trihydrate (computed by PubChem), which consequently causes more steric hindrance.

The synthesized bimetallic catalysts were investigated using Transmission Electron Microscopy (TEM). The composition of the particles was studied using STEM (High Angle Annual Dark Field, HAADF) and EDXS mapping. In the CuA-Au/TiO<sub>2</sub> sample, the TEM analysis revealed that primary nanoparticles were clustered to form more oversized agglomerates during the formation stage itself (Figure 30). The results of the TEM analysis showed that Ti, O, and Cu are evenly distributed throughout the sample surface (Figure 30 d-e).

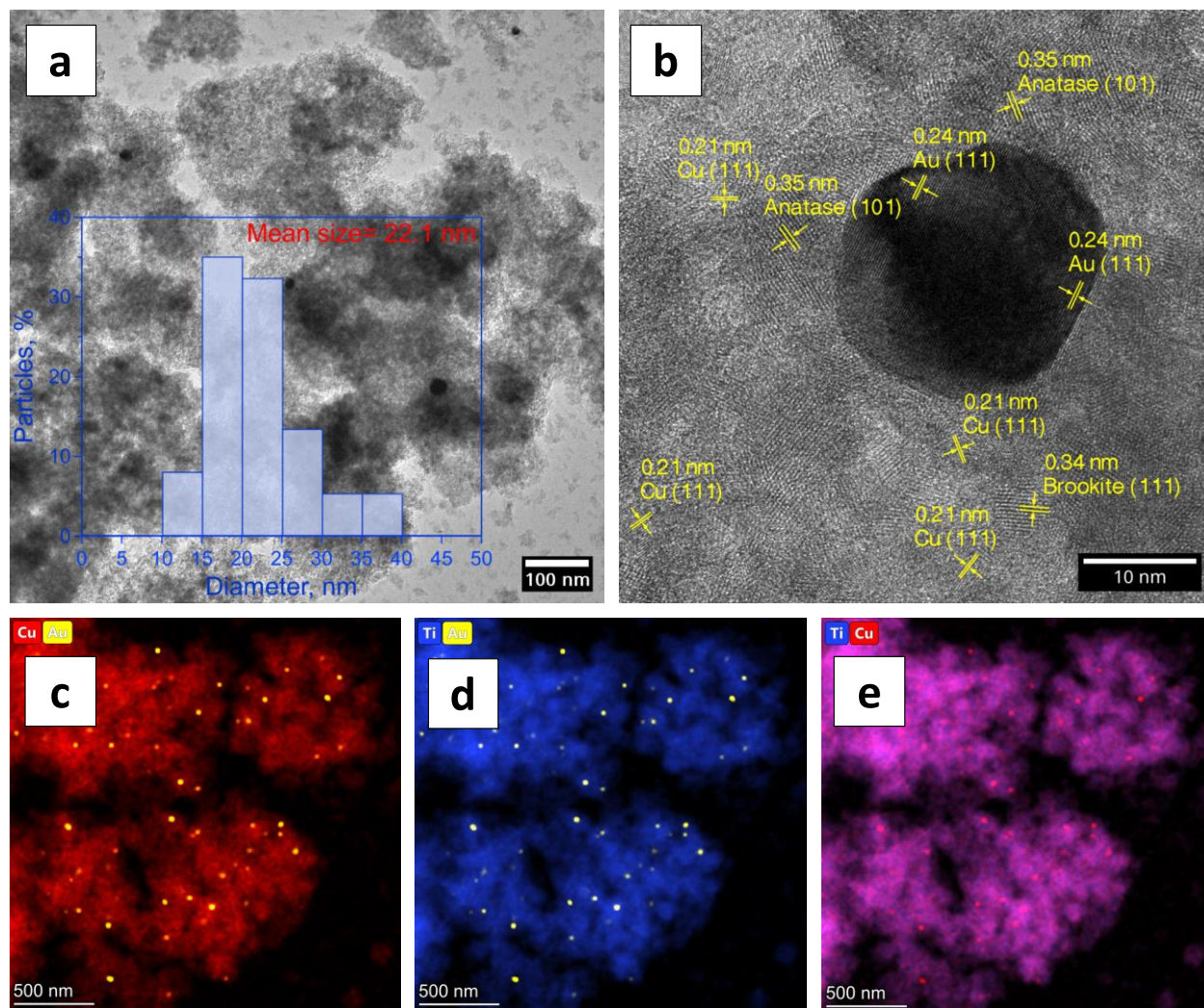


**Figure 30.** TEM images of obtained CuA-Au/TiO<sub>2</sub> sample: SE mode with a particle size distribution (a), SE mode (b), EDS HAADF analysis of Cu (c) and Au, EDS HAADF analysis of Ti and Au (d), EDS HAADF analysis of Ti and Cu (e).

The application of the HAADF method confirmed the presence of the expected elements, such as Ti, Cu, and Au (Figure 30 c-e), and also, from XPS analysis of CuA-Au/TiO<sub>2</sub>, we were able to confirm the presence of 0.1 at% Cu, 0.03 at% Au in the catalyst surface (Figure S16). Gold and copper nanoparticles were evenly distributed in the tested sample (Figure 30 b-d) which is very important in terms of the influence on the photocatalytic activity. Based on TEM analysis (Figure 30), UV-Vis DRS spectra (Figure S15), and XPS analysis (Figure S16), it can be deduced that surface incorporation of Cu and Au atoms on the TiO<sub>2</sub> has occurred. On UV-Vis spectra, the red shift of absorption for CuA-Au/TiO<sub>2</sub> in comparison to bare TiO<sub>2</sub> and no obvious peak from copper nanoparticles can be seen. The absence of the peak coming from Cu NPs could be due to the low amount of Cu NPs on the TiO<sub>2</sub> surface. The same results regarding the slightly red shift of absorption to 403 nm for copper nanospheres coupled with TiO<sub>2</sub> were obtained by Monga et al. and also other research groups.<sup>194-196</sup> The distinct peak derived from Au nanoparticles occurred at 560 nm due to the charge transfer from metal ion to TiO<sub>2</sub>.<sup>195</sup> The above-mentioned absorption in the range of visible irradiation may be due to the localized surface plasmon resonance (LSPR). It has been shown that in the mechanism using LSPR, metal can act as an electron trap and thus inhibit the recombination process of electron-hole pairs.<sup>197,198</sup> The characteristic LSPR band maximum at 555 nm<sup>199</sup> indicates the presence of Au nanoparticles in the CuN-Au/TiO<sub>2</sub> sample, shown on UV-Vis DRS spectra (Figure S15).

It can be clearly seen in the TEM pictures (Figure 30 b) that the obtained gold nanoparticles have a spherical shape, and the particle size distribution of Au was in the range of 10-40 nm, with the highest contribution of the fraction from 15 to 25 nm and mean size equal to 22.1 nm (Figure 30 a). The nanometric size and shape of the obtained Au particles are good enough to provoke LSPR.<sup>194,200</sup> This proves that the particles in nanoscale with a favorable spherical shape were successfully obtained during the synthesis procedure. Gołabiewska et al.<sup>201</sup> have shown that the spherical shape of gold nanoparticles was very beneficial for increasing the photocatalytic activity in the range of visible irradiation. They compared the photoactivity of different shapes of Au particles deposited on TiO<sub>2</sub> microspheres and proved that visible light activity decreased in the following order: spheres > rods > stars<sup>201</sup>. It can also be added that in the case of CuA-Au/TiO<sub>2</sub> sample, the inter-planar spacing for gold was 0.24 nm, which corresponds to the separation between (111) lattice planes of Au (Figure 30 b), which was consistent with the results obtained by XRD analysis (Table 5.1).



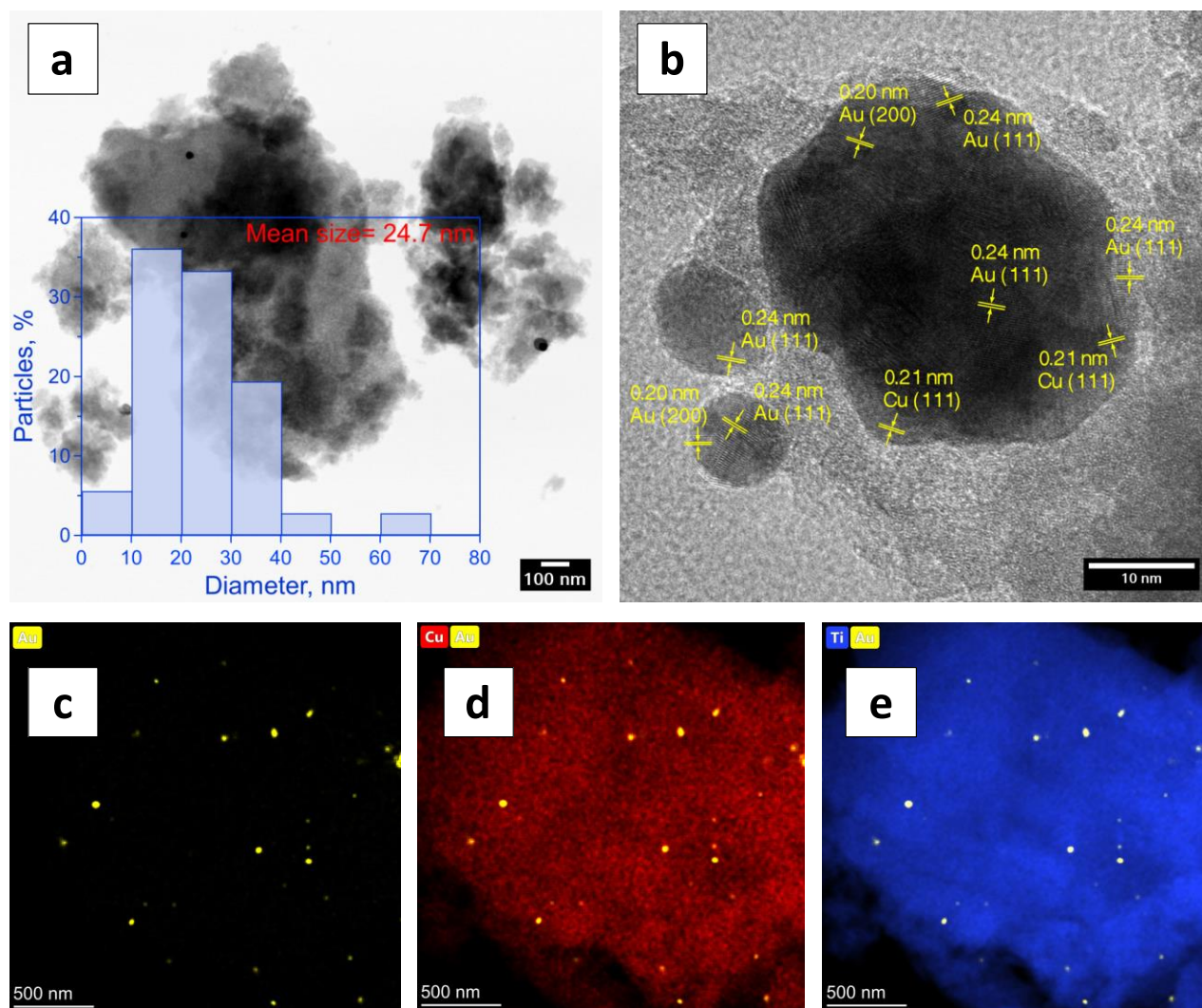


**Figure 31.** TEM images of obtained CuN-Au/TiO<sub>2</sub> sample: SE mode with particle size distribution (a), SE mode (b), EDS HAADF analysis of Au (c), EDS HAADF analysis of Cu and Au (d), EDS HAADF analysis of Ti and Au (e).

Very similar to the CuA-Au/TiO<sub>2</sub> TEM analysis results were obtained for the CuN-Au/TiO<sub>2</sub> sample, where the gold particles have a nanometric size and spherical shape; also, they were evenly distributed over the entire sample (Figure 31 a-e). The difference in the photocatalytic activity of these samples was probably due to the precursors used (nitrate and acetate). The average size of the Au particles ranges between 10-50 nm also less than 5% in the range 60-70 nm, with a significant predominance of particles with sizes from 10 to 30 nm, where the mean size was 24.7nm (Figure 31 a) Moreover, Au particle has planes (111) and (200), which correspond to the 0.24 and 0.20 nm, respectively. (Figure 31 b).



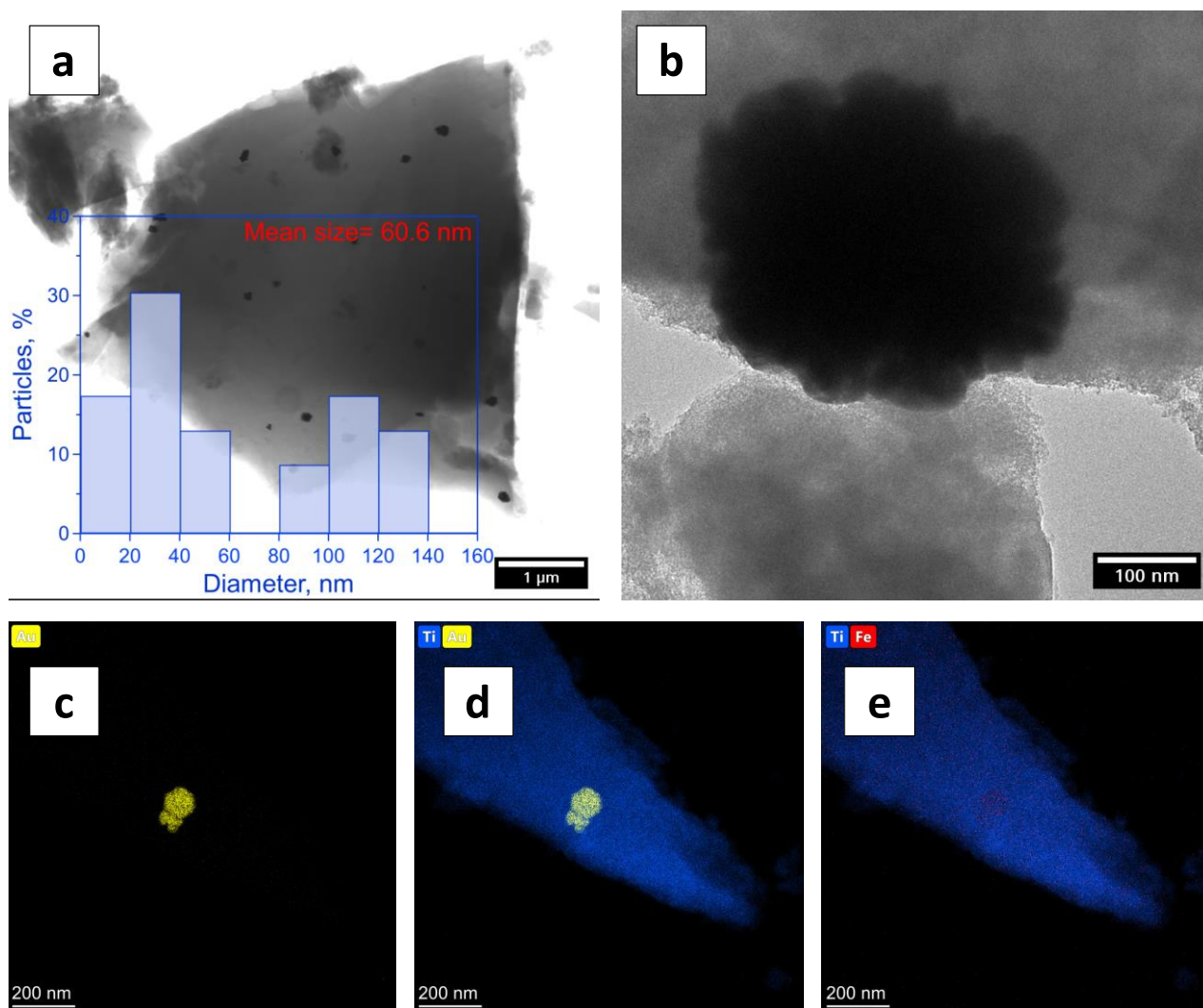


**Figure 32.** TEM images of obtained FeN-Au/TiO<sub>2</sub> sample: SE mode with particle size distribution (a), SE mode (b), EDS HAADF analysis of Au (c), EDS HAADF analysis of Ti and Au (d), EDS HAADF analysis of Ti and Fe (e).

The TEM micrographs of FeN-Au/TiO<sub>2</sub> shown in Figure 32 gave a bright observation of the sample in which the particles are much bigger than those obtained in the case of the samples containing copper (mean sizes of particles was 22.1 nm for CuN-Au/TiO<sub>2</sub> and 24.7 nm for CuA-Au/TiO<sub>2</sub>). The particle size was found in the range of up to 60 nm and also in the range from 80 to 140 nm, with the mean size equal to 60.6 nm. (Figure 32 a). It should be emphasized that in the UV-Vis DRS spectrum (Figure S15), no characteristic peak from the LSPR of gold particles was detected. Similar results were obtained by Duan et al., where despite the presence of gold particles in the sample, confirmed by other analytical methods, the characteristic peak of approx. 550 nm was not observed.<sup>202</sup> Similar results were obtained for FeN-Au/TiO<sub>2</sub> sample, big agglomerates which caused an uneven distribution of Au particles on the TiO<sub>2</sub>

(Figure 32 d, e), which can be the reason for the absence of the peak from Au NPs in the UV-Vis DRS spectra. However, a significant shift of absorption towards the visible spectrum ( $> 400\text{nm}$ ) for FeN-Au/TiO<sub>2</sub> in comparison with unmodified TiO<sub>2</sub> was observed on UV-Vis DRS (Figure S15), and also the presence of Fe 2p 3/2 on the surface of the catalyst (confirmed by XPS analysis) indicate the probable surface incorporation of Fe and Au atoms on the TiO<sub>2</sub>. The aim of introducing the Fe atoms to the sample was to increase the absorption toward visible light wavelength and thus increase the photocatalytic activity in the visible range.<sup>203</sup> The distribution of Fe atoms observed on TEM connected with UV-Vis DRS and XPS results can testify to the surface incorporation of Fe atoms.<sup>204,205</sup>

In the SEM images of the bimetallic TiO<sub>2</sub> particles, presented in Figure 33, it was observed that the sample prepared using acetate precursor has a more sponge-like surface, with more cavities in the structure, compared to those obtained with nitrate precursor. CuN-Au/TiO<sub>2</sub> and FeN-Au/TiO<sub>2</sub> particles were poorly formed with highly irregular shapes.

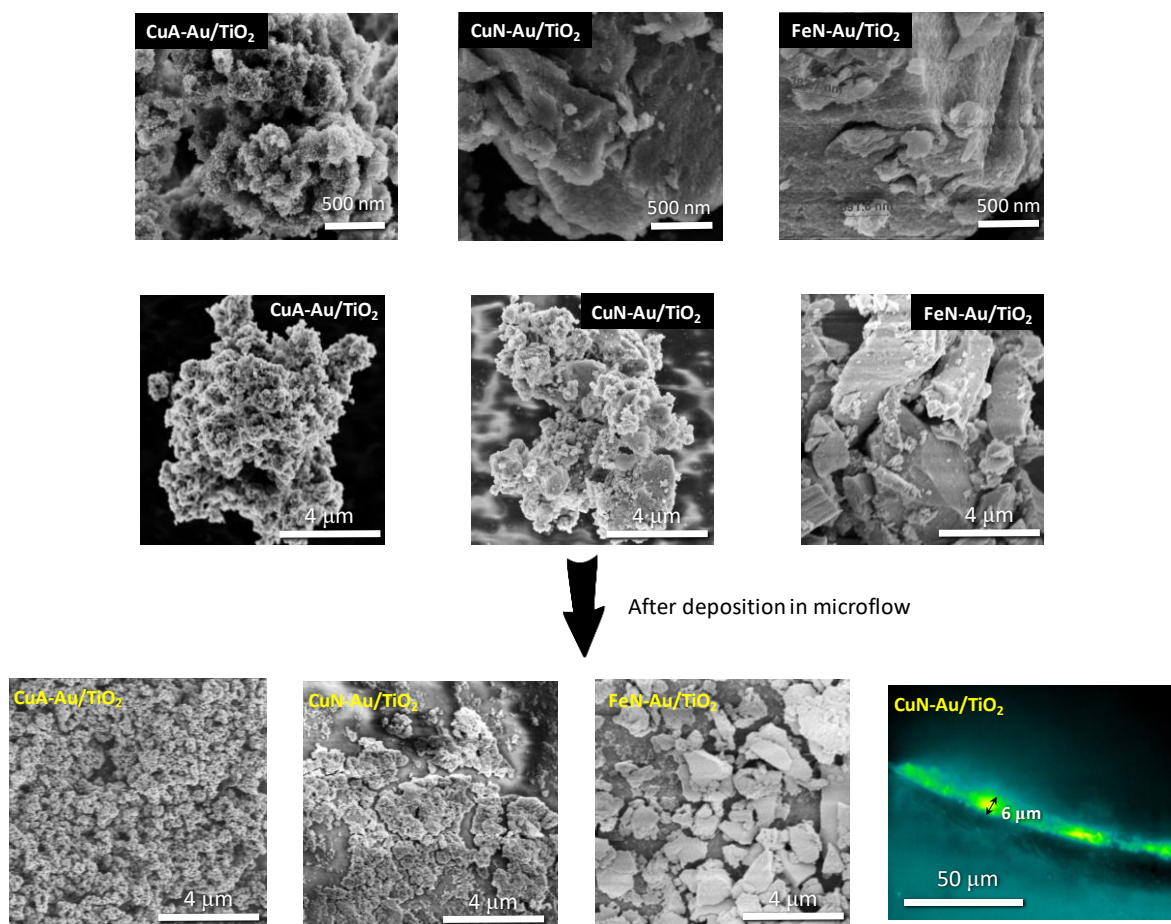


**Figure 33.** SEM and optical microscope image of sol-gel synthesized bimetallic  $\text{TiO}_2$  and after deposition in PFA microreactor.

The use of sonication improves catalyst deposition in a microreactor aided by enhanced mass deposition, which subsequently improves the overall photocatalytic conversion.<sup>206</sup> We link this activity to the higher availability of the active sites upon the deposition on the wall of the microreactor. On the deposition of these catalysts in the microflow system under the influence of ultrasound, the breakage of the agglomerations into smaller sizes was observed. The big aggregates (300-500 nm) in the case of  $\text{CuA-Au/TiO}_2$  disturb the flow of the solution inside the microtube, reducing the activity of the catalyst (Figure 33). The small agglomerations (80-250 nm) and well dispersion in the case of  $\text{CuN-Au/TiO}_2$  and  $\text{FeN-Au/TiO}_2$  (Figure 33) can lead to improved transfer of light and better interaction of reagent with the surface of the catalyst. The thickness of the deposited catalyst inside the wall of the microreactor was 5-7  $\mu\text{m}$ , measured with an optical microscope image, hence the better photocatalytic activity in the microflow system for this catalyst.

The synthesized CuA-Au/TiO<sub>2</sub> catalyst was considered for the oxidation of aromatic alcohols (vanillyl alcohol (VanOH), coniferyl alcohol (ConOH), and cinnamyl alcohol (CinOH) under UV (375nm) light, as this catalyst showed better activity under UV light for BnOH oxidation (Figure 28 a) in a batch system. Before light experiments, dark adsorption studies were performed to determine the adsorption/reactivity, and the duration to reach adsorption equilibrium was 30 min. Strong adsorption of VanOH (37%) and ConOH (30%) was observed on the surface of bimetallic CuA-Au/TiO<sub>2</sub> in the dark, which might be because of the complex formation between these alcohols with TiO<sub>2</sub>.

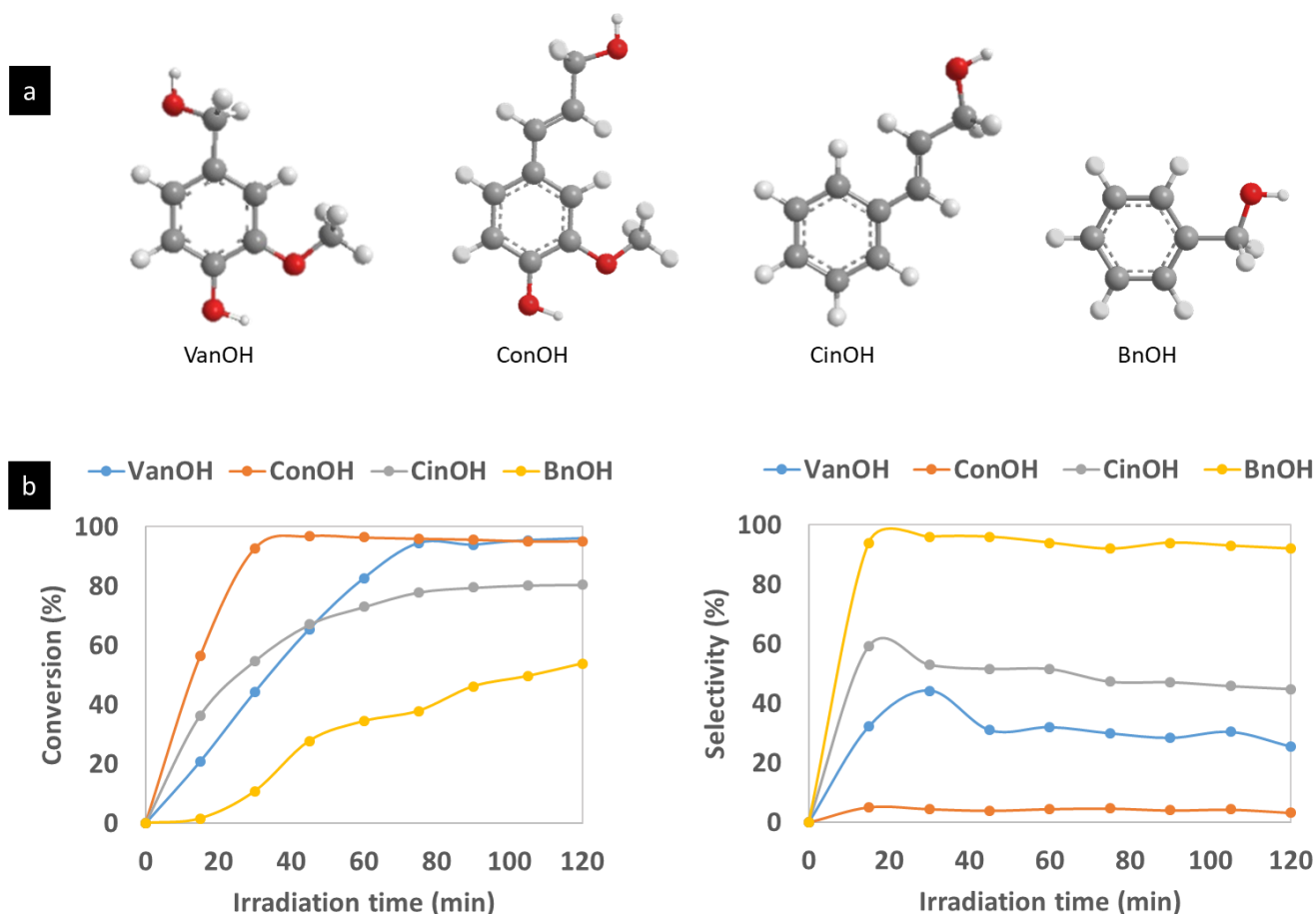


**Figure 34.** Chemical structure of the aromatic alcohols (vanillyl alcohol (VanOH), coniferyl alcohol (ConOH), cinnamyl alcohol (CinOH), and benzyl alcohol (BnOH)) (Atomic representation: White - Hydrogen, Grey- Carbon, Red- Oxygen ) (a) and Photocatalytic oxidation with CuA-Au/TiO<sub>2</sub> under UV light with 1mM of aromatic alcohols in batch (b).

After 2 hrs of the light experiment, BnOH and VanOH conversion was 54% and 95%, respectively (Figure 34 b). Comparing the structure of the molecules of BnOH and VanOH (Figure 34 a), it can be seen that the main difference between these two alcohols was that VanOH has in its structure, OH group directly connected with aromatic ring and also methoxy ( $\text{OCH}_3$ ) group connected with the next carbon atom of the aromatic ring. In contrast, benzyl alcohol has only an OH group at the end of the alkyl chain, which was not directly connected with the aromatic ring, and no methoxy group. As mentioned above, OH and  $\text{OCH}_3$  groups in the vanillyl alcohol are electrons donating groups those were providing the electrons to the aromatic ring. An excess of electrons causes lower production of aldehyde, which results in low selectivity towards aldehyde in the case of VanOH (25%) in comparison to the BnOH (100%) under UV irradiation (Figure 34 b) after 2 hrs of the light experiment. As the selectivity of producing vanillyl aldehyde (VanAld) was strongly reduced, other products of vanillyl alcohol oxidation were achieved (Figure S17-19). Furthermore, the lower selectivity can also be ascribed to the strong adsorption (37%) of alcohol on the surface of the catalyst, which can lead to partial oxidation, dimerization, or C-O, C-C coupling products.

Considering ConOH and CinOH alcohols, it can be seen that very high conversions were achieved (95% and 81%, respectively). In the case of ConOH, the selectivity of producing coniferyl aldehyde (ConAld) was very low (5%), with 7% selectivity towards VanAld (Figure 34), with additional products verified by GC-MS analysis (Figure S17-19). Along with  $\text{OCH}_3$  and OH groups, ConOH has a double bond in their structure, which potentially can also provide the electrons to the aromatic ring, which further causes reduction, lowering the selectivity. The side products formed are benzaldehyde from CinOH and vanillyl aldehyde from ConOH (partial oxidation)<sup>207</sup>, as well as 3-phenoxy benzaldehyde from ConOH (C-O coupling product), which probably was the result of many complex chemical reactions leading to the dimerization of ConOH under the influence of the oxidizing environment (UV radiation).<sup>208</sup> The conversion of aromatic alcohols and the selectivity to its aldehyde were the main criteria to estimate catalyst performance as the other products were in traces. For CinOH oxidation, the selectivity towards cinnamyl aldehyde (CinAld) was 45%. Further, the catalyst showed highly selective toward BnOH oxidation to BnAld.

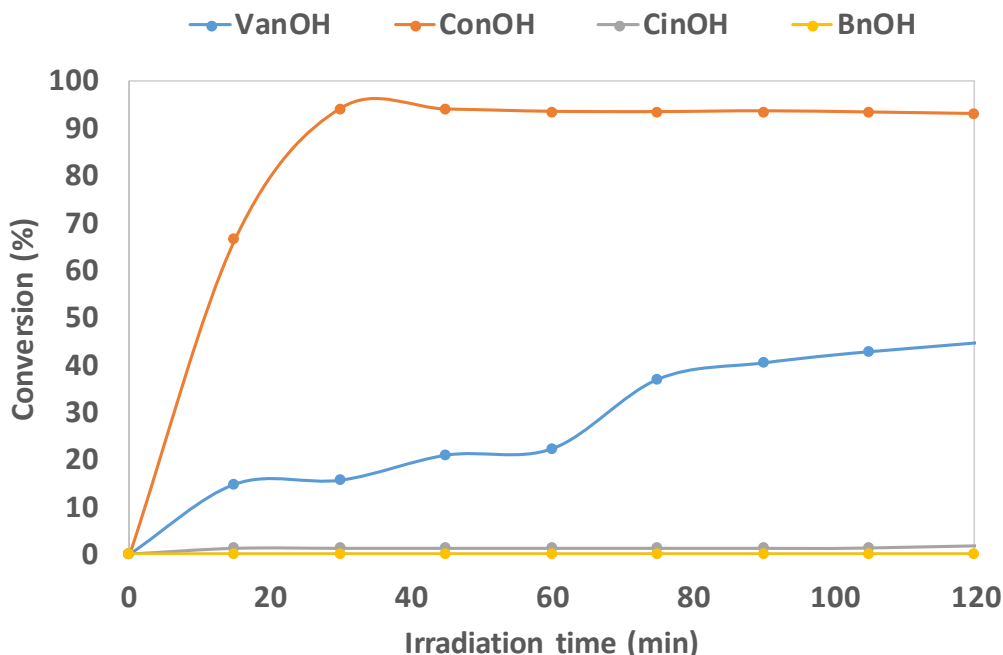


**Figure 35.** Visible light (515nm) activity of other aromatic alcohols with bimetallic CuA-Au/TiO<sub>2</sub> in batch.

After conducting the selective photocatalytic oxidation experiments in the UV radiation, the CuA-Au/TiO<sub>2</sub> photocatalyst was selected for experiments also under visible light in the batch system (Figure 35). Under visible irradiation (515 nm), the satisfactory conversion of the alcohols was obtained only for ConOH and VanOH (93% and 52%, respectively), with 8% and 17% selectivity towards their respective aldehydes, with the formation of other side products. Increased photocatalytic conversion in the range of visible radiation for ConOH and VanOH, with a complete lack of activity for BnOH and CinOH, was probably related to the structures of these alcohols. In the case of BnOH and CinOH, there are no groups that could be a direct source of additional electrons for the aromatic ring and no group which can form complexes with TiO<sub>2</sub>. In order to explain this, UV-Vis DRS and FTIR analyzes were performed for the aromatic alcohols adsorbed TiO<sub>2</sub> complexes (Figure 36 and Figure 37).<sup>209,210</sup>

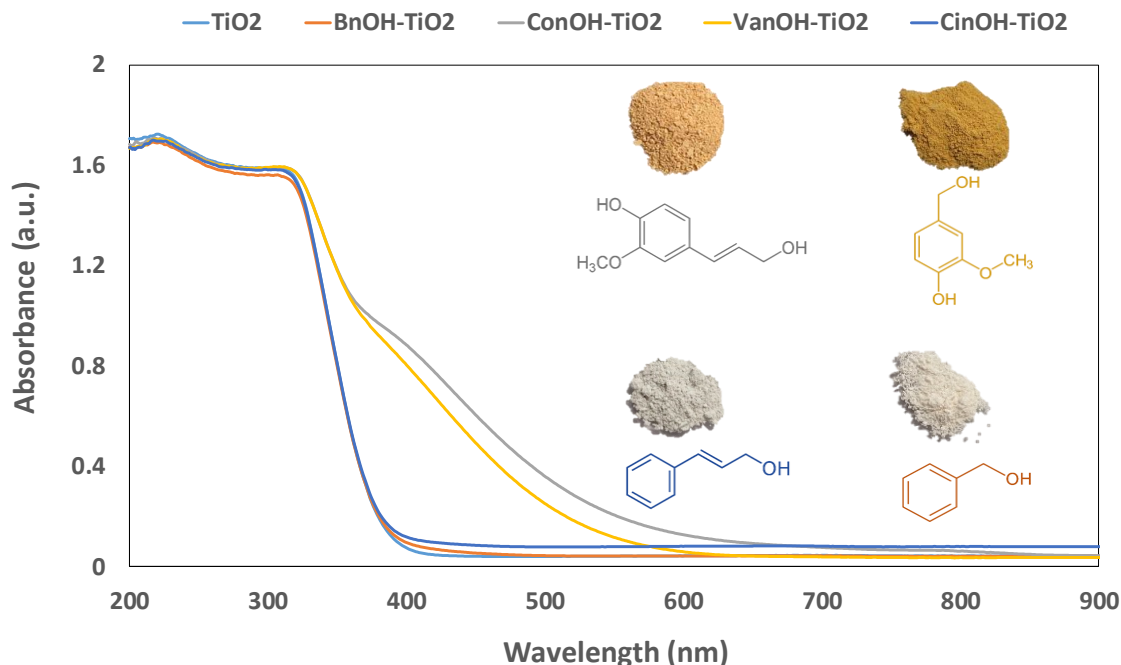
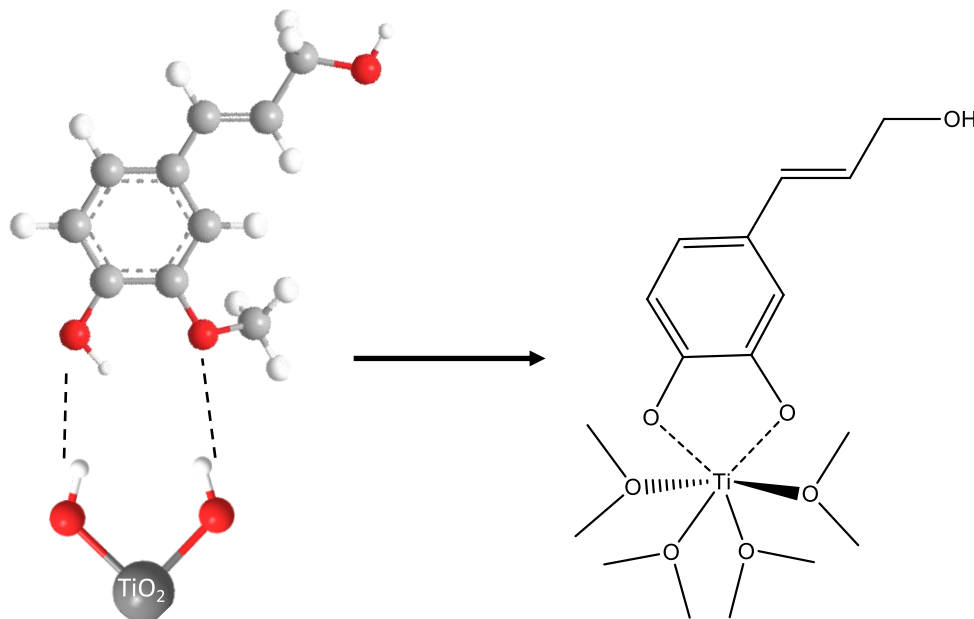


**Figure 36.** UV-Visible diffuse reflectance absorption spectra of  $\text{TiO}_2$  and aromatic alcohols adsorbed  $\text{TiO}_2$  complex.

As a result of the adsorption of ConOH and VanOH on the  $\text{TiO}_2$  catalyst, it can be clearly seen a significant change in the color of the catalyst from white to yellow, which resulted in a shift of absorption toward visible radiation (Figure 36). A plausible reason can be complex formation by the ligand-to-metal charge transfer (LMCT).<sup>211,212</sup> During this process, electrons are transferred from the highest occupied molecular orbital of substrates/ adsorbates to the conduction band of  $\text{TiO}_2$  upon visible light irradiation. (Scheme 1).<sup>209</sup> Consequently, the samples forming the colorful complexes exhibited an excellent conversion of aromatic alcohols under visible light (Figure 36).



*Scheme 1. Possible structure of the Ti (IV)-ligand complexes with coniferyl alcohol in the TiO<sub>2</sub>-based materials with alcohols.<sup>211</sup>*

The formation of complexes between TiO<sub>2</sub> and ConOH, and VanOH was also supported by the FTIR analysis results (Figure 37). Characteristic IR bands for alcohols have also been observed for alcohol-adsorbed titania samples, especially in TiO<sub>2</sub>-VanOH and TiO<sub>2</sub>-ConOH (Figure S20). This worked an indication of complex formation via the adsorption of alcohol.

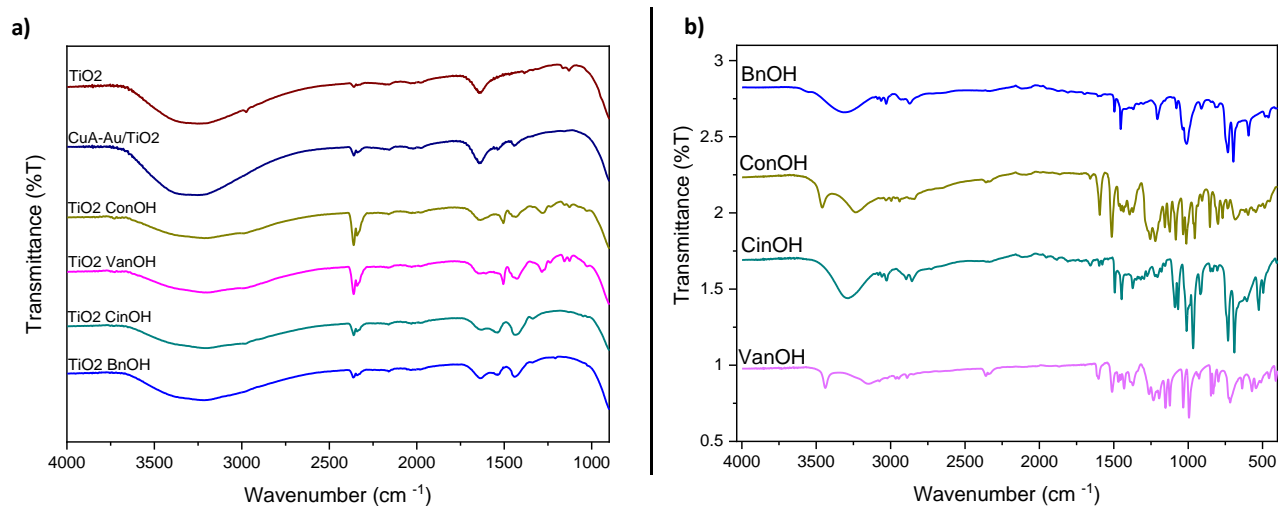


**Figure 37.** Fourier-transform infrared spectroscopy (FT-IR) of alcohol adsorbed TiO<sub>2</sub> (a) and aromatic alcohols (b).



It was mentioned above that adsorption of alcohols (VanOH and ConOH) on the surface of TiO<sub>2</sub> occurred by a dissociative mechanism, which means that OH and O-CH<sub>3</sub> groups interacted between titania and aromatic alcohols. In that case, alcohol and TiO<sub>2</sub> would be linked via the C-O bond. The presence of C-O stretching vibrations was observed at 1000-1200 cm<sup>-1</sup> (Figure S20), which can be seen in the case of TiO<sub>2</sub>-VanOH and TiO<sub>2</sub>-ConOH; two bands were observed in this region (1118 and 1158 cm<sup>-1</sup>). The bands in the range 1000-1050 cm<sup>-1</sup> were assigned to the presence of =C-H bonds derived from the aromatic ring (Figure 37 and Figure S20). The bands around 1460 cm<sup>-1</sup> originated from CH<sub>2</sub> vibrations and around 1640 cm<sup>-1</sup> from C=C.<sup>209</sup> Similar spectra were observed for bimetallic CuA-Au/TiO<sub>2</sub> as well, confirming the formation of the complex with the above aromatic alcohol (Figure S20), which confirms that the metals did not take part in this complex formation. It was worth adding that the oxidation of VanOH and ConOH was successful under visible irradiation due to the formation of the above-mentioned complex with TiO<sub>2</sub>. To further confirm the role of the OH group in the LMCT complex formation, the synthesized TiO<sub>2</sub> was calcined at a high temperature (600 °C) to remove surface OH through condensation (Figure S21). Interestingly, this catalyst was found inactive, suggesting the OH groups are crucial for LMCT complex formation and visible light activity of the catalyst.

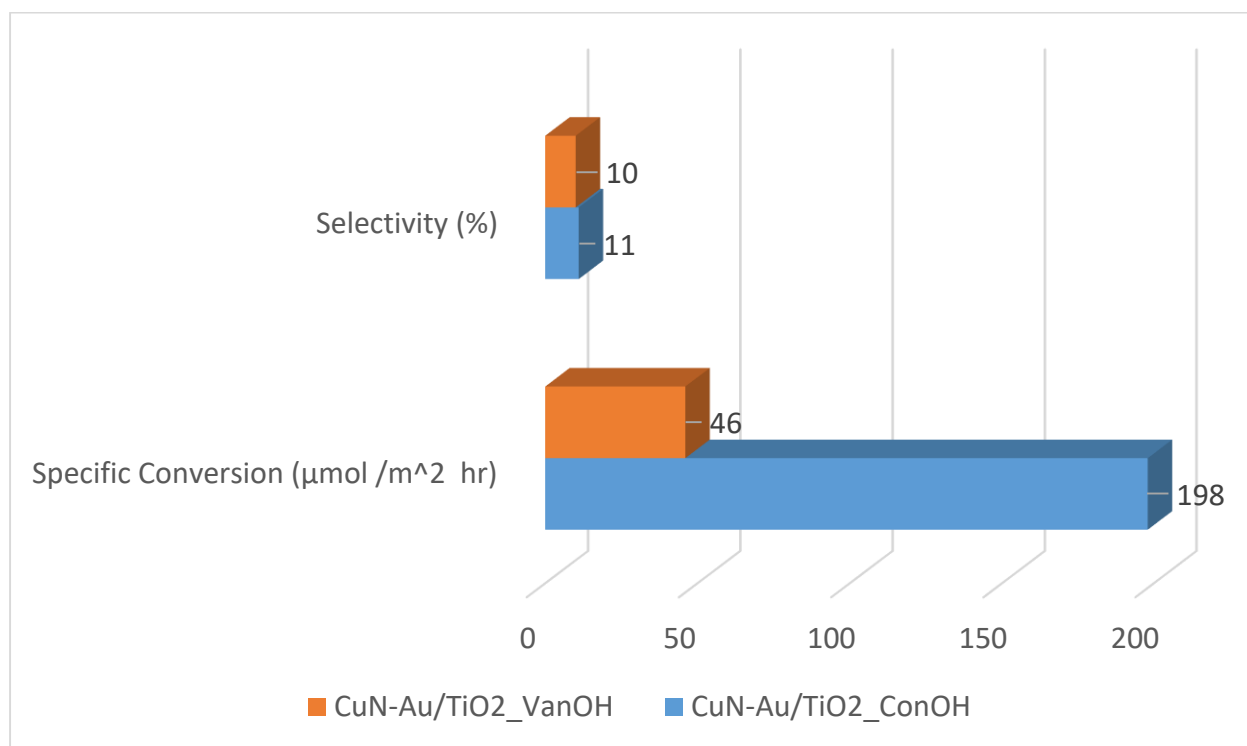


**Figure 38.** Photocatalytic activity of CuN-Au/TiO<sub>2</sub> under visible light with ConOH and VanOH in microflow system.

The experiment with CuN-Au/TiO<sub>2</sub> coated microreactor for other aromatic alcohols oxidation was performed under visible light irradiation as; (1) CuN-Au/TiO<sub>2</sub> in the microflow system showed better activity (Figure 28), and (2) other aromatic alcohols showing better conversion under visible light (Figure 35). Like the batch experiment, BnOH and CinOH did not show any activity in the microflow system under visible light, whereas, ConOH and VanOH did. The specific conversion rate of ConOH was higher (198  $\mu\text{mol}/\text{m}^2\text{ hr}$ ) compared to VanOH (46  $\mu\text{mol}/\text{m}^2\text{ hr}$ ), with 11 and 10% selectivity towards their respective aldehydes (Figure 38). Other side products, like batch experiments, were also observed.

After deposition, the catalyst's surface was more selective towards ConAld for ConOH oxidation than batch (8%). The elevated selectivity in batch compared to the microflow system might be because of the higher availability of the catalyst's active sites upon deposition. Additional side products (as discussed above) were confirmed from GC/MS; however, because of the trace amount of some products, it was not easy to calculate the selectivity towards them (Figure S19). The sol-gel synthesized CuN-Au/TiO<sub>2</sub> catalyst showed promising activity in batch as well as in microflow systems for ConOH oxidation. Furthermore, from the catalyst-deposited microtubes, no leaching was confirmed with the ED-XRF analysis after 60 min of the experiment (Figure S22). The recycling test was performed by washing the catalyst with acetonitrile and water, and the activity of the catalyst was retained (Figure S23).

## 5.5 Conclusions

In this study, we have made an attempt to promote green chemistry by improving the utilization of lignin – an important waste from paper and pulp industry, which otherwise would have been disposed of contaminating our environment. For this cause, we propose to improve the conversion of the model alcohols, by targeting and improving the catalytic activity of TiO<sub>2</sub> doped with bimetals like Cu-Au, and Fe-Au. In batch systems, as high as 100% benzaldehyde (BnAld) selectivity was obtained for benzyl alcohol (BnOH) conversion of ~ 60% using CuA-Au/TiO<sub>2</sub> photocatalyst. The high conversion could be explained by the high average pore size (6.8 nm) and better crystallinity of CuA-Au/TiO<sub>2</sub> catalyst, which were confirmed in subsequent XRD, and N<sub>2</sub> physisorption analysis.

Our studies further revealed that the LMCT complex formation of TiO<sub>2</sub> with the methoxy (OCH<sub>3</sub>) and OH groups (directly connected with the aromatic ring) exists in the structure of coniferyl alcohol (ConOH) and vanillyl alcohol (VanOH), which was crucial to activate the catalyst under visible light.

This hypothesis has further been corroborated by UV-Vis and FTIR studies. Additionally, the whole process was green/environment-friendly as the catalyst synthesis process did not include any high-temperature calcination step, unlike commercial P25 TiO<sub>2</sub>, and the photocatalytic selective oxidation route was additive-free (no additional molecular oxygen). We also developed catalyst decorated microreactor using ultrasonic irradiation, which helped to increase the turbulence of the liquid phase and to improve the active surface area of our catalyst via the de-agglomeration and fragmentation of the nanoparticles.

In a broader context, we believe that the presented work demonstrates the potential of an ultrasonic-assisted bimetallic TiO<sub>2</sub> wall-coated microreactor for selective oxidation of lignin-based model compounds using solar energy and will serve as a conceptual blueprint for further developments.

## Chapter 6

### 6. Research summary

#### 6.1 Contributions and impacts

Waste generated from large scale manufacturing process is an ever-growing source of environmental hazard, and reducing the production of these harmful chemicals has been a dominant area of research in green and sustainable chemistry. In this doctoral research, I have proposed a novel approach to produce value added products from lignin-based model compounds, which is a major source of waste generated from the paper and pulp industries. The goal of my thesis was to use recent advancements in the field of photocatalyst, microfluidics, and ultrasound to develop a system for lignin based model compound valorization by adopting a greener approach.

- In Chapter 2, I have presented a comprehensive review of state of art methods for preparing wall coated microflow reactors which are used for photocatalytic oxidation reactions. I further identified the scope of developments in polymer-based microtubes by using low energy-based ultrasound for deposition of catalyst in the wall of microreactor. This chapter was published as a review article in *Molecules* journal.
- Following the research gaps identified above, in Chapter 3, I synthesized  $\text{TiO}_2$  by following simple sol-gel method and deposited it inside perfluoroalkoxy alkane (PFA) tube using ultrasonic bath. I optimized the key parameters like power of ultrasound, time of deposition and length of tube for catalyst deposition. I performed comparison study of commercial P25 with my synthesized  $\text{TiO}_2$  both in batch and microflow system for selective oxidation of benzyl alcohol ( $\text{BnOH}$ , model compound for lignin). The findings showed greener approach to coat the inner walls of a microtube with a thin layer of photoactive  $\text{TiO}_2$  in order to utilize the obtained microreactors towards the selective photocatalytic partial oxidation of benzyl alcohol, without the use of any addition reagent (like oxidant). This work has already been cited 24 times by researchers working in this domain.

- I further modified the photocatalyst ( $\text{TiO}_2$ ) by doping metal Fe, Cu and Co to it. In chapter 4, I optimized the atomic percentage of metal in  $\text{TiO}_2$  and did comparative photocatalytic activity study of the three metals. I also performed required characterizations to explain the experimental results. I showed that, among all the metal  $\text{TiO}_2$  samples, the 0.5 at % Fe- $\text{TiO}_2$  (cheap and abundant metal) photocatalyst exhibited the highest BnOH conversion under visible light (515 nm) in microflow system.
- In Chapter 5, to make our catalyst active under visible light, which is dominant part of solar radiation, I tried to modify monometallic  $\text{TiO}_2$  with Au. Though there was no remarkable activity under visible light (515 nm), the addition of this second metal in a co-catalytic amount to  $\text{TiO}_2$  helped to increase the selectivity of the catalyst towards benzaldehyde (~ 100%) under UV light (375 nm). Furthermore, I extended my study to other lignin-based model compounds like coniferyl, cinnamyl, and vanillin alcohols. The methyl and hydroxy group of vanillin and coniferyl alcohol form a complex with  $\text{TiO}_2$ , which makes the system active under visible light.

The powerful new approaches discussed above could address the key hypothesis formulated at the beginning of the thesis. Below, I do a quick recap by running through them again:

*Hypothesis 1:* Photocatalytic activity of the catalyst can be improved for lignin-based model compounds (benzyl alcohol, BnOH) oxidation in microflow over the batch system with better product yield.

Utilization of microreactors as an eco-friendly, in terms of simplicity, safety, time, energy, material cost, and environmental impact approach for the selective upgrade of biomass-derived compounds were performed by our research group to enhance the capability of the photoreactors and to determine which factors and features of the catalyst play the most crucial role. In Chapter 3, I showcased that the photocatalytic conversion of benzyl alcohol in the microflow system increased compared to the batch reactor. Upon deposition on the microreactor's walls, the synthesized material revealed a better photo-reactivity regarding benzyl alcohol conversion and benzyl aldehyde selectivity, a trend in absolute contrast with the batch experiments case. For monometallic catalysts, in Chapter 4, among all the metal  $\text{TiO}_2$  samples, the 0.5 at% Fe- $\text{TiO}_2$  (cheap and abundant metal) photocatalyst exhibited the highest BnOH conversion (28%) under visible light (515 nm) in microflow system.

*Hypothesis 2:* Using ultrasound for surface modification can further help in better deposition of catalyst onto the wall of the PFA tube.

In this thesis, I considered the optimization of parameters like length of tube, ultrasonic power, and time of deposition for coating of catalyst and studied the photocatalytic activity with all the microtubes prepared with combinations from Design Expert. In chapter 3, I observed that ultrasonication during the coating process plays a vital role, leading to an enhanced mass deposition and as a result, better photoreactivity compared to deposition without ultrasound. The higher availability of the active sites in this wall-coated microreactor helped in better conversion.

*Hypothesis 3:* Introduction of transition metal (metal-containing; e.g., Cu, Fe, Co) and co-catalytic amount of noble metal (bimetal containing; e.g., Cu, Fe with Au) to improve the photocatalytic activity of the synthesized catalysts.

Chapter 4 of this thesis shows the benefits of using metal  $\text{TiO}_2$  (e.g., Cu, Fe, Co). The metal-containing  $\text{TiO}_2$  showed higher photocatalytic activity under UV irradiation than the synthesized  $\text{TiO}_2$  in the batch system. Among the three metals, although Cu and Fe showed almost similar activity in the batch system under UV light, in the microflow system (after deposition of catalyst in the wall of PFA), Fe- $\text{TiO}_2$  showed better activity under UV and Vis light. Though adding a second metal (Au) to this monometal  $\text{TiO}_2$  enhanced the benzaldehyde selectivity to 100%, it did not improve the activity of the catalyst under visible light as we hypothesized.

*Hypothesis 4:* Alcohol can be chemisorbed over  $\text{TiO}_2$  and form a visible light-active ligand-to-metal charge transfer (LMCT)-complex involving the methoxy ( $\text{OCH}_3$ ) and hydroxy (OH) group of alcohols with  $\text{TiO}_2$ .

In chapter 5, I showcased that the LMCT complex formation of  $\text{TiO}_2$  with the methoxy ( $\text{OCH}_3$ ) and OH groups (directly connected with the aromatic ring) exists in the structure of coniferyl alcohol (ConOH) and vanillyl alcohol (VanOH), is crucial to activate the catalyst under visible light. This has further been corroborated by UV-Vis and FTIR studies. Removing OH group from  $\text{TiO}_2$  with high temperature, I observed the deactivation of catalyst under visible light confirming that the OH groups are crucial for LMCT complex formation and visible light activity of the catalyst.

In summary, I presented herein a “green chemistry” oriented approach to coat the inner walls of a microtube with a thin layer of photoactive  $\text{TiO}_2$  in order to use the obtained microreactors towards the selective photocatalytic partial oxidation of lignin-based model compounds. Additionally, the whole process was developed to be environment-friendly as the catalyst synthesis process did not include any high-temperature calcination step, unlike commercial P25  $\text{TiO}_2$ , and the photocatalytic selective oxidation route was additive-free (no additional oxidants).  $\text{TiO}_2$ -based heterogeneous photocatalysis carried out under mild experimental conditions such as ambient pressure and temperature, utilizing oxygen (present in the reaction medium) as an oxidizing agent, and UV and visible light as irradiation sources is a green and economical approach for the valorization of biomass-based platform chemicals. In a broader context, we believe that the presented work demonstrates the potential of an ultrasonic-assisted bimetallic  $\text{TiO}_2$  wall-coated microreactor for selective oxidation of lignin-based model compounds using solar energy and will serve as a conceptual blueprint for further developments. On the other hand, even though modifications were done to sol-gel synthesized ZnO with metals (considering the optimized parameters from experiments with  $\text{TiO}_2$ ), commercially available ZnO showed better activity compared to our synthesized ZnO and metal modified ZnO.

## 6.2 Challenges and future perspectives

During this doctoral research, I explored many innovative strategies to push the boundaries towards valorization of lignin compounds. However, there still exist many challenges that could be hurdle to widespread adoption; while simultaneously opening up possible research directions for future works. They are:

- According to our initial plan, our aim was to use ultrasound for the synthesis of our catalyst. We also used it for the synthesis of  $\text{TiO}_2$ . Whereas, addition of metal to the process made the gel thicker by making the mixing process difficult. Hence, we shifted to mechanical mixing (magnetic stirrer). May be the use of high power ultrasound for this sol-gel synthesis can improve the crystallinity of the catalyst, which might will improve the activity of the catalyst.
- As the catalyst depositions occur at micro scale, it was difficult to characterize or study the catalysts inside microflow system deeply. This still is an active challenge to overcome.

- The current work uses irradiation light for photocatalysis using LED light sources. Going forward, this source should be replaced with naturally available solar irradiation. To start with, we can use solar light simulators.
- We can improve the catalysts by changing synthetic route - 80 °C which might activate the rutile phase (or overall crystallinity) and activate the catalyst under visible light. Also, we can shift towards greener solvent, like water, for photocatalytic experiment.
- In future, we can work on scaling up the system in order to work in an industrial scale.



# Chapter 7

## APPENDIX I

### A1.1. Information about LED light setup

The LED light system setup, inside which the photocatalytic (batch and flow) studies were carried out, is of great importance. The intensity of the green LEDs was measured to be  $18 \times \sim 9 \text{ W/m}^2$ , determined via light meter (Delta OHM HD 2302.0) with LP 471 RAD probe having 400-1050 nm spectral range. The photocatalytic oxidation of alcohols was also carried out under UV and visible light using UV LED lamp ( $\lambda = 375$  and  $515 \text{ nm}$ , respectively) measured by a Delta OHM HD 2302.0 light meter (with a LP 471 UVA probe with a spectral range of 315-400 nm and with LP 471 RAD probe having 400-1050 nm spectral range, respectively).

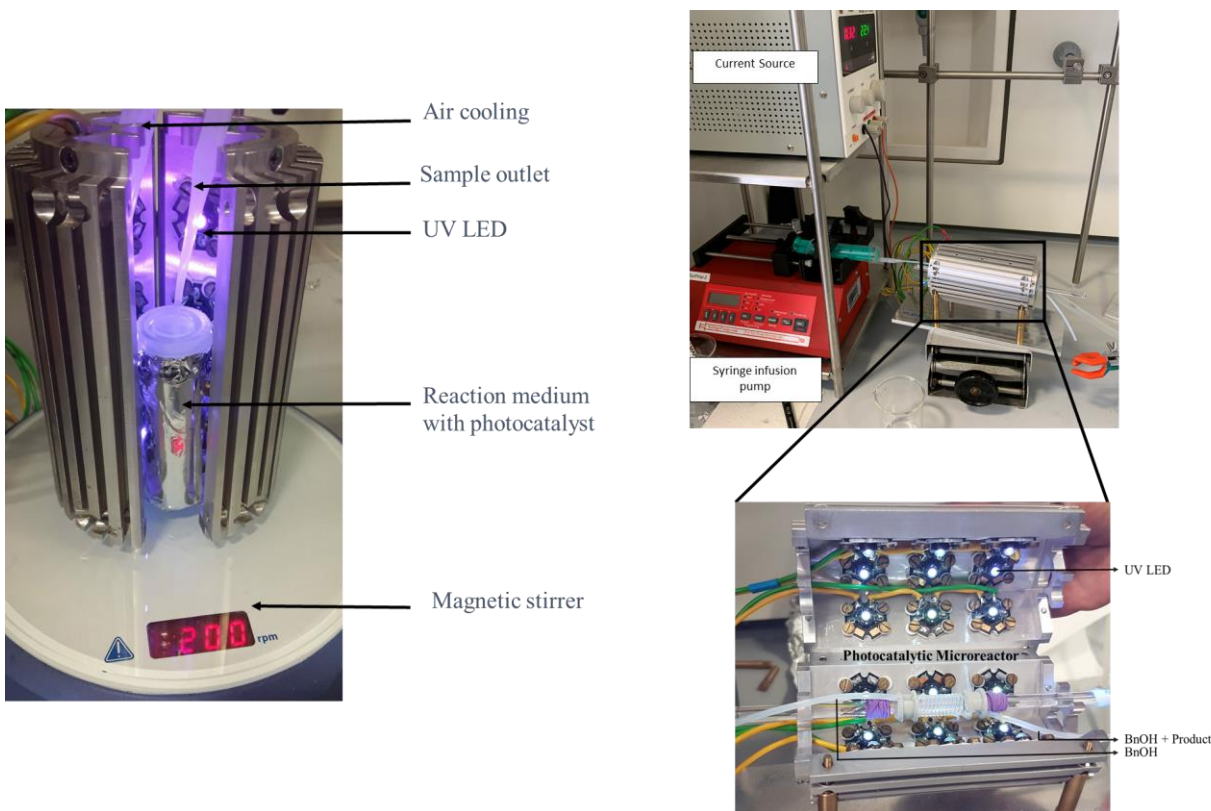


Figure AI. 1. Experimental setup for batch (left) and microflow (right) experiment.

The distance between the photoreactor wall and the irradiation source was maintained to be  $\sim 2 \text{ cm}$ . At given illumination time intervals,  $0.15 \text{ mL}$  aliquots were collected, and subsequently filtered via nylon

filter (CHROMAFIL, 0.2  $\mu\text{m}$  pore size, 15 mm diameter) to remove the photocatalyst. The same experiments were performed with all photocatalysts. The experimental set-up used for the photocatalytic experiment is shown in Figure AI. 1. With continuous flow of air (fan), the temperature inside the cylinder was maintained to room temperature.

Commercial P25  $\text{TiO}_2$  was used in 25 mL batch reactor, and for photocatalytic reaction 20 mg of catalyst and 20 mL of 1mM BnOH solution were used with stirring (400 RPM). Experiments were carried out for 6 hrs and samples were collected at different interval time. Table I.1 presents list of experiments carried in batch system (Figure AI. 1) in different experimental conditions.

*Table I.1. List of batch experiments carried out to observe the effect of different parameters with commercial P25  $\text{TiO}_2$*

Sample name	Reaction type
B1	Dark adsorption of BnOH 1mM in AcN
B2	Photolysis of BnOH 1 mM in AcN (without cooling)
B3	Dark adsorption of BnOH 1mM in $\text{H}_2\text{O}$
B4	Photolysis of BnOH 1mM in $\text{H}_2\text{O}$ (without cooling)
B5	Photocatalytic reaction of BnOH 1mM in $\text{H}_2\text{O}$
B6	Photocatalytic reaction of BnOH 1mM in AcN
B7	Photocatalytic reaction of BnOH solution at 45 $^\circ\text{C}$ (Effect of temperature)
B8	Photolysis of BnOH 1mM in $\text{H}_2\text{O}$ with cooling
B9	Photocatalytic reaction of BnOH 1mM in $\text{H}_2\text{O}$ with cooling
B10	Photocatalytic reaction of BnOH 1mM in AcN with cooling
B11	Photocatalytic reaction of BnOH 1mM in AcN, closed reactor, with cooling
B12	Photocatalytic reaction of BnOH 1mM in $\text{H}_2\text{O}$ , closed reactor, with cooling

It should be noted that some of the experiments were carried out without any external cooling, as in experiments B2 and B4 batch experiments to see the effect on our experimental setup.

Dark adsorption studies with different solvents (water and AcN) were carried out for 10 mg of catalyst in 20 mL of solution (optimized concentration 0.5 g/ L) in room temperature. It is observed that after 30 min the BnOH concentration remains stable (Table I.2) for both the solvents.

Table I.2. Results for dark sorption studies in batch systems

Time [min]	Sample B1 (AcN)	Sample B3 (H <sub>2</sub> O)
	BnOH concentration [mM]	
0	1.02	1.07
15	1.00	1.05
30	1.01	1.06
60	1.01	1.06
90	1.02	1.06
120	1.01	1.07

It can be observed that with AcN solvent (without cooling system), there is no photolysis occurring (Table I.3), however for water, small change in the BnOH concentration have been observed. That is why test experiments with cooling system as well as at 45 °C were performed to check influence of temperature.

Table I.3. Results of photolysis experiment

	Photolysis without cooling		Photolysis with cooling	Experiment at 45°C
	Conversion [%]			
t (min)	Sample B2 (AcN) Without cooling	Sample B4 (H <sub>2</sub> O) Without cooling	Sample B8 (H <sub>2</sub> O) With cooling	Sample B7 (H <sub>2</sub> O)
0	0	0	0	0
30	0	1	0	0
60	0	3	0	0
120	0	5	1	0
240	0	11	1	0
360	0	13	-	0

Table I.4. Temperature reading during photolysis experiment

Photolysis without cooling		Photolysis with cooling	Experiment at 45 °C
Temperature before experiment (at 0 min) / after 6 hrs of experiment (°C ) of solution			
Sample B2 (AcN)	Sample B4 (H <sub>2</sub> O)	Sample B8 (H <sub>2</sub> O)	Sample B7 (H <sub>2</sub> O)
23 / 54.3	20 / 51	25 / 29.9	Constant 45 °C

From results showed in tables above (Table I.3 and I.4) it can be observed that photolysis (with cooling) does not occur with both the solvents. Also, it was found that cooling system is very efficient as for those experiments temperature remained below 30 °C (Table I.4).

To check the influence of temperature two sets of photocatalytic experiments were performed – with and without cooling, in two solutions – water (Table I.5) and AcN (Table I.6).

*Table I.5. Batch experiments using water as solvent*

	<b>Without cooling (B5)</b>		<b>With cooling (B9)</b>	
<b>Time [min]</b>	<b>Conversion (%)</b>	<b>Selectivity (%)</b>	<b>Conversion (%)</b>	<b>Selectivity (%)</b>
<b>0 (dark adsorption)</b>	2		2	
<b>15</b>	17	5	13	5
<b>30</b>	24	8	17	9
<b>60</b>	36	10	21	15
<b>120</b>	57	13	44	15
<b>240</b>	91	3	72	7
<b>360</b>	100	0	91	2

Initial temperature of reaction solution for B5 sample was 19 °C (after dark adsorption) and 21.5 °C for B9. After 6 hrs of experiment, the temperatures reached around 58.6 °C and 31 °C respectively.

Table I.6. Batch experiments using acetonitrile (AcN) as solvent

	Without cooling (B6)		With cooling (B10)	
Time [min]	Conversion (%)	Selectivity (%)	Conversion (%)	Selectivity (%)
0 (dark adsorption)	0		0	
15	60	89	57	86
30	83	87	78	82
60	93	79	86	77
120	99	66	90	66
240	99	58	93	55
360	99	47	96	43

Initial temperature of reaction solutions for B6 sample was 22 °C (after dark adsorption) and 20.5 °C for B10. After 6 hrs of experiment, the temperatures reached to 52.2 °C and 25.7 °C respectively. From the experiments with H<sub>2</sub>O as a solvent, we can observe that the selectivity increased until 2 hrs of experiment and after that it started to fall. Similar trend was observed for AcN as solvent upto 60 min of reaction. To check if those systems were hermetic for air cooling, additional two test were performed (Table I.7).

Table I.7. Results for closed (sealed with cap) reactor

	Sample B11 (AcN)		Sample B12 (H <sub>2</sub> O)	
Time [min]	Conversion (%)	Selectivity (%)	Conversion (%)	Selectivity (%)
0 (dark adsorption)	3		0	
120	86	72	44	14

Similar results were observed for previous reactions. Initial temperature of reaction solution for B11 sample was 22.3 °C, and for B12 it was 21.2 °C. After reaction temperatures reached to 26 °C for B11 and 26.3 °C for B12. We can conclude that the optimum time for highest conversion of BnOH (86%) and highest BnAld selectivity (77%) was observed for the batch experiment carried out using 0.5 g/ L of TiO<sub>2</sub> in AcN solution for 60 mins with cooling system.

## A1.2. Characterization of US bath

The ultrasonic bath used for the experiments (Elma Elmasonic P) can work in two frequency modes, 37 and 80 kHz. Studies were performed at 100% (120 W) power for both modes, amount of liquid inside the bath was set to maximum of its volume.

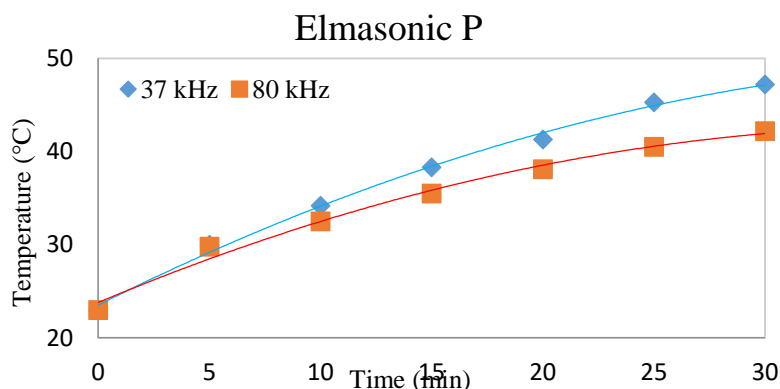


Figure A I.2. Temperature studies of conventional ultrasonic bath.

For the ultrasonic bath, after 30 min of continuous work, temperature was found to be around 47 °C for 37 kHz, and around 42 °C for 80 kHz. Because of its popularity in many laboratories, “low” temperature obtained and usage of water (as medium), it was decided to use it for our future work.

Table I.8. Detailed information about achieved temperatures after specific time in different US sources

Generator	Frequency (kHz)	Amplitude (%)	Mode	Time of reaction (generator) (min)	T (°C) after 30min reaction time						
					0	5	10	15	20	25	30
Elma	37	100 (120W)	continuous	30	23	30	34	38	41	45	47
Elmasonic P	80				23	29	32	35	38	40	42

### A1.3. Optimization of Ultrasonic bath

In order to know the effectiveness of ultrasonic wave (on the PFA tube) inside the bath at different height from the bottom, two set of foil tests<sup>213</sup> were performed. Firstly, the aluminum foil was kept parallel with the bottom of the ultrasound at different depths. It was observed that with increasing the height from the bottom, the effect of ultrasound (US) on the foil (Figure A I.3 (a)) was reduced. For both 70 % and 100 % power, 2 cm height from the bottom found to be the better position to get the effect of US.

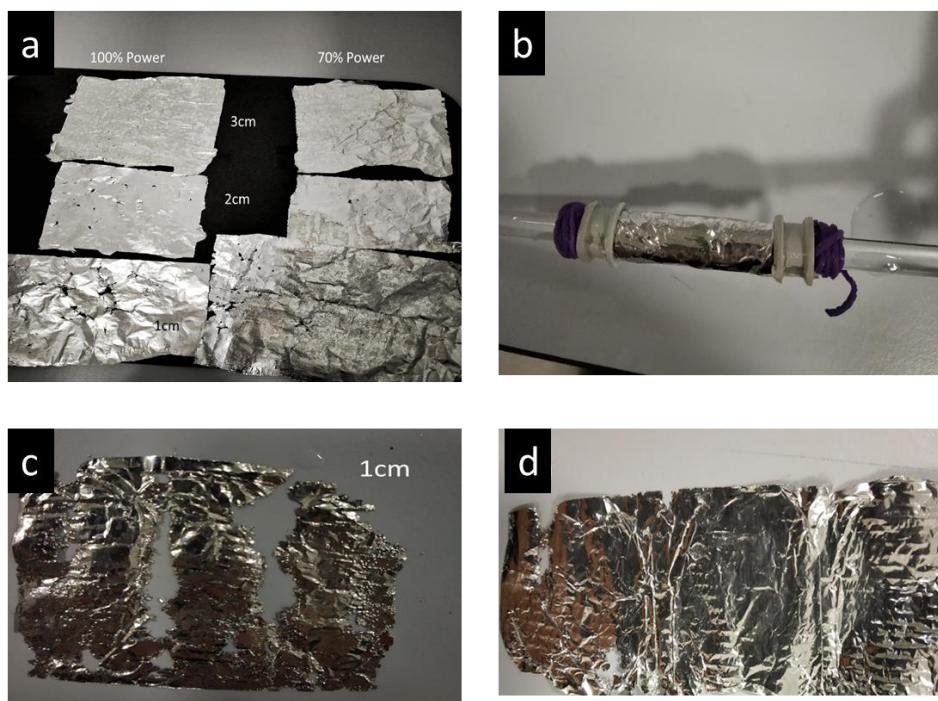


Figure A I.3. Two different methods used for ultrasonic bath aluminum foil inside US bath (a), aluminum foil wrapped around glass rod (b, c and d).



Secondly, to observe the effect of US around the spirally bound PFA tube on a glass rod, similar study was performed with foil wrapped around glass rod. From this experiment also, it can be concluded that 2cm height from bottom of the US bath is effective for the coiled system (Figure A I.3 (b, c, d)).

From these above studies, it can be concluded that for our experiment, between 1 to 2 cm height from the bottom of the US bath is the preferable height. The effect of ultrasound at this region can be useful for the modification of the surface of PFA tube.

#### A1.4. Pretreatment of Fluoropolymer (PFA) microtubes

Pretreatment of perfluoroalkoxy alkane (PFA, chemically similar to FEP) microtube was carried out using ultrasonic bath (37 kHz at 100 % (120 W) power for 15 min, placed at 2 cm height from bottom) with continuous flow (0.15 mL/ min) of water. Followed by this step, the tubes were dried and later characterized using Scanning Electron Microscope (SEM). This technique can give more visual insights into steps by step modification after specific pretreatment method. It was important to check if there is any modification on surface (holes or physical deformations created after cavitation or other effects of ultrasounds).

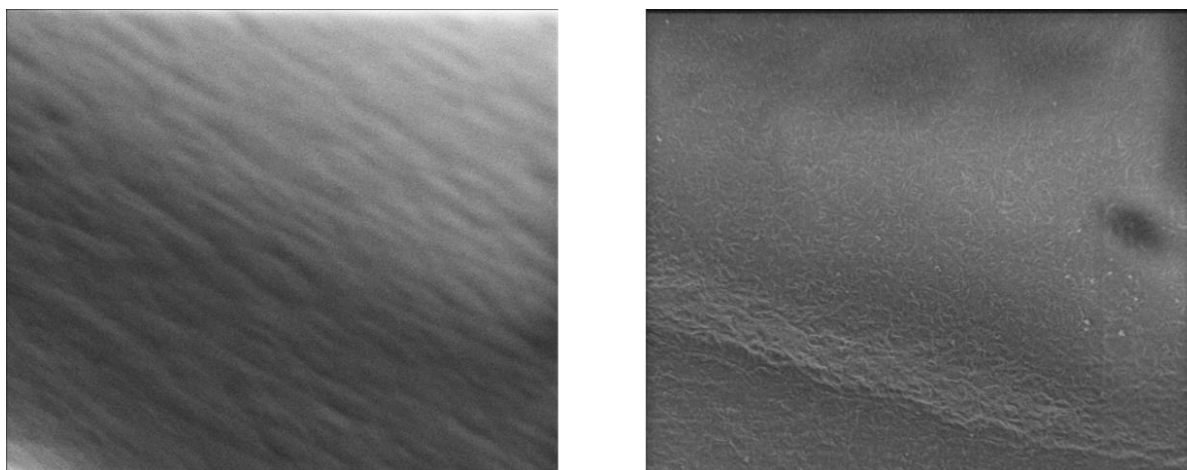


*Figure A I.4. SEM image of two different tubes, commercial available PFA (left), and ultrasound pretreated PFA (right).*

From the SEM image some artifacts were spotted, which can confirm the use of ultrasound helped in etching of the PFA surface. Another experiment was performed where ultrasound was applied during the deposition of the catalyst and the photocatalytic result was compared with the tube deposited with

catalyst after pretreatment. For this case the conversion and selectivity showed better values (9 % and 75 % respectively) compared to catalyst deposited after 1 hr of pretreatment (Figure A I.4).

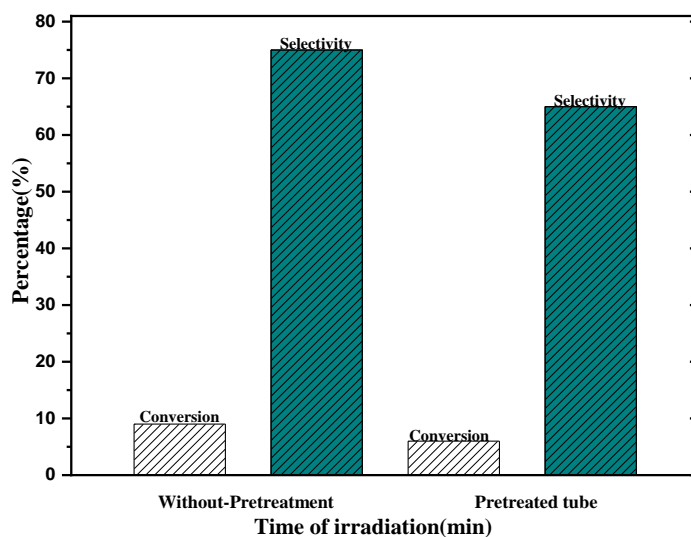


Figure A I.5. Photocatalytic activity after 30 min of illumination time with pretreatment and without pretreatment tube deposited with P25 TiO<sub>2</sub>.

### A1.5. Deposition of TiO<sub>2</sub> catalyst inside PFA microtube

To optimize the photocatalyst coating upon the inner walls of the fluoropolymer microtubes, Design Expert software was used where the parameter like time of deposition (30-120 min), Ultrasound power (40-100%) and length of the tube (30-50 cm) were considered. Based on these data the software generated 17 number of experiments as shown in table I.9. To generate these, we used Box–Behnken design. This was also discussed in the section 3.2.3.

Table I.9. Design experiment data for deposition of catalyst inside PFA tube.

	Std	Run	Factor 1 A:time of deposition min	Factor 2 B:ultrasound power %	Factor 3 C:length of the tubes cm
	13	1	75	70	40
	5	2	30	70	30
	16	3	75	70	40
	17	4	75	70	40
	10	5	75	100	30
	7	6	30	70	50
	2	7	120	40	40
	6	8	120	70	30
	8	9	120	70	50
	4	10	120	100	40
	15	11	75	70	40
	14	12	75	70	40
	12	13	75	100	50
	11	14	75	40	50
	9	15	75	40	30
	3	16	30	100	40
	1	17	30	40	40

In initial step, the desired length tube was washed with Milli-q water and AcN. The water was passed with syringe through the tube at the rate of 1 mL/ min. After this, it was for drying inside an hot air oven at 80 °C for overnight. Then through the dry tube, placed inside an ultrasonic bath, TiO<sub>2</sub> aqueous suspension was passed in order to carry out the deposition. Flow rate (calculated from length of tube and deposition time), ultrasonic power and time of deposition was taken from the list generated by the Design Expert.

After the deposition, the tubes were kept inside an oven for overnight. The dried tubes were used for the photocatalytic study under UV-LED lamp, by maintaining constant temperature inside the system with cooling fan.

Time: 30-120 min, US power: 40-100 % (100 % = 120 W), Length of tube: 30-50 cm and responses were R1: conversion % and R2: Selectivity %.

After performing all the probable experiments suggested by Design Expert software, we filled the response column and tried to generate a response surface.

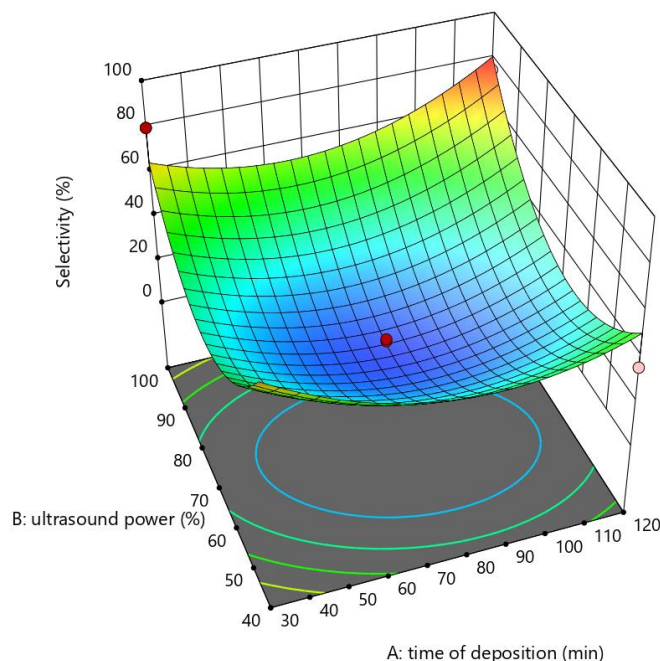


Figure A I.6. Response surface generated from Design Expert software.

The TiO<sub>2</sub> coated PFA microtube having a deposition time of 120 min using ultrasound power of 70 % showed highest amount of TiO<sub>2</sub> deposition of 0.2 mg in 30 cm length of PFA microtube.

### A1.6. Photocatalytic experiment with sol-gel synthesized TiO<sub>2</sub>

Investigation on source of oxygen for oxidation process, experiments has been performed by considering dissolved oxygen in solvent and oxygen in the atmosphere. Acetonitrile was degassed and bubbled with air to observe the effect of dissolved oxygen on photocatalytic activity. Experiment with H<sub>2</sub>O<sub>2</sub> (H<sub>2</sub>O<sub>2</sub> : BnOH = 0.5 : 1) has been carried out to determine the potential effect of the presence of oxidative agent on the photocatalytic oxidation. Also, an experiment in inert atmosphere (N<sub>2</sub> atm) was carried out to eliminate the possibility of oxidation from atmospheric oxygen.

Based on the evaluations of the BnOH conversion and selectivity to BnAld till 60 min of UV irradiation, it was observed that though degassed AcN in normal air showed better conversion, the selectivity reached 41 %. On the other hand, photocatalytic experiment in normal condition (i.e., in atmospheric

air and with commercial solvent) showed 75 % of BnAld selectivity. In inert atmosphere, the catalyst showed negligible selectivity. The conclusion can be made from the above studies that the experiment in normal atmospheric conditions provided required state for the photocatalytic oxidation experiment, which suggests that the dissolved oxygen in solvent and from atmospheric air helps in the oxidation of BnOH.

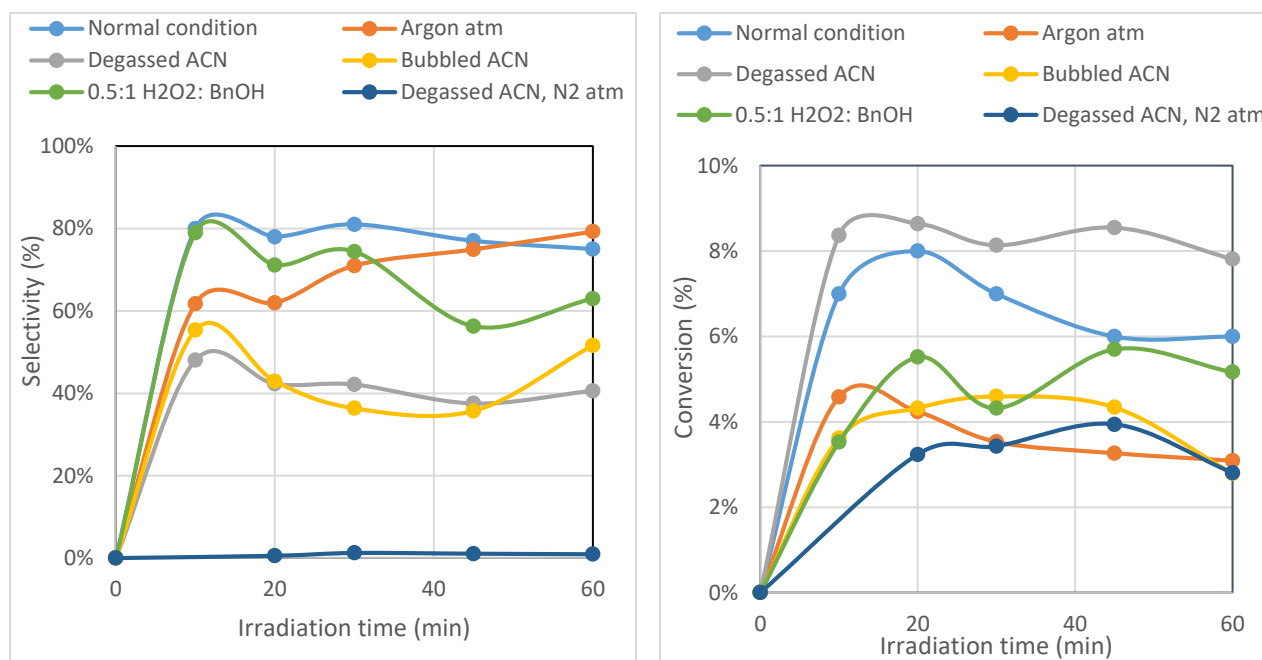


Figure A I.7. Photocatalytic activity of sol-gel synthesized TiO<sub>2</sub> in batch (0.5 g/ L) with different conditions under UV light with 1mM BnOH.

### A1.7. Photocatalytic experiment with different residence time in TiO<sub>2</sub> coated microtube

To study the effect of residence time of BnOH inside microtube (under UV light) on the photocatalytic activity, the experiments with different flow rates were performed. Table I. 10 shows the residence time and corresponding flow rate for the experiments.

Experiments with synthesized TiO<sub>2</sub> deposited PFA microtube under UV light with 1mM BnOH were carried out. The results are shown in the Figure A I.8

Table I.10. Residence time and corresponding flow rate

Residence time (min)	Flow rate (mL/ min)
30	0.025
25	0.03
15	0.05
5	0.15
2	0.37
1	0.7
0.5	1.5

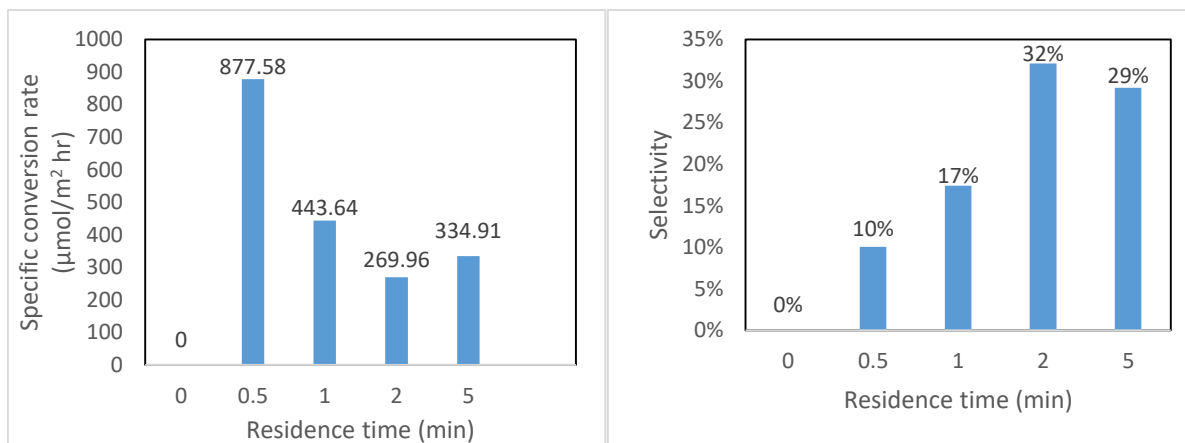


Figure A I.8. Photocatalytic activity of synthesised  $\text{TiO}_2$  deposited PFA tube under UV light with different retention time.

With varying residence time, the change in the photocatalytic activity was witnessed. The specific conversion of BnOH was high ( $877 \mu\text{mol}/\text{m}^2 \text{ hr}$ ) in case of 0.5 min compared to others, whereas the selectivity of BnAld was highest (32 %) in case of 2 min of retention time. Analyzing the results from the above experiments it can be said that with increase the residence time, there was improvement in BnAld selectivity. The benzaldehyde (BnAld) concentration increased and became stable after 5 min of residence time. So for further experiments, flow rate was set at 0.15 mL/ min (5 min residence time).

## A1.8. Optimization of intensity of light

The influence of light intensity on the photocatalytic BnOH conversion inside microtube (under UV light) has been examined at constant (optimized) catalyst loading (0.5 g/ L). The following table shows the temperature of system and intensity of light.

*Table I.11. Measured temperature with UV light intensity after 30min*

UV LED intensity	3 W/ m <sup>2</sup>	10 W/ m <sup>2</sup>	15 W/ m <sup>2</sup>	25 W/ m <sup>2</sup>
Intensity of system (W/m <sup>2</sup> )	7	24	36	54
Temperature (°C)  After 30 min	25	27	29	38

Experiments were carried out with different intensities of light (3, 10, 15, 25 W/m<sup>2</sup>). The specific conversion rate obtained for synthesized TiO<sub>2</sub> deposited PFA microtube under different intensities of UV LED with 1mM BnOH are presented in Figure A I.9.

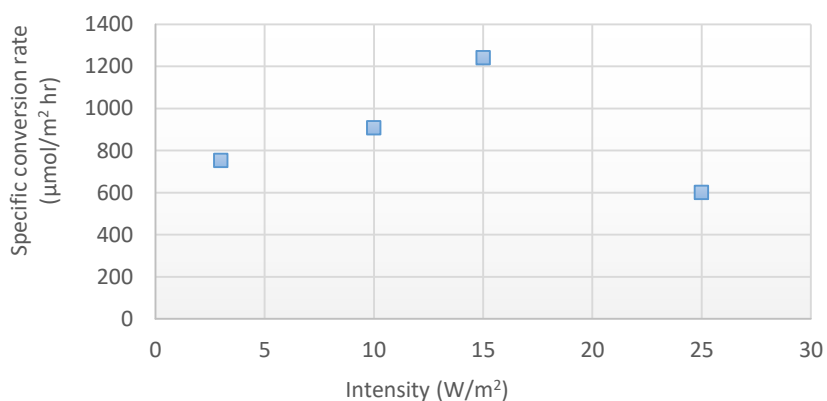


*Figure A I.9. Photocatalytic activity of synthesised TiO<sub>2</sub> deposited PFA tube under different intensities of UV light*

With varying the light intensity, change in photo catalytic activity was observed. The light intensity affects the degree of absorption of light by the catalyst surface. Without light the TiO<sub>2</sub> catalyst powder cannot promote the oxidation. Here, the specific conversion rate of BnOH increased (with increasing

intensities) to  $1239 \mu\text{mol}/\text{m}^2\text{hr}$  under  $15 \text{ W}/\text{m}^2$ , whereas the selectivity of BnAld was lowest (5 %) in this case. With  $25 \text{ W}/\text{m}^2$  we cannot confirm the result as the temperature of the system increased ( $38^\circ\text{C}$  after 30 min) which might will affect the performance of LED light. In a review article, Ollis<sup>214</sup> stated that the rate would increase linearly with respect to intensity at low light intensities, and the rate is independent of intensity at high light intensities. In order to work with low power, we chose  $10 \text{ W}/\text{m}^2$  as the values of conversion and selectivity are similar to that of  $15 \text{ W}/\text{m}^2$ .

### A1.9. Photocatalytic study with double coated $\text{TiO}_2$ catalyst (inside PFA microtube):

On next step, second layer deposition of commercial as well as synthesized catalysts was performed. For this  $0.5 \text{ g}/\text{L}$  of commercially available Degussa P25, and sol-gel synthesized catalyst were taken. The results of first 30 min of photocatalytic experiments are given below.

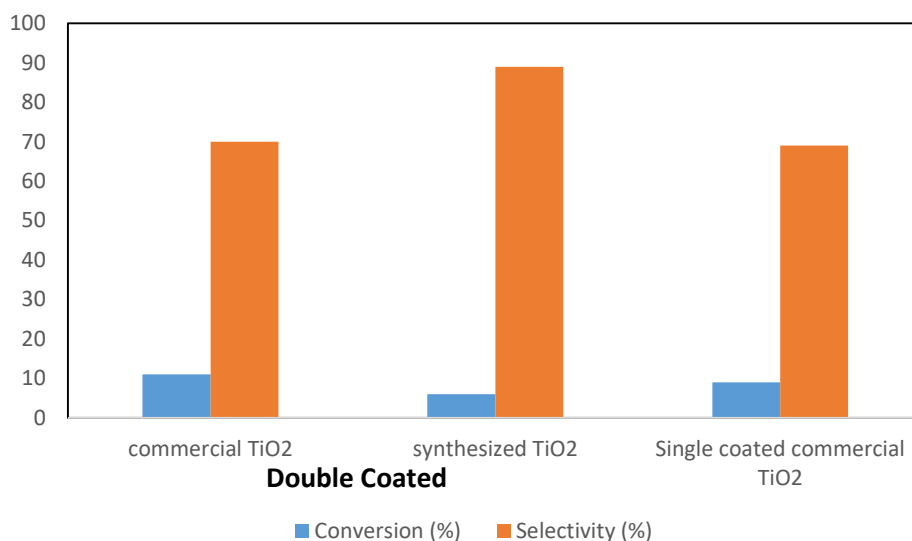
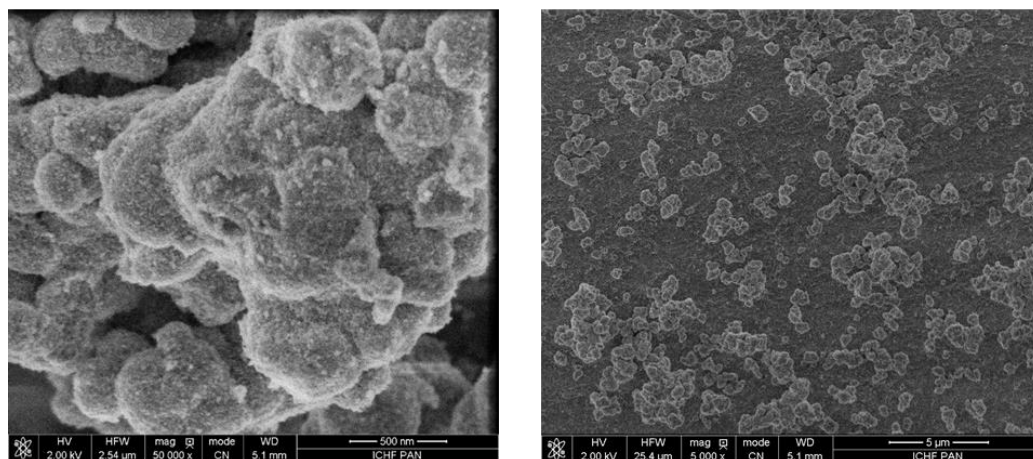


Figure A I.10. Selectivity and conversion of commercial as well as synthesized  $\text{TiO}_2$  with single and double coating.

Double coated commercial P25  $\text{TiO}_2$  showed better BnAld selectivity compared to single coating. Both the tubes deposited with commercial P25  $\text{TiO}_2$  and synthesized  $\text{TiO}_2$  were pictured under Scanning Electron Microscope (SEM). The results are shown in Figure A I.11.



Single coating of synthesized 100% US power



Single coating of commercial P25

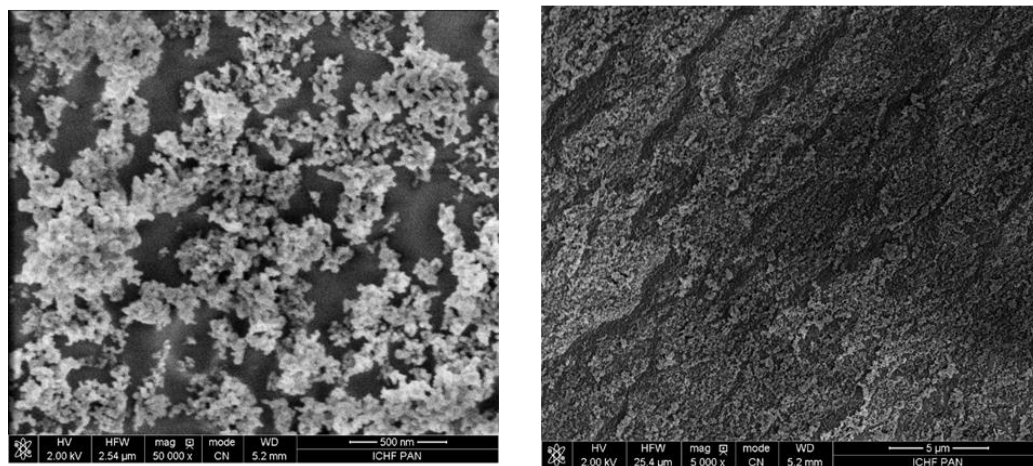


Figure A I.11. SEM images of synthesized and commercial catalyst inside PFA tube

It can be seen from Figure A I.10 that the synthesized  $\text{TiO}_2$  with double layer showed highest (89%) selectivity towards BnAld compared to other systems, as the surface of PFA tube has more catalysts also high agglomerations (Figure A I.11) compared to P25 coated tube.

#### A1.10. Reynolds number

Photocatalytic experiments with benzyl alcohol under UV light were performed in 2 mm diameter tube to observe the effect of tube diameter on it. In order to maintain the same residence time inside the tube during the photocatalytic flow experiments the internal volume of the tube was the kept similar to the volume of 0.8 mm tube. The conditions in the ultrasonic bath during deposition were the same as in the

case of the 0.8 mm tube (100% power, 37 kHz, 75 min). The photocatalytic experiment in this tube showed no conversion of benzyl alcohol. The reason for this could be the fact that although the volume of the reactor remained constant the internal surface area decreased.

Flow characteristics generally influenced by; properties of liquid (Density, viscosity etc), dimension of solid-liquid interface, velocity of the fluid. Calculation of the Reynolds Number helps to determine if the flow in the pipe is laminar or turbulent flow. Here Reynolds number for both the tube with 0.8 and 2 mm diameter tubes were calculated by using following formula.

$$R_e = \frac{V \cdot D \cdot \rho}{\mu}$$

Where,  $\rho$  = density of the AcN (778 kg/m<sup>3</sup>)

D = diameter of the tube ( $0.8 \times 10^{-4}$  m)

$\mu$  = viscosity of AcN ( $3.4 \times 10^{-4}$  Pas )

V = flow speed = flow rate/ cross sectional area = (0.004 m/sec)

Table I. 13. Dimensions and conditions in 0.8 mm and 2 mm diameter tube reactors (by keeping the volume constant)

Diameter (m)	Length (m)	Internal surface area (m <sup>2</sup> )	Reynolds number
0.0008	0.3	$7.54 \times 10^{-4}$	7.9
0.002	0.048	$3.02 \times 10^{-4}$	3.2

From Table I.13, we can confirm that that the flow during our reaction is laminar flow for both the tubes. Low values of Reynolds number for both the 0.8 mm and 2 mm diameters indicate that flow in the microreactor is laminar which means that the flow speed has a parabolic profile and there is no turbulence present in the microreactor. This means that mixing in the radial direction is determined only by diffusion.

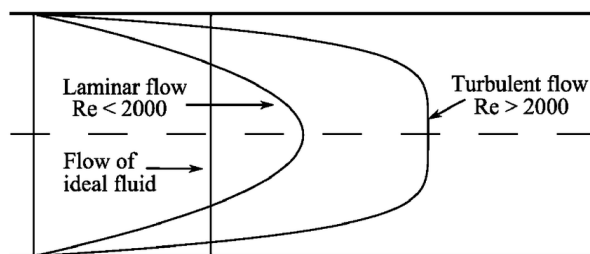


Figure A I.12. Velocity profiles of laminar and turbulent flow<sup>216</sup>

- Additionally, during synthesis process, while metal was added to sol-gel synthesis method, we were not able to perform the synthesis using US bath as gel was thick and mixing was not homogenous. For this reason, US bath was replaced with magnetic stirrer for synthesis of monometal/ bimetal  $TiO_2$ .

## APPENDIX II

### A2.1. Photocatalytic selective oxidation of benzyl alcohol with ZnO

ZnO could be easily grown, and is suitable for medical, industrial, and technical applications due to its diverse properties which strongly depend on their morphology.<sup>217</sup> ZnO has been proposed as an alternative photocatalyst to TiO<sub>2</sub> as it is a cheaper catalyst which possesses similar band gap energy.<sup>141,218</sup> Looking into the photocatalytic activity of ZnO in our setup, we carried out our reactions with commercially available ZnO (< 100 nm, Sigma-Aldrich, Pure 99.9 %) as reference material. Prior to light experiments under UV irradiation (375 nm), dark adsorption equilibrium studies were carried out in order to determine the photolysis and the duration to reach adsorption equilibrium (15 min).

In batch photocatalytic system we carried out the optimization with the parameters which can majorly affect the photocatalytic activity:

- (a) catalyst concentration (b) effect of different solvent (c) mixing speed (RPM, rotation/revolutions per minute).

- (a) Optimization of catalysis concentration:

The optimization of batch photocatalytic study was initiated with the concentration of ZnO catalyst in reaction mixture. Batch photocatalytic experiments were with 1 g/L, 2 g/L and 3 g/L of ZnO catalyst at 400 RPM mixing speed with 1mM BnOH in AcN solvent. Figure A II.1 demonstrates that, after 3 hrs of photocatalytic oxidation reaction, 3 g/L of ZnO shows better conversion (19 %) compared to 2 g/L (5 %). The possible reason for the instabilities in values in Figure A II.1 could be the non-homogenous structure of ZnO (confirmed from SEM image Figure A II.6) and low surface area of the ZnO catalyst. Above this concentration (3 g/L), the turbidity of the suspension reduces the light transmission through it, while below this it is assumed that surface of catalyst and absorption of light by the catalyst are the limiting factor.

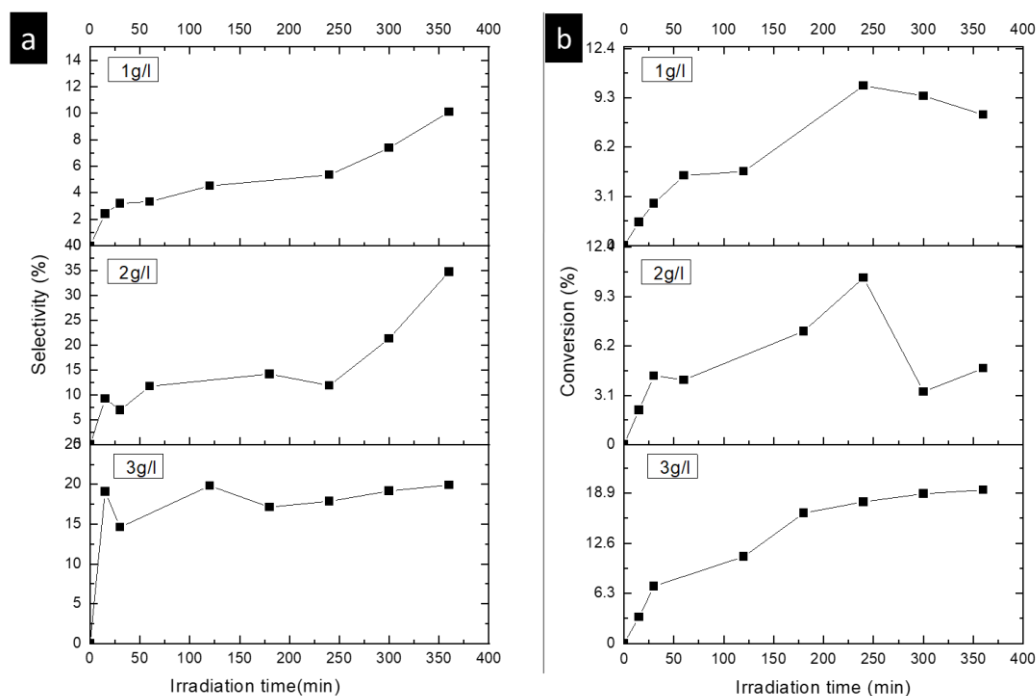


Figure A II.1. Photocatalytic activity with different concentrations (3 g/ L, 2 g/ L and 1 g/L) of ZnO catalyst in batch reactor (6hrs of irradiation of light) BnOH

From the Figure A II. 1, It can be seen that, though 2 g/ L catalyst shows 30% of selectivity at the end of 6 hrs of experiment, 3 g/ L of catalyst have better conversion and stable selectivity (20 %). Hence, this concentration of ZnO was chosen for further investigations.

(b) Effect of different solvent:

Other parameters like the effect of RPM and solvents were studied using 3 g/ L of catalyst. To study the effect of solvent on the photocatalytic activity, experiments were performed with different solvents (Water, 10/ 90 (v/v) AcN/Water, 90/10 (v/v) AcN/Water, AcN).

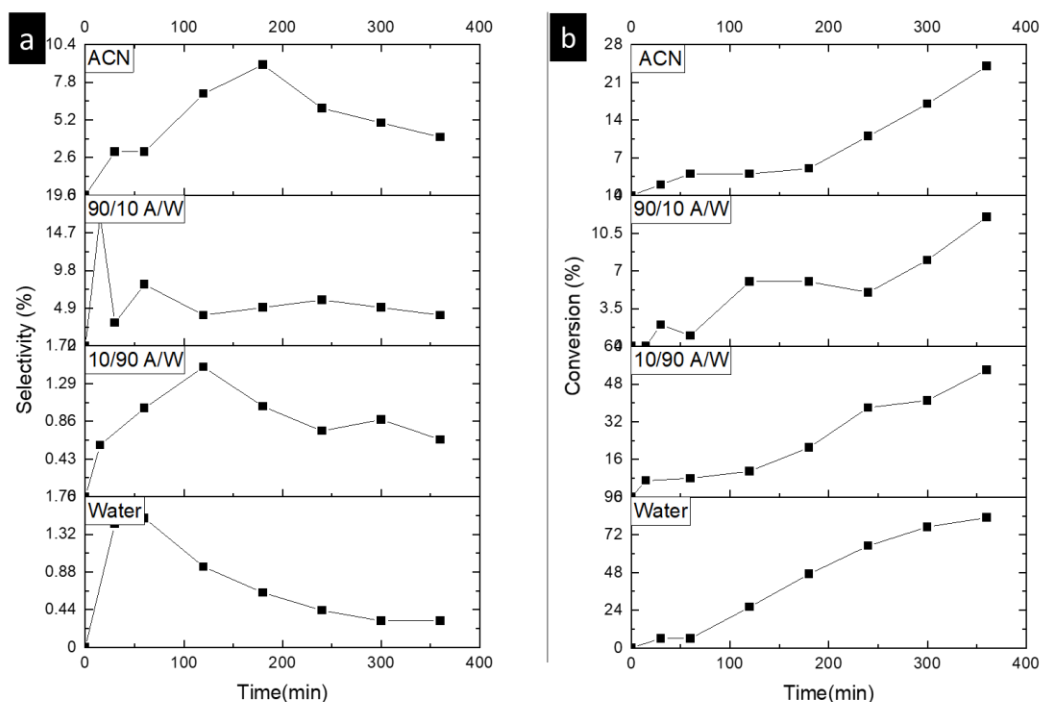


Figure A II.2. Conversion and selectivity for different solvents a) water, b) 10/90 AcN/Water, c) 90/10 AcN/Water d) AcN with ZnO at 400 RPM

From Figure A II.2, after 6 hrs of experiment though the conversion was very high for water and 10/90 AcN/Water solvent (75 and 50 % respectively) but the selectivity was almost negligible compared to AcN. So, AcN was selected as a suitable solvent for our next set of experiments, as it showed considerable selectivity towards benzaldehyde (BnAld) with 26 % conversion.

#### (c) Optimization of RPM:

To look upon the effect of RPM on the photocatalytic batch studies, experiments were performed in the same condition (3 g/ L in AcN solvent) with different mixing speed (200, 400, and 600 RPM). At 400 RPM, BnOH conversion was better (15 %) and stable compared to 200 and 600 RPM after 2 hrs of irradiation time. The reason might be that the time of interaction of light with the catalyst surface is better in this 400 RPM speed.

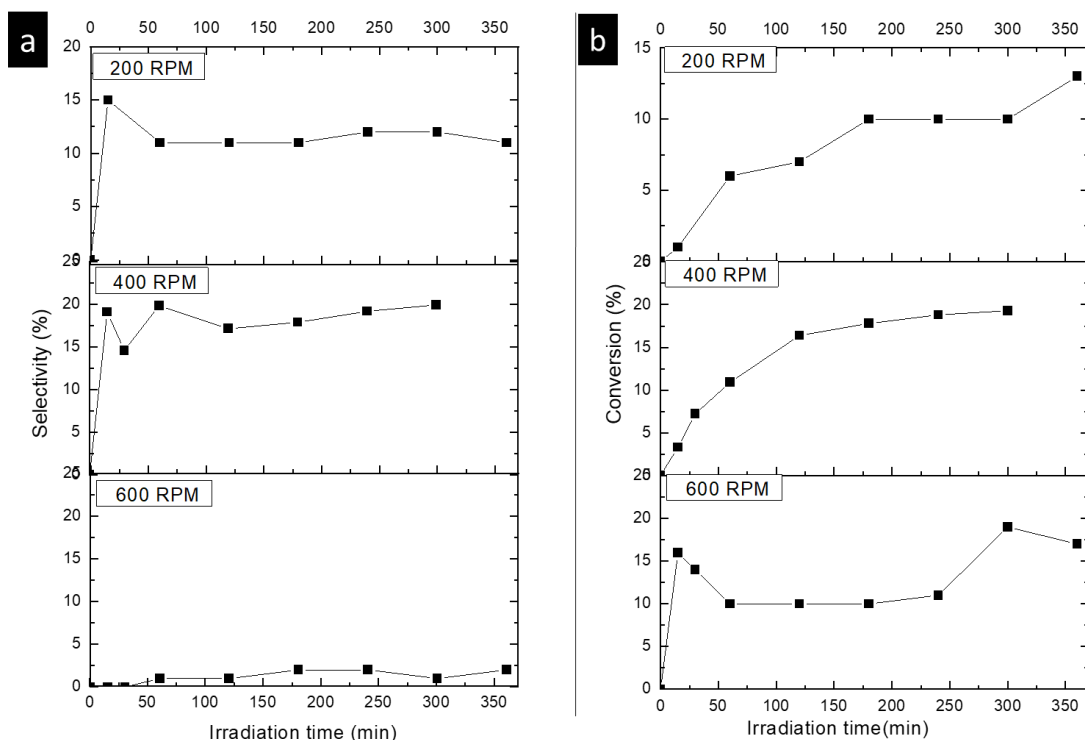


Figure A II.3. Conversion and selectivity for ZnO catalyst at different mixing speed (RPM).

At 600 RPM the selectivity falls drastically after 240 min, which concludes that this is not a good mixing speed for our experiment. From these above optimization experiments it can be concluded that 3 g/ L of catalyst with AcN solvent at 400 RPM mixing speed showed better activity. In our next step we moved from batch to microflow system with the above optimized parameters.

## A2.2. Batch photocatalytic experiment

To a 25 mL vial 72 mg of synthesized ZnO and 24 mL (3 g/ L) of 1mM solution of benzyl alcohol were introduced. The mixture was sonicated for 15 mins using ultrasonic bath (Sonorex-digital RC, 37 kHz, 70% amplitude, sweep mode) to have a homogenous suspension. Then vial was placed on magnetic stirrer and put inside LED lamp ( $\lambda = 375$  nm) cylinder for photocatalytic experiment. The suspension was stirred at 400 RPM. The samples were collected from the photoreactor and filtered to glass vials at specified interval times. Later the samples were kept in the fridge and analyzed by using an HPLC (Waters, Acquity Arc) equipped with a UV-Vis detector (Waters 2487) and a SunFire™ C18 column.

### A2.3. Deposition and Photocatalytic study with commercial ZnO catalyst coated inside PFA microtube:

On next step, ultrasonic assisted deposition of ZnO catalysts was carried out inside PFA tube. For this, 0.5 g/ L (from previous optimizations) of commercially available Degussa P25, and 3 g/ L ZnO catalyst were taken. The photocatalysis experiments were carried out inside the microchannel of PFA (0.8 mm of internal diameter). With the help of syringe infusion pump, BnOH solution was passed through the tube at the rate of 0.16 mL/ min (Optimized data from batch experimental study). The results of first 30 mins of photocatalytic experiment are shown Figure A II. 4.

The suspension of commercial ZnO in MilliQ water (3 g/ L) used for deposition was previously sonicated (70% US power, 37 kHz, sweep mode) for 15 min and then transferred to a syringe, which was then used for deposition by continuous introduction of the suspension to the PFA microtube. At the end of the experiment i.e. after 60 min, some catalyst particles were settled at the bottom of the syringe. It means that not the whole amount of catalyst was passing through the microtube. This problem might be caused because of the high concentration of suspension with commercial zinc oxide which is six times higher than concentration used for TiO<sub>2</sub> – P25 (0.5 g/ L). To tackle this issue, the suspension of catalyst in MilliQ water used for deposition was previously sonicated (70 % US power, 37 kHz, sweep mode) for 15 min and then transferred to a syringe. During this step time of sonication had to be elongated to 30 min to overcome the above problem by making the suspension more homogenous. Also, the suspension was separated in two parts and deposition was carried out to avoid precipitation of catalyst in syringe.



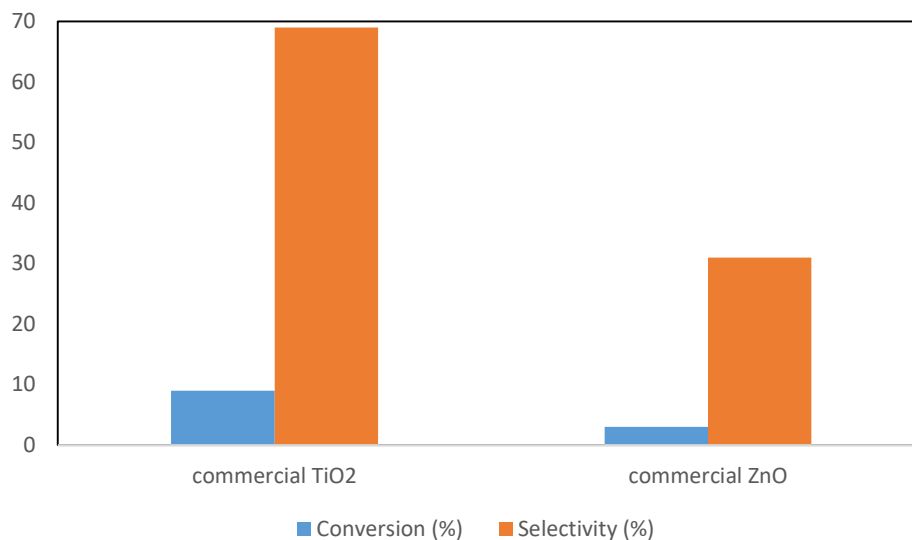


Figure A II.4. Selectivity and conversion of commercial TiO<sub>2</sub> and ZnO catalyst deposited microtube after 30 mins of photocatalytic test under UV light with 1mM BnOH.

The activity of commercial TiO<sub>2</sub> was observed better with comparison to commercial ZnO with single coating. After 30 min of irradiation time, the BnAld selectivity reached to 70% for TiO<sub>2</sub> whereas for ZnO it was 30%. Also, the BnOH conversion is low in case of ZnO.

Table II.1. Optimized parameters (Design Expert 11) for deposition of catalyst in microflow reactor

Tube	US Power (%)	Length of tube	Time of Deposition (min)	Deposition (mg)
B1	40	30 cm	75	0.2
B2	100		75	0.2
B3	70		30	0.1
B4	70		120	0.2

For deposition of ZnO catalysts inside a microtube, similar procedure and conditions as  $\text{TiO}_2$  were followed. The photocatalytic experiments were performed with those catalyst coated tubes and results with 30 cm tubes are given below in Figure A II. 5.

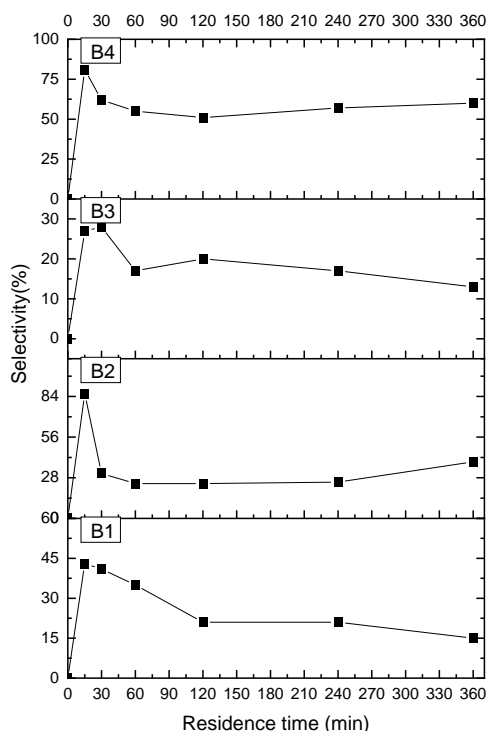


Figure A II.5. Selectivity and conversion of ZnO coated PFA tube for photocatalytic oxidation of BnOH (30cm tube)

From these above data, It can be concluded that B4 (30 cm tube, 120 min of deposition under ultrasonic bath with 70 % (85 W) power) showed better selectivity (60 %) compared to other cases. Conversion was <5% for all the above cases. Compare to batch photocatalytic experiment, ZnO showed low (5 %) BnOH conversion, with ~ 40 % more selectivity towards BnAld.

#### A2.4. Catalyst Synthesis:

In order to increase the photocatalytic activity, ZnO was synthesized by following previously established sol-gel method <sup>166,180</sup>. Also, different approach to aging step was taken during the synthesis process (24 hrs aging without mixing, 24 hrs aging with mixing using magnetic stirrer). After this step the product was separated and cleaned in three centrifugation cycles of 6000 RPM for 10 min with water

(2 times) and isopropanol (once). The remained clean and white product was left to dry at 80°C for 24 hrs in an oven. The obtained white material was ground in an agate mortar and transferred to a sealed vial.

#### A2.5. Characterization of synthesized catalysts:

ZnO, synthesized by following sol-gel method similar to TiO<sub>2</sub> was characterized by SEM, XRD and N<sub>2</sub> physisorption. The results from SEM imaging are given in Figure A II.6.

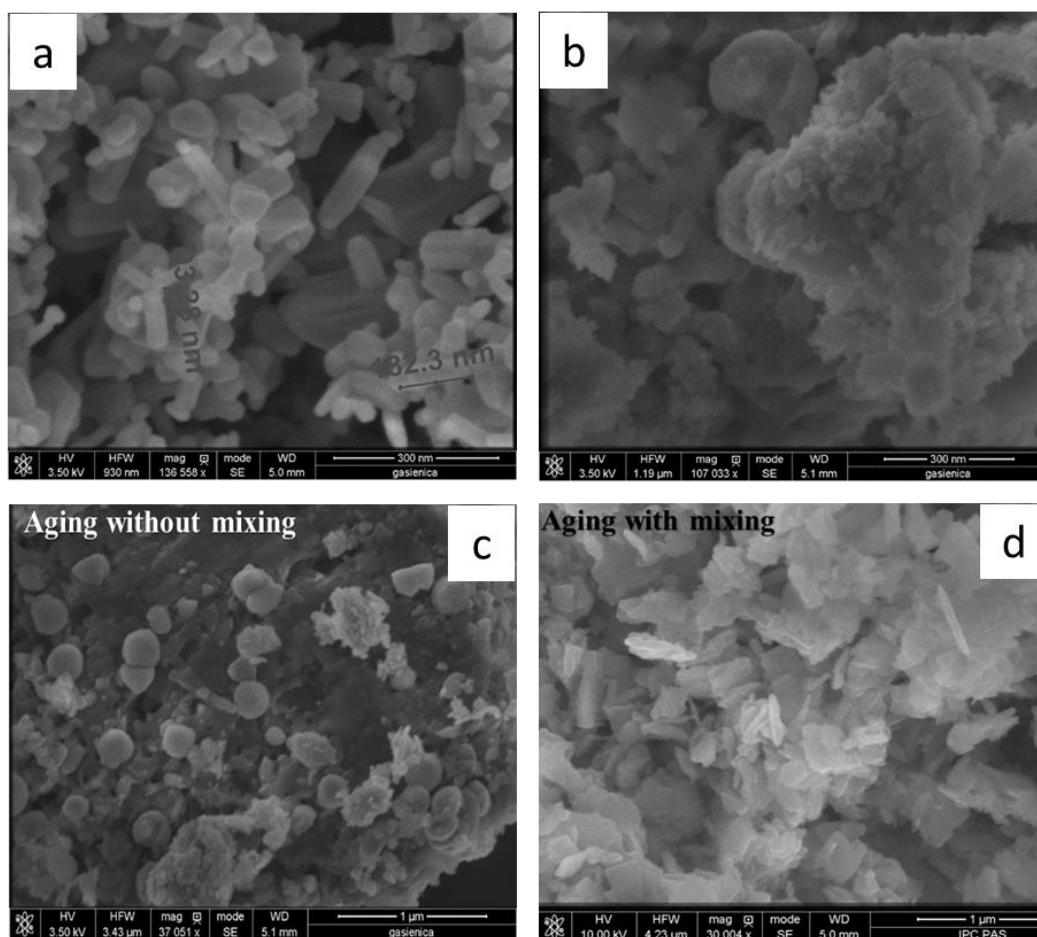


Figure A II.6. SEM image of a) commercial, b) synthesized (ZnO-SG) c) Synthesized (24 hr aging without mixing) d) Synthesized (24 hr aging with mixing)

Nanoparticles synthesized using ultrasonication, were almost spherical in morphology, and they have been agglomerated to form larger particles. Whereas, commercial catalyst has nanorod like structures with 70 – 200 nm lengths with surface area of 13 m<sup>2</sup>/ g. After implementing aging and mixing, the

agglomeration of nanoparticles was still observed. SEM images illustrates that synthesized catalysts (without mixing, aging) in Figure A II.6c had highly agglomerated structure than the commercial catalyst i.e Figure A II.6a. The sample prepared by following 24 hrs aging with mixing (on magnetic stirrer at 400 RPM) showed plate like or sheet like structures (Figure A II.6d) with 50-100 nm. XRD analysis was also performed with these above samples and are shown in Figure A II.7.

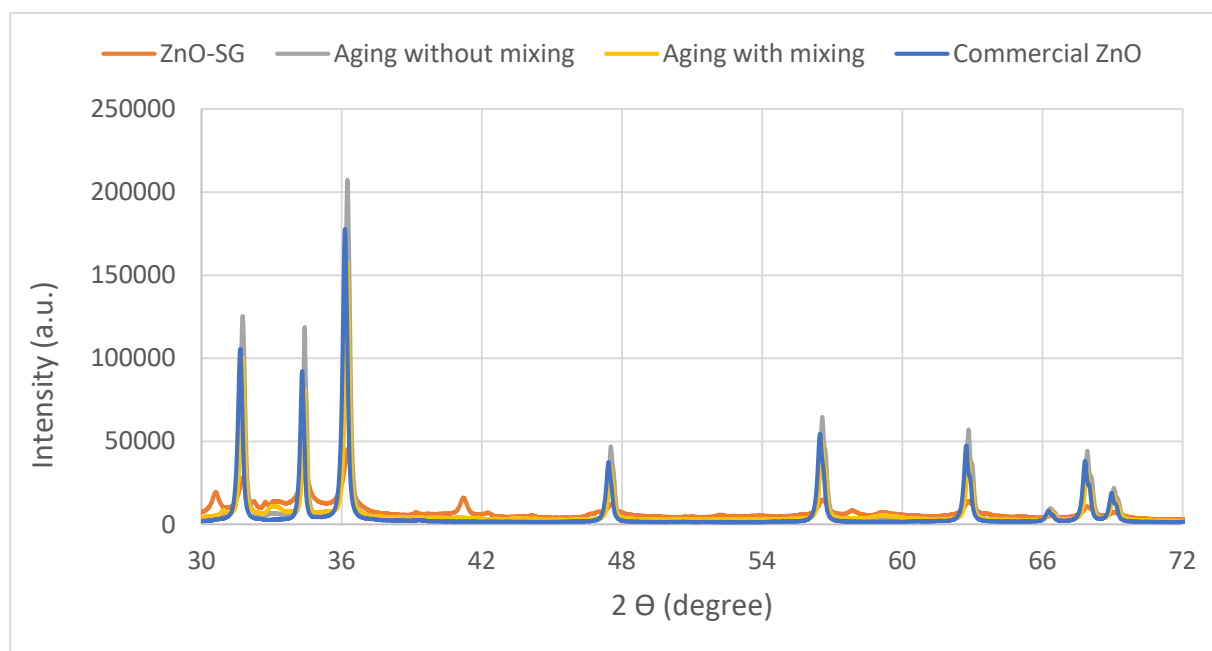


Figure A II.7. XRD analysed image of synthesized (ZnO-SG), Synthesized ZnO 24 hr aging with mixing, Synthesized ZnO 24 hr aging without mixing, Commercial ZnO

There were many peaks observed for ZnO-SG from additional non-stoichiometric phase/s that are not in the database of our XRD, so only the crystallite size could be estimated (101 peak, Zincite, was used for calculation by Scherrer method). The crystallite size for ZnO-SG sample was found to be 15 nm. The crystallinity increased by introducing aging step. The size for ZnO aging without mixing and with mixing is 32 nm and 34 nm, respectively.

For further information about our synthesized catalysts, textural study by N<sub>2</sub> physisorption was carried out.

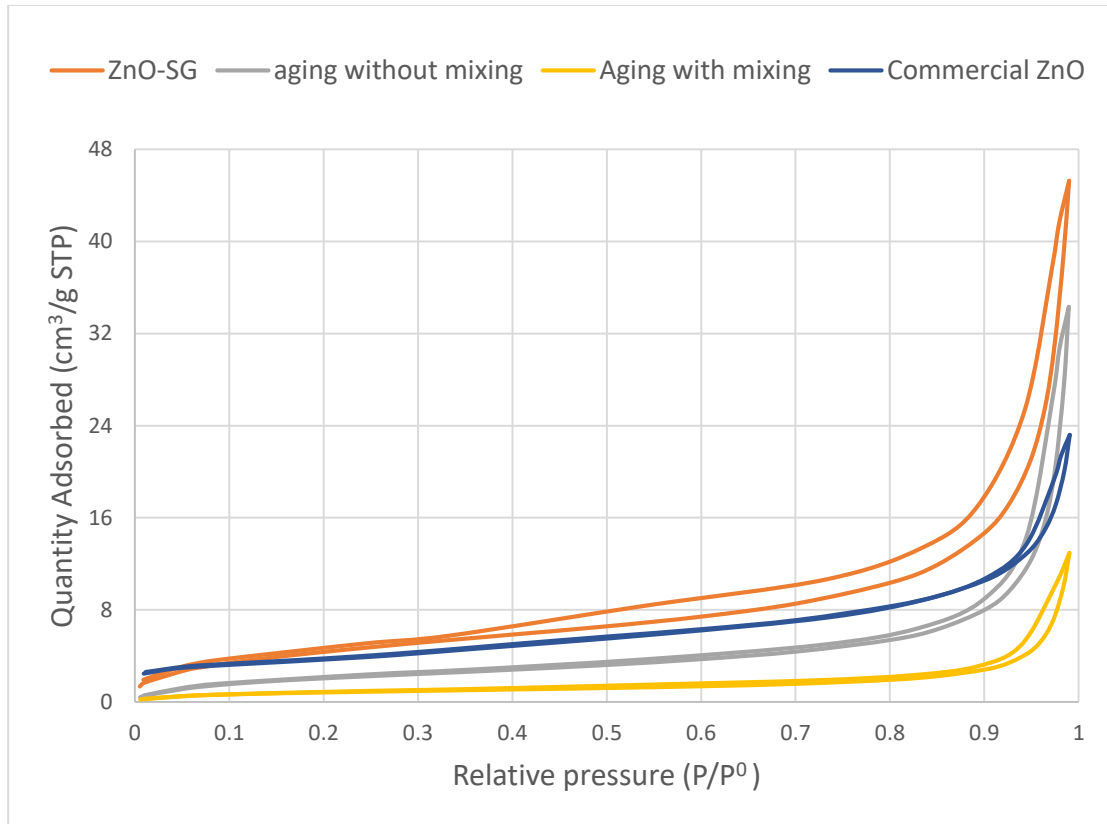


Figure A II.8.  $N_2$  physisorption of commercial ZnO, sol-gel synthesized, synthesized with 24 hr aging without mixing and synthesized with 24 hr aging with mixing ZnO

Table II.2. Data obtained from  $N_2$  physisorption

	Specific surface area ( $m^2/g$ )	Pore volume ( $cm^3/g$ )	Pore width (nm)
<b>ZnO-SG</b>	16	0.06	12.8
<b>Commercial ZnO</b>	13	0.03	9.5
<b>ZnO - aging without mixing</b>	7	0.04	19.8
<b>ZnO - aging with mixing</b>	3	0.01	17.2

From Figure A II.8, it can be observed that all the catalysts showed type IV isotherm with H3 hysteresis loop, which indicates that the sample has a mesoporous texture. Larger hysteresis loops for the ZnO-SG nanoparticles confirm that their surface areas and pore volumes have been increased compared to other ZnO.

## A2.6. Photocatalytic study in batch with ZnO

Photocatalytic study in batch system were performed with these above catalysts and compared the results with commercial ZnO (Figure A II.9). Experiments were carried out with 3 g/ L of catalyst concentration under UV LED light (375nm) with 1mM BnOH.

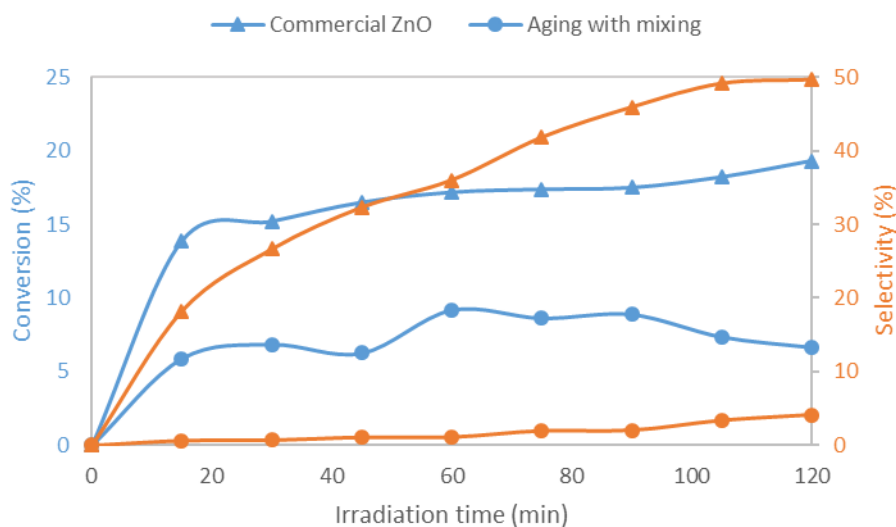


Figure A II.9. Photocatalytic experiment with 3 g/ L of ZnO (commercial ZnO and synthesized with aging step with mixing) in batch under UV light.

The calculations showed that the commercial ZnO had better activity (19 % conversion, 50 % BnAld selectivity) compared to any synthesized ZnO in batch.

In the next step, immobilization of catalysts inside PFA microtube was carried out using a US bath. In microflow experiments, neither of these ZnO showed any activity. The very low surface area of the catalysts can be the reason for the inadequate immobilization of catalyst inside tube, and the reason behind lowering the activity in flow as it lowers the number of active sites for the BnOH reaction. From

the results, we can say that the synthesized catalyst does not show a good activity compared to commercial catalyst.

In the next step, incorporation of metal to the catalyst was carried out expecting the increase the activity of ZnO. To follow the photocatalytic activities of the above catalysts, experiments in microflow system were carried out.

### A2.7. Synthesis of 0.5 at % Cu-ZnO

By following the previously optimized amount of metal on  $\text{TiO}_2$ , the batch synthesis of 0.5 at % Cu ZnO was done in beaker by following the sol-gel method. Zinc acetate dihydrate (Chempur, analytical grade) and copper (II) acetate monohydrate (98 % pure, ABCR) were used as the precursors. As the suspension was difficult to mix under US, magnetic stirrer at 800 RPM was used.

A microflow experiment was carried out with the synthesized Cu-ZnO catalyst to study the photocatalytic effect.

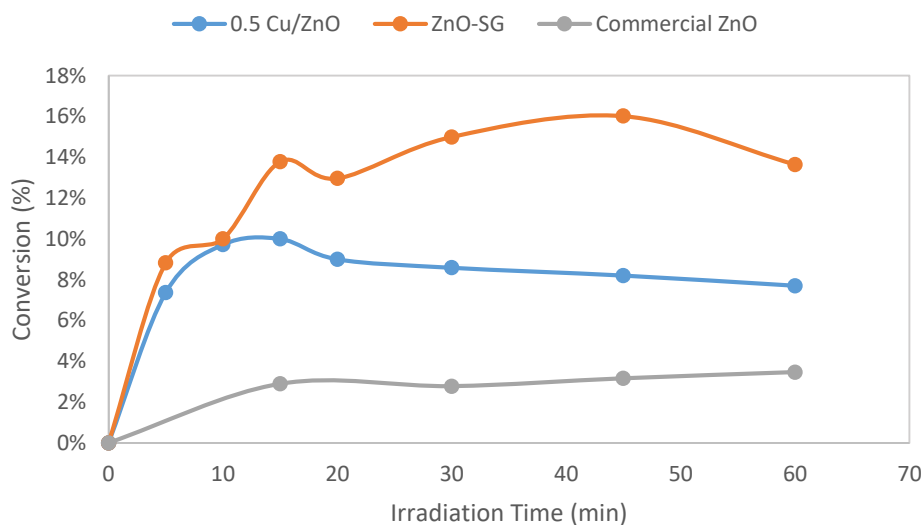


Figure A II.10. Photocatalytic activity of synthesized 0.5 at% Cu-ZnO catalyst (3 g/L) under UV light with 1mM BnOH in microflow system under UV light.

From the above analysis (Figure A II.10), it can be concluded that the incorporation of Cu to the synthesized ZnO showed no visible improvement on photocatalytic activity. The BnOH conversion

reached to 10 % with very low BnAld selectivity (4 %) after 15 min of irradiation time. One more experiment was performed under visible light (515 nm) system to follow the activity of Cu-ZnO. There was zero activity of the catalyst under visible light in microflow system. The concentration of BnOH was measured by HPLC and it remained same after 3 hrs of light irradiation.

The commercial ZnO showed better activity in batch as well as in microflow compared to other synthesized ZnO. The nanorod like structure (Figure A II. 6) and low pore width (9.5 nm) can be the reason for the improved activity. Presence of additional phases (from XRD, Figure A II.7) in case of ZnO-SG reduced the activity of ZnO in our experimental conditions. In microflow system, none of our synthesized catalyst is showing good activity.



## APPENDIX III

### Supporting information

#### S 1. Selective oxidation of Benzyl alcohol

Conversion and selectivity were calculated from the benzyl alcohol (BnOH) and benzaldehyde (BnAld) concentrations determined by HPLC:

$$\text{Conversion (\%)} = \frac{\text{Converted BnOH moles}}{\text{Initial BnOH moles}} \times 100\%$$

$$\text{Selectivity (\%)} = \frac{\text{Produced BnAld moles}}{\text{Converted BnOH moles}} \times 100\%$$

#### S 2. Characterization of catalysts and microtubes

The optical properties of the synthesized powder samples were determined based on the diffuse reflectance UV-visible spectra (DRS UV-vis) on U-3900 made by Hitachi (Hitachi Limited Company, Tokyo, Japan). Powder X-ray diffraction (XRD) measurements were performed in a Bruker D8 DISCOVER A25 diffractometer (Bruker Corporation, Billerica, MA, USA) equipped with a vertical goniometer under theta-theta geometry using Ni filtered  $\text{CuK}$  ( $\lambda = 1.5418 \text{ \AA}$ ) radiation and operated at 40 KeV and 40 mA. Wide angle scanning patterns were collected from  $10^\circ$  to  $80^\circ$  with a step size of  $0.01^\circ$  and counting time of 500 s per step. The average crystallite size (D in nm) was determined according to the Scherrer equation:

$$D = k \lambda / \beta \cos \theta$$

where D is the average crystallite size of the catalyst (nm),  $\lambda$  is the wavelength of the  $\text{Cu } \alpha$  X-ray radiation ( $\lambda = 0.154056 \text{ nm}$ ), k is a coefficient usually taken as 0.9,  $\beta$  is the full width at half maximum intensity of the peak observed at  $2\theta$  (radian), and  $\theta$  is the diffraction angle. The morphology of the samples were also obtained by scanning electron microscopy (SEM). The textural properties of  $\text{TiO}_2$  were determined by  $\text{N}_2$  physisorption experiments using a Micromeritics automated system (Micromeritics Instrument Corporation, ASAP 2020) based on the Brunauer-Emmet-Teller (BET) and the Barret-Joyner-Halenda (BJH) methods. Prior to

adsorption measurements, samples were degassed under vacuum (0.1 Pa) for 6 h at 80 °C. The selected pieces of the deposited microtubes were cut off (cross-sectional) and prepared for determination of coating thickness and surface morphology by high resolution scanning electron microscope (HR-SEM) by a FEI Nova NanoSEM 450.

Samples collected from the outlet the catalyst deposited PFA microtube during photocatalysis test, were examined using the energy dispersive X-ray fluorescence (EDXRF) spectrometer (Mini-Pal 4, PANalytical & Co.) with Rh tube and silicon drift detector to check potential leaching. The spectra were collected in air atmosphere, without using a filter, at a tube voltage of 30 kV.

To identify and quantify the BnOH, BnAld and acid present, as well other possible aromatic or aliphatic products, the collected samples were analyzed using high-pressure liquid chromatography (HPLC), equipped with a dual absorbance detector (Waters 2487) and the SunFire™ column provided by Waters, using a mobile phase containing a mixture of organic solvents and a 0.05 % H<sub>3</sub>PO<sub>4</sub> (5 M) aqueous solution (CH<sub>3</sub>CN : CH<sub>3</sub>OH : H<sub>2</sub>O = 20 : 2.5 : 77.5 v/v).

### S 3. Experimental Section

#### BATCH EXPERIMENTS

##### Optimization of catalyst concentration

In order to determine the optimum catalyst concentration, three different loadings were tested (0.5, 1, and 2 g/ L). The batch experiments were performed with 1mM of BnOH in AcN as solvent at room temperture at 400 RPM under UV-LED (375nm) irradiation. The results after monitoring the BnOH conversion and BnAld selectitivity are collected in Figure S1. Before illumination, we carried out in the dark adsorption experiment with batch system as well as in flow system and the values are given in Table III.1. 0.5 g/ L of commercial P25 catalyst showed the highest selectivity, while the conversion per mass of catalyst was also the highest even after 120 min compared to other two concentrations.

Table III.1. Results for dark adsorption studies in batch and microflow systems.

Time [min]	Batch	Flow
	BnOH concentration (in mM)	
0	1.02	0.98
15	1.01	0.79
30	1.00	0.99
60	1.01	0.99
90	1.01	1.00
120	1.0	1.00

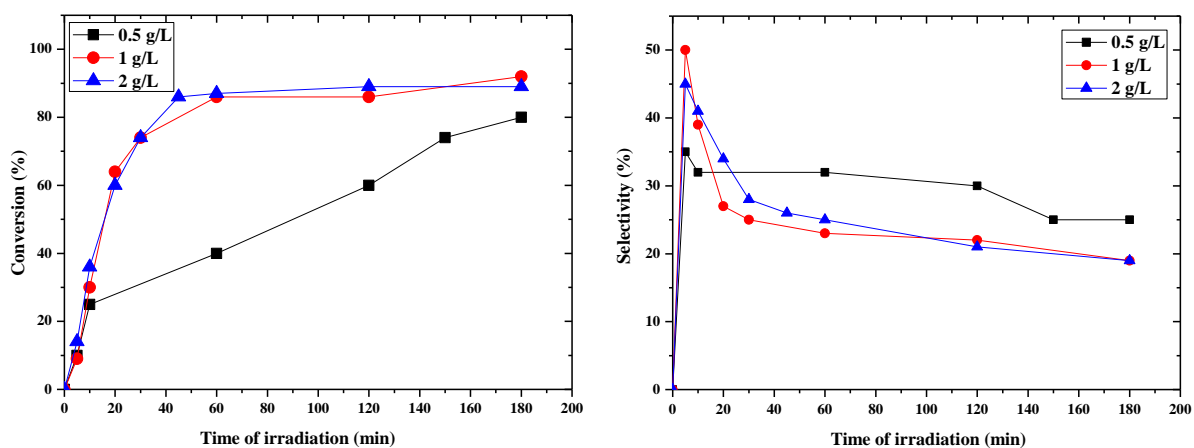


Figure S1. Conversion, and selectivity in batch photocatalysis system for different TiO<sub>2</sub> P25 concentrations (conditions: 400 RPM, room temperature, 1 mM initial BnOH concentration in AcN, UV-LED).

### Optimization of RPM (rotation/revolutions per minute)

Other parameters like the effect of RPM and solvents were studied using 0.5 g/ L of catalyst. The optimized result found from these above factors is, 0.5 g/ L of catalyst in acetonitrile at mixing speed of 400 RPM gives better conversion and selectivity compared to other results in batch system. To study the effect of RPM on the photocatalytic activity, experiments were performed under different mixing speed (200, 400, and 600 RPM). From the result (Figure S2), it can be seen that the best selectivity (26%) was achieved at 400 RPM and also reached to a comparable conversion after 3 hrs of light illumination with other two RPM conditions.

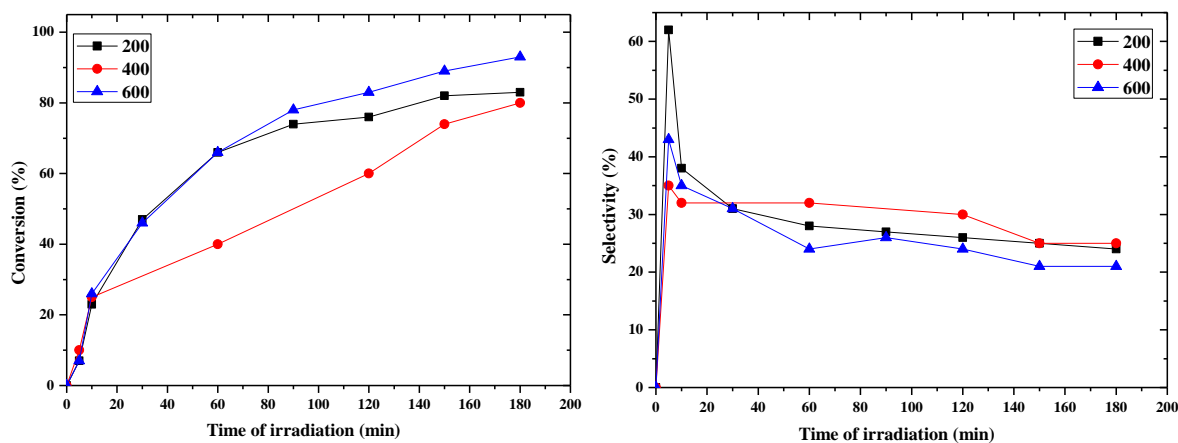


Figure S2. Conversion and selectivity in batch photocatalysis system for different RPM using  $\text{TiO}_2$  P25 catalyst in AcN (room temperature (25 °C), 1 mM initial BnOH concentration in AcN, UV-LED).

### Effect of the Solvent

In order to look upon the effect of solvent on the photocatalytic batch studies, these experiments were performed in the similar condition as before (0.5 g/ L at 400 RPM) with different solvents (AcN, Water, 10/90 AcN/Water, 90/10 AcN/Water).

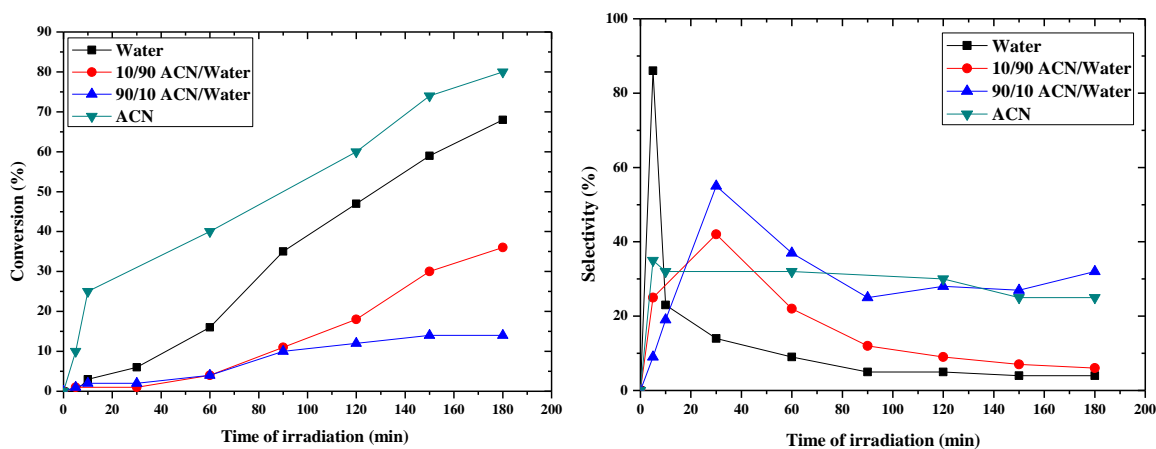


Figure S3. Conversion and selectivity in batch photocatalysis system for different solvents a) water, b) 10/90 AcN/Water, c) 90/10 AcN/Water with P25 TiO<sub>2</sub> at 400 RPM.

From this result, it can be concluded that the mixture of solvents gave very good selectivity during the initial phase of the reaction, but later, there was a decrease (Figure S3). For water as a solvent, the selectivity was observed to be low (5 %). Hence it was concluded that AcN is better solvent for selective oxidation of BnOH using TiO<sub>2</sub> as BnOH conversion (78 %) and selectivity (36 %) towards BnAld was better compared to other solvent conditions after 3hrs of illumination.

The photocatalytic experiments in the batch reactor with commercial P25 catalyst were repeated two times and the relative error was less than 8 % (Figure S4). This shows that the results were reproducible.

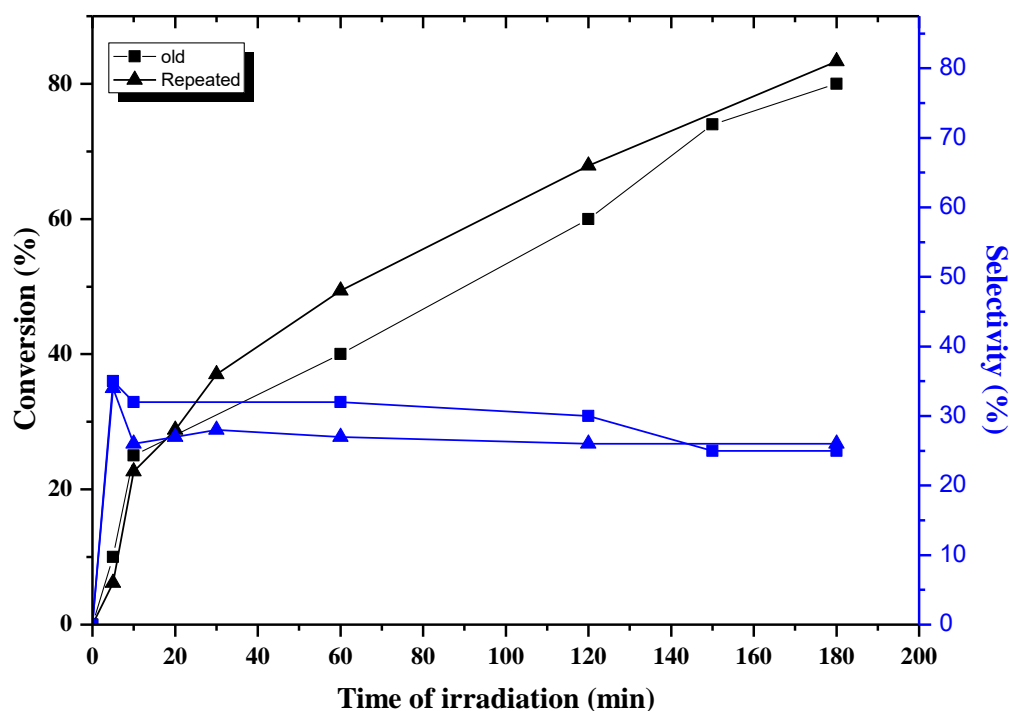


Figure S4. Comparison between repeated values of conversion and selectivity for 0.5g/L of  $\text{TiO}_2$  in 1mM AcN solution at 400 RPM in batch.

## S 4. Experiments with microflow system

### Ultrasound assisted deposition

Initially, PFA tubes of a suitable length were taken and washed by passing MilliQ water and ethanol (EtOH) through the tube with the help of the syringe pump. Later the tubes were kept for drying inside an oven at  $80^\circ\text{C}$  overnight. The deposition of commercial  $\text{TiO}_2$  (P25, Evonik) in the dried PFA tubes were carried out by passing aqueous  $\text{TiO}_2$  suspension, prepared in MilliQ water. During the deposition, the microtubes were kept inside an ultrasonic bath (Sonorex-digital RC, 37 kHz). Three factors provided as input i.e.; time of deposition under ultrasound exposure (30-120 mins), ultrasound power during deposition (40 - 100 %, where 100 % = 120 W) and length of the tube (30-50 cm). Based on these parameters, the optimization of the experimental methodology was established using the Design Expert software (Table I.9).

To determine the deposited mass of catalyst inside the tubes, all tubes were weighted before and after the deposition of catalyst using a high precision weighing balance from Mettler Toledo. showcases the amount of  $\text{TiO}_2$  deposited in microtubes (Table 3.1) at different conditions.

Using the optimized parameters achieved from the batch photocatalytic experiments (0.5 g/ L catalyst in AcN), the photocatalysis experiments were carried out inside a wall coated PFA microchannel. Using a syringe infusion pump, BnOH solution (20 mL) was injected through the tube at the rate of 0.133 mL/ min (optimized data from batch experimental study). Adsorption experiment of BnOH in dark condition was carried out for 30 min and at different time intervals (calculated from rate of flow) samples were collected from the outlet and analyzed.

Table 3.1 collects the results after 30 min of photocatalytic test for each tube. From those results, it can be concluded that B2 test (Deposition condition: 30 cm tube length, 100 % amplitude = 120 W US power, and 75 min of irradiation time) revealed the best selectivity (87 %) and conversion (8 %) (having 0.3 mg catalyst deposited inside the microtube).

## S 5. Pretreatment of PFA microtube before deposition of catalyst

By passing 5 mL MilliQ water (1 mL/ min) through a clean tube (cleaned with water and ethanol before using) under the influence of ultrasound (100 % amplitude, 120W US power, 37 kHz), Pretreated PFA (P-PFA) was prepared. After drying it in the oven at 80 °C for 1h, the tube was used for deposition of commercial P25  $\text{TiO}_2$  (PT-PFA) inside this microtube.

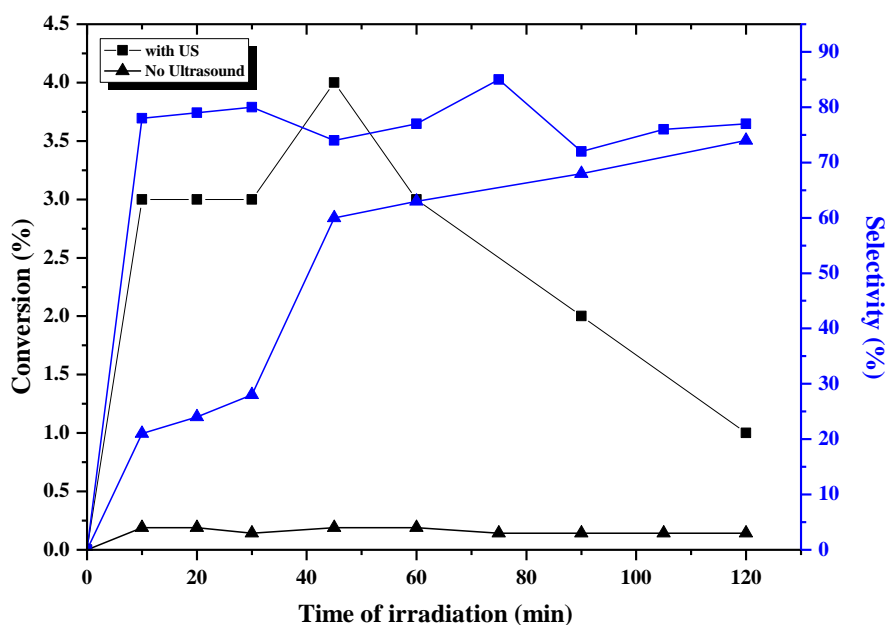


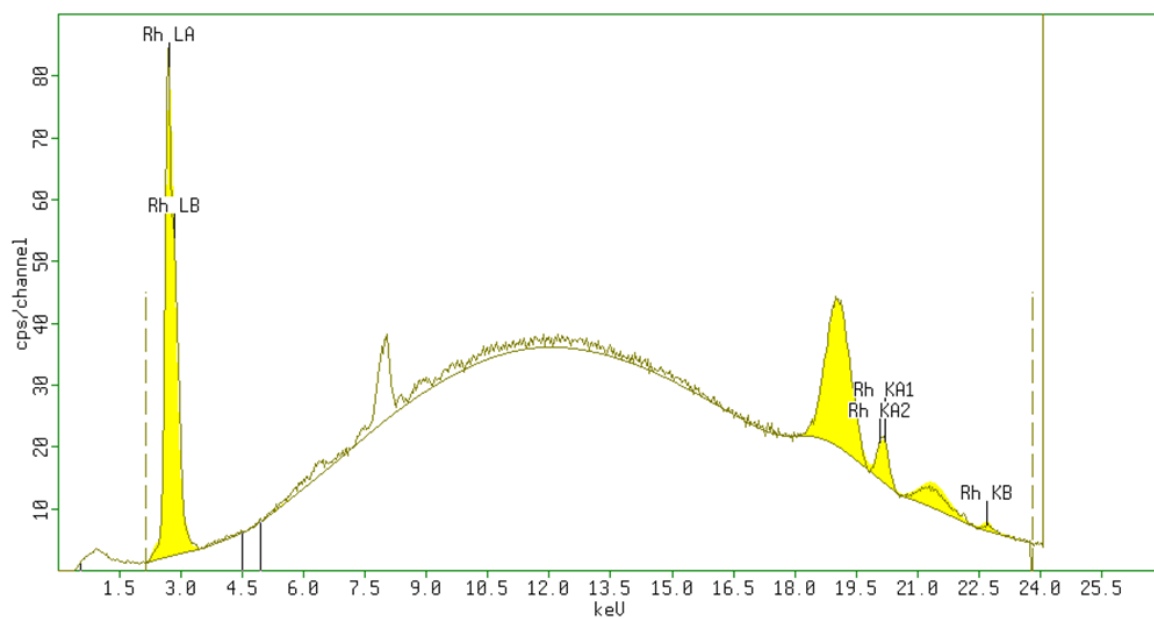
Figure S5. Photocatalytic activity of microtube deposited with P25 catalyst with and without the presence of ultrasound.

## S 6. Titanium dioxide leaching test

The EDXRF characterization carried out to determine possible titanium leaching in the sample collected after photocatalytic test from the outlet of microtube after 60 min. The results (Figures S6, S7) showed the absence of any titanium cation in the solution, confirming that no leaching of  $\text{Ti}^{4+}/\text{TiO}_2$  occurred during the reaction process as well as the strong and stable attachment of the nanocatalysts particles on the inner walls of the PFA tubes.



a)



b)

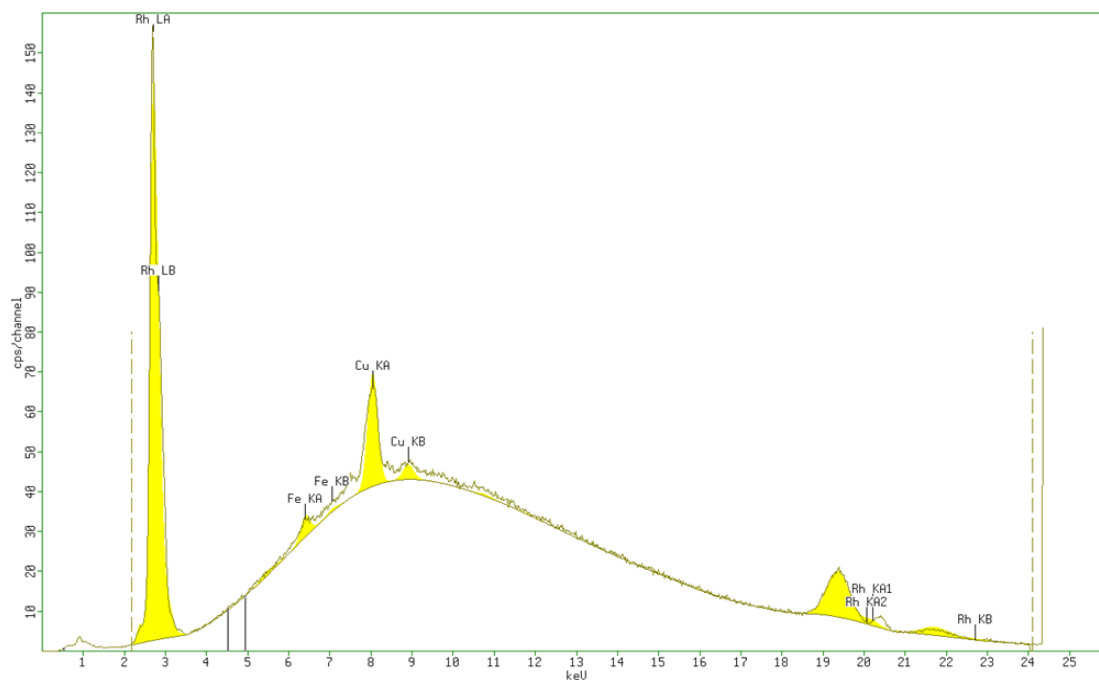


Figure S6. EDXRF measurements of the samples from the outlet of a) P25  $\text{TiO}_2$  and b) synthesized  $\text{TiO}_2$  deposited PFA.

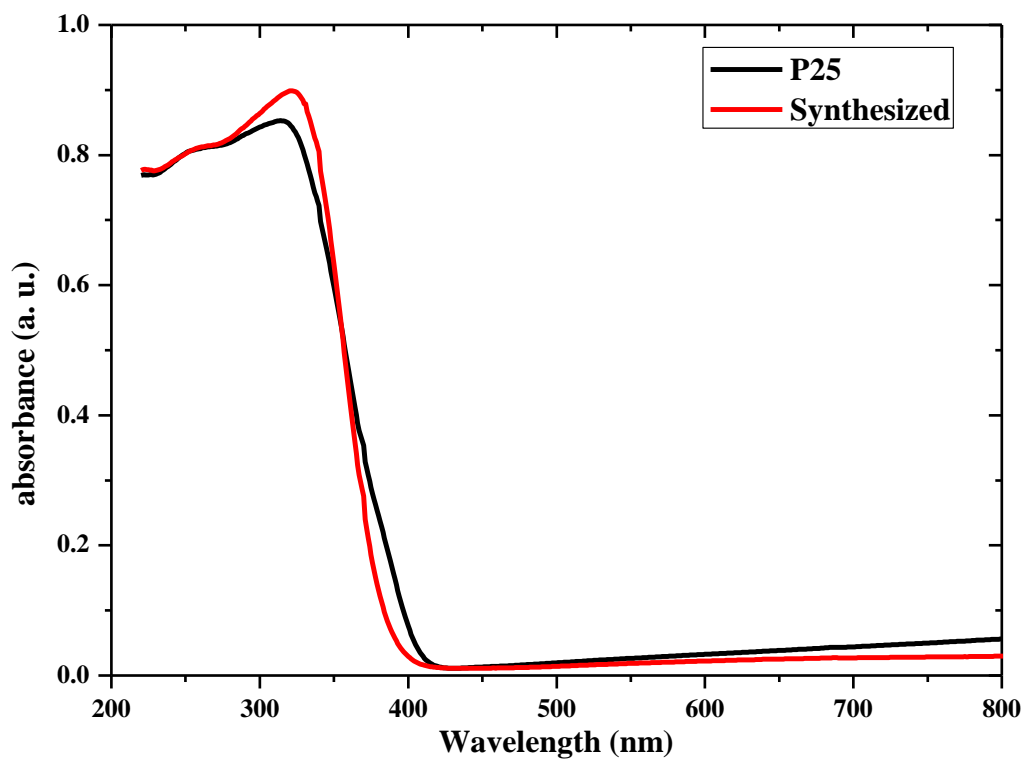


Figure S7. UV-vis DRS of commercial P25 and synthesized  $\text{TiO}_2$  nanoparticles.

To have an insight for the photocatalytic activity with amorphous phase of  $\text{TiO}_2$ , experiments were carried using an amorphous  $\text{TiO}_2$  material catalyst deposited on the microreactor's walls. The result (Figure S8) showed that the conversion (7 %) as well as selectivity (3 %) is very low for amorphous  $\text{TiO}_2$  catalyst.

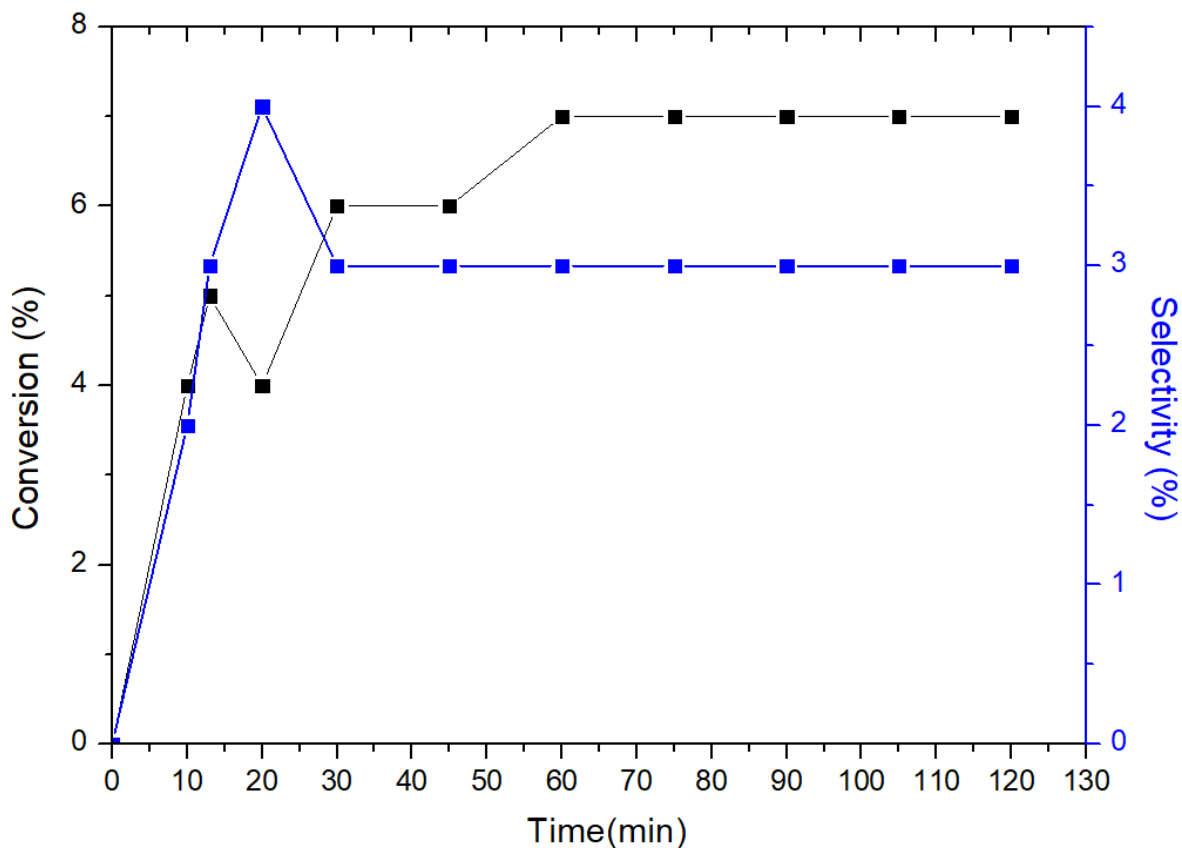


Figure S8. Photocatalytic results from amorphous  $\text{TiO}_2$  catalyst deposited microtube.

## S 7. Ultrasound-assisted deposition of catalysts in PFA

A 30 cm PFA microtube (microcapillary 0.8 mm ID), pure from the market, undergoes a cleaning process by passing through 5 mL of MilliQ water (analytical grade) and 5 mL of ethanol. Both solvents are introduced into the microtube at a flow rate of 1 mL/ min using a syringe infusion pump (New Era Pump Systems, Inc.). The tube is placed in the oven for 1h at approx. 80 °C and used for further deposition. For the catalyst deposition, an ultrasonic bath (Sonorex-digital RC, 37 kHz, 100% amplitude) was used in sweep mode. The tube was placed in the ultrasonic bath (Figure S. 1). The catalyst suspension was passed through a cleaned PFA microtube under the influence of ultrasound (120 W) using a syringe pump for 75 mins (0.34 mL/ min).

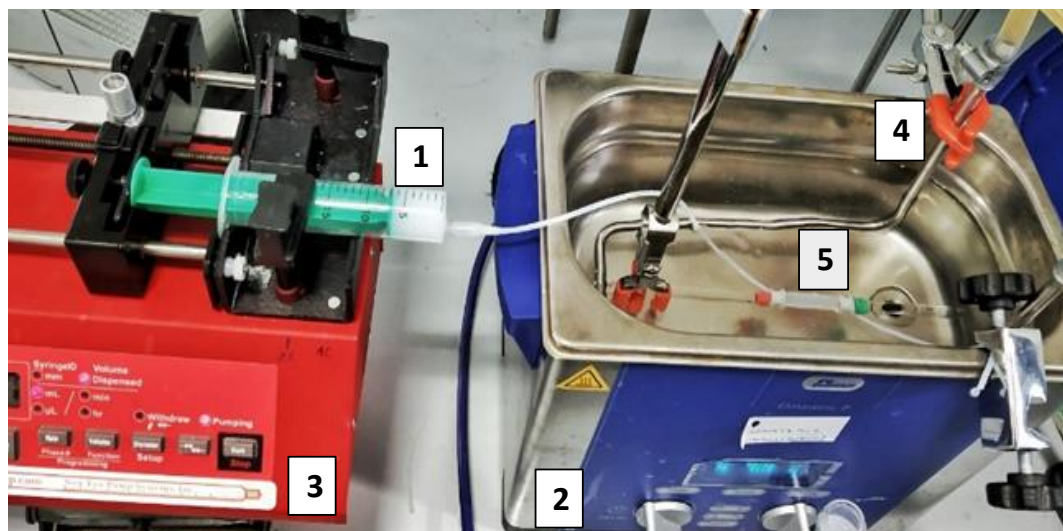


Figure S9. Catalyst deposition to the inner wall of the PFA microtube; (1) semiconductor oxide suspension, (2) ultrasonic bath, (3) Syringe infusion pump, (4) water cooling system, and (5) PFA microtube.

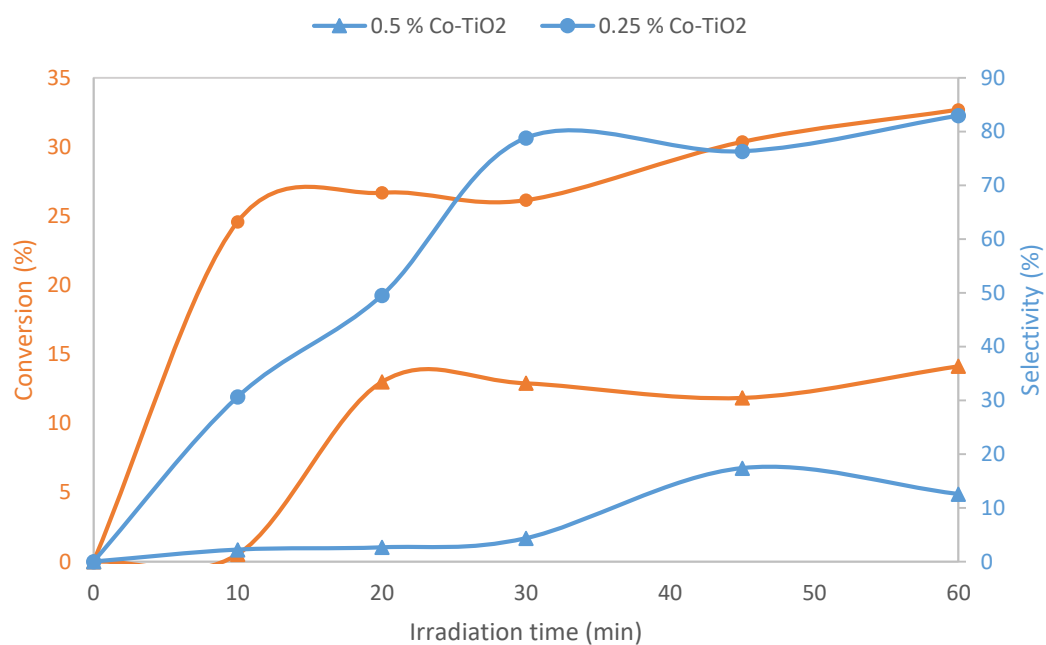


Figure S10. Optimization of at% of Co-TiO<sub>2</sub> (0.5g/ L) under UV light with 1mM BnOH in batch system.

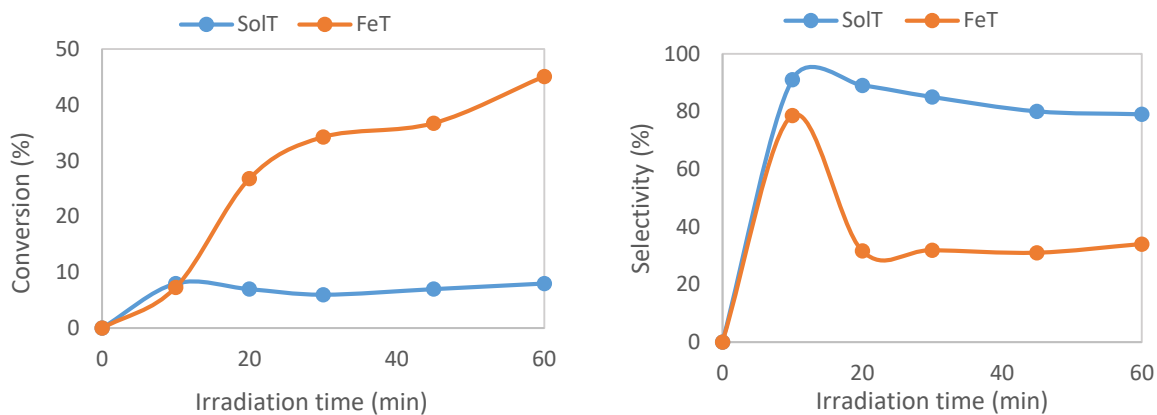


Figure S11. Photocatalytic activity of synthesized  $\text{TiO}_2$  ( $\text{TiO}_2\text{-SG}$ ) and 0.5 at %  $\text{Fe-TiO}_2$  (FeT) under UV light with 1mM BnOH in batch system.

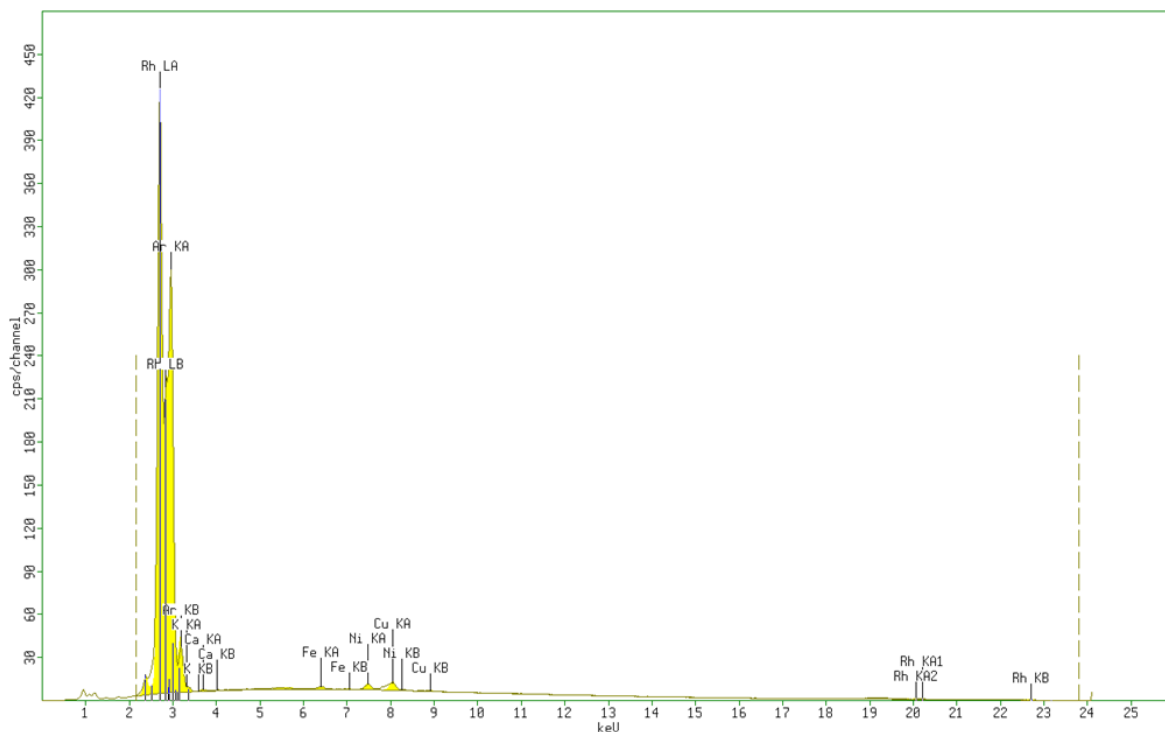


Figure S12. EDXRF measurement of the sample from the outlet of synthesized  $\text{Fe-TiO}_2$  deposited PFA tube. (Rh-peak from Rh lamp, Fe and Cu peaks- are finger prints from the spectrometer).

EDXRF analysis confirmed (no traces of Ti presence) no leaching from the catalyst coated microtube after one hour of the experiment.

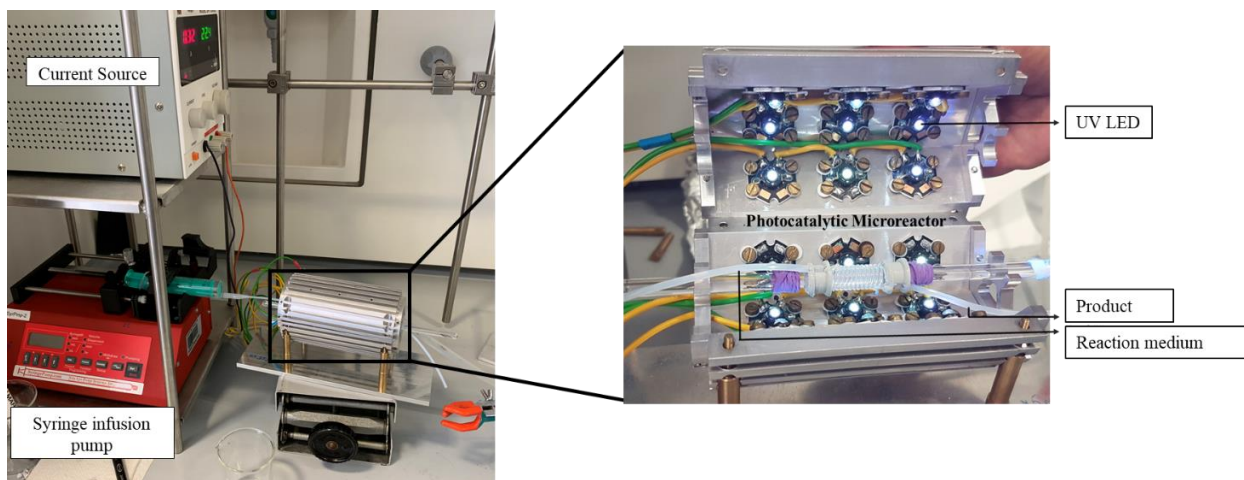


Figure S13. Experimental set up for photocatalysis in microflow system.

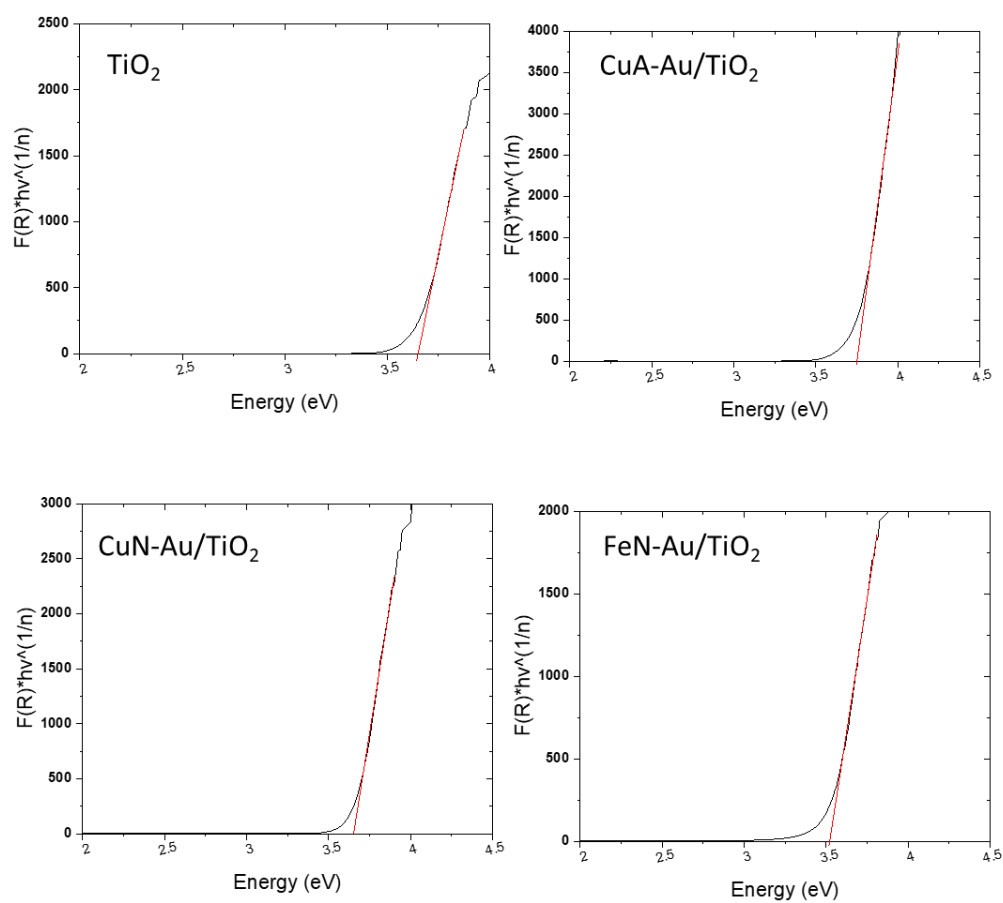


Figure S14. Bandgap calculation of sol-gel synthesized  $\text{TiO}_2$  and bimetallic  $\text{TiO}_2$  ( $\text{CuA-Au/TiO}_2$ ,  $\text{CuN-Au/TiO}_2$ ,  $\text{FeN-Au/TiO}_2$ ) catalysts.

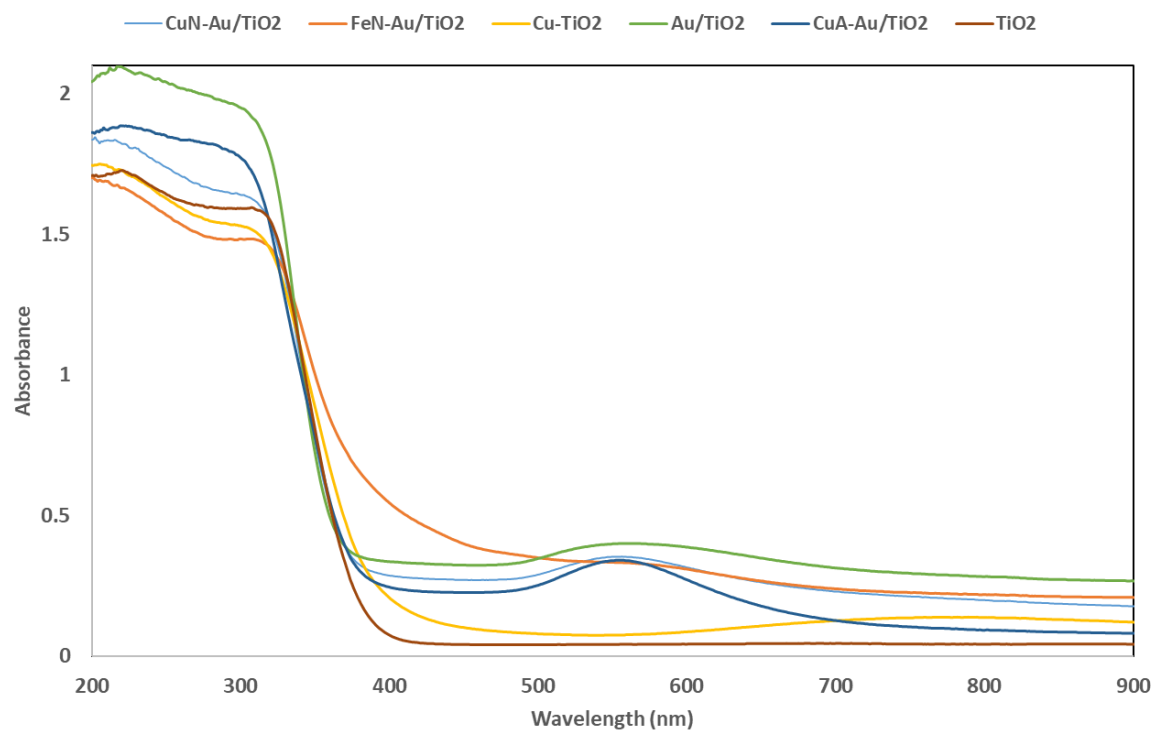
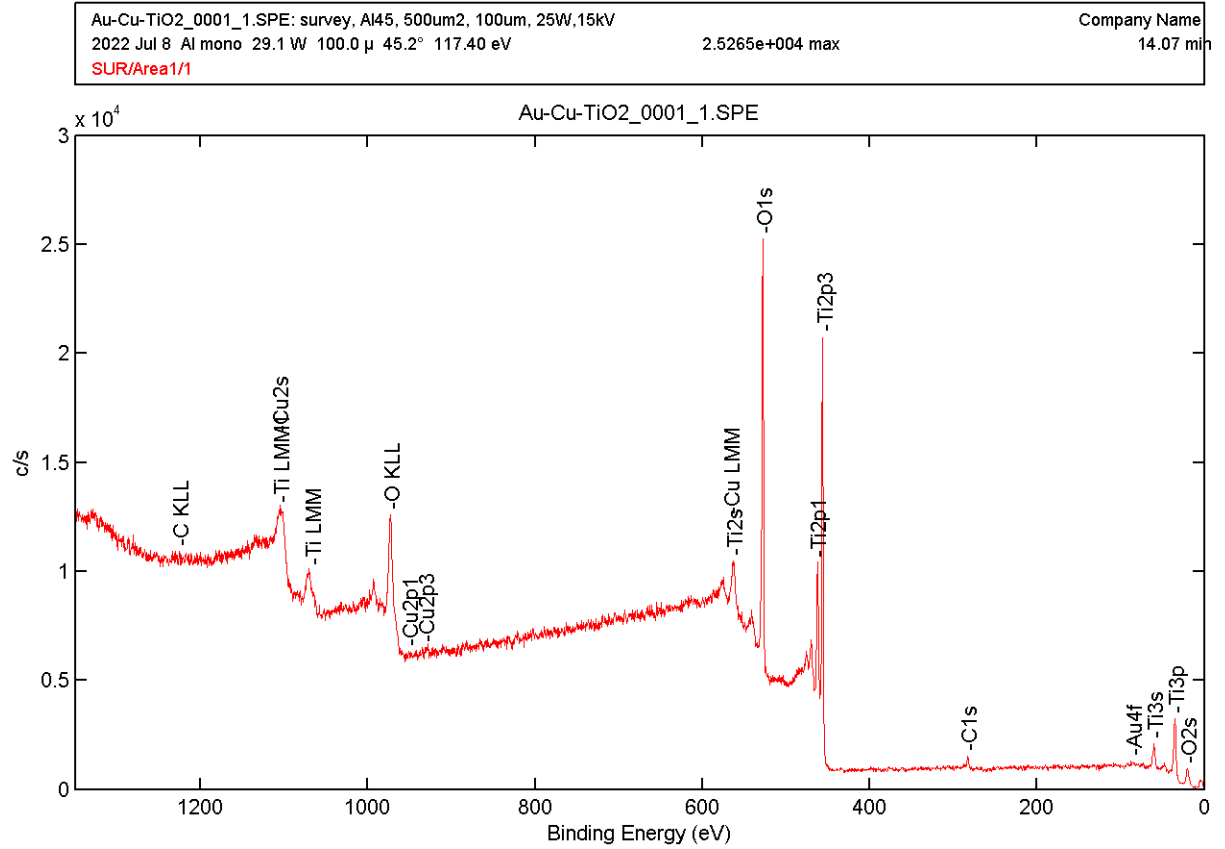


Figure S15. UV-vis diffuse reflectance spectra of synthesized bimetallic  $\text{TiO}_2$ .





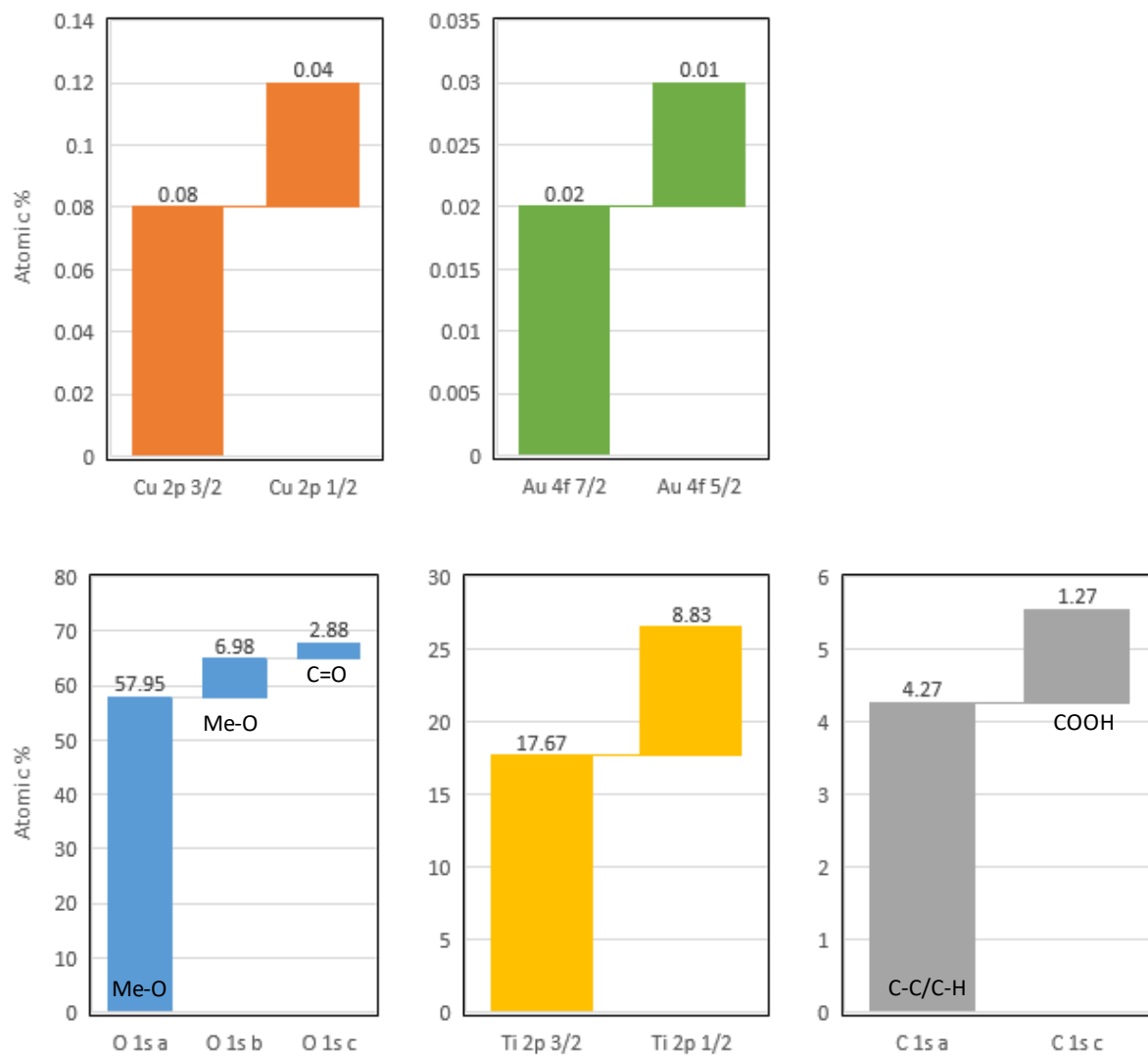


Figure S16. Surface analysis of CuA/Au-TiO<sub>2</sub> by X-ray photoelectron spectroscopy (XPS).

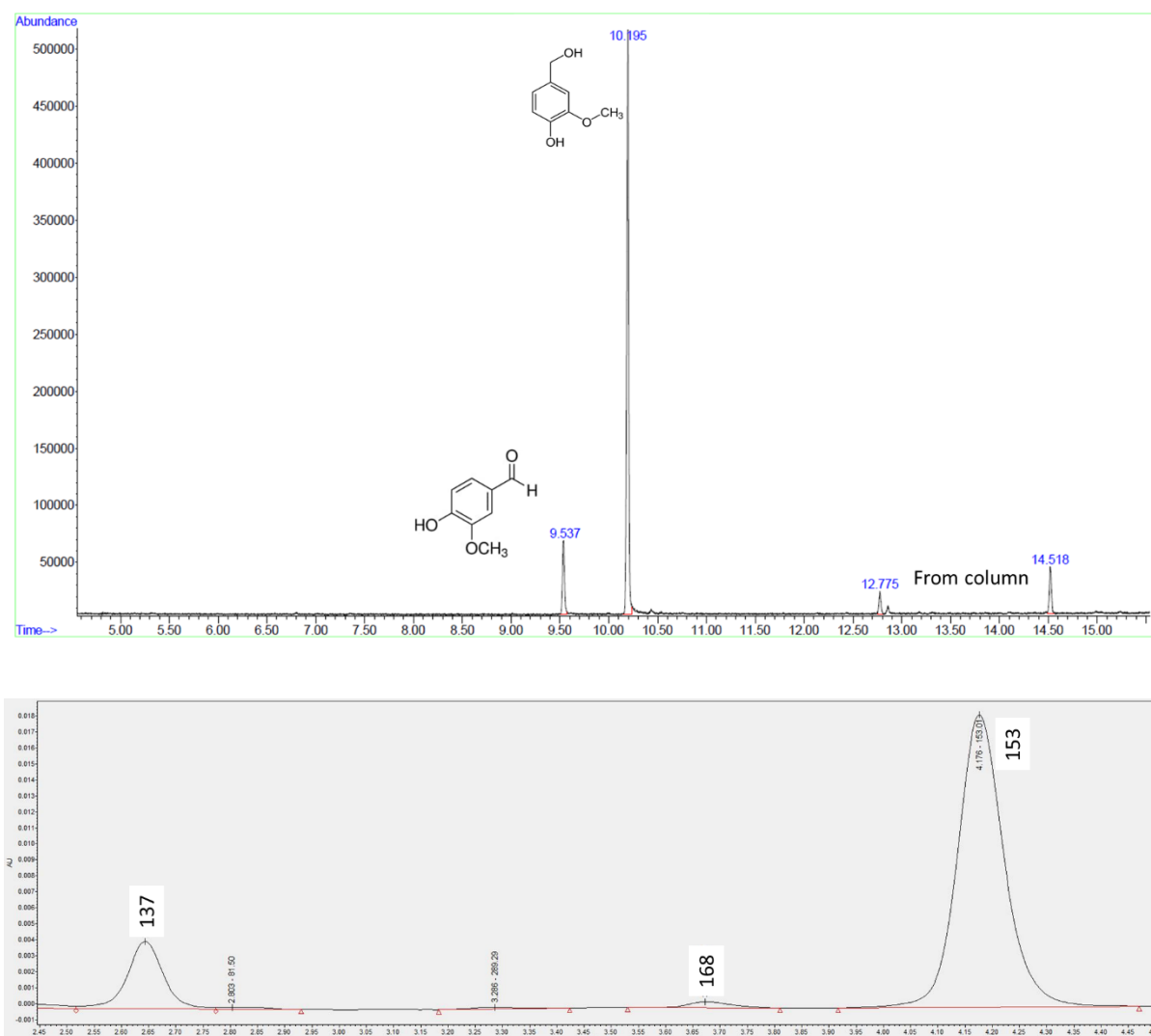


Figure S17. Oxidation products from vanillin alcohol (VanOH) analyzed with GC-MS and HPLC-MS.

Abundance

950000

900000

850000

800000

750000

700000

650000

600000

550000

500000

450000

400000

350000

300000

250000

200000

150000

100000

50000

0

Time-->

3.50 4.00 4.50 5.00 5.50 6.00 6.50 7.00 7.50 8.00 8.50 9.00 9.50 10.00 10.50 11.00 11.50 12.00 12.50 13.00 13.50 14.00 14.50

3.429

7.064

7.792

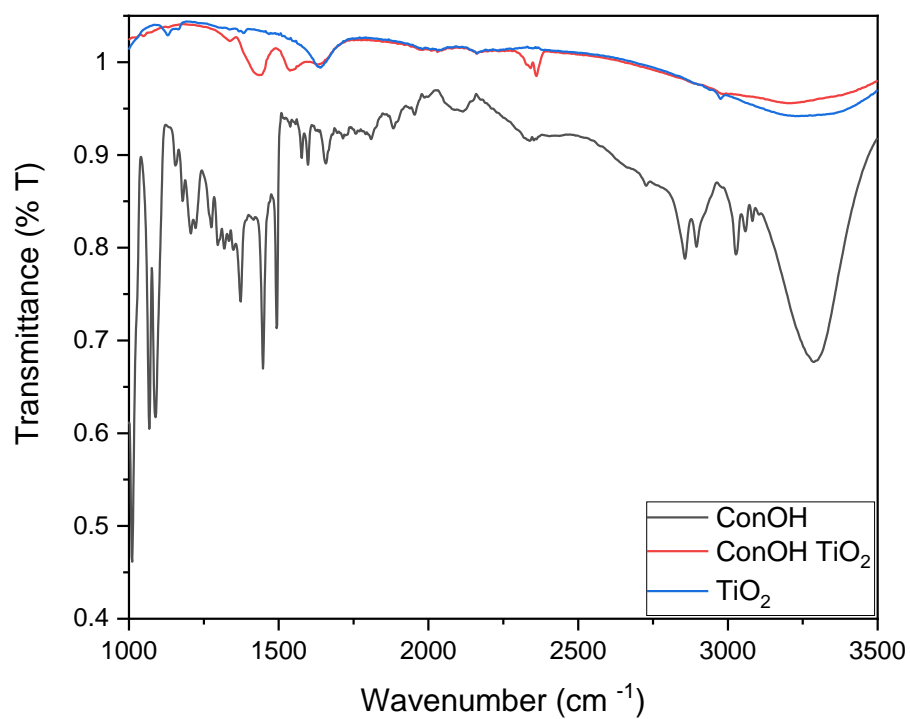
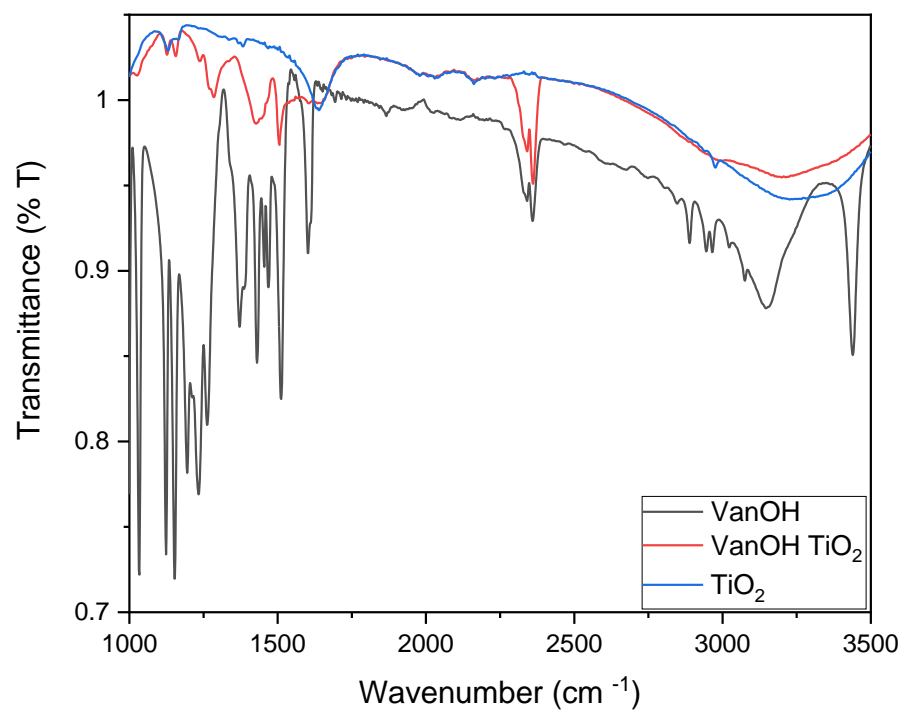
8.258

O=CC1=CC=CC=C1

O=CC=Cc1ccccc1

OCC=Cc1ccccc1

Figure S19. Oxidation products from cinnamyl alcohol (CinOH) analyzed with GC-MS.



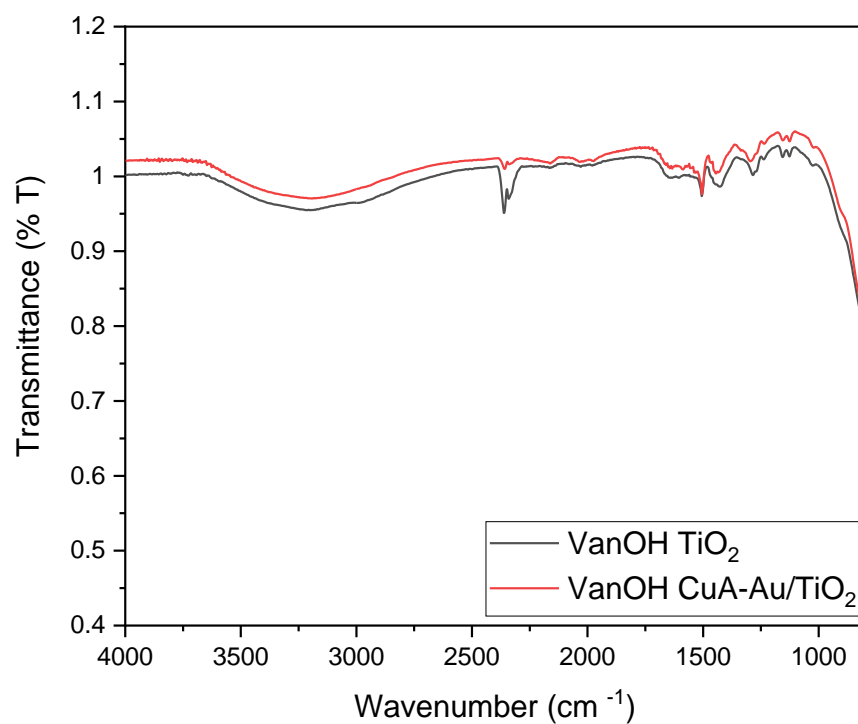
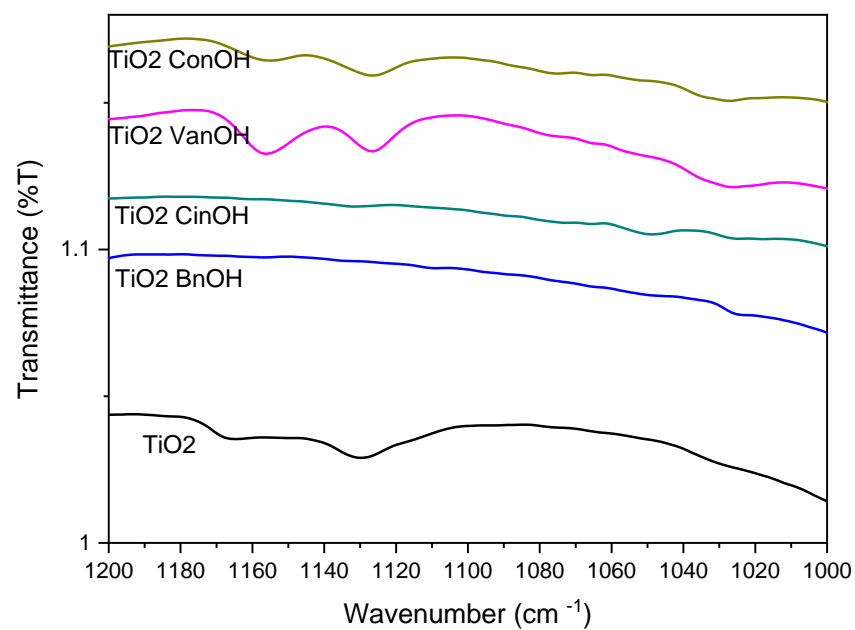


Figure S20. FT-IR spectra of aromatic alcohols (BnOH, CinOH, VanOH and ConOH) adsorbed  $\text{TiO}_2$  and VanOH adsorbed bimetallic  $\text{CuA-Au-TiO}_2$ .

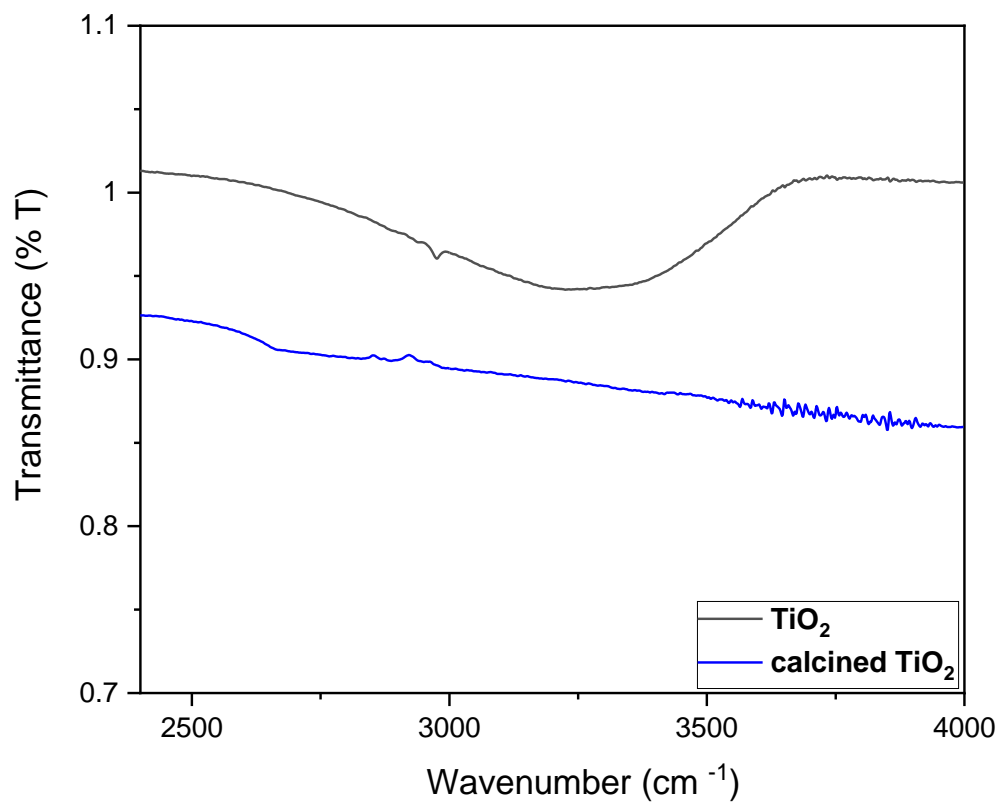


Figure S21. FT-IR spectra of sol-gel synthesized  $\text{TiO}_2$  and calcined under air (600  $^{\circ}\text{C}$ )  $\text{TiO}_2$  confirming removal of OH group.

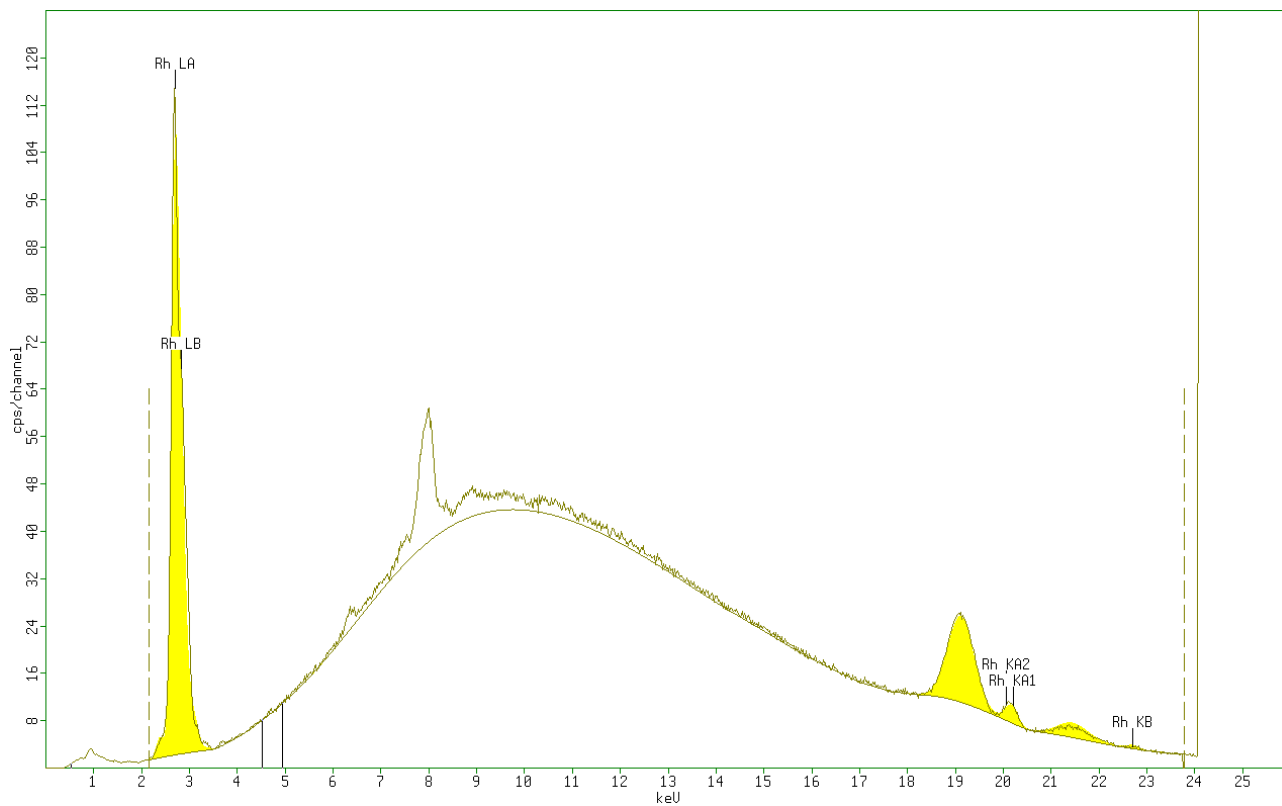


Figure S22. XRF image of sample from CuN/Au TiO<sub>2</sub> deposited microtube.

Good reusability of the catalyst was demonstrated, while no metals were detected in the filtered reaction mixtures. There were no traces of Ti or other metals in liquid sample. The other observed peaks are the fingerprint from the instrument.

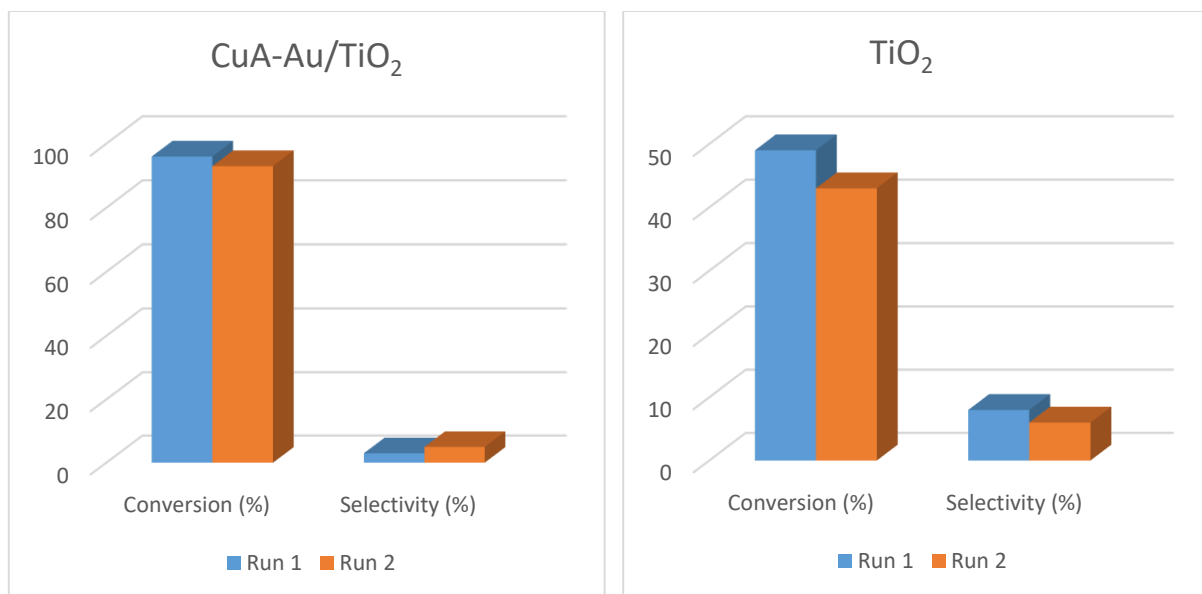


Figure S23. Photocatalytic activity with CuA-Au/TiO<sub>2</sub> (left) and sol-gel synthesized TiO<sub>2</sub> (right) (Run 1) and after washing the catalyst with ACN and H<sub>2</sub>O (Run 2) under UV irradiation (60min) in batch system with ConOH.

After each run the synthesized TiO<sub>2</sub> was recovered by decanting the solvent washed three times with water, dried in hot air oven for 48 hrs at 80 °C and used again in the next run with fresh aromatic alcohol solution. This procedure was repeated up to two times of application and the activity remain unchanged.



## REFERENCES

- 1 S. E. Vollset, E. Goren, C. W. Yuan, J. Cao, A. E. Smith, T. Hsiao, C. Bisignano, G. S. Azhar, E. Castro, J. Chalek, A. J. Dolgert, T. Frank, K. Fukutaki, S. I. Hay, R. Lozano, A. H. Mokdad, V. Nandakumar, M. Pierce, M. Pletcher, T. Robalik, K. M. Steuben, H. Y. Wunrow, B. S. Zlavog and C. J. L. Murray, *Lancet*, 2020, **396**, 1285–1306.
- 2 J. Zakzeski, P. C. A. Bruijninx, A. L. Jongerius and B. M. Weckhuysen, *Chem. Rev.*, 2010, **110**, 3552–3599.
- 3 S. R. Kadam, V. R. Mate, R. P. Panmand, L. K. Nikam, M. V. Kulkarni, R. S. Sonawane and B. B. Kale, *RSC Adv.*, 2014, **4**, 60626–60635.
- 4 S. Rana, N. Gupta and R. S. Rana, *Mater. Today Proc.*, 2018, **5**, 4218–4224.
- 5 T. Noël, Y. Cao and G. Laudadio, *Acc. Chem. Res.*, 2019, **52**, 2858–2869.
- 6 N. Kockmann, R. Hartman and A. Kulkarni, *J. Flow Chem.*, 2021, **11**, 211–212.
- 7 X. Zhang, Y. Wang, F. Hou, H. Li, Y. Yang, X. Zhang, Y. Yang and Y. Wang, *Appl. Surf. Sci.*, 2017, **391**, 476–483.
- 8 K. M. Lee, C. W. Lai, K. S. Ngai and J. C. Juan, *Water Res.*, 2016, **88**, 428–448.
- 9 Z. Gao, C. Pan, C. Choi and C. Chang, *Symmetry (Basel)*, 2021, **13**, 1325.
- 10 S. R. Pradhan, R. F. Colmenares-Quintero and J. C. C. Quintero, *Molecules*, , DOI:10.3390/molecules24183315.
- 11 N. Wang, X. Zhang, Y. Wang, W. Yu and H. L. W. Chan, *Lab Chip*, 2014, **14**, 1074–1082.
- 12 Y. Su, N. J. W. Straathof, V. Hessel and T. Noël, *Chem. - A Eur. J.*, 2014, **20**, 10562–10589.
- 13 S. Vidyacharan, B. T. Ramanjaneyulu, S. Jang and D. P. Kim, *ChemSusChem*, 2019, **12**, 2581–2586.

- 14 B. Ramos, S. Ookawara, Y. Matsushita and S. Yoshikawa, *J. Environ. Chem. Eng.*, 2014, **2**, 1487–1494.
- 15 J. J. Richardson, M. Björnmalm and F. Caruso, *Science (80-. )*, , DOI:10.1126/science.aaa2491.
- 16 C. Khositanon, S. Deepracha, S. Assabumrungrat, M. Ogawa and N. Weeranoppanant, *Ind. Eng. Chem. Res.*, 2022, **61**, 1322–1331.
- 17 D. Fernandez Rivas and S. Kuhn, *Top. Curr. Chem.*, 2016, 374.
- 18 M. Schoenitz, L. Grundemann, W. Augustin and S. Scholl, *Chem. Commun.*, 2015, **51**, 8213–8228.
- 19 A. P. U. S. Kuhn, Z. Dong, C. Delacour, K. Carogher, *Mater. Sci. Eng.*, 2020, **13**, 344.
- 20 R. Sadowski, A. Wach, M. Buchalska, P. Kuśtrowski and W. Macyk, *Appl. Surf. Sci.*, 2019, **475**, 710–719.
- 21 Y. Jiang, Y. Sun, H. Liu, F. Zhu and H. Yin, *Dye. Pigment.*, 2008, **78**, 77–83.
- 22 G. Varshney, S. R. Kanel, D. M. Kempisty, V. Varshney, A. Agrawal, E. Sahle-Demessie, R. S. Varma and M. N. Nadagouda, *Coord. Chem. Rev.*, 2016, **306**, 43–64.
- 23 M. Sankar, N. Dimitratos, P. J. Miedziak, P. P. Wells, J. Kiely and G. J. Hutchings, *Chem Soc Rev*, 2012, **41**, 8099–8139.
- 24 P. T. Anastas and J. C. Warner, *Green Chemistry: Theory and Practice.*, 1998.
- 25 X. Meng, Z. Zhang and X. Li, *J. Photochem. Photobiol. C Photochem. Rev.*, 2015, **24**, 83–101.
- 26 J. C. Colmenares, P. Lisowski and D. Łomot, *RSC Adv.*, 2013, **3**, 20186–20192.
- 27 Z. Yang, M. Liu and C. Lin, *Chem. Eng. J.*, 2016, **291**, 254–268.
- 28 X. Yao, Y. Zhang, L. Du, J. Liu and J. Yao, *Renew. Sustain. Energy Rev.*, 2015, **47**, 519–539.

- 29 J. C. Colmenares, R. S. Varma and V. Nair, *Chem. Soc. Rev.*, 2017, **46**, 6675–6686.
- 30 S. Aljbour, T. Tagawa and H. Yamada, *J. Ind. Eng. Chem.*, 2009, **15**, 829–834.
- 31 J. P. Knowles, L. D. Elliott and K. I. Booker-Milburn, *Beilstein J. Org. Chem.*, 2012, **8**, 2025–2052.
- 32 R. Munirathinam, J. Huskens and W. Verboom, *Adv. Synth. Catal.*, 2015, **357**, 1093–1123.
- 33 J. Yue, *Catal. Today*, 2018, **308**, 3–19.
- 34 L. Licklider and W. G. Kuhr, *Anal. Chem.*, 1994, **66**, 4400–4407.
- 35 S. Dimov and O. Gasenko, in *MATEC Web of Conferences*, 2017, vol. 115, p. 3011.
- 36 P. N. Nge, C. I. Rogers and A. T. Woolley, *Chem. Rev.*, 2013, **113**, 2550–2583.
- 37 S. Sohrabi, M. Keshavarz Moraveji and D. Iranshahi, *Rev. Chem. Eng.*, 2020, **36**, 687–722.
- 38 H. C. Aran, D. Salamon, T. Rijnaarts, G. Mul, M. Wessling and R. G. H. Lammertink, *J. Photochem. Photobiol. A Chem.*, 2011, **225**, 36–41.
- 39 O. Wörz, K. P. Jäckel, T. Richter and A. Wolf, *Chem. Eng. Sci.*, 2001, **56**, 1029–1033.
- 40 M. Krivec, K. Žagar, L. Suhadolnik, M. Čeh and G. Dražić, *ACS Appl. Mater. Interfaces*, 2013, **5**, 9088–9094.
- 41 H. Eskandarloo, A. Badiei, M. A. Behnajady and G. M. Ziarani, *Chem. Eng. J.*, 2015, **270**, 158–167.
- 42 D. F. Rivas, P. Cintas and H. J. G. E. Gardeniers, *Chem. Commun.*, 2012, **48**, 10935–10947.
- 43 R. J. Wood, J. Lee and M. J. Bussemaker, *Ultrason. Sonochem.*, 2017, **38**, 351–370.
- 44 P. Cintas, *Ultrason. Sonochem.*, 2016, **28**, 257–258.
- 45 Z. Dong, S. Zhao, Y. Zhang, C. Yao, Q. Yuan and G. Chen, *AIChE J.*, 2017, **63**, 1404–1418.

- 46 H. Wang, H. Nakamura, M. Uehara, M. Miyazaki and H. Maeda, *Chem. Commun.*, 2002, **2**, 1462–1463.
- 47 D. Chandrasekhar, S. Borra, J. S. Kapure, G. S. Shivaji, G. Srinivasulu and R. A. Maurya, *Org. Chem. Front.*, 2015, **2**, 1308–1312.
- 48 M. Oelgemoeller, *Chem. Eng. Technol.*, 2012, **35**, 1144–1152.
- 49 Y. Matsushita, T. Ichimura, N. Ohba, S. Kumada, K. Sakeda, T. Suzuki, H. Tanibata and T. Murata, *Pure Appl. Chem.*, 2007, **79**, 1959–1968.
- 50 O. Pandoli, T. Del Rosso, V. M. S. A, R. de S. Rezende and B. A. Marinkovic, *Quim. Nova*, 2015, **38**, 859–863.
- 51 K. Ren, J. Zhou and H. Wu, *Acc. Chem. Res.*, 2013, **46**, 2396–2406.
- 52 N. Wang, L. Lei, X. M. Zhang, Y. H. Tsang, Y. Chen and H. L. W. Chan, in *Microelectronic Engineering*, 2011, vol. 88, pp. 2797–2799.
- 53 D. Cambié, C. Bottecchia, N. J. W. Straathof, V. Hessel and T. Noël, *Chem. Rev.*, 2016, **116**, 10276–10341.
- 54 T. Noël, J. R. Naber, R. L. Hartman, J. P. McMullen, K. F. Jensen and S. L. Buchwald, *Chem. Sci.*, 2011, **2**, 287–290.
- 55 V. Nair, J. C. Colmenares and D. Lisovytskiy, *Green Chem.*, 2019, **21**, 1241–1246.
- 56 S. Aljbour, H. Yamada and T. Tagawa, *Chem. Eng. Process. Process Intensif.*, 2009, **48**, 1167–1172.
- 57 R. L. Hartman, J. R. Naber, N. Zaborenko, S. L. Buchwald and K. F. Jensen, *Org. Process Res. Dev.*, 2010, **14**, 1347–1357.
- 58 J. C. Colmenares, W. Ouyang, M. Ojeda, E. Kuna, O. Chernyayeva, D. Lisovytskiy, S. De, R. Luque and A. M. Balu, *Appl. Catal. B Environ.*, 2016, **183**, 107–112.

- 59 V. G. Pol, H. Grisar and A. Gedanken, *Langmuir*, 2005, **21**, 3635–3640.
- 60 Z. Zhong, Y. Mastai, Y. Koltypin, Y. Zhao and A. Gedanken, *Chem. Mater.*, 1999, **11**, 2350–2359.
- 61 S. Liu, Z. Guo, X. Qian, J. Zhang, J. Liu and J. Lin, *Sustain. Energy Fuels*, 2019, **3**, 1048–1054.
- 62 P. Qiu, B. Park, J. Choi, B. Thokchom, A. B. Pandit and J. Khim, *Ultrason. Sonochem.*, 2018, **45**, 29–49.
- 63 C. Y. Teh, T. Y. Wu and J. C. Juan, *Chem. Eng. J.*, 2017, **317**, 586–612.
- 64 J. C. Yu, L. Zhang and J. Yu, *New J. Chem.*, 2002, **26**, 416–420.
- 65 S. Das and V. C. Srivastava, *Photochem. Photobiol. Sci.*, 2016, **15**, 714–730.
- 66 S. Tao, M. Yang, H. Chen, M. Ren and G. Chen, *J. Colloid Interface Sci.*, 2017, **486**, 16–26.
- 67 S. Sachdev, R. Maugi, C. Kirk, Z. Zhou, S. D. R. Christie and M. Platt, *Colloids Interface Sci. Commun.*, 2017, **16**, 14–18.
- 68 I. R. Baxendale, S. C. Schou, J. Sedelmeier and S. V. Ley, *Chem. - A Eur. J.*, 2010, **16**, 89–94.
- 69 G. Jas and A. Kirschning, *Chem. - A Eur. J.*, 2003, **9**, 5708–5723.
- 70 J. P. McMullen and K. F. Jensen, *Org. Process Res. Dev.*, 2011, **15**, 398–407.
- 71 J. E. Kreutz, A. Shukhaev, W. Du, S. Druskin, O. Daugulis and R. F. Ismagilov, *J. Am. Chem. Soc.*, 2010, **132**, 3128–3132.
- 72 J. C. Pastre, D. L. Browne and S. V. Ley, *Chem. Soc. Rev.*, 2013, **42**, 8849–8869.
- 73 D. G. Shchukin and D. V. Sviridov, *J. Photochem. Photobiol. C Photochem. Rev.*, 2006, **7**, 23–39.

- 74 R. Lakerveld, G. S. J. Sturm, A. I. Stankiewicz and G. D. Stefanidis, *Curr. Opin. Chem. Eng.*, 2014, **5**, 37–41.
- 75 J. Saien and A. R. Soleymani, *J. Ind. Eng. Chem.*, 2012, **18**, 1683–1688.
- 76 M. E. Leblebici, G. D. Stefanidis and T. Van Gerven, *Chem. Eng. Process. Process Intensif.*, 2015, **97**, 106–111.
- 77 D. Heggo and S. Ookawara, *Chem. Eng. Sci.*, 2017, **169**, 67–77.
- 78 C. Shen, Y. J. Wang, J. H. Xu and G. S. Luo, *Chem. Eng. J.*, 2015, **277**, 48–55.
- 79 M. Liu, X. Zhu, R. Chen, Q. Liao, H. Feng and L. Li, *Chem. Eng. J.*, 2016, **301**, 35–41.
- 80 B. Stephan, L. Ludovic and W. Dominique, *Chem. Eng. J.*, 2011, **169**, 216–225.
- 81 Y. Chen and D. D. Dionysiou, *J. Mol. Catal. A Chem.*, 2006, **244**, 73–82.
- 82 G. Charles, T. Roques-Carmes, N. Becheikh, L. Falk, J. M. Commenge and S. Corbel, *J. Photochem. Photobiol. A Chem.*, 2011, **223**, 202–211.
- 83 S. Corbel, N. Becheikh, T. Roques-Carmes and O. Zahraa, *Chem. Eng. Res. Des.*, 2014, **92**, 657–662.
- 84 M. Oelgemöller and O. Shvydkiv, *Molecules*, 2011, **16**, 7522–7550.
- 85 N. Padoin, L. Andrade, J. Ângelo, A. Mendes, R. de F. P. M. Moreira and C. Soares, *AIChE J.*, 2016, **62**, 2794–2802.
- 86 W. Liao, N. Wang, T. Wang, J. Xu, X. Han, Z. Liu, X. Zhang and W. Yu, *Biomicrofluidics*, 2016, **10**, 14123.
- 87 M. K. Moharana, N. R. Peela, S. Khandekar and D. Kunzru, *Renew. Sustain. Energy Rev.*, 2011, **15**, 524–533.
- 88 D. Wilms, J. Klos and H. Frey, *Macromol. Chem. Phys.*, 2008, **209**, 343–356.

- 89 C. H. Hornung, B. Hallmark, M. Baumann, I. R. Baxendale, S. V. Ley, P. Hester, P. Clayton and M. R. MacKley, *Ind. Eng. Chem. Res.*, 2010, **49**, 4576–4582.
- 90 G. Davis, *Innov. Pharm. Technol.*, 2008, 24–27.
- 91 H. Song, D. L. Chen and R. F. Ismagilov, *Angew. Chemie - Int. Ed.*, 2006, 45, 7336–7356.
- 92 J. P. McMullen, M. T. Stone, S. L. Buchwald and K. F. Jensen, *Angew. Chemie - Int. Ed.*, 2010, **49**, 7076–7080.
- 93 J. R. Naber and S. L. Buchwald, *Angew. Chemie - Int. Ed.*, 2010, **49**, 9469–9474.
- 94 A. Okawa, R. Yoshida, T. Isozaki, Y. Shigesato, Y. Matsushita and T. Suzuki, *Catal. Commun.*, 2017, **100**, 1–4.
- 95 A. R. Hawkins and H. Schmidt, *Handbook of Optofluidics*, 2010.
- 96 M. Ohering, *Materials Science of Thin Films, Deposition and Structure*, Academic Press: San Diego, 2002.
- 97 A. Visan, D. Rafieian, W. Ogieglo and R. G. H. Lammertink, *Appl. Catal. B Environ.*, 2014, **150–151**, 93–100.
- 98 H. O. Pierson, *Handbook of Chemical Vapor Deposition: Technology, and Applications*, Noyes Publications: Norwich, 2001.
- 99 D. Grosso, *J. Mater. Chem.*, 2011, **21**, 17033–17038.
- 100 K. J. Edler and S. J. Roser, *Int. Rev. Phys. Chem.*, 2001, **20**, 387–466.
- 101 Z. Meng, X. Zhang and J. Qin, *Nanoscale*, 2013, **5**, 4687–4690.
- 102 D. Rafieian, R. T. Driessen, W. Ogieglo and R. G. H. Lammertink, *ACS Appl. Mater. Interfaces*, 2015, **7**, 8727–8732.
- 103 L.-D. Piveteau, L.-D. Piveteau, B. Gasser and L. Schlapbach, .

- 104 A. Manivannan, N. Spataru, K. Arihara and A. Fujishima, *Electrochem. Solid-State Lett.*, , DOI:10.1149/1.2007427.
- 105 R. Y. Chein, L. C. Chen, Y. C. Chen and J. N. Chung, *Int. J. Hydrogen Energy*, 2009, **34**, 5398–5408.
- 106 S. Lopez-Orozco, A. Inayat, A. Schwab, T. Selvam and W. Schwieger, *Adv. Mater.*, 2011, **23**, 2602–2615.
- 107 A. Tanimu, S. Jaenicke and K. Alhooshani, *Chem. Eng. J.*, 2017, 327, 792–821.
- 108 N. D. Banić, B. F. Abramović, D. V. Šojić, J. B. Krstić, N. L. Finčur and I. P. Bočković, *Chem. Eng. J.*, 2016, **286**, 184–190.
- 109 H. Nakamura, X. Li, H. Wang, M. Uehara, M. Miyazaki, H. Shimizu and H. Maeda, *Chem. Eng. J.*, 2004, **101**, 261–268.
- 110 E. V. Rebrov, A. Berenguer-Murcia, H. E. Skelton, B. F. G. Johnson, A. E. H. Wheatley and J. C. Schouten, *Lab Chip*, 2009, **9**, 503–506.
- 111 L. Li, D. Tang, Y. Song and B. Jiang, *Chem. Eng. J.*, 2018, **339**, 71–77.
- 112 L. Suhadolnik, M. Krivec, Ž. Kristina, G. Dra and M. Ceh, *J. Ind. Eng. Chem.*, 2017, **47**, 384–390.
- 113 J. C. Colmenares, V. Nair, E. Kuna and D. Łomot, *Ultrason. Sonochem.*, 2018, **41**, 297–302.
- 114 Polish patent Nr. PAT.231485, 2017.
- 115 A. G. Corrêa, V. G. Zuin, V. F. Ferreira and P. G. Vazquez, *Pure Appl. Chem.*, 2013, **85**, 1643–1653.
- 116 K. Wu and S. Kuhn, *Chim. Oggi/Chemistry Today*, 2014, **32**, 62–66.
- 117 A. E. Cassano and O. M. Alfano, *Catal. Today*, 2000, **58**, 167–197.



- 118 A. Kar, Y. R. Smith and V. Subramanian, *Environ. Sci. Technol.*, 2009, **43**, 3260–3265.
- 119 J. Colina-Márquez, F. MacHuca-Martínez and G. L. Puma, *Environ. Sci. Technol.*, 2010, **44**, 5112–5120.
- 120 F. Lévesque and P. H. Seeberger, *Org. Lett.*, 2011, **13**, 5008–5011.
- 121 X. Wang, G. D. Cuny and T. Noël, *Angew. Chemie - Int. Ed.*, 2013, **52**, 7860–7864.
- 122 J. C. Colmenares, *ChemSusChem*, 2014, **7**, 1512–1527.
- 123 Z. R. Tang, X. Yin, Y. Zhang and Y. J. Xu, *RSC Adv.*, 2013, **3**, 5956–5965.
- 124 G. Chatel, S. Valange, R. Behling and J. C. Colmenares, *ChemCatChem*, 2017, **9**, 2615–2621.
- 125 X. Hangxun, B. W. Zeiger and K. S. Suslick, *Chem. Soc. Rev.*, 2013, **42**, 2555–2567.
- 126 M. Bora and M. Shusteff, *Lab Chip*, 2015, **15**, 3192–3202.
- 127 J. J. John, S. Kuhn, L. Braeken and T. Van Gerven, *Chem. Eng. Process. Process Intensif.*, 2016, **102**, 37–46.
- 128 K. Thangavadivel, M. Konagaya, K. Okitsu and M. Ashokkumar, *J. Environ. Chem. Eng.*, 2014, **2**, 1841–1845.
- 129 P. Sathishkumar, R. V. Mangalaraja and S. Anandan, *Renew. Sustain. Energy Rev.*, 2016, **55**, 426–454.
- 130 D. Rossi, R. Jamshidi, N. Saffari, S. Kuhn, A. Gavriilidis and L. Mazzei, *Cryst. Growth Des.*, 2015, **15**, 5519–5529.
- 131 M. Jiang, C. D. Papageorgiou, J. Waetzig, A. Hardy, M. Langston and R. D. Braatz, *Cryst. Growth Des.*, 2015, **15**, 2486–2492.
- 132 D. F. Rivas, E. Castro-Hernández, A. L. Villanueva Perales and W. van der Meer, *Chem. Eng. Process. Process Intensif.*, 2018, **123**, 221–232.

- 133 M. L. Wang and V. Rajendran, *J. Mol. Catal. A Chem.*, 2007, **273**, 5–13.
- 134 S. H. Kwon, J. H. Kim and D. Cho, *J. Ind. Eng. Chem.*, 2009, **15**, 157–162.
- 135 L. H. Thompson and L. K. Doraiswamy, *Ind. Eng. Chem. Res.*, 1999, **38**, 1215–1249.
- 136 G. Laudadio, H. P. L. Gemoets, V. Hessel and T. Noël, *J. Org. Chem.*, 2017, **82**, 11735–11741.
- 137 J. Joseph, S. Kuhn, L. Braeken and T. Van Gerven, *Chem. Eng. Process. Process Intensif.*, 2017, **113**, 35–41.
- 138 B. A. Rizkin, F. G. Popovic and R. L. Hartman, *J. Vac. Sci. Technol. A*, 2019, **37**, 50801.
- 139 D. A. Giannakoudakis, A. Qayyum, V. Nair, A. Khan, S. R. Pradhan, J. Prekodravac, K. Rekos, A. P. LaGrow, O. Bondarchuk, D. Łomot, K. S. Triantafyllidis and J. C. Colmenares, *Mol. Catal.*, 2021, **514**, 111664.
- 140 R. Del Angel, J. C. Durán-Álvarez and R. Zanella, in *Titanium Dioxide - Material for a Sustainable Environment*, InTech, 2018.
- 141 Q. Zhang, Q. Zhang, H. Wang and Y. Li, *J. Hazard. Mater.*, 2013, **254–255**, 318–324.
- 142 R. A. Torres, G. Sarantakos, E. Combet, C. Pétrier and C. Pulgarin, *J. Photochem. Photobiol. A Chem.*, 2008, **199**, 197–203.
- 143 S. Ko, J. Pekarovic, P. D. Fleming and P. Ari-Gur, *Mater. Sci. Eng. B Solid-State Mater. Adv. Technol.*, 2010, **166**, 127–131.
- 144 J. F. Guayaquil-Sosa, B. Serrano-Rosales, P. J. Valadés-Pelayo and H. de Lasa, *Appl. Catal. B Environ.*, 2017, **211**, 337–348.
- 145 P. Kubelka and F. Munk, *Z. Tech. Phys.*, 1931, **12**, 593–601.
- 146 S. M. Gupta and M. Tripathi, *Chinese Sci. Bull.*, 2011, **56**, 1639–1657.

- 147 L. L. Tan, W. J. Ong, S. P. Chai and A. R. Mohamed, *Nanoscale Res. Lett.*, 2013, **8**, 1–9.
- 148 J. Lombardi, L. Yang, F. A. Pearsall, N. Farahmand, Z. Gai, S. J. L. Billinge and S. O'Brien, *Chem. Mater.*, 2019, **31**, 1318–1335.
- 149 H. M. Rietveld, *J. Appl. Crystallogr.*, 1969, **2**, 65–71.
- 150 S. Yurdakal, G. Palmisano, V. Loddo, O. Alagöz, V. Augugliaro and L. Palmisano, *Green Chem.*, 2009, **11**, 510–51.
- 151 T. A. Kandiel, L. Robben, A. Alkaim and D. Bahnemann, in *Photochemical and Photobiological Sciences*, Royal Society of Chemistry, 2013, vol. 12, pp. 602–609.
- 152 K. S. W. Sing and R. T. Williams, *Adsorpt. Sci. Technol.*, 2004, **22**, 773–782.
- 153 G. Srinivas, V. Krungleviciute, Z. X. Guo and T. Yildirim, *Energy Environ. Sci.*, 2014, **7**, 335–342.
- 154 Y. Park, W. Kim, D. Monllor-Satoca, T. Tachikawa, T. Majima and W. Choi, *J. Phys. Chem. Lett.*, 2013, **4**, 189–194.
- 155 D. Friedmann, C. Mendive and D. Bahnemann, *Appl. Catal. B Environ.*, 2010, **99**, 398–406.
- 156 F. Li, D. Hu, Y. Yuan, B. Luo, Y. Song, S. Xiao, G. Chen, Y. Fang and F. Lu, *Mol. Catal.*, 2018, **452**, 75–82.
- 157 T. Chen, Z. Xu, L. Zhou, J. Qiu, M. Wang and J. Wang, *Mol. Catal.*, 2019, **474**, 110422.
- 158 C. Han, S. H. Li, Z. R. Tang and Y. J. Xu, *Chem. Sci.*, 2018, **9**, 8914–8922.
- 159 C. Han, Z. R. Tang, J. Liu, S. Jin and Y. J. Xu, *Chem. Sci.*, 2019, **10**, 3514–3522.
- 160 X. Lang, W. Ma, C. Chen, H. Ji and J. Zhao, *Acc. Chem. Res.*, 2014, **47**, 355–363.
- 161 Q. Xu, Y. Ma, J. Zhang, X. Wang, Z. Feng and C. Li, *J. Catal.*, 2011, **278**, 329–335.

- 162 T. Lv, J. Zhao, M. Chen, K. Shen, D. Zhang, J. Zhang, G. Zhang and Q. Liu, *Materials (Basel)*, 2018, **11**, 1946.
- 163 J. Chen, F. Qiu, W. Xu, S. Cao and H. Zhu, *Appl. Catal. A Gen.*, 2015, 495, 131–140.
- 164 S. P. Pitre, T. P. Yoon and J. C. Scaiano, *Chem. Commun.*, 2017, **53**, 4335–4338.
- 165 M. Roseau, N. Dhaouadi, C. Rolando, L. Chausset-Boissarie and M. Penhoat, *J. Flow Chem.*, 2020, **10**, 347–352.
- 166 S. R. Pradhan, V. Nair, D. A. Giannakoudakis, D. Lisovytskiy and J. C. Colmenares, *Mol. Catal.*, 2020, **486**, 110884.
- 167 C. Garlisi, G. Scandura, J. Szlachetko, S. Ahmadi, J. Sa and G. Palmisano, *Appl. Catal. A Gen.*, 2016, **526**, 191–199.
- 168 F. Mostaghni and Y. Abed, *Mater. Res.*, 2016, **19**, 741–745.
- 169 A. El Mragui, O. Zegaoui, I. Daou and J. C. G. Esteves da Silva, *Environ. Sci. Pollut. Res.*, 2021, **28**, 25130–25145.
- 170 B. Abebe, H. C. A. Murthy and E. Amare, 2018, 225–255.
- 171 S. Banerjee, D. D. Dionysiou and S. C. Pillai, *Appl. Catal. B Environ.*, 2015, **176–177**, 396–428.
- 172 H. H. Do, D. L. T. Nguyen, X. C. Nguyen, T. H. Le, T. P. Nguyen, Q. T. Trinh, S. H. Ahn, D. V. N. Vo, S. Y. Kim and Q. Van Le, *Arab. J. Chem.*, 2020, **13**, 3653–3671.
- 173 A. Carabin, P. Drogui and D. Robert, *J. Taiwan Inst. Chem. Eng.*, 2015, **54**, 109–117.
- 174 A. A. Kashale, A. S. Rasal, G. P. Kamble, V. H. Ingole, P. K. Dwivedi, S. J. Rajoba, L. D. Jadhav, Y. Ling, J. Chang and A. V Ghule, *Compos. Part B*, 2019, **167**, 44–50.
- 175 A. El Mragui, I. Daou and O. Zegaoui, 2018, 29–34.

- 176 A. K. Gupta, A. Pal and C. Sahoo, *Dye. Pigment.*, 2006, **69**, 224–232.
- 177 Ł. Justyna and M. Paszkiewicz-gawron, *ChemCatChem*, 2017, **9**, 4377–4388.
- 178 A. Khan, M. Goepel, A. Kubas, D. Łomot and W. Lisowski, 2021, 1–13.
- 179 M. V. Dozzi, A. Saccomanni, M. Altomare and E. Selli, *Photochem. Photobiol. Sci.*, 2013, 595–601.
- 180 S. R. Pradhan, D. Lisovytskiy and J. C. Colmenares, *Catal. Commun.*, 2022, **162**, 106375.
- 181 A. El Mragui, Y. Logvina, L. Luís Pinto da Silva, O. Zegaoui and J. C. G. E. da Silva, *Materials (Basel).*, 2019, **12**, 3874.
- 182 A. Gołębiewska, W. Lisowski, M. Jarek, G. Nowaczyk, M. Michalska, S. Jurga and A. Zaleska-Medynska, *Mol. Catal.*, 2017, **442**, 154–163.
- 183 H. Liu, Y. Liu, Y. Li, Z. Tang and H. Jiang, 2010, 13362–13369.
- 184 G. M. Mullen, L. Zhang, E. J. Evans, T. Yan, G. Henkelman and C. B. Mullins, *J. Am. Chem. Soc.*, 2014, **136**, 6489–6498.
- 185 T. Jiang, C. Jia, L. Zhang, S. He, Y. Sang, H. Li, Y. Li, X. Xu and H. Liu, 2015, 209–217.
- 186 R. Kavitha and S. G. Kumar, *Chem. Pap.*, 2020, **74**, 717–756.
- 187 L. J. Durndell, C. M. A. Parlett, N. S. Hondow, K. Wilsona and A. F. Lee, 2013, **123**, 5412–5419.
- 188 L. Wan, M. Jiang, D. Cheng and F. Chen, *React. Chem. Eng.*, 2022, **7**, 490–550.
- 189 S. Borra, D. Chandrasekhar, S. Adhikary, S. Rasala, S. Gokulnath and R. A. Maurya, *J. Org. Chem.*, 2017, **82**, 2249–2256.
- 190 G. Leofanti, M. Padovan, G. Tozzola and B. Venturelli, *Catal. Today*, 1998, **41**, 207–219.

- 191 X. Yu, J. Yu, B. Cheng and M. Jaroniec, *jpcc*, 2009, **113**, 17527–17535.
- 192 Y. Chen, W. Li, J. Wang, Y. Gan, L. Liu and M. Ju, "*Applied Catal. B, Environ.*", 2016, **191**, 94–105.
- 193 Z. Liu, J. Wu, J. Wang, R. Wang, G. Liu, Y. Qi, W. Xu, G. Luo and M. Xu, *Colloids Surfaces A*, 2021, **610**, 125702.
- 194 T. Nogawa, T. Isobe, S. Matsushita and A. Nakajima, *Mater. Lett.*, 2012, **82**, 174–177.
- 195 A. Monga, A. Bathla and B. Pal, *Sol. Energy*, 2017, **155**, 1403–1410.
- 196 N. Li, D. Geng and J. Zhou, *Catal. Letters*, 2022, **152**, 124–138.
- 197 X. Zhang, Y. L. Chen, R. Liu and D. P. Tsai, *Rep. Prog. Phys.*, 2013, **76**, 46401.
- 198 A. Go, A. Zieli and A. Zaleska, *J. Adv. Oxid. Technol.*, 2012, **15**, 71.
- 199 S. Liu and Y. Xu, *Nat. Publ. Gr.*, 2016, 1–13.
- 200 Y. Zhuang, L. Liu, X. Wu, Y. Tian, X. Zhou, S. Xu and Z. Xie, *Part. Part. Syst. Charact.*, 2019, **1800077**, 1–8.
- 201 A. Goł, A. Malankowska, M. Jarek, W. Lisowski, G. Nowaczyk, S. Jurga and A. Zaleska-medynska, *Appl. Catal. B Environ.*, 2016, **196**, 27–40.
- 202 Z. Duan, Y. Huang, D. Zhang and S. Chen, *Sci. Rep.*, 2019, 1–8.
- 203 D. I. Anwar and D. Mulyadi, *Procedia Chem.*, 2015, **17**, 49–54.
- 204 Z. Wang, L. S. De Soto, C. Me, S. Casale and L. Delannoy, *ChemComm*, 2021, **57**, 7031–7034.
- 205 S. Kruanetr and R. Wanchanthuek, *Mater. Res. Express*, 2017, **4**, 76507.
- 206 V. K. Bulasara, R. Uppaluri and M. K. Purkait, *Mater. Manuf. Process.*, 2012, **6914**, 201–206.

- 207 G. Wu, G. L. Brett, E. Cao, A. Constantinou, P. Ellis, S. Kuhn, G. J. Hutchings, D. Bethell and A. Gavriilidis, *Catal. Sci. Technol.*, 2016, **6**, 4749–4758.
- 208 R. Taboada-puig, T. Moreira, J. M. Lema, K. Fagerstedt and H. Heikkinen, *biotechnol. prog.*, 2018, **34**, 81–90.
- 209 G. Zhang and W. Choi, *ChemComm*, 2012, **48**, 10621–10623.
- 210 S. Kim and W. Choi, *J. Phys. Chem. B*, 2005, **109**, 5143–5149.
- 211 C. Imparato, G. D’Errico, W. Macyk, M. Kobielski, G. Vitiello and A. Antonio, *Langmuir*, 2022, **38**, 1821–1832.
- 212 G. Zhang, G. Kim and W. Choi, *Energy Environ. Sci.*, 2014, **7**, 954.
- 213 T. J. Mason, *Ultrason. Sonochem.*, 2016, **29**, 519–523.
- 214 E. Pelizzetti and M. Schiavello, *Photochemical Conversion and Storage of Solar Energy*, Kluwer Academic Publishers, 1991.
- 215 T. Tsompanoglou, *Dr. Thesis*.
- 216 I. Kharlamova, A. Kharlamov and P. Vlasák, *Eng. Mech.*, 2014, **21**, 103–110.
- 217 M. Mustafa, sheraz ali, D. Ahmed Mohammed Osman and M. Abbas Mustafa, *J. Nanosci. Nanoeng.*, 2015, **1**, 248–251.
- 218 Z. Mirzaeifard, Z. Shariatnia, M. Jourshabani and S. M. Rezaei Darvishi, *Ind. Eng. Chem. Res.*, 2020, **59**, 15894–15911.